



**HAL**  
open science

# Morphology, statistics, and time dynamics of the liquid jet breakup in coaxial two-fluid atomization

Oliver Tolfts

► **To cite this version:**

Oliver Tolfts. Morphology, statistics, and time dynamics of the liquid jet breakup in coaxial two-fluid atomization. Fluid Dynamics [physics.flu-dyn]. Université Grenoble Alpes [2020-..], 2023. English. NNT : 2023GRALI056 . tel-04246388

**HAL Id: tel-04246388**

**<https://theses.hal.science/tel-04246388>**

Submitted on 30 Nov 2023

**HAL** is a multi-disciplinary open access archive for the deposit and dissemination of scientific research documents, whether they are published or not. The documents may come from teaching and research institutions in France or abroad, or from public or private research centers.

L'archive ouverte pluridisciplinaire **HAL**, est destinée au dépôt et à la diffusion de documents scientifiques de niveau recherche, publiés ou non, émanant des établissements d'enseignement et de recherche français ou étrangers, des laboratoires publics ou privés.

THÈSE

Pour obtenir le grade de

**DOCTEUR DE L'UNIVERSITÉ GRENOBLE ALPES**

École doctorale : I-MEP2 - Ingénierie - Matériaux, Mécanique, Environnement, Energétique, Procédés, Production

Spécialité : MEP - Mécanique des fluides Energétique, Procédés

Unité de recherche : Laboratoire des Ecoulements Géophysiques et Industriels

**Morphologie, statistique et dynamique temporelle de la rupture d'un jet liquide en atomisation assistée**

**Morphology, statistics, and time dynamics of the liquid jet breakup in coaxial two-fluid atomization**

Présentée par :

**Oliver TOLFTS**

Direction de thèse :

**Nathanaël MACHICOANE**  
Université Grenoble Alpes

Directeur de thèse

Rapporteurs :

**Jean-Philippe MATAS**

PROFESSEUR DES UNIVERSITES, Université de Lyon 1 - Claude Bernard

**Alberto ALISEDA**

FULL PROFESSOR, University of Washington

Thèse soutenue publiquement le **10 juillet 2023**, devant le jury composé de :

**Nathanaël MACHICOANE**

CHARGE DE RECHERCHE, CNRS délégation Alpes

Directeur de thèse

**Jean-Philippe MATAS**

PROFESSEUR DES UNIVERSITES, Université de Lyon 1 - Claude Bernard

Rapporteur

**Henda DJERIDI**

PROFESSEUR DES UNIVERSITES, Grenoble INP

Présidente

**Alberto ALISEDA**

FULL PROFESSOR, University of Washington

Rapporteur

**Nicolas RIMBERT**

PROFESSEUR DES UNIVERSITES, Université de Lorraine

Examineur

Invités :

**Christophe DUMOUCHEL**

DIRECTEUR DE RECHERCHE, Laboratoire CORIA







UNIVERSITÉ DE GRENOBLE ALPES  
**ÉCOLE DOCTORALE I-MEP2**

Ingénierie - Matériaux, Mécanique, Environnement, Energétique, Procédés, Production.

**T H È S E**

pour obtenir le titre de

**Docteur en sciences**

de l'Université Grenoble Alpes

**Mention : MÉCANIQUE DES FLUIDES, ENERGÉTIQUE,  
PROCÉDÉS**

Présentée et soutenue par

**Oliver TOLFTS**

**Morphologie, statistique et dynamique temporelle de la  
rupture d'un jet liquide en atomisation assistée**

Thèse dirigée par Nathanaël MACHICOANE

préparée au Laboratoire des Écoulements Géophysiques et  
Industriels

soutenue le 10/07/2023

**Jury :**

*Présidente :* Henda DJERIDI  
*Rapporteurs :* Jean-Philippe MATAS  
Alberto ALISEDA  
*Examineur :* Nicolas Rimbart  
*Directeur :* Nathanaël MACHICOANE



# Acknowledgements

Je tiens à remercier les membres du jury, Alberto, Henda, Jean-Philippe et Nicolas d'avoir pris le temps de lire et de juger mon travail. I especially thank the reviewers, Alberto and Jean-Philippe, for sharing your expertise and for your suggestions of improvements on this manuscript.

Nathanaël, je te remercie pour les innombrables explications que tu as su m'apporter pendant ces trois années. Tu as su me guider sur la voie de la recherche expérimentale en jonglant entre ta casquette de physicien, ta casquette d'informaticien et ta casquette de technicien tout au long de ma thèse et je t'en remercie.

Je remercie l'intégralité des membres des services instrumentation, informatique, administratif, mécanique et du bureau de développement du LEGI, pour leur bonne humeur et leur aide tout au long de ces trois années. Je remercie particulièrement Pascal, Muriel et Francois, pour votre disponibilité et le temps que vous avez passé à mettre votre expertise au service de l'élaboration et de l'amélioration de l'installation expérimentale.

I thank all the Ph.D. students from LEGI, for all the great moments we spent together, et pour votre bonne humeur au quotidien.

Je tiens à remercier ma Maman pour l'amour inconditionnel qu'elle m'apporte, pour son soutien tout au long de ma scolarité, et sans qui je n'aurais jamais accompli ce doctorat.

I would like to give a special thanks to my older brother Harold, who accepted to read this manuscript and corrected my spelling mistakes.

Je voudrais également remercier Antoine. Notre relation a été un socle sur lequel je savais que je pouvais compter. Tu m'as apporté du réconfort, de la compassion et de la chartreuse quand j'en avais le plus besoin.

Je remercie plus généralement ma famille et mes amis de m'avoir soutenu jusqu'au bout. Vous m'avez écouté me plaindre et vous avez été aux petits oignons avec moi dans les moments difficiles, malgré vos propres difficultés, m'apportant le soutien qu'il me fallait durant ce périple.

Enfin je remercie Jeanne, qui a quelque part rempli tous ces rôles et qui me donne une raison d'avancer au quotidien.

## Résumé de la thèse

### Introduction

L'atomisation est le processus de séparation d'un objet en fragments de lui-même, formant dans le cas du liquide un spray. De nombreuses méthodes d'atomisation liquide existent et celle étudiée dans ce manuscrit est l'atomisation assistée par courant gazeux en géométrie coaxiale. Dans cette situation un jet liquide rond est entouré d'un courant annulaire de gaz à haute vitesse. L'interaction des deux fluides mène à la rupture du jet liquide, créant un nuage de gouttes : un spray. Les nombres sans dimension utilisés dans ce manuscrit pour décrire le phénomène d'atomisation sont principalement le nombre de Weber  $We$ , comparant les forces aérodynamiques à la tension de surface, le nombre de Reynolds liquide  $Re_l$  et le rapport des pressions dynamique gaz-liquide  $M$ , qui compare la pression dynamique du courant gazeux sur l'interface à celle du courant liquide sur l'interface. Différentes longueurs caractéristiques du processus d'atomisation sont introduites, avec une attention particulière portée à la longueur du cœur liquide  $L_B$ , définie comme la longueur de la portion de liquide hydrauliquement connectée à l'injecteur, qui sera le sujet du chapitre 3. Un historique des travaux réalisés à l'aide d'imagerie par rayon X présents dans la littérature et portant sur l'atomisation est présentée. L'avantage de cette méthode est qu'elle donne une information quantitative sur la répartition massique du liquide. Une technique d'analyse de films à rayon X à haute fréquence d'acquisition a été développée et utilisée durant cette thèse, et sera présentée dans le chapitre 4.

### Matériel et méthodes

Ce chapitre, attaché aux moyens et aux choix liés à l'installation expérimentale, débute sur une description géométrique de la buse d'atomisation utilisée durant cette thèse. L'acheminement des fluides jusqu'à la buse ainsi que le programme développé pour piloter l'installation expérimentale sont soigneusement décrits et permettent à un futur utilisateur de prendre en main l'installation rapidement. Une attention particulière est donnée à la reproductibilité des conditions d'injection et aux incertitudes liées à l'installation expérimentale. La méthode mise en place pour moduler les propriétés turbulentes du courant de gaz est décrite, mais l'influence de ces propriétés sur le processus d'atomisation n'a malheureusement pas pu être étudiée durant la thèse. La majorité des études présentes dans la littérature sont réalisées à un nombre de Reynolds liquide  $Re_l$  constant, et les conditions d'injections diffèrent seulement par la vitesse du courant de gaz. L'espace des paramètres exploré durant cette thèse a été choisi pour faire varier  $Re_l$  dans un large intervalle (entre 700 et 20000), pour étudier à la fois les jets liquides laminaires et turbulents. La vitesse du jet de gaz est variée sur la gamme la plus large réalisable avec l'installation. Deux techniques d'imagerie ont été utilisées : l'imagerie rétroéclairée et l'imagerie par rayon X

(radiographie). La première consiste à éclairer le jet liquide à l'aide de lumière visible et de filmer de l'autre côté. Les rayons de lumière visibles rencontrant une interface liquide-gaz sont déviés et n'atteignent donc pas le capteur. Les zones de l'espace où se trouve du liquide apparaîtront donc sombres sur l'image. Cette technique est ici principalement utilisée pour mesurer  $L_B$ , qui fera l'objet du chapitre 3. La technique de traitement d'image pour la mesure de  $L_B$  est expliquée et des considérations expérimentales, comme l'influence du type d'éclairage, sont abordées. Cette méthode est très différente de la radiographie, dans laquelle les rayons utilisés (des rayons X) ne sont que très faiblement déviés aux interfaces. En revanche, lorsqu'un rayon traverse le liquide, celui-ci est partiellement absorbé par le liquide. L'absorption dépend de l'épaisseur de liquide traversée et sa mesure permet ainsi de cartographier l'épaisseur de liquide traversée. Différents types de sources de rayonnements X sont présentés et leurs avantages sont comparés. Dans le cas de l'étude présentée ici les contraintes sont la nécessité d'avoir un rayon de grande intensité (nécessaire pour avoir des temps d'exposition faibles), d'avoir un rayon d'au moins quelques fois le diamètre liquide, et d'avoir un rayon monochromatique (afin de pouvoir calculer l'épaisseur de liquide traversée). L'utilisation de rayons X produits par un synchrotron semble le mieux répondre à ces problématiques. Une discussion autour de ces contraintes, alimentée par les paramètres d'acquisition, d'éclairage et les conditions d'installation dans le synchrotron est alors développée et permet d'expliquer le choix de l'espace des paramètres étudiés.

## Description statistique et temporelle de la rupture d'un jet liquide par un courant gazeux

Ce chapitre est publié dans *Physical Review Fluids* [1]. Le chapitre porte sur la longueur du cœur liquide  $L_B$ , et propose une étude statistique et temporelle de cette grandeur dans un large espace des paramètres. Les deux premières sections reprennent des éléments de l'introduction et du chapitre matériel et méthodes. L'étude statistique de  $L_B$  porte sur les trois premiers moments de la distribution de  $L_B$  et sur leur évolution avec les nombres sans dimension caractérisant les paramètres d'injection. La moyenne suit une loi de puissance avec le rapport des pressions dynamiques gaz-liquide  $M$  telle que  $\langle L_B \rangle = 12.8M^{-0.34}$ , ce qui confirme les résultats déjà présents dans la littérature [2]. L'écart type de  $L_B$ ,  $L_{B,RMS}$ , semble également suivre une loi de puissance avec  $M$  tel que  $L_{B,RMS} = 2.12M^{-0.3}$ . Il est intéressant de souligner que ces lois de puissances sont très proches, et nous montrons que le rapport  $I_{L_B} = \frac{L_{B,RMS}}{\langle L_B \rangle}$  est constant. Ces observations sont faites sur une large gamme de paramètres d'injection, dans laquelle différents régimes d'atomisation sont rencontrés, et qui semblent ne pas avoir d'influence sur les lois d'évolution des deux premiers moments statistiques de  $L_B$ . L'étude des fonctions de densité de probabilités (pdf) de la longueur du cœur liquide montre que les pdfs de  $L_B$  suivent des fonctions gaussiennes asymétriques. En complétant l'étude paramétrique faite sur les deux premiers moments avec une étude du moment d'ordre trois (le paramètre d'asymétrie  $\beta_{L_B}$ ), la description statistique de  $L_B$  sera donc complète.  $\beta_{L_B}$  a une évolution non monotone avec le nombre de Reynolds du

courant de gaz  $Re_g$  : pour de faibles valeurs de  $Re_g$ ,  $\beta_{L_B}$  est proche de zéro et augmente jusqu'à  $Re_g = 33000$  où le paramètre d'asymétrie semble atteindre la valeur asymptotique de 0.46. Cette évolution du paramètre d'asymétrie est également mise en évidence sur les pdfs de la variable centrée et normée  $\tilde{L}_B = \frac{L_B - \langle L_B \rangle}{L_{B,STD}}$ . Il est intéressant de souligner que la valeur de  $Re_g = 33000$  correspond à l'apparition du mécanisme de rupture par épluchage (*fiber-type atomization*), dont l'apparition est déterminée par observation qualitative. Nous avons donc mis en évidence une signature du régime d'atomisation sur les grandeurs statistiques associées à  $L_B$ , et nous avons montré que deux paramètres (la moyenne et le paramètre d'asymétrie) suffisent pour la description statistique complète de  $L_B$ , réduit à un seul paramètre pour les conditions à  $Re_g > 33000$ , lorsque la valeur asymptotique de  $\beta_{L_B}$  est atteinte. D'autre part, l'étude présentée porte sur des conditions d'injection liquide variées, comprenant des jets liquides turbulents à l'injection d'une part, et des jets liquides laminaires à l'injection d'autre part. Aucune influence de l'état turbulent du jet liquide à l'injection n'est observée sur les grandeurs statistiques de  $L_B$ . Les fonctions d'autocorrélation de  $L_B$  sont utilisées pour caractériser la dynamique temporelle associée, et un temps caractéristique  $\tau_c$ , déterminé par intégration, est mesuré pour chaque condition d'injection. Nous montrons que ce temps caractéristique évolue avec  $Re_g^{-1}$ , avec une faible contribution de l'état turbulent du jet liquide à l'injection. La superposition des fonctions d'autocorrélation en fonction du décalage temporel normalisé  $\tau/\tau_c$  met en évidence deux dynamiques distinctes: pour les faibles valeurs de nombre de Reynolds du jet de gaz ( $Re_g < 33000$ ), la décorrélation est exponentielle, tandis que pour de hautes valeurs de  $Re_g$  ( $Re_g > 33000$ ), la décorrélation est initialement plus rapide qu'une exponentielle. Cette transition, correspondant à la transition mise en évidence avec le moment d'ordre 3 de  $L_B$ , est également interprétée comme une signature du régime d'atomisation.

## Étude du processus d'atomisation assistée en champ proche par imagerie rapide à rayons X

Dans ce dernier chapitre, les conditions à haute vitesse gaz sont étudiées grâce à des films corrélés temporellement, réalisés à l'aide d'imagerie par rayons X. Une seule étude du champ proche du processus d'atomisation réalisé avec cette technique est présente dans la littérature [3], les observations et mesures associées sont rares et ont un intérêt à la hauteur des défis expérimentaux associés. Une première partie portée sur des observations qualitatives de la structure du jet liquide durant sa rupture vient compléter les observations des travaux précédents. Machicoane et. al [3] ont mis en évidence que la structure du jet liquide présente une morphologie riche qui dépend des conditions d'injection. Un premier régime, dit de cœur intacte (*intact core regime*), dans lequel le jet liquide est plein, et aucune recirculation de gaz ne creuse le jet liquide. Un régime dit de couronne (*crown regime*), identifié par la forme caractéristique du jet liquide qui prend la forme d'une couronne retournée. Un régime transitoire entre les deux précédent, qui n'avait jamais été observé, caractérisé par la présence de nombreuses cavités dans le jet liq-

---

uide qui sont issues de petites recirculations de gaz perforant l'interface liquide-gaz. Le dernier régime est appelé le régime de couronne instable (*unstable crown regime, also referred to as the Angry Octopus regime*) et est similaire au régime de couronne, à la différence que dans ce régime les recirculations de gaz poussent le jet liquide sur un coté, ainsi le jet liquide tourne sur les bords de la buse. Une interprétation est proposée pour expliquer les différents régimes observés, en considérant une superposition des situations de liquide seul et de gaz seul. Quand aucun liquide n'est injecté, le gaz crée une recirculation vers le centre de la buse, comme montré par [4]. Quand aucun gaz n'est injecté, le jet liquide est rond à l'injection et aucune bulle ne peut traverser l'interface liquide-gaz. Aux faibles vitesses gaz, la situation est similaire à celle sans gaz : les recirculations de gaz ont une énergie trop faible pour percer l'interface liquide-gaz, cette situation correspond à celle au régime de cœur intacte. Lorsque la vitesse du gaz augmente, certaines recirculations vont pouvoir percer l'interface du jet liquide et des inclusions de bulles sont ainsi observées au sein du jet liquide. Lorsque la vitesse du gaz est encore augmentée, une recirculation de gaz grande échelle s'installe, poussant le jet liquide dans sa forme de couronne inversée. Lorsque la vitesse du gaz est encore augmentée, la recirculation de gaz devient instable mais maintient le cœur liquide dans sa forme de couronne retournée. Il est montré que la transition entre le régime transitoire et le régime de couronne, et que la transition entre le régime de couronne et celui de couronne inversée correspond à des courbes iso- $M$  dans l'espace des phases, ce qui est cohérent avec l'interprétation précédente. Un des objectifs de cette campagne expérimentale est de réaliser des cartes de l'épaisseur de liquide afin d'étudier la dynamique de rupture du jet liquide de façon quantitative et de caractériser les régimes précédemment identifiés. Les nombreuses difficultés expérimentales rendant ce processus complexe sont discutées, la difficulté principale étant que le faisceau incident est polychromatique, ce qui complexifie grandement l'inversion de l'équation de Beer-Lambert. Grâce à une calibration effectuée sur des films où l'épaisseur de liquide est connue, une méthode de détermination de l'épaisseur de liquide est développée et présentée. Les limites de la mesure ainsi que les incertitudes associées sont discutées et nous montrons que cette méthode permet d'étudier la dynamique du jet liquide, mais qu'elle ne permet pas de détecter de façon fiable les petites structures qui s'en détachent. La méthode est ensuite appliquée à la caractérisation du centre de masse du jet liquide proche de l'injection. Nous mettons en évidence que la position du centre de masse dans le cas du régime de couronne instable est caractérisée par une distribution bimodale, contrairement à un pic centré pour les autres régimes, et un modèle simple est développé pour expliquer cette observation. Une étude préliminaire sur l'évolution temporelle de la position du centre de masse dans le régime de couronne instable permet de mettre en évidence l'influence du moment angulaire dans la phase gaz (le *swirl*) sur la dynamique du centre de masse du jet liquide.



## Conclusion et perspectives

La description statistique de la longueur de cœur liquide, réalisée sur un large espace des paramètres, a permis de montrer que les fonctions de densité de probabilité de  $L_B$  suivent des fonctions Gaussienne asymétrique. Une loi d'échelle de l'évolution de l'écart-type de  $L_B$  avec  $M$  a été reportée pour la première fois, et nous avons montré que le rapport de l'écart-type et de la moyenne de  $L_B$  était constant. L'étude paramétrique du paramètre d'asymétrie de  $L_B$  montre que  $\beta_{L_B}$  croît avec  $Re_g$ , jusqu'à atteindre une valeur asymptotique pour  $Re_g = 33000$ . Cette valeur seuil de  $Re_g$  coïncide avec un changement du régime d'atomisation correspondant à l'apparition du mécanisme d'atomisation par épluchage. Ce changement de régime correspond également à un changement de comportement de la dynamique temporelle de  $L_B$ , et nous avons donc identifié deux critères du changement de régime d'atomisation sur  $L_B$ . Des films à rayons X à haute fréquence d'acquisition ont permis d'observer différentes morphologies du cœur liquide, d'identifier une nouvelle morphologie, et de dresser le diagramme de phase associé dans l'espace des paramètres  $\{We_g; Re_l\}$ . Une méthode d'analyse de radiographie à haute fréquence d'acquisition est développée et utilisée pour étudier les différentes morphologies du cœur liquide. Nous trouvons un critère quantitatif du passage au régime de couronne instable, et étudions la dynamique temporelle du centre de masse du cœur liquide dans ce régime. Bien que préliminaires, ces résultats montrent que la méthode développée constitue un outil d'analyse intéressant pour étudier l'atomisation à haut  $Re_g$ . Les difficultés expérimentales rencontrées et discutées permettront d'affiner la technique pour de futures expériences.

# Contents

<b>1</b>	<b>Introduction</b>	<b>1</b>
1.1	An overview of atomization . . . . .	2
1.2	Cylindrical liquid jet breakup . . . . .	4
1.3	Role of operating parameters and flow conditions . . . . .	8
1.4	A word on simulations . . . . .	10
1.5	Liquid breakup lengths . . . . .	11
1.6	High-speed X-ray radiography of spray formation processes . . . . .	13
<b>2</b>	<b>Experimental methods</b>	<b>17</b>
2.1	Experimental Setup . . . . .	18
2.2	Parameter space . . . . .	28
2.3	Acquisition system . . . . .	31
<b>3</b>	<b>Statistics and dynamics of a liquid jet under fragmentation by a gas jet</b>	<b>49</b>
3.1	Introduction . . . . .	50
3.2	Materials and methods . . . . .	52
3.3	Statistical moments and distributions . . . . .	57
3.4	Time scales of the liquid core length . . . . .	62
3.5	Discussion . . . . .	65
3.6	Conclusions . . . . .	70
<b>4</b>	<b>Synchrotron X-Ray high-speed radiography of the near-field of a coaxial two-fluid atomizer</b>	<b>75</b>
4.1	Qualitative comparison of back-lit and X-ray imaging . . . . .	77

---

4.2	Liquid jet breakup morphologies . . . . .	82
4.3	Beam characteristics and backgrounds . . . . .	97
4.4	Measuring the equivalent path length . . . . .	100
4.5	Quantitative measurements of the equivalent path length . . . . .	112
4.6	Discussion and future work . . . . .	120
<b>Conclusion</b>		<b>122</b>
<b>Bibliography</b>		<b>143</b>
<b>A</b>	<b>Influence of the user-defined threshold</b>	<b>144</b>
<b>B</b>	<b>Influence of the 2D projection on the determination of the statistical moments of <math>L_B</math></b>	<b>147</b>
<b>C</b>	<b>Determination of the statistical moments and convergence</b>	<b>152</b>
C.1	Convergence study . . . . .	152
C.2	Overcoming clipping biases . . . . .	152

# Introduction

---

Atomization can be defined as the breakup of amalgamated matter into smaller portions of itself. The word *atomization* comes from the word *atom*, referring to the idea that breaking the original matter into the smallest possible entity would mean separating the atoms constituting the matter being atomized. In this manuscript, atomization is the break-up of a liquid bulk into a cloud of small droplets, forming a spray. No alteration of the chemistry of the liquid is considered and the smaller entities ejected from the fragmented liquid bulk, i.e. droplets and ligaments, are much larger than the molecules, let alone the atoms, which make up the liquid. As Lavoisier phrased it in his native language:

*"La trituration, la porphirisation & la pulvérisation ne sont, à proprement parler, que des opérations mécaniques préliminaires, dont l'objet est de diviser, de séparer les molécules des corps, & de les réduire en particules très-fines. Mais quelque loin qu'on puisse porter ces opérations, elles ne peuvent jamais résoudre un corps en ses molécules primitives & élémentaires: elles ne rompent pas même, à proprement parler, son aggrégation; en sorte que chaque molécule après la trituration & la porphirisation, forme encore un tout semblable à la masse originare qu'on avoit eu pour objet de diviser, à la différence des opérations vraiment chimiques, telles, par exemple, que la dissolution qui détruit l'aggrégation du corps, & écarte les unes des autres les molécules constitutives & intégrantes qui le composent."*

Antoine Laurent Lavoisier, *Traité Élémentaire de Chimie*, 1789.

In this manuscript, I will present my modest contribution to the understanding of the mechanical operations leading to the liquid fragmentation observed in spray formation, namely atomization.

## 1.1 An overview of atomization

### 1.1.1 Applications

Formation of drizzle at the crest of waves and sea sprays involved in the ocean-atmosphere balance, fragmentation of magma during explosive volcanic events: the atomization process is widely spread in nature, and its understanding may come with useful knowledge of our world. The oldest human application for atomization most likely goes back to prehistoric cave paintings. The artists would put clay in their mouths and blow against the walls of the cave. Nowadays, from pharmaceutical tablet manufacturing to rocket propulsion, atomization finds its applications in numerous industrial fields. In the case of fuel propulsion, the atomization of the fuel prior to its combustion is a critical step to avoid incomplete combustion which would lead to increased pollutant emission and reduced fuel efficiency. In the case of airplanes, air enters the engine from the front and travels to the combustion chamber see Fig. 1.1, and the interaction of the airflow with the fuel at the entrance of the combustion chamber leads to the atomization of the fuel, which is then burned to create the thrust that propels the airplane forward. From the take-off during which the plane requires tremendous thrust, to the cruise flight, jet engines have to be functional in a wide range of operating conditions, already considering only the change of gas density with altitude. The properties of the airflow involved in the atomization process also vary during a flight, thus the atomization occurring inside the engine has to be efficient on a wide parameter space. Mastering the atomization process involved in these different situations is key to increasing the efficiency of the motor along with reducing risks.

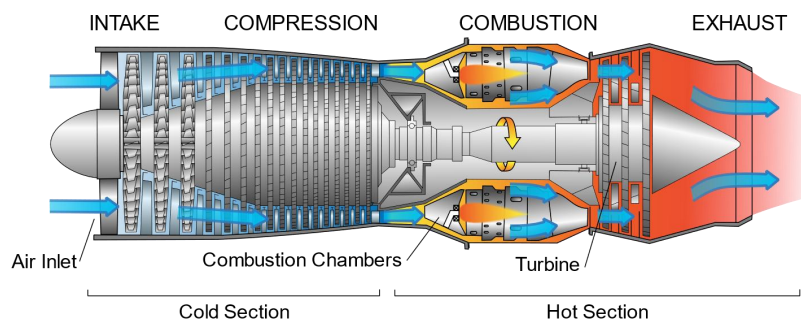


Figure 1.1: Sketch of an aircraft turbojet engine. Source: Jeff Dahl, CC BY-SA 4.0

One of the primary features of atomization is the drastic increase in the surface-to-volume ratio of the liquid being atomized, critical to enhance surface exchange processes between the atomized fluid and its environment. To fulfill the requirements of each of the applications, various methods of atomization, involving different physical mechanisms and nozzle geometries were designed and a few will be presented in the following section.

## 1.1.2 Methods of atomization

Although other forms of atomization exist, such as liquid-liquid atomization, the most common is liquid spray formation. A liquid jet discharging in a gaseous environment is perturbed (for example by the hydrodynamic interactions with the surrounding fluid), leading to the fragmentation of the liquid phase into numerous droplets, namely a spray.

The simplest configuration consists of a liquid jet discharging through a circular orifice nozzle in a still gaseous environment. Atomization then occurs when the velocity of the liquid jet is high enough. This atomization technique is for example used in diesel injectors. Note that for low velocities, although the liquid jet is fragmented, the issuing drops are of the same order of size as the liquid nozzle (see Sec. 1.2.1 for more details). In this situation, the resulting flow is not a spray but rather a sequence of large drops, which is considered here as outside of the framework of atomization. Other types of single-fluid nozzles use the geometry of the nozzle to fragment the liquid jet and do not require an initial pressurization of the liquid, such as surface impingement spray nozzles which use the impact of a liquid on a solid to break the liquid phase, rotary atomizers which use moving parts to fragment the liquid phase, or liquid sheet nozzles, to only cite a few.

When the liquid phase has a high enough conductivity, droplets can be extracted from the liquid jet when applying a high voltage at the exit of the nozzle. The issuing spray can then be guided using electric fields. This technique, while limited to low liquid flow rates, yields fine control over the spray characteristics, useful for managing microscale flows. Atomizers based on this technique are called electrosprays and are for example used as an ion source for mass spectroscopy [5].

If the liquid phase being atomized is viscous, or in the context of the atomization of large liquid volumes, a gas coflow can be added. The interaction of the two fluids leads to the breakup of the liquid jet into a spray. This method is referred to as gas-assisted atomization or airblast atomization. The additional gas coflow gives the operator extra parameters to better tune and control the spray formation than with single-fluid nozzles, yet maintaining high liquid flow rates. Due to the variety of applications such as spray cooling, powder production, and spray drying in the food and pharmaceutical industry, a wide palette of two-fluid injectors geometries was developed (coaxial with liquid or gas-centered atomizers, crossflow injectors, planar configuration, etc.). The present manuscript focuses on coaxial two-fluid atomization, with a round liquid jet at the center of the atomizer, surrounded by an annular gas jet. This is used for example in jet engines of airplanes, in which the fuel is fragmented by a gas flow to optimize its combustion. For rocket engines, two-fluid atomization can be found, as well as impinging liquid jets, and in the former case, planar geometry can be used. This case is further discussed in Sec. 1.3.2, while coaxial atomization will be described throughout this manuscript.

## 1.2 Cylindrical liquid jet breakup

In this section, we will describe the mechanisms which have been identified as responsible for the breakup of a cylindrical liquid jet. An initial description of the behavior of a liquid jet discharging in a still gaseous environment, without a gas coflow, is conducted. Then, gas-assisted atomization is discussed.

### 1.2.1 Liquid jet discharging into a quiescent atmosphere

The breakup of a liquid jet discharging in a still gas environment has been studied for centuries [6]. In the case of the round liquid jet, the description of the mechanisms involved in the breakup is agreed upon and a full description of the breakup process can be found in [7]. Five breakup regimes are identified and characterized by the velocity of the liquid jet at injection. Figure 1.2 shows the average breakup length, defined as the average of the length of the continuous jet connected to the injector, as a function of the liquid Reynolds number. This plot, obtained with the coaxial gas-assisted atomization setup used during this Ph.D., is commonly called the jet stability curve [7–9].

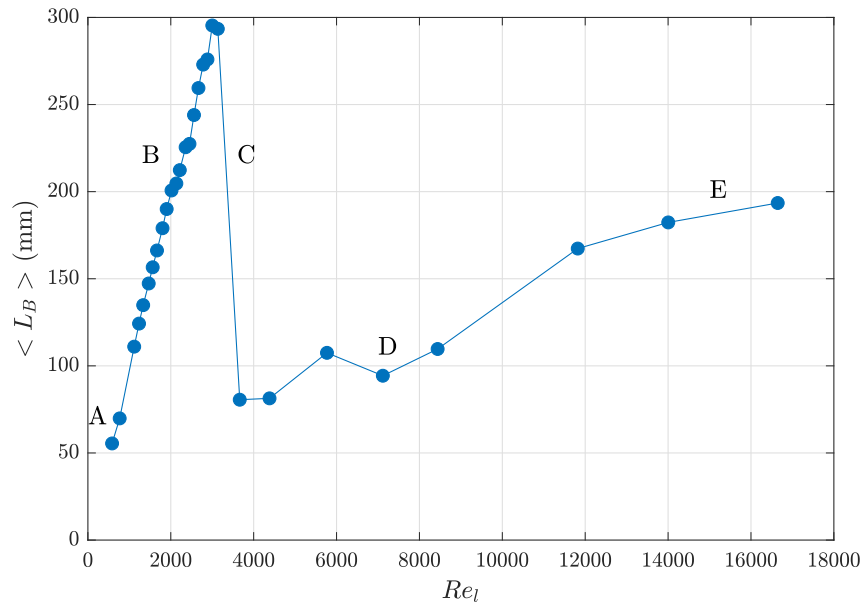


Figure 1.2: Stability curve of a cylindrical liquid jet. The average liquid breakup length is plotted as a function of the liquid Reynolds number  $Re_l$ . The measurements were conducted on the experimental setup built during this Ph.D.

- For low liquid injection velocities, liquid drops exit the nozzle, and no continuous liquid jet is observed. This is referred to as the dripping regime and corresponds to region A of Fig. 1.2.
- The second regime (region B of Fig. 1.2) is called the Rayleigh regime. In this regime, a capillary instability destabilizes the liquid jet's surface, which leads to the detachment of drops when the amplitude of the perturbation reaches the diameter of the liquid jet [6]. Similarly to the dripping regime, the ejected drops in this regime are relatively large (of the order of the size of the liquid nozzle).
- In the first wind-induced regime (region C of Fig. 1.2), the growth of the perturbation originates from the interaction of the liquid with the gaseous environment [10]. The drops released in the first wind-induced regime still have a size similar to that of the liquid jet's diameter, but the production of satellite droplets is enhanced leading to a wider range of emitted drop sizes.
- Region D of Fig. 1.2 corresponds to the second wind-induced regime. In this regime the breakup phenomena becomes multiscale since turbulence is occurring in the liquid and gas phase, with a wide range of perturbation length-scales, leading to a wider range of emitted droplet size than in the previous regimes. Here two mechanisms are involved in the liquid fragmentation: peeling of small liquid drops occurs at the nozzle exit, while larger liquid ligaments are detached further downstream.
- The breakup of the liquid jet in the atomization regime, corresponding to region E in Fig. 1.2, produces drops much smaller than the liquid jet's diameter. The physics involved in this regime is richer than in the previous regimes. The turbulence state of the liquid jet at injection [11] and cavitation inside of the liquid nozzle [12] was shown to drastically influence the liquid jet's breakup in this regime. This makes the transition between regimes D and E more challenging to generalize since these phenomena are difficult to measure and are not reported in many studies. A tighter sampling of the measurement points, as well as a broader range of Reynolds numbers and complementary measurements, would be needed to define it in the current study.

At first, in regions A and B, capillary effects dominate and produce relatively large drops. Increasing the injection velocity, the slip velocity between the gaseous environment and the liquid jet increases, and the effects of aerodynamic stresses dominate (region C). Further increasing the injection velocity, both the aerodynamic stresses and the turbulent state of the liquid jet influence the breakup of the liquid jet, in regions D and E. The mechanisms involved in these regions produce smaller droplets than that of the capillary effects. A review of the transition between these regimes is conducted in [9], describing the changes of regimes with critical values of dimensionless parameters. Note that the aerodynamic stress-related breakup events produce finer drops than the other mechanisms involved. Adding a gas coflow gives the operator finer control over the tuning and triggering of these breakup processes and can lead to smaller droplet production.



## 1.2.2 Two-fluid coaxial atomization

Adding a gas coflow, the initial perturbation of the liquid originates from a Kelvin-Helmholtz instability [13–17], creating a wave-like shape on the surface of the liquid jet. Similarly to the work conducted by Pilch and Erdmann [18] on the breakup of an immobile drop subjected to a gas jet, the wave-like shape on the surface of the liquid jet can go through different breakup mechanisms according to its velocity difference with the gas coflow. Pilch and Erdman [18] used the Weber number, comparing the inertial forces to the cohesion forces of the gas-liquid interface (the surface tension), to classify the different breakup mechanisms involved in the drop disintegration. A similar classification is done for the breakup of liquid jets in coaxial two-fluid atomization [7, 12, 19–21]. For low Weber numbers ( $We < 15$ ), the breakup is similar to what is observed in the Rayleigh regime introduced in the previous section, where the breakup is axisymmetric and the diameter of the issued drops is of the order of the jet diameter. The breakup occurs closer to the nozzle, compared to where the breakup occurs in the Rayleigh regime, but no further notable effect of the gas coflow is reported. Increasing the Weber number ( $15 < We < 25$ ), the breakup becomes non-axisymmetric, and a meandering motion of the liquid jet is observed. The liquid jet still breaks up as a whole due to a Rayleigh capillary pinching mechanism, but non-spherical portions of liquid are ejected when the breakup occurs where the jet is curved. Note that the atomization regimes have not been reached yet. This large-scale motion of the entire liquid jet, making the liquid jet flap, is referred to as flapping [22–24] and plays a role in the cascade of breakup processes. Note that the flapping instability remains when the Weber number is increased.

Further increasing the Weber number ( $25 < We < 70$ ), the meandering of the liquid jet permits the formation of a thin membrane due to the gas flow inflating the liquid jet. When the amplitude of the wave-shaped instability on the surface of the liquid jet is large enough, it can also be inflated by the gas jet. The thin liquid membranes created, called bags, will eventually break into droplets. This mechanism is referred to as a membrane breakup or bag breakup. Note that the liquid rim supporting the membrane is also fragmented and that the droplets issued from the breakup of the membrane are much thinner than the ones coming from the breakup of the liquid rim [25].

For higher Weber numbers, the wave-like shape is accelerated by the high-speed gas, stretched into ligaments, and undergoes a Rayleigh-Taylor instability that breaks it into droplets. This breakup mechanism, referred to as fiber-type breakup, gives the impression that droplets are being peeled off of the liquid jet.

It can be useful to define atomization regimes, such as membrane breakup and fiber-type atomization, where each regime is dominated by one of the mechanisms described above. Note that on a wide range of injection conditions, both of these breakup mechanisms coexist and conjointly participate in the spray formation, both impacting the characteristics of the spray,

discussed in Sec. 1.2.3.

All of the cited mechanisms conjointly contribute to the richness of the breakup process. Decorrelating the effects of the small-scale and of the large-scale instabilities to study them independently is challenging. The breakup process involved in gas-assisted atomization in a planar geometry involves the same instabilities as in the coaxial geometry, with the exception of the flapping instability that cannot exist in this configuration. Raynal [13] and Ben Rayana [26] used planar configurations to study the effects of the small-scale instabilities. By considering the mixing boundary layer, Raynal [13] developed a linear stability analysis predicting that the frequency of the initial Kelvin-Helmholtz scales with the gas velocity, and the scaling law he predicted showed good agreement with his experimental results. In an effort to extend the parameter space covered, Ben Rayana [26] showed that this scaling law is still valid for higher values of the gas-to-liquid dynamic pressure ratio  $M$ . In the meantime, Marmottant [27] showed that the scaling law predicted in the planar case [13] is also verified on a coaxial setup. Interestingly, the three authors report different prefactors, highlighting that our understanding of the initial instability remains incomplete, which led to the consideration of other parameters, discussed in Sec. 1.3.2.

### 1.2.3 Spray dispersion

The drops and the ligaments issuing from the breakup mechanisms previously described can undergo secondary breakup, further dividing the liquid phase into smaller portions of liquid. With this secondary breakup comes turbulent mixing within the two-phase flow. The spray characteristics in the far field are the result of the primary breakup, and the secondary breakups events, as well as the turbulent mixing. These features can be described using simple geometrical considerations from visualizations, e.g. spray angle, or studying the size and spatiotemporal distributions of the droplets in the spray. Even the simplest approach can be of paramount importance in the applications, to roughly estimate how the spray fills a combustion chamber in propulsion for instance. Models of the spray characteristics have been developed [16, 28, 29], but no universal and predictive model of the spray characteristics, based on the meaningful physical parameters of the breakup process, has yet emerged.

## 1.3 Role of operating parameters and flow conditions

### 1.3.1 Definition of the dimensionless parameters

The physical variables of a coaxial gas-assisted atomization setup are the liquid and gas velocities ( $U_l$  and  $U_g$ ), the liquid and gas jets diameters ( $d_l$  and  $d_g$ ), the density of each fluid ( $\rho_l$  and  $\rho_g$ ), their viscosity ( $\nu_l$  and  $\nu_g$ ), and the surface tension  $\sigma$  between the liquid and the gas phase. With 9 different variables, which units are combinations of 3 fundamental units, the  $\pi$  theorem predicts only  $9 - 3 = 6$  dimensionless parameters are needed to describe the system. The dimensionless parameters commonly used to describe coaxial two-fluid atomization are:

- The liquid Reynolds number, comparing the inertial and viscous forces within the liquid jet, defined as  $Re_l = \frac{U_l d_l}{\nu_l}$ ;
- The gas Reynolds number, defined as  $Re_g = \frac{4Q_g}{\nu_g \sqrt{4\pi A_g}}$ , where  $A_g$  is the exit area of the gas jet. This definition is equivalent to  $Re_g = \frac{U_g d_{eff}}{\nu_g}$ , with  $d_{eff}$  the effective diameter of the gas exit area, taking into account the annular shape of the gas jet, used as the characteristic length of the gas jet and defined as  $d_{eff} = \sqrt{4A_g/\pi}$ ;
- The Weber number, comparing the aerodynamic stresses to the surface tension force of the liquid jet, defined as  $We = \frac{\rho_g U_s^2 d_l}{\sigma}$  where  $U_s = |U_g - U_l|$  is the slip velocity between the gas and the liquid phase;
- The gas-to-liquid dynamic pressure ratio (often called momentum ratio in the literature), compares the dynamic pressure (or velocity pressure) applied by the gas flow on the liquid-gas interface to the one of the liquid and is defined as  $M = \frac{\rho_g U_g^2}{\rho_l U_l^2}$ ;
- The liquid mass loading, comparing the mass injection rates of the liquid jet and of the gas jet,  $m = \frac{\rho_l A_l U_l}{\rho_g A_g U_g}$ ;
- The Ohnesorge number, comparing the viscous forces with the cohesion forces, defined as  $Oh = \frac{\mu_l}{\sqrt{\rho_l \sigma d_l}}$ .

In the case of our study, the liquid mass loading is always smaller than  $m = 0.21$ , and the Ohnesorge number is also negligible ( $Oh < 0.042$ ), so these parameters will not be used here.

A different definition of the Weber number is found in the literature, referred to here as a gas Weber number, defined as  $We_g = \frac{\rho_g U_g^2 d_l}{\sigma}$  [19]. This definition of the Weber number will be used to compare our results with the literature. In the case of our study, where the physical properties of both fluids are kept constant, the gas Reynolds number and the gas Weber number equivalently capture changes related to variations in the gas injection velocity. The geometry of the atomizer is also kept constant throughout the manuscript, therefore the only control parameters are the injection rate of both fluids, namely the liquid volumetric flow rate  $Q_l$  and the gas volumetric flow rate  $Q_g$ . In this situation only 2 dimensionless parameters are needed to describe trends, and we chose to use  $Re_l$  and  $Re_g$ , (or equivalently  $Re_l$  and  $We_g$ ).

### 1.3.2 Role of turbulence

Inconsistency between results obtained using different injectors led to studies focused on the influence of geometry on the near-field of the breakup process. Although the role of geometry has been characterized [30] it fails to explain all the differences observed. One hypothesis is that these discrepancies come from differences in the turbulent state of the gas phase. The conditioning of the gas jet, for example, the internal geometry of the nozzle or the injection method, has a strong influence on the turbulent properties of the gas phase which can therefore vary from one setup to another. Matas et al. [31] studied the influence of gas turbulence intensity on the early stages of the atomization process, in a planar configuration. Before their study, the breakup was characterized using only mean flow quantities, and the influence of fluctuations, for example, fluctuations of the gas velocity, had been left aside. Figure 1.3 shows a sketch of the setup they used to modulate the turbulent intensity of the gas phase. Adding a pulsed gas jet, or an obstacle in the gas channel, they were able to tune the turbulent intensity of the gas phase from about 1 to 10% and double the frequency of the initial Kelvin-Helmholtz instability despite keeping mean quantities constant.

One of the initial goals of this Ph.D. was to produce a setup capable of tuning the turbulent intensity of the gas phase in a coaxial two-fluid atomizer configuration. Inspired by previous work [31], a setup was built and is described in Sec. 2.1.3. Unfortunately, due to a lack of time allocated to this, the study of the influence of turbulent intensity was not conducted. The setup being operational, I hope it will be used in a future project on.

### 1.3.3 Role of swirl

In some coaxial gas-assisted atomizer setups, the geometry of the gas channel ensures the gas flow is longitudinal when it exits the nozzle. However, it is possible to induce angular momentum in the gas coflow. This can be done by modifications to the mechanical design of the gas nozzle

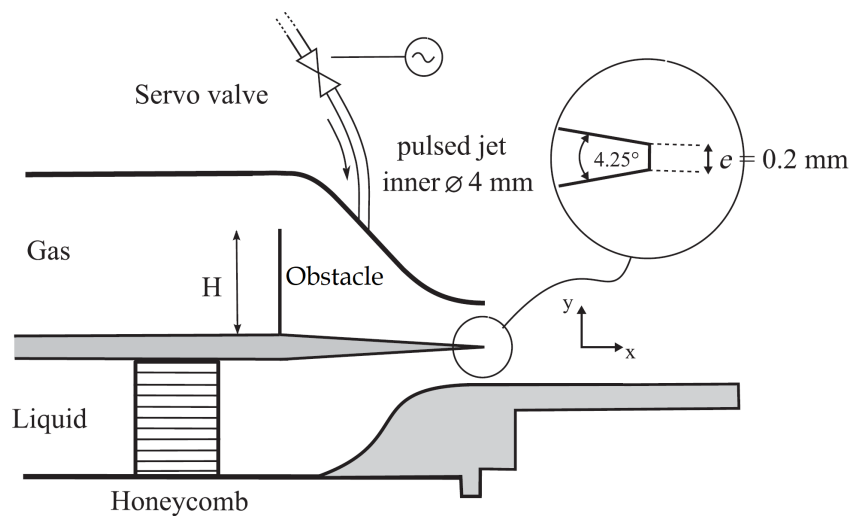


Figure 1.3: Sketch of the experimental setup used by Matas et al. [31] to modulate the turbulent intensity in the gas flow of a planar atomization setup.

(e.g. veins, grooves, such as done in jet engines) or by changing the gas injection protocol. Early work by Hopfinger & Lasheras [32] and Hardalupas & Whitelaw [33] used that latter strategy and were able to obtain a tunable amount of swirl in the gas jet using a fixed and simple geometry. This spinning motion of the gas flow, referred to as swirl, is used in many applications [34], especially in combustion where it is known to improve flame stability by generating a toroidal gas vortex allowing for better recirculation of the products of combustion [35].

Studies of swirl in coaxial gas-assisted atomization have primarily focused on the far-field characterization of the spray (spray angle, liquid spatiotemporal distribution, and drop size distribution) [33, 35] and on the location of the breakup [36–38]. Preliminary work on the influence of swirl on the morphology of the liquid breakup was conducted by Machicoane et al. [3]. However, the understanding of the impact of swirl on coaxial two-fluid atomization remains incomplete, especially in the near-field of the breakup process where modifications of the mechanisms involved in the liquid jet breakup due to swirl have not been characterized.

## 1.4 A word on simulations

Airblast atomization has been primarily studied using an experimental approach, and direct simulations were left aside due to the complexity of the system. With the advent of numerical methods for two-phase flows, simulations of airblast atomization have emerged since the 2000s with the work of Desjardins et al. [39–41], Zaleski et al. [42, 43], to only cite a few. One of the main difficulties of these simulations is the high difference in density between both phases, which leads to numerical instabilities [44]. Simulating the flow inside the atomizer has also been

an issue, and is most likely a key element in the understanding of the breakup process, as mentioned in Sec. 1.3.2. It is worth mentioning that an ANR research project conducted in 5 French institutes (Institut d'Alembert, CERT-ONERA, IMFT, CORIA, and LEGI) was conducted between 2005 and 2009 and was aiming to produce a virtual atomizer. LEGI, with its knowledge of experimental studies of atomization, was in charge of producing the experimental measurements. In this effort to produce a virtual atomizer numerous numerical issues were overcome (e.g. tackling density ratio between phases of up to 1000, instead of typically 10 in previous work). This joint experimental-numerical work also shed light on some underlying mechanisms involved in the primary breakup [17]. More recently a Multi-University Research Initiative funded by the Office of Naval Research (ONR MURI) developed a joint experimental-numerical approach, led by O. Desjardins (Cornell University) and A. Aliseda (University of Washington). In this context, Vu [45] showed that resolving the internal flow led to a large increase in accuracy of the simulation of gas-assisted atomization, and can be managed at a moderate cost using multi-block approaches.

## 1.5 Liquid breakup lengths

The first studies of coaxial two-fluid atomization typically focused on the drop size distribution [46]. The need for a geometrical description of the spray led to the study of characteristic liquid length. The intact length  $L_C$ , also referred to as the cone length, corresponding to the longitudinal extent of the region always containing liquid (which has a cone shape), received attention early on since its measurement could be achieved using optical systems with long exposure time. Then, imaging equipment with exposure times short enough, relative to timescales of the atomization process, to capture sharp images of the liquid jet were used, although the images were independent and therefore uncorrelated due to slow repetition rates on analog cameras. Qualitative morphological studies of the liquid core, defined as the portion of liquid hydraulically connected to the nozzle, were conducted using these images [20, 47, 48]. The liquid core length  $L_B$ , also referred to as the liquid breakup length, defined as the longitudinal extent of the liquid core, was measured for multiple operating conditions. The average value of  $L_B$  received attention due to its importance in combustion applications regarding flame stability. Figure 1.4 illustrates the detection of the liquid core length on an image of the near field of the atomization process. Despite the low number of images, relative to what can be captured with the video cameras available nowadays, the gas-to-liquid dynamic pressure ratio  $M = \frac{\rho_g U_g}{\rho_l U_l}$  was identified as being the driving parameter for the average liquid core length [2, 49]. Intuitively the breakup length is expected to decrease with  $U_g$  and to increase with  $U_l$ , which is an agreement with the reported scaling from [2] ( $\langle L_B \rangle \propto M^{-0.3}$ ). Recent studies refined the work previously conducted on the liquid core length, showing that the scaling law of  $L_B$  with the dynamic pressure ratio is valid on a wide range of  $M$  and revealed that the prefactor is driven by the nozzle geometry [23, 30]. A flapping length  $L_{flap}$  was also introduced by Delon et al. [50] and defined as the length at which

the amplitude of the radial displacement of the jet is equal to the liquid jet's radius.

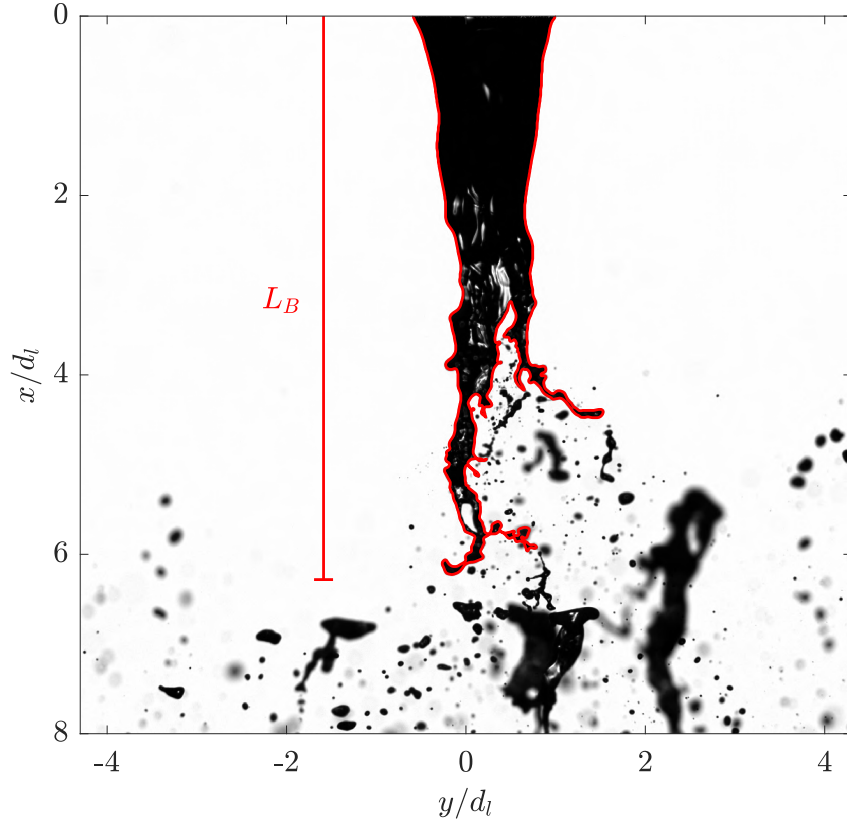


Figure 1.4: Back-lit image of the near field of the atomization process in a coaxial two-fluid configuration. The red contour highlights the outline of the liquid core and its longitudinal extent  $L_B$  is shown on the left.

Despite the advances of high-speed cameras and numerical storage capacities, allowing to capture and save correlated images of the liquid core on a large number of images (orders of magnitude higher than what was available in the past), and its importance regarding flame stability in combustion, only sparse work was conducted on the higher-order statistical moments of the distributions of the liquid core length. Recent work has been conducted on the shape of the probability density function of  $L_B$  [24, 36], revealing the non-Gaussian behavior of the distribution. Regarding the temporal dynamics found in spray formation processes, on top of the work conducted on the small- and large-scale instabilities presented in Sec. 1.2.2, auto-correlation functions of time series of  $L_B$  were recently reported [36, 51]. They concluded that the timescale extracted from the auto-correlation functions decreased with  $M$ , but their studies were conducted by varying the gas injection velocity at constant liquid injection velocity, therefore the influence of the liquid velocity is yet to be shown.

High-speed back-lit imaging is commonly used to measure the liquid core length [2, 30, 36,



38, 49], Fig. 1.4 shows an example visualization of the liquid core using back-lit imaging, the liquid core length is easily measured on the image and the process can be automated to deal with a high number of frames. A different approach to measure  $L_B$ , referred to as the electrical connectivity technique, consists in applying a voltage between the liquid nozzle and a needle located further downstream. If the liquid jet is continuous from the nozzle to the needle, it closes the electrical circuit, which can be detected by monitoring the electrical system circuit. This technique was developed by [52] and refined by [53, 54]. Charalampous et al. [55, 56] introduced a novel technique for measurements of the liquid core in atomization. They introduce a fluorescence dye in the liquid, and visualize the jet via a laser directed through the liquid nozzle, into the liquid jet. The laser beam, guided by the hydraulically connected portion of liquid, induces fluorescence within the liquid jet up to its breakup where the laser light transmission is low enough to be considered interrupted. The liquid core is therefore highlighted on the images, allowing for a reliable detection of  $L_B$ . A comparison between these techniques can be found in [57]. For high gas flow rates, the atomization process yields a dense two-phase flow. Multiple overlapping detached liquid structures hide the liquid core, preventing proper imaging of the breakup using back-lit imaging. A new probing method is needed to study the nature of the breakup of the liquid jet occurring at high gas Weber numbers. Penetrative imaging techniques (i.e. weakly scattered by interfaces) allow the user to see through the overlapping structures and are therefore well suited to study the liquid core and to characterize its morphology. These visualization methods, and especially X-rays, are introduced in the following section.

## 1.6 High-speed X-ray radiography of spray formation processes

X-ray imaging is a penetrative-source imaging technique. Penetrative light is only partially absorbed by the medium, with mostly no scattering at interfaces. It is well suited for the study of systems that yield numerous interfaces, like the spray formation process [58].  $\gamma$ -rays also could be used for their penetrative nature, but their spatial resolution is typically coarser due to the larger size of the associated detectors [59], therefore X-rays are more appropriate. Note also that contrary to  $\gamma$ -rays, X-ray sources emit only when they are powered and are therefore safer for the user. Similarly, while doped water could be used to perform neutron radiography, the beam energy is typically a few orders of magnitude lower than with synchrotron-produced X-rays.

### 1.6.1 Definition of X-ray techniques

The absorption of X-rays along their travel in a medium follows the Beer-Lamberts law, written in Eq. 1.1 for the simplified situation where an X-ray beam travels a distance  $\Delta z$  through



a uniform sample.  $I$  and  $I_0$  are the intensity of the beam after, respectively before, it passes through the sample,  $\mu(\lambda)$  is the absorption coefficient of the sample at a wavelength  $\lambda$ . This law links the absorption of the X-ray beam to the density of the medium it goes through.

$$I = \int I_0 e^{-\mu(\lambda)\Delta z} d\lambda \quad (1.1)$$

Further simplifying the situation by considering a monochromatic X-ray beam, Beer-Lambert law simplifies to Eq. 1.2.

$$\Delta z = \frac{1}{\mu} \log \left( \frac{I_0}{I} \right) \quad (1.2)$$

The absorption, defined as  $A = -\log \left( \frac{I}{I_0} \right)$ , is measured by comparing the intensity measured with and without the sample. Knowing the absorption coefficient of the sample at the beam's wavelength, the user can process the size of the sample  $\Delta z$ . In practice, when using high-energy X-rays, the spatial and temporal variations in the intensity of the X-ray beam after the sample can be measured by using a cristal scintillator which converts X-rays into visible light. The intensity of the visible light coming out of the cristal is proportional to the intensity of the incoming X-ray, the absorption of the sample is measured via the recording of the visible light the cristal outputs. Note that by using a high-speed camera to record the visible light, the operator can capture time-resolved radiograph movies. Other instruments can be used to record the intensity of the X-ray beam, such as an image intensifier or a pin diodes. The former is used to both convert and amplify the X-ray signal into visible light to be imaged by a high-speed camera, and the latter, acts like a photodiode that directly converts the X-ray intensity into an electronic signal.

In the case of a liquid-gas system, the cumulative absorption of the liquid and of the gas phase add up to the overall absorption, but the absorption coefficient of the gas phase is orders of magnitude smaller than the liquid's absorption coefficient and the contribution of the gas can be neglected. For atomization, the liquid phase is composed of multiple superimposed structures. The thickness measured using Beer-Lamberts law, therefore, corresponds to the cumulative liquid path the beam went through, namely the equivalent path length noted EPL. The structures overlapping the liquid core, relatively small compared to the liquid core, contribute very little to the absorption and are therefore largely filtered by this imaging method, while they would block visible light and prevent measurements of the liquid core. The liquid core can therefore be visualized on the radiographs movies of the atomization process.

The quality of the determination of the liquid thickness from the X-ray absorption highly depends on the spectrum of the X-ray beam. Although the computation of the equivalent path length via Eq. 1.2, valid for monochromatic beams, is simple, the inversion of the non-linear Eq.

1.1 for polychromatic beams is much more complicated. The absorption coefficient is highly dependent on the wavelength (typically scaling with  $\sim \lambda^3$ ), making the determination of the composition of the medium very complex for polychromatic beams [60]. Note that when an instrument is used to convert the intensity of the X-ray into an electric signal, the device can also have a non-trivial spectral response, further introducing spectral dependencies.

There are two main sources of X-rays. Tube sources, also called cone sources, like those found in medical facilities, provide a relatively low-cost X-ray source that can be handled in a lab, and owe their name to the divergent nature of the beam. A high voltage applied between a cathode and an anode extracts electrons from the cathode, and accelerates the electrons before they impact the anode. During the collision on the anode, a small portion of the electrons energy is radiated out in the form of X-rays. A hole lets the X-ray propagate along a main direction, yielding a typical conical shape for the beam intensity map (similar to what is obtained with a spotlight). The first studies of multiphase flows using X-rays were conducted in the 60s using tube sources [61, 62]. Since then, improvements in the equipment [59] and in the post-processing techniques [63] have been developed. Although tube sources of X-ray produce a polychromatic beam that is relatively weak, they have for example been used to perform tomographic reconstructions of multiphase flows [64–67]. The second source of X-rays is synchrotrons. The X-ray beam is produced by the interaction of accelerated electrons, located in a ring under vacuum, with an undulator. The interaction between the electrons and the undulator deducts energy from the electrons in the ring and emits X-rays. Synchrotrons produce collimated beams that are much brighter than tube sources, making them more reliable for quantitative measurements, and offer high spatial and temporal resolutions, relative to other noninvasive measurement techniques.

X-ray imaging has been primarily developed to perform 3D reconstruction of the composition of a sample, tomography, in the context of medical applications and material science. To compute the 3D structure of the sample in one configuration, hundreds of radiographs taken from different angles are typically captured, obtained by spinning the sample on a turntable. Tomographic measurements of sprays would require spinning the atomizer on a timescale hundreds of times smaller than the timescales of the atomization process, leading to non-negligible Coriolis effects and non-trivial mechanical issues. These tomography techniques are adapted to systems with time scales orders of magnitude longer than the timescales of turbulent two-phase flows. Many developments in X-ray imaging techniques adapted to two-phase flows have emerged over the past few decades. In the context of cavitation, where the spatial and temporal scales are similar to those of atomization, 2D measurements of the void fraction with high temporal resolution ( $\simeq 10$  kHz) have been conducted using tube-sources X-rays [68–71]. Even higher temporal resolutions ( $\simeq 100$  kHz) were reached using synchrotron-produced X-rays [72].

The next section reviews the work conducted using X-ray to probe coaxial two-fluid atomization.

## 1.6.2 X-rays in atomization

X-rays in atomization have primarily been used to study diesel injectors. Many measurements of the 3D average liquid distribution in space, obtained using low acquisition frequency measurements, have been reported [73–75]. We mentioned in Sec. 1.2.1 that cavitation occurring inside the nozzle had a strong influence on the breakup process [12], which was confirmed experimentally on industrial atomizers using X-ray visualization [76].

Coaxial gas-assisted atomizers received only moderate interest. Using polychromatic synchrotron X-rays to image the spray, Wang et al. [77] acquire independent snapshots of the atomization process. More recently Machicoane et al. [3] were able to perform time-resolved movies of the atomization process of a coaxial gas-assisted atomizer using the combination of a scintillator and a high-speed camera to capture synchrotron X-rays. They were able to observe the liquid core during its breakup and showed that bubbles are entrapped within the liquid core, leading to unexpected morphologies of the liquid core during its breakup process. A comparison between the different techniques used to image the atomization process can be found in [78].

With synchrotron-produced X-rays at the European Synchrotron Radiation Facility<sup>1</sup> (ESRF), we performed high-speed radiography of the near field of a coaxial two-fluid atomizer during this Ph.D. The details of the experimental setup used for the imaging, along with explanations of the physical principles it relies on, are discussed in Sec. 2.3.2. A qualitative investigation of the morphology of the liquid jet breakup is conducted using raw radiographs. Then a method to measure the projected liquid thickness is introduced, aiming to find quantitative indicators of the different liquid jet morphologies.

---

<sup>1</sup><https://www.esrf.fr/>.

## Experimental methods

---

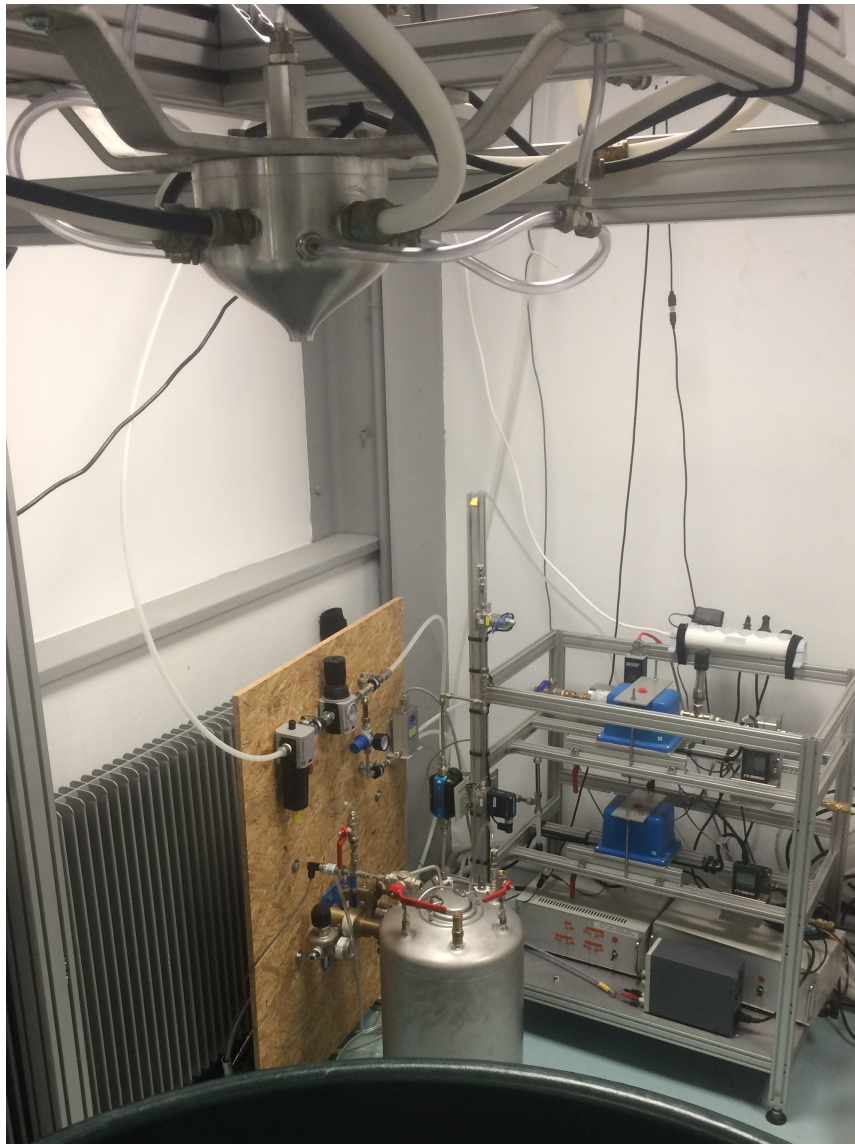


Figure 2.1: Image of the coaxial two-fluid atomizer at LEGI. The nozzle is attached to a frame on the top of the image and the flowloop regulating the flows is shown in the back.

## 2.1 Experimental Setup

A two-fluid coaxial atomizer was built and tested during this Ph.D. The monitoring of the injection parameters is straightforward and can easily be modified to serve the user's purpose best. I wish to give a thorough description of how it operates and I hope this will be useful for future work on this setup. This chapter begins with a presentation of the experimental installation and the parameter space which was explored, followed by a description of the experimental techniques used to probe the atomization process.

### 2.1.1 Overview of the atomizer

The experimental setup consists of a coaxial two-fluid atomizer (also referred to as airblast atomizer in the literature), sketched in Fig. 2.2. In an effort to obtain a database with comparable results, the design is based on the open-source geometry that can be found on N. Machicoane's professional webpage<sup>1</sup>. The design and the manufacturing procedures are available to the community so that any research group can use them. Note that the 3D geometry is also available for simulation [3, 79]. The liquid nozzle is 100 mm long, with an inner diameter  $d_l = 1.98$  mm. This geometry ensures that a fully developed Poiseuille flow is established in the liquid flow before exiting the nozzle in the case of a laminar liquid flow, or a fully developed plug flow if the liquid is in a turbulent state [80]. The liquid nozzle is placed at the center of a gas nozzle. The liquid nozzle's outer wall and the gas nozzle's inner wall form a cavity that channels the gas into an annular exit plane with an inner diameter  $D_l = 3.1$  mm and an outer diameter  $d_g = 9.985$  mm. Note that  $d_l$ ,  $D_l$ , and  $d_g$  were measured with the same accuracy of  $1 \mu\text{m}$ . The lip  $e$ , namely the region separating the liquid and gas exit boundaries (also called splitter plate in the literature), hence has a thickness of  $e = (D_l - d_l)/2 = 0.56$  mm. The atomizer's axis is aligned with gravity, spraying downward.

There is a total of 12 gas inlets, divided into 3 different groups of inlets that serve different purposes. All inlets are drilled into the gas nozzle lateral wall and are hence in horizontal plans.

- Four of them carry a constant (in time) gas flow oriented toward the axis of the atomizer, they are referred to as the main gas inlets. The outer wall of the liquid nozzle and the inner wall of the gas nozzle present a cubic-spline shape ensuring the gas flow of the main inlets is longitudinal when it exits the nozzle. These inlets are shown in black in Fig. 2.2a) and b).
- Four inlets are referred to as swirl inlets and are shown in green in Fig. 2.2b). These

---

<sup>1</sup>[http://www.legi.grenoble-inp.fr/people/Nathanael.Machicoane/research\\_data.html](http://www.legi.grenoble-inp.fr/people/Nathanael.Machicoane/research_data.html)

inlets also carry a constant gas flow but they are off-axis and therefore produce an angular momentum in the gas flow.

- Following the idea of Matas et al. [31] to modulate the turbulent tuning of a gas flow in a planar atomization system, 4 inlets similar to the main gas inlets were added, in which one can send bursts of gas at a high frequency. These inlets are sketched in red in Fig. 2.2a) and c) and are referred to as turbulent tuning inlets. Unlike the swirl inlets, they are added in a horizontal plane slightly downstream of the main inlet, to allow for room for the fittings.

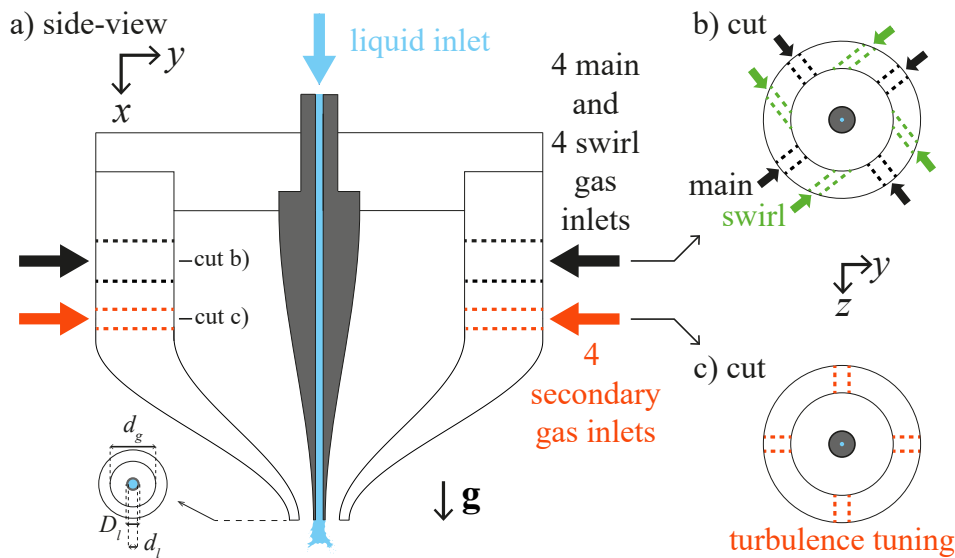


Figure 2.2: a) Schematic side-view of the atomizer showing the different inlets of the atomizer.  $D_l$ ,  $d_l$ , and  $d_g$  are shown on the sectional view of the bottom of the atomizer pointed to by an arrow. b) Horizontal cross-section of the atomizer, highlighting the relative position of the swirl inlets to the main inlets. c) Cross-section of the atomizer, showing the position of the turbulent tuning inlets.

Structural frames were designed and built to hold the flow loop elements and associated electronics, see Fig. 2.3. They were designed to be able to be transported so the experiment can easily be moved to be reproduced elsewhere, such as at ESRF (see Sec. 2.3.2). These flow loop elements and their monitoring ensure robust control of the flows, allowing for reproducible conditions, as will be shown in the following section.



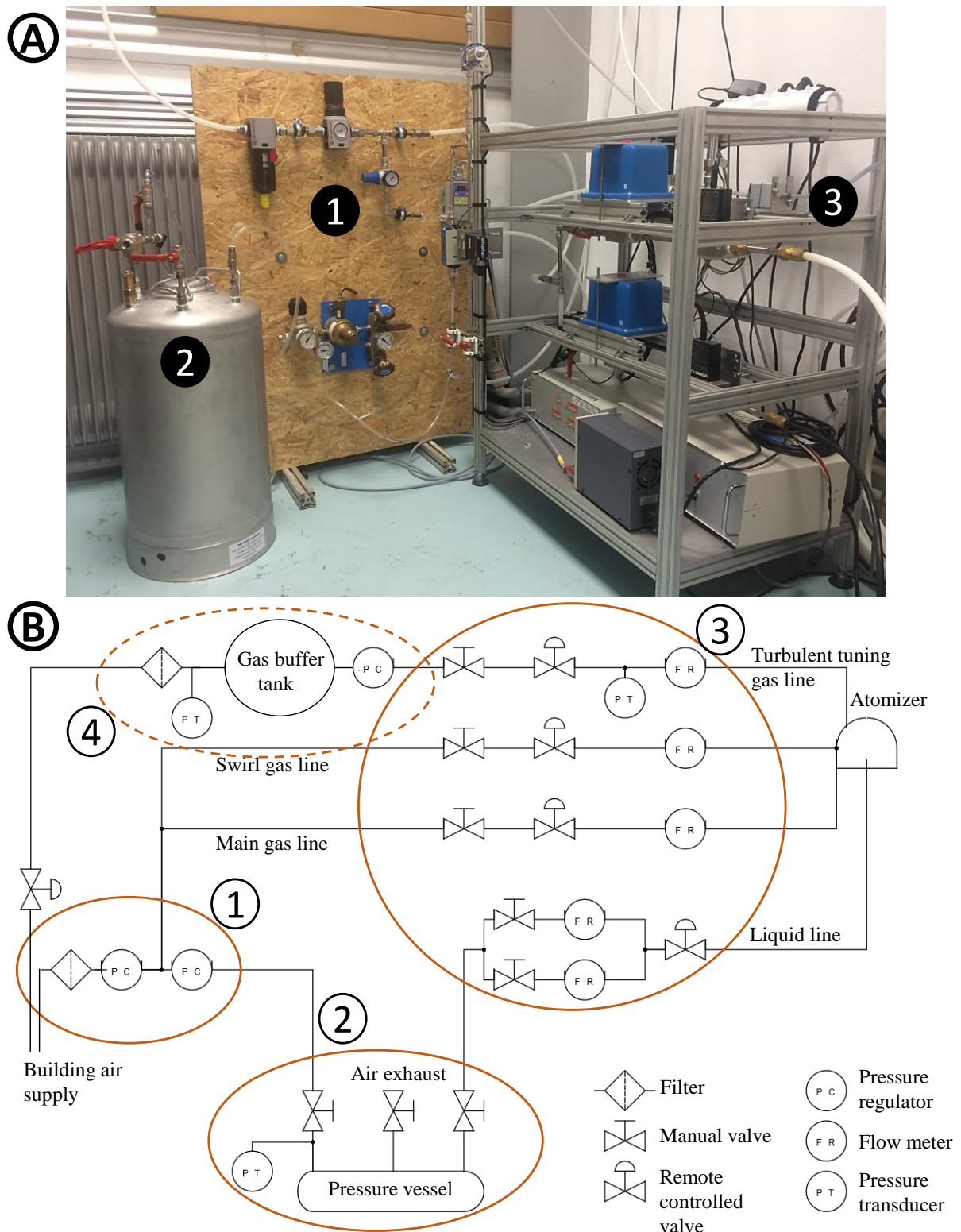


Figure 2.3: A) Structures holding the flow loop. 1) Structure holding the flow conditioning system. 2) Pressure vessel. 3) Structure holding the gas and liquid lines. B) Sketch of the different components of the flow loop. The orange circles regroup the components found on the 3 structures described in A). The elements regrouped in the orange dashed-line circle labeled 4) are not shown in A) and will be discussed in Sec. 2.1.3.

## 2.1.2 Two-fluid coaxial atomizer with gas swirl

### 2.1.2.1 Monitoring of the liquid and gas injection rates

Before getting into the details of how each individual flow line operates, the monitoring of the experiment is presented in this section. All the flows are monitored by a Labview program that was designed for this experiment, see Fig. 2.4. The program lets the user set the different flow rates and outputs the measurement of the instantaneous flow rates. When conducting high-speed imaging measurements, the camera is set to be used in *Post-trigger*: it continuously records and stops its recording when it receives a trigger input. The output movie corresponds to the  $N$  images that the camera captured before receiving the trigger input ( $N$  being the number of images in the camera buffer). To synchronize the output of the Labview file with the movie, the trigger is sent and captured by the Labview program.

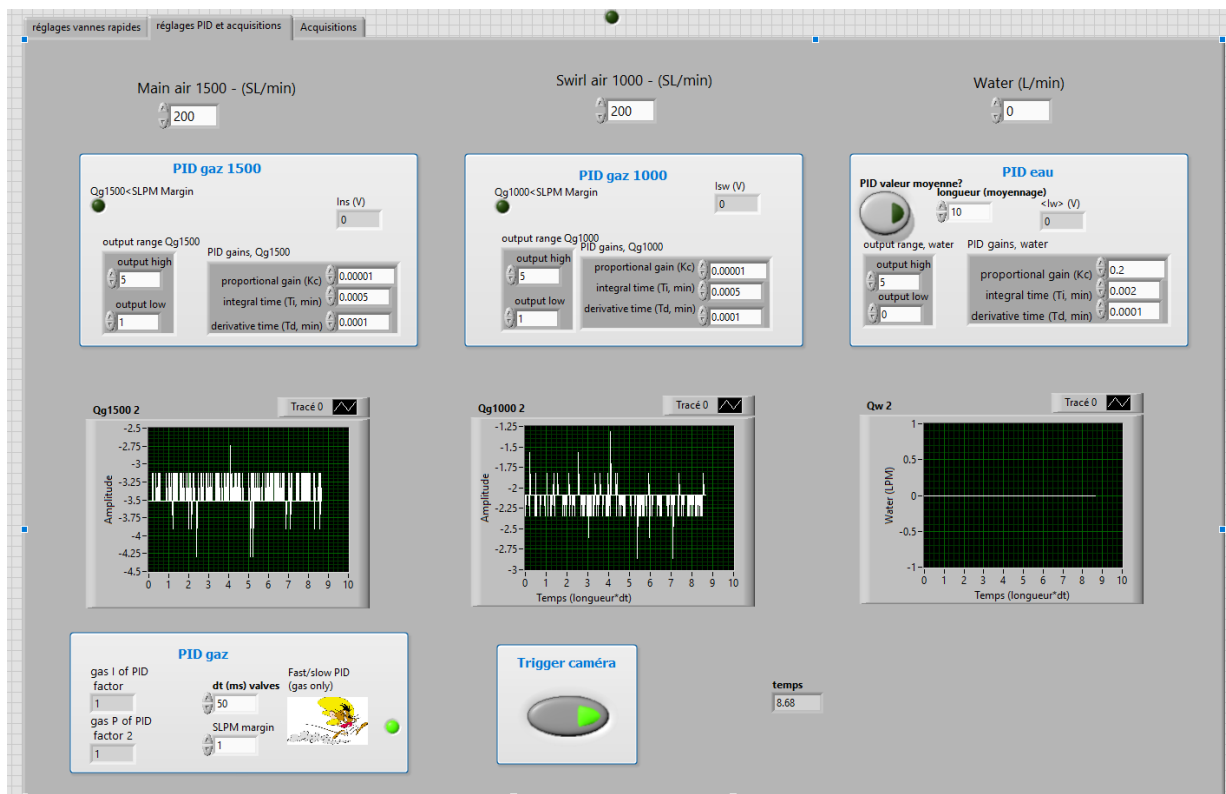


Figure 2.4: Front panel of the Labview program designed for the experiment.

Figure 2.5 illustrates the synchronization procedure. The user monitors the flow rates, with the camera continuously recording. When the flow rates reach a steady state, the user presses the trigger button which is recorded by the Labview output file, and stops the camera recording (shown in dashed line in Fig. 2.5). In the case illustrated in Fig. 2.5, the orange area corresponds



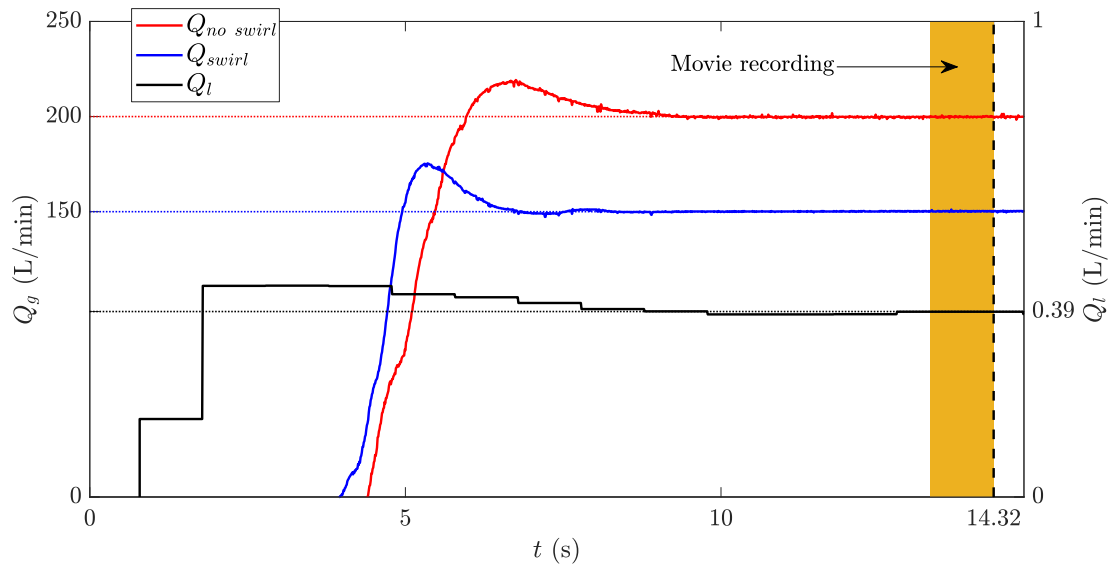


Figure 2.5: Output of the Labview program for a typical run. The red and blue solid curves respectively show the measured main gas flow rate and swirl flow rate. The black solid curve shows the measured liquid flow rate. The red, blue, and black dotted lines represent the target flow rates set by the user for the main gas flow rate, swirl gas flow rate, and liquid flow rate respectively. The dashed line highlights the trigger sent to the camera, and the orange area corresponds to the duration of the associated movie.

to the recording period of the camera and was synchronized with the Labview output knowing the recording duration and that the movie ends when the trigger is fired (an information recorded by the Labview program). The measured flow rates of the run correspond to the flow rates measured within this orange area. The average flow rates are then calculated for the run, along with their associated standard deviations. Although the flow rates are measured for each run, this method allows the user to visualize the flow rates while the camera is recording, ensuring the actual flow corresponds to the desired set flow during the recording.

### 2.1.2.2 Gas inlets

The gas that was used to conduct the experiments presented in the following sections is air. The gas source used is the building's compressed air supply. The conditioning of the gas, such as its compression or its transit through the building's network, may introduce particles and oil. A filtration system is installed at the entrance of the gas flow loops to prevent this pollution during the experiments. The filter is followed by a pressure regulator so that the variations in pressure that may occur in the gas source do not affect the experiment.

The gas lines that feed both the main and swirl inlets have the same design. They

both consist of a proportional valve and a flow meter, as illustrated in Fig. 2.3. A proportional–integral–derivative controller (PID controller), a specific type of feedback loop, allows for the setting of the gas flow introduced in each of these lines and is monitored by the Labview program presented in the previous section. Once the target value for the gas flow  $Q_{set}$  is within a given margin  $\Delta Q$ , the PID controller stops controlling the valve. It will take over if the measured gas flow increases or decreases beyond the bounds set by the target value and margin. This method allows for a stable flow, in which unsteadiness is not added by the valve constantly moving. The margin can freely be chosen by the user and is typically set to  $\Delta Q = 2.5$  L/min for the explored atomizing conditions, which is at most two percent of the set value. For each run, the standard deviation of the measured gas flows is calculated, which will be used to estimate the uncertainties in the gas velocity. The gas flow rate values are expressed here in normal liter per minute, translating into the flow rate exiting the nozzle where atmospheric conditions of pressure and temperature are maintained. A dimensionless parameter, the swirl ratio  $SR$ , is used to quantify the amount of swirl introduced [24, 36]. The swirl ratio is defined as  $SR = Q_{main}/Q_{swirl}$ , with  $Q_{main}$  the gas flowrate introduced via the main inlets and  $Q_{swirl}$  the gas flowrate introduced via the swirl inlets.

### 2.1.2.3 Liquid injection

The liquid used is reverse-osmosis purified water. The flow is generated by a pressurized tank containing the water. Similarly to a syringe pump, the air in the tank pushes the water into the liquid line, creating the flow. As for the main and swirl gas lines, a flow meter and a valve monitored by a PID controller ensure that the liquid flow reaches the set value. Due to the liquid exiting the tank, variations in the tank's pressure are observed. These variations are not always well compensated by the pressure regulator feeding the liquid tank. To take this slow drift into account, the PID controller does not stop when it reaches a certain margin on the set flow rate. However, the gain of the PID controller is set at a low value once the flow rate is in the neighborhood of the set value, and the acquisition time is slower than for the gas line by a factor of 10, further affecting the PID pace. In addition, unlike the gas line which has a well-calibrated mass flow meter, the liquid flow meter uses ultrasound Doppler measurements, that are sensitive to slight changes in the fluid properties (inducing changes in the speed of sound). A calibration run was hence done by setting a constant flow with the PID controller and measuring the liquid flow rate with the modest bucket and stopwatch method. The liquid jet is recovered in a bucket for 3 minutes (much longer than the few seconds of human reaction, ensuring weighting of at least 200 g to limit the errors based on scale accuracy) and the average flow rate is measured by weighing the bucket at the beginning and at the end of the run (avoiding bias in remaining liquid in the bucket). Note that the bucket is deep enough to prevent loss of liquid due to splashing. Figure 2.6 shows the measured liquid flow rate as a function of the set liquid flow rate, after calibration of the liquid flow meter. The inset of Fig.

2.6 shows the relative error of the measured flow rate by the bucket and stopwatch method to the set flow rate as a function of the set flow rate. The error is 4% at most for the lowest flow rates (<0.1 L/min), 2% otherwise. The maximum error found for low flow rates is smaller than the flow meters resolution of 0.006 L/min. The uncertainty  $\Delta Q_l$  on the measurement of the liquid flow rate is therefore taken as the maximum of 0.006 L/min or 2% of the set value of the flow rate.

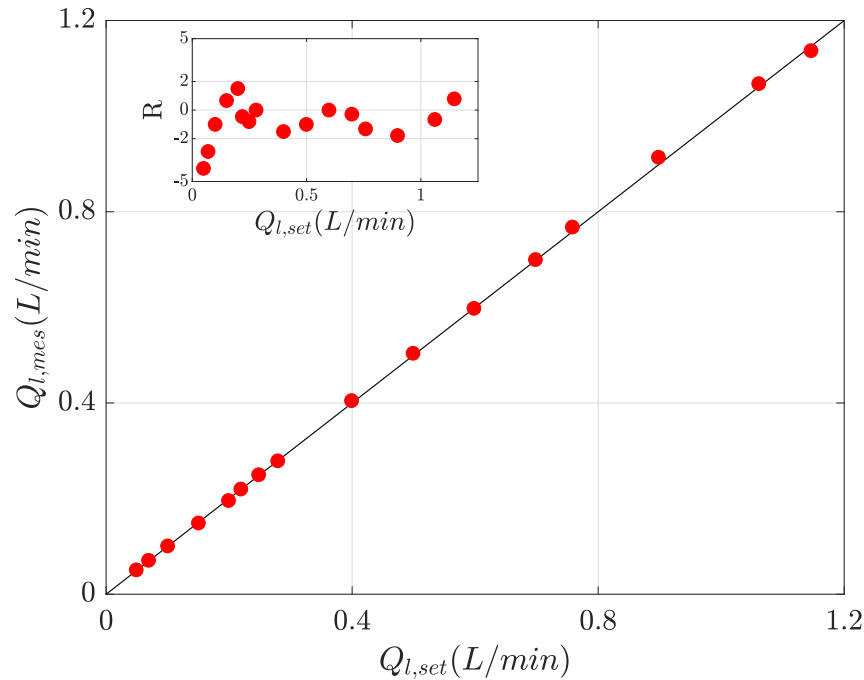


Figure 2.6: Measured liquid flow rate as a function of the set liquid flow rate. The inset figure shows the corresponding relative error  $R = (Q_{l,set} - Q_{l,mes}) / Q_{l,set}$  as a function of the set liquid flow rate.

#### 2.1.2.4 Reducing gas recirculation and droplet reentrainment

Ideally, the flow should be as unconstrained as possible as if the spray was discharging into an infinite still atmosphere. In reality, the spray is aimed at a 2 m wide pool located 2 m below the atomizer's exit plan. For the high gas velocities explored, this confinement leads to intense gas recirculations, easily seen when small water droplets seed the gas jet, see Fig. 2.8. To prevent this, 4 layers of metallic grids (breaking the large-scale structure of the gas jet), and 6 fans are added to the side of the pool, see Fig. 2.7. The large cross-sectional area of the pool makes this a negligible velocity-momentum sink, preventing the confinement of the spray that would happen if a suctioning system was used. This system is efficient and mitigates droplet recirculation which otherwise could lead to parasite droplets on the images of the jet.

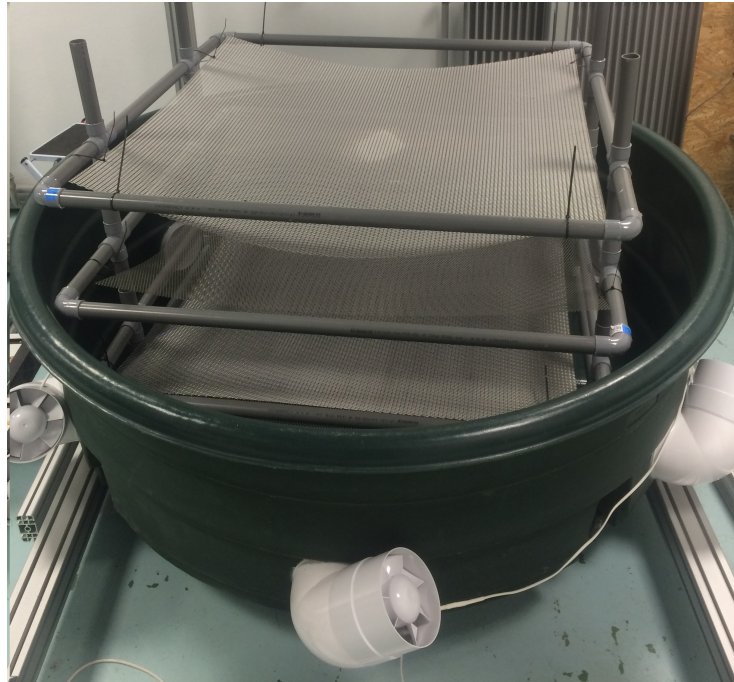


Figure 2.7: Recovering pool for the spray. 4 layers of metallic grids, as well as 6 exhaust fans, are installed in the pool to prevent gas recirculations that would affect the spray and carry small droplets.

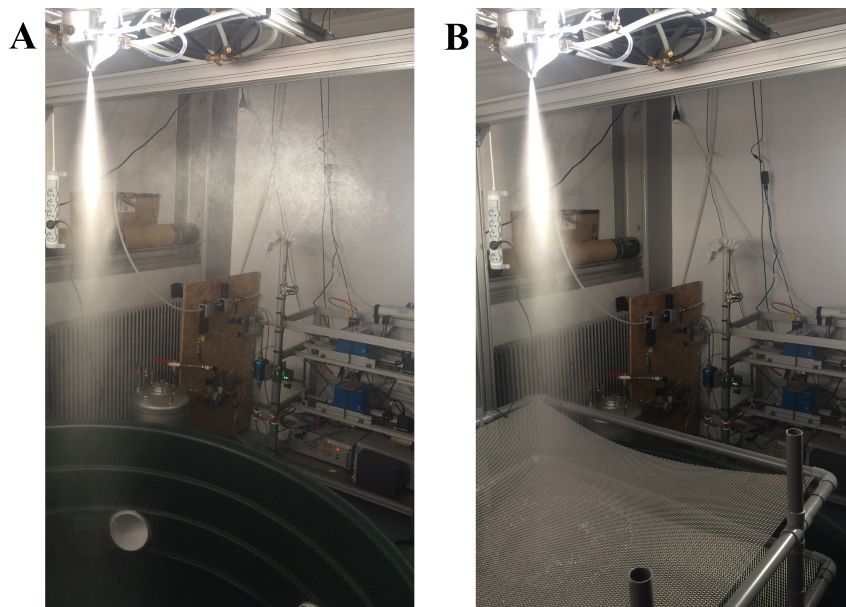


Figure 2.8: A) Image of the jet with high-velocity gas and liquid injection without the anti-recirculation device. A signature of the gas recirculations is seen by the presence of liquid droplets next to the spray. B) Image of the jet with the same injection parameters as A), shown with the anti-recirculation device. No droplets are seen next to the spray.

### 2.1.3 Turbulent tuning

Matas et al. [31] describe an experimental modulation of the turbulent intensity in the gas phase using two methods. The first method was inserting an obstacle in the gas channel, effectively modulating the turbulent intensity. By changing the height of the wall in the gas channel they were able to obtain different turbulent intensities. The second method consists of adding a jet that injected gas into the channel with a high-frequency forcing. Both the amplitude and the frequency of the pulsed gas jet were controlled and they showed this method gives the operator better control of the turbulent intensity. These methods are illustrated in Fig. 1.3. Inspired by the work of Matas et al. [31], a setup to modulate the turbulent intensity of the gas flow in a coaxial gas-assisted atomizer was built, using the pulsed gas jet method.

#### 2.1.3.1 Fast modulation of the flow

Four gas inlets, referred to as turbulent tuning inlets (shown in red in Fig. 2.2), are added to the base design of the atomizer. These inlets are fed by a fast valve to add bursts of gas in the gas phase and modulate the turbulent intensity, modulating the inlet gas flow at up to 500 Hz on 64 flow levels. Such performances cannot be achieved using a typical proportional or solenoid valve. The valve consists of 6 actuators which all have different fluid flows but lead to a common output. Each of the actuators has to be monitored independently, therefore 6 binary signals are sent to set an overall opening of the valve, leading to  $2^6 = 64$  different valve openings. The change in between two openings can occur in 2 ms, the valve can therefore actuate at 500 Hz. However, the valve cannot sinusoidally modulate its opening at 500 Hz. If the sinusoidal modulation is done on 20 steps of flow rate, the time in between each level is at least 2 ms, leading to a maximum frequency of the modulation of  $\frac{500}{20} = 25$  Hz. One way to reach 500 Hz modulations would be to send a step function, opening and closing the different actuators at the same time. The program monitoring the valve is presented in Sec. 2.1.3.3. The flow in the turbulent tuning line is then measured by a flow meter and a fast-response pressure transducer, both monitored by the same program as the valve.

A second turbulent tuning gas flow loop was designed, in which the four gas inlets of the atomizer are fed with different flows. With this second method, each of the nozzle inlets is fed by a single fast on-off actuator. This method is inspired by active grids which modulate turbulence in a flow, for which each of the ports of the active grid can be independently opened and closed (see for example [81] for an explanation of the active grid principle). However, this second method was implemented but not tested during the Ph.D.

### 2.1.3.2 Gas buffer tank

Initial tests revealed that the fast valve yields a high pressure drop. If the building air supply, which can provide up to 800 L/min at  $P_{building} = 7.8$  bars, feeds both the main gas inlets and the turbulent tuning inlets, only a weak flow was attained through the fast valve, limiting the modulation of the turbulent intensity. To overcome this difficulty a parallel line with a gas buffer, effectively doubling the number of gas sources available, was designed and added to the system. The idea is to feed the turbulent line with a pressure tank acting as a buffer, see Fig. 2.9, that is refilled up to  $P_{building}$  by the building air supply in between two runs. The line feeding the gas to the pressure tank is composed of an on-off actuator to control the tank refill and a gas filter. The tank discharges in the turbulent tuning gas line via a pressure controller, set to  $P_{out} = 5$  bars. As long as the pressure inside the buffer tank is higher than  $P_{out}$ , the buffer tank acts like a regulated gas source. The turbulent tuning flow line is sketched in Fig. 2.3B.

### 2.1.3.3 Monitoring of the turbulent tuning line

A Labview program was designed to monitor the turbulent tuning gas flow loop. A set of common periodic signals to control the fast responsive valve are embedded in the program. The number of flow rate levels along with the frequency of the overall signal is fully controllable for each of these periodic signals. The fast-response valve opening signal can also be manually tuned by the user. The actuation signal for the 4 actuators of the second turbulent tuning method described in Sec. 2.1.3.1 can also be monitored by the program: the duration of the opening of the actuators, along with the associated frequency and the delay between each actuator can freely be set by the user.

Once the turbulent tuning method and the signal have been set and started, the flow rate and the pressure inside the gas turbulent tuning line are monitored and saved in an output file. The program also monitors the buffer tank's refill via its internal pressure, indicating to the user when the pressure inside the tank is low, meaning the tank requires refilling. This program was tested and added to the previous one presented in Sec. 2.1.2.1 so that the entire system can be monitored by a unique program.

Unfortunately, choices had to be made regarding the management of the time left during this Ph.D. after the implementation of the turbulent tuning gas line. Therefore no experiments were conducted using this turbulent line yet<sup>2</sup>.

---

<sup>2</sup>At the time where I am writing this manuscript, a postdoc (Santanu KUMAR SAHOO) is working on the coaxial atomization setup previously described and will take-forward on the study of the influence of the turbulence in the gas phase, starting with a characterization of the gas phase with turbulent modulation, followed by a study of the influence of the modulation on the liquid core length.





Figure 2.9: Buffer tank used at the inlet of the turbulent tuning gas line

## 2.2 Parameter space

The parameter space explored throughout the Ph.D. is described in the following section.

### 2.2.1 Controlling parameters

Using air and water at ambient conditions, the surface tension and viscosity were kept constant for all the experiments presented in this manuscript. The geometry of the nozzle presented in 2.1.1 was kept identical for all the runs. The control parameters are the gas and the liquid injection rates, respectively  $Q_g$  and  $Q_l$ , which are equivalently described by  $U_g$  and  $U_l$ , the gas and liquid velocity at the exit of the nozzle respectively (exit velocity corresponding to a spatial

and temporal average here). Each run is described by the dimensionless parameters introduced in the introduction  $Re_g$ ,  $Re_l$ ,  $We_g$ ,  $We_r$ , and  $M$ . Note that changes in the gas velocity are equally described by changes in the gas Reynolds number or the gas Weber number. For each run, the actual flow rates are monitored and measured as described in sec. 2.1.2.1, and the associated dimensionless parameters along with their error bars are calculated with this measurement.

### 2.2.2 Choice of the parameter space

The conditions presented in this manuscript were set to cover a large atomization parameter space, displaying both fiber-type atomization and membrane breakup. Figure 2.10 shows the studied cases in the  $\{We_g; Re_l\}$  parameter space. Note that the error bars were calculated using the uncertainty of the flow rates presented in Sec. 2.1.2.2 and 2.1.2.3. Thanks to the efforts put into the experimental setup and in its monitoring, the measurement uncertainty of the dimensionless parameters is very low, as illustrated in Fig. 2.10. Future figures will be shown without the error bars associated with these dimensionless parameters to keep the figures as clear as possible.

The liquid Reynolds number was varied from 750 to 20000, encompassing the transition from a laminar to a turbulent flow, expected to occur in between  $Re_l \simeq 3000$  and  $Re_l \simeq 10000$  in a pipe flow [80]. The range of liquid Reynolds number was set considering that below  $Re_l = 750$ , when no gas is added, the liquid jet is in the dripping regime where no continuous liquid column is formed. For  $Re_l = 750$ , when no gas is added, the liquid jet is in the Rayleigh regime and exhibits a continuous liquid jet for around ten liquid diameters. Above  $Re_l = 20000$  the pressure vessel empties itself too fast which leads to fluctuations in the liquid flow. More details on the state of the liquid jet can be found in Sec. 1.2.1 and a thorough description of the different liquid regimes is conducted in [7]. The range of liquid Reynolds number encompasses the range that has already been studied for this atomizers geometry ([3, 24, 36, 79, 82]), but also extends it to study the influence of the turbulent state of the liquid jet at injection on the atomization process. The gas Reynolds number's range is set on one side by the minimum gas velocity that triggers atomization for the lowest liquid flow rate, and on the other side by the maximum gas velocity attainable in this setup. This leads to a gas Reynolds number varied from 13000 to 200000. Equivalently the Weber number  $We_g$  varies in the [13; 31000] range. This leads to a gas-to-liquid dynamic pressure ratio  $M$  varying over 4 decades, from  $M = 0.019$  to  $M = 631$ . Table 3.1 shows the parameters of a sample of conditions, chosen to highlight the maximum and the minimum value of each parameter.



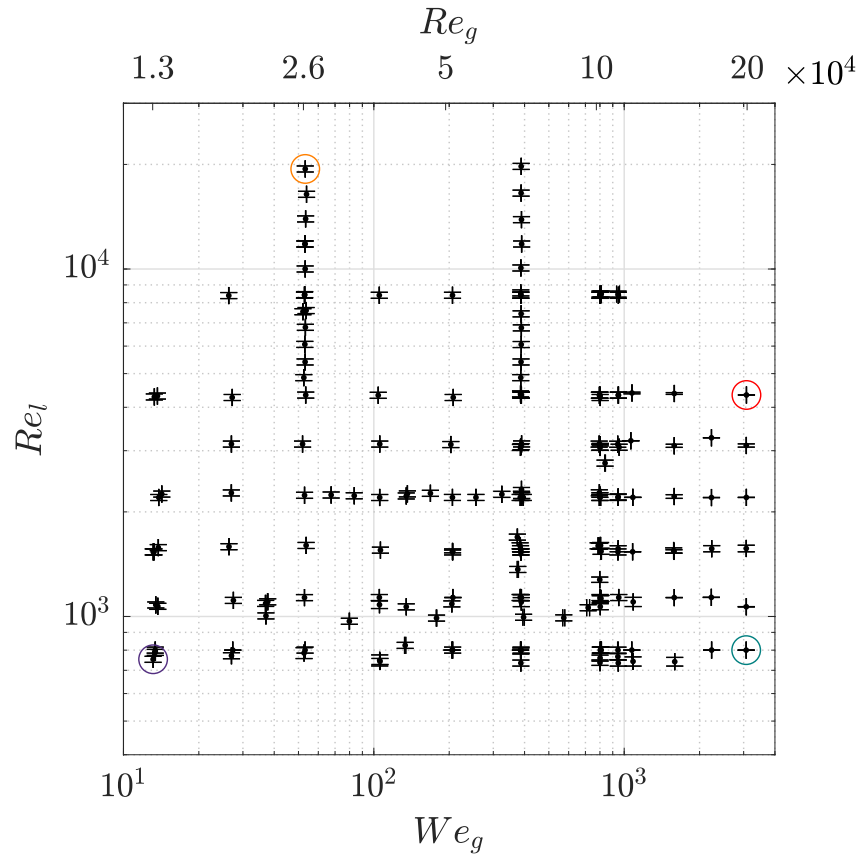


Figure 2.10: Conditions explored throughout this Ph.D in the  $\{We_g; Re_l\}$  parameter space. The error bars are calculated with the uncertainty of the flow rates. The circled points correspond to the conditions highlighted in Table 3.1.

$U_l$ (m/s)	$U_g$ (m/s)	$M$	$Re_l$	$Re_g$	$We_g$	
10	41.9	<b>0.019</b>	<b>20000</b>	26000	53	o
0.43	318	<b>631</b>	800	<b>200000</b>	<b>31000</b>	o
2.3	318	21.5	4300	<b>200000</b>	<b>31000</b>	o
0.40	20.8	3.05	<b>750</b>	<b>13000</b>	<b>13</b>	o

Table 2.1: Sample from the investigated operating conditions, with their corresponding dimensionless parameters. The maximum and minimum values of the presented parameters are highlighted in bold. The last column indicates the points highlighted in Fig. 2.10.

Due to the high range of parameters explored, various topologies of the jet's breakup were observed, for which different imaging systems had to be used. The following section presents the different acquisition systems.

## 2.3 Acquisition system

Two different imaging techniques were used to probe the atomization process. Both of these will be presented in this section, along with their limitations and compared assets.

### 2.3.1 Back-lit imaging

An example back-lit image of the atomization process is shown in Fig. 2.11.



Figure 2.11: Snapshot of the atomization process captured using back-lit imaging,  $U_l = 0.41$  m/s,  $U_g = 30$  m/s,  $Re_l = 770$  and  $We_g = 27$ .

### 2.3.1.1 Principle

Back-lit imaging is a widely used imaging technique. The object that one studies is lit from behind and shadows the light targeted to the camera, as illustrated in Fig. 2.12. In the case of atomization, the liquid blocks the light from getting to the camera. In binary terms, pixels which capture the presence of liquid are black and the others are white. The cameras that were used are either Phantom V2012 or Phantom V2640. These high-speed imaging cameras have performances that were well-suited to capture the multi-scale phenomenon that occurs during the atomization process. The imaging frequency and imaging windows were adapted to the speed and size of the phenomenon observed: the frequency ranges from 10 to 35kHz and the windows range from  $30 \times 12$  to  $80 \times 30$  mm<sup>2</sup> (the large dimension being aligned with the spray's axis). The associated resolution ranges from 23 to 40  $\mu\text{m}/\text{pixels}$ .

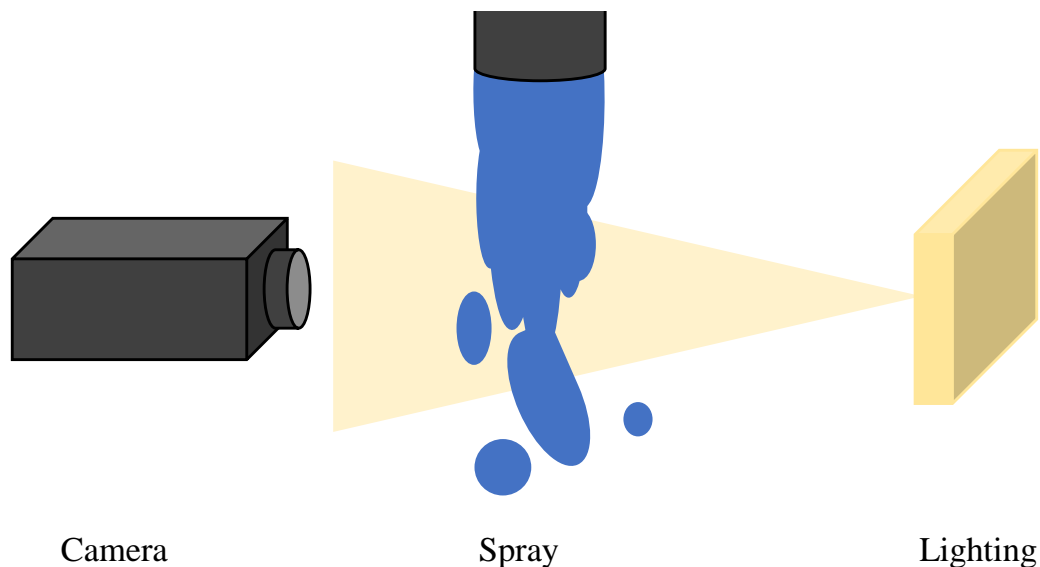


Figure 2.12: Sketch of the back-lit imaging. The spray is lit from one side and imaged from the opposite side. The liquid phase shadows the light targeted at the camera.

### 2.3.1.2 Liquid presence analysis

To best use the image processing tools that are available, it is useful to have binary images. The idea of a binary image is to have a black pixel where the liquid is located and a white pixel where no liquid is encountered. Figure 2.13 shows an example of the 3-step process to extract the binarized image from the raw footage. Starting from the raw image in Fig. 2.13A, the background is removed by a normalization process. Tests of the best normalization procedures were conducted: subtraction of the background to the raw image, division of the raw image by the background, and the combination of both. It appeared that the combination of subtraction

and division by the background,  $I_{norm} = \frac{I_{raw} - I_{background}}{I_{background}}$ ,  $I_{raw}$  being the intensity of the raw image and  $I_{background}$  the intensity of the background, is the most effective, as pointed out in [36] for similar conditions. The resulting normalized image of Fig. 2.13A is shown in Fig. 2.13B.

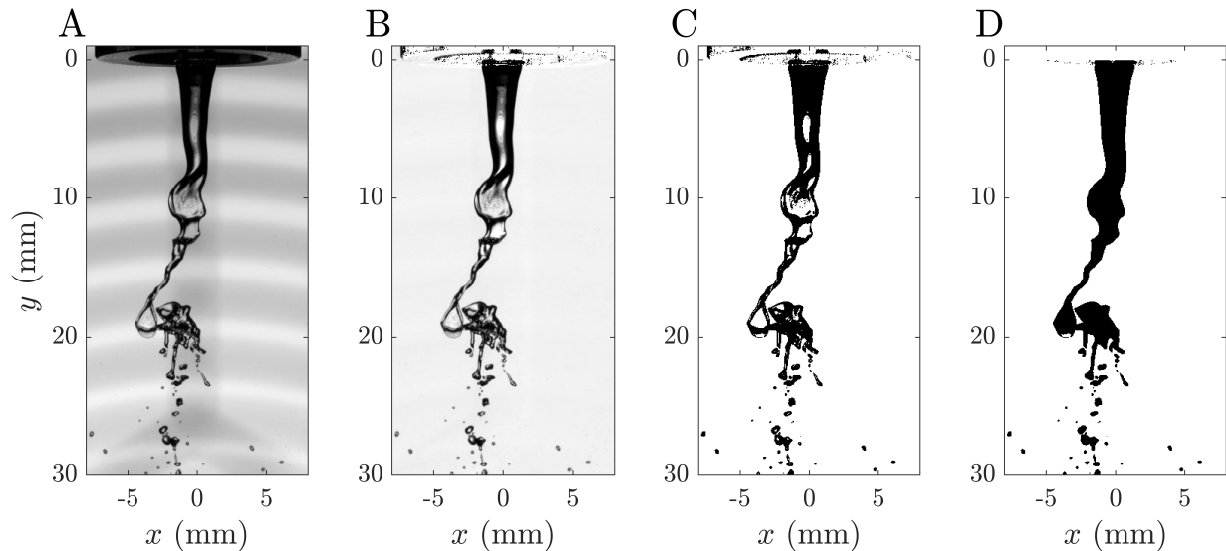


Figure 2.13: Four stages of the binarization of an image of the breakup of a liquid jet. This example represents cases with a light source that presents the most inhomogeneities among the different sources used. A) Raw image on a 12-bit scale. B) Image normalized by a background, the image is displayed using the full range of the colormap [0 1]. C) Binarized image using a threshold. D) Filled binarized image.

The normalized image has pixel values between 0 and 1, and the associated binarized image is obtained using thresholding. The threshold is defined by the user. A function that allows the user to visualize a raw image and two binarized images obtained with thresholds that the user chooses is used for this process. The function scans a movie using random images in the movie, allowing the user to find the threshold that best suits the condition. Although the process might appear user-dependent, thresholding tests were conducted and revealed that with the highly contrasted images that were used, this process leads to a robust choice of threshold. These tests are shown in Appendix A. The binarized image then goes through a *filling* procedure, during which the holes of the binarized image are filled with dark pixels, see Fig.2.13D. This final step is done with the in-built Matlab function `imfill( $I_{binarized}$ , 'holes')`, where  $I_{binarized}$  is the binarized image, and leads to an image for which a dark pixel stands where some liquid is encountered and a white pixel stands otherwise.

### 2.3.1.3 Influence of light

The choice of the lighting system is critical to the quality of the images, therefore many lights were tested. When imaging high-speed moving objects, the exposure time  $\tau_{exp}$  has to be short to avoid motion blur on the image. This would result otherwise in the presence of streaks, left by objects that travel more than a fraction of a pixel during  $\tau_{exp}$ , leading to deformed and blurred objects. Regarding this, the exposure time has to be minimized, although it comes at the cost of image intensity.

The depth of field has to be sufficient to contain the spray formation region so that the liquid boundary is sharp on the entire image. To increase the depth of field of the imaging system, one can simply close the aperture, which also comes at the cost of brightness. A bright imaging system addresses both the issue of minimizing the exposure time and increasing the depth of field.

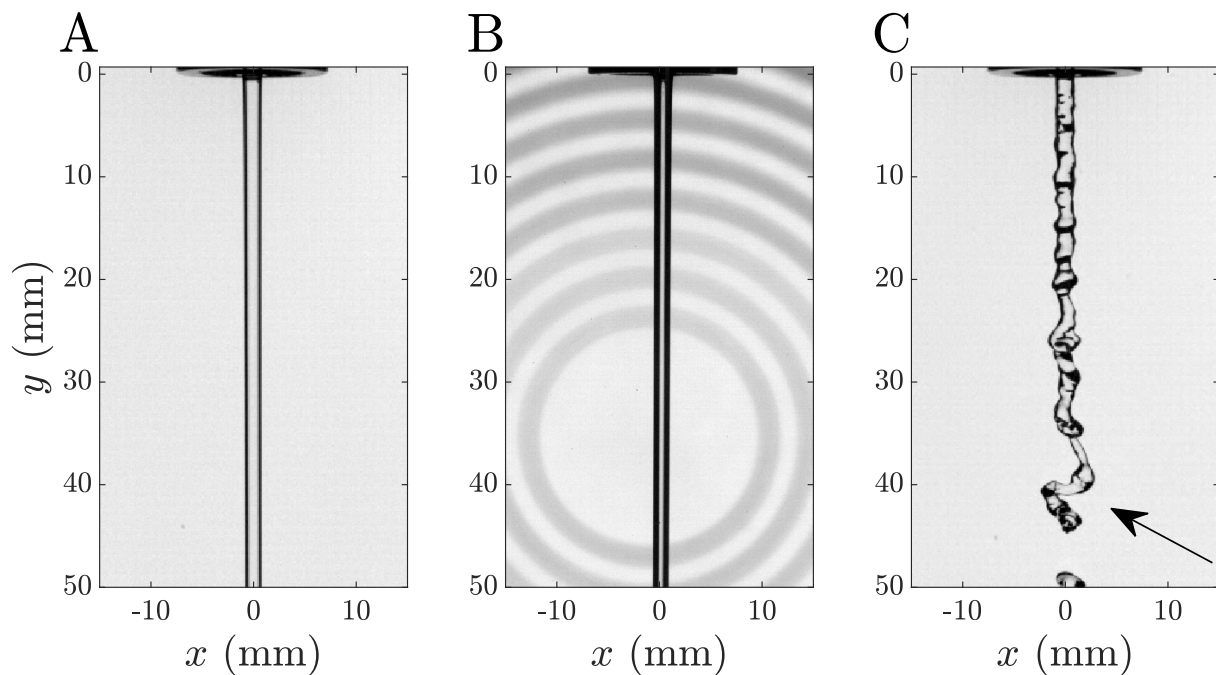


Figure 2.14: A) Liquid jet lighted by a LED panel. B) Liquid jet lighted by a LED spotlight with a Fresnel lens. The rings observed correspond to the sections of the Fresnel lens. C) Sinuous liquid jet lighted by a LED panel (same lighting as A)). The arrow points to a region where the jet boundary becomes very narrow.

Although it can be tempting to use LED panels to have homogeneous lighting over a large area, these types of light can create issues during the analysis process. The liquid jet acts similarly to a lens, therefore a broad-angle light source will lead to a wide bright region in the liquid jet and makes the detection of boundaries harder. Figure 2.14A shows a laminar liquid jet illuminated

by a LED panel and Fig. 2.14B shows a laminar liquid jet lit by a LED spotlight with a Fresnel lens. Going back to binary terms, the goal is to have a dark pixel where water is encountered by the light beam. As explained in Sec. 2.3.1.2, as long as the boundaries of the liquid jet are detected, the filling procedure will fulfill the objective of having dark pixels where water stands, despite having bright pixels in the liquid jet. Although some bright pixels remain in the center of the liquid jet shown in Fig. 2.14B, the liquid boundary is much better seen than in Fig. 2.14A. In the case of a laminar liquid jet, the difference might appear derisory, but when the liquid-gas interface is curved the boundary can be distorted because of this effect, making accurate detection more challenging. Figure 2.14C shows a sinuous liquid jet lighted with the same LED panel as Fig. 2.14A. The arrow points at a location of the liquid jet where the boundary is very narrow due to the broad-angle lighting through the lens-like liquid jet, which leads to an important portion of the liquid jet not being detected. Note that the inhomogeneities of the background seen in Fig. 2.14B are easily corrected, see Sec. 2.3.1.2 that used a similar Fresnel lens.

The ideal imaging system consists of an intense source of light, which beams are directed towards the camera. Different spotlights were used to achieve this goal, the main difference between them is their size and brightness. As discussed in the introduction, it was shown that the size of the average liquid core length decreases when increasing the gas-to-liquid dynamic pressure ratio  $M = \rho_g U_g^2 / \rho_l U_l^2$ . Therefore conditions with lower values of  $M$  require wider imaging windows than conditions with higher values of  $M$ . The conditions with high values of  $M$  also yield high speeds objects. Motion blur is prevented when the imaging pixel size exceeds the product of the object's speed and the exposure time. In the example of conditions with 180 m/s gas velocity, small drops are peeled from the liquid jet and their velocity quickly reaches 100 m/s (or more). With a pixel of 25  $\mu\text{m}$ , this means the exposure time has to be less than 250 ns (which is tuned manually in practice in this vicinity to prevent the visual occurrence of motion blur). Note that the minimum exposure time is 150 ns. Decreasing the exposure time comes to the cost of brightness, therefore small and bright sources were used for the smallest imaging windows with the fastest objects, while weaker but larger sources were used for wide imaging windows.

#### 2.3.1.4 Imaging parameters

As explained in the previous section, various imaging windows were used. Considering the fixed camera resolution, the size of the field of view and the pixel size are correlated and trade-off strategies were employed. The study was limited to the initial breakup of the liquid jet and the imaging window is therefore set to capture the initial breakup without exceeding this length. In addition, at their full resolutions cameras cannot always reach the required acquisition frequency. Reducing the number of pixels on captured frames allows to access higher frequency. It is the gas flow that accelerates portions of liquid, and therefore the fastest objects are seen with the highest gas flows. The acquisition frequency  $f_{acquisition}$  was adapted to the gas velocity to

capture the time dynamics. Fortunately increasing the gas velocity also decreases the length of the liquid portion that has to be filmed therefore the pixel size was not impacted. The acquisition frequency could be adapted and was not a limiting factor for capturing high gas flow conditions. Table 2.2 shows a subset of the typical imaging parameters associated with different imaging windows used, giving an overview of the range of optical setups used. Many more imaging windows were used to optimize the imaging setup of each condition.

Window size height $\times$ width (mm)	pixel size ( $\mu\text{m}$ )	Acquisition rate (Hz)	Exposure Time ( $\mu\text{s}$ )
$30 \times 12$	23	35000	0.1 - 0.15
$40 \times 12$	30	20000	0.15 - 0.28
$80 \times 30$	40	12000	0.2 - 5

Table 2.2: Table of a subset of imaging parameters used to acquire the liquid jet with back-lit imaging.

### 2.3.1.5 Parameter space explored with back-lit imaging

Adapting the imaging setup allowed the exploration of a wide parameter space. As explained in Sec. 2.2, the low limit of the gas flow was chosen to match the early stages of atomization without tackling the matter of the transition to atomization. Conditions below that limit present long liquid jets that can break over a broad region along the spray axis. In that case, an appropriate trade-off between the dimensions of the field of view and the pixel size cannot be reached, and measurements have to be undertaken with two synchronized cameras, each imaging two regions on top of each other. The limitation of back-lit imaging lies in high values of gas flow, for which a dense two-phase flow in the vicinity of the breakup prevents proper identification of the liquid-gas interface [36]. Figure 2.15 shows the conditions explored using back-lit imaging in the  $\{Re_l, We_g\}$  parameter space. Table 2.3 shows the parameters of a sample of conditions, chosen to highlight the maximum and the minimum value of each parameter.

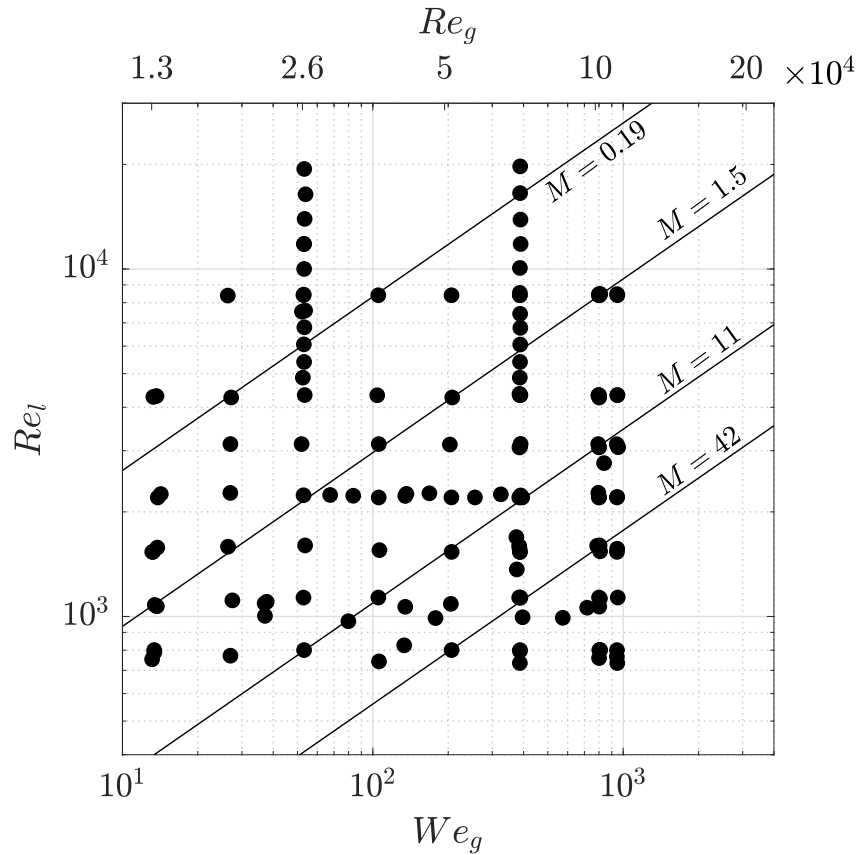


Figure 2.15: Conditions explored with back-lit imaging in the  $\{Re_l, We_g\}$  parameter space. The black lines correspond to iso- $M$  curves. Since the mean liquid core length scales with  $M$ , cutting the parameter space into iso- $M$  indicates the different fields of view that are required.

$U_l$ (m/s)	$U_g$ (m/s)	$M$	$Re_l$	$Re_g$	$We_g$
10	41.9	<b>0.019</b>	<b>20000</b>	26000	53
0.39	177	<b>230</b>	<b>730</b>	<b>110000</b>	<b>950</b>
0.40	20.8	3.05	750	<b>13000</b>	<b>13</b>

Table 2.3: Sample from the investigated operating conditions for back-lit imaging, with their corresponding dimensionless parameters. The maximum and minimum values of the gas-to-liquid dynamic pressure ratio  $M = \frac{\rho_g U_g^2}{\rho_l U_l^2}$ , the liquid Reynolds number  $Re_l = \frac{U_l d_l}{\nu_l}$ , and the gas Reynolds number  $Re_g = \frac{4Q_g}{\sqrt{4\pi A_g \nu_g}}$  are highlighted in bold.  $We_g = \frac{\rho_g U_g^2 d_l}{\sigma}$  is the Weber number based on the liquid diameter.



### 2.3.2 X-Ray imaging

As discussed in the introduction, a few attempts at probing liquid jets with X-ray measurements can be found in the literature [3, 77, 78, 83, 84]. A phase-contrast high-speed radiography technique was tested on liquid jets, using Synchrotron X-ray, and is presented in this section. An example phase-contrast radiograph of coaxial atomization is shown in Fig. 2.16.

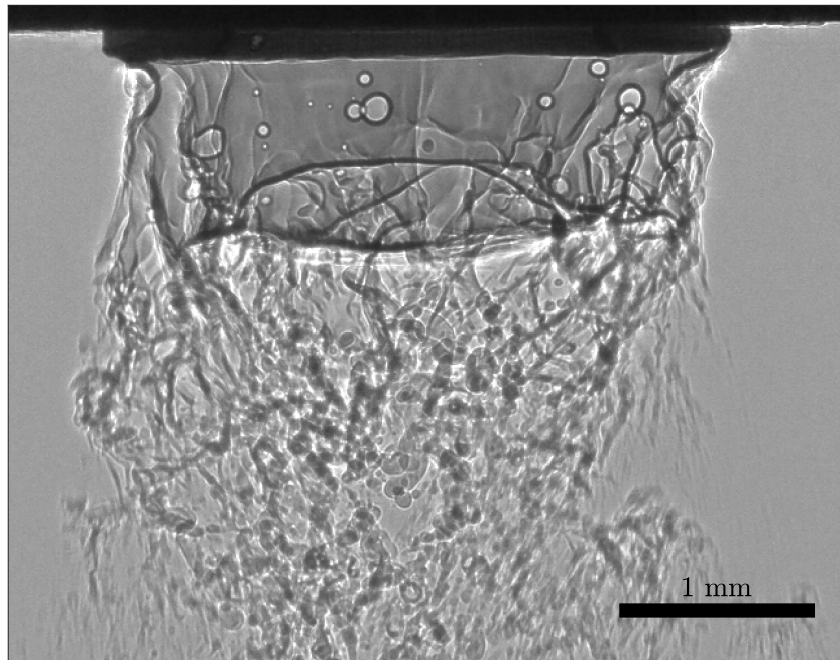


Figure 2.16: X-ray high-speed radiograph of the atomization process, captured at the European Synchrotron Radiation Facility,  $U_l = 0.59$  m/s,  $U_g = 160$  m/s,  $Re_l = 1100$  and  $We_g = 703$ .

#### 2.3.2.1 X-ray imaging in atomization

Unlike lower-frequency waves, such as visible light, X-rays are much less sensitive to deviation on interfaces and are only partially absorbed while traveling through dense materials. The attenuation of the beam is linked to the amount of material it went through, letting one determine the material's thickness by comparing the intensity of the X-ray beam with ( $I$ ) and without ( $I_0$ ) the material. This feature permits the use of tomography on dense objects, which is a 3D reconstruction technique based on the combination of multiple radiographs (typically a thousand) obtained from different views. This technique is widely used in material science, where sampled rotation is leveraged to obtain projections from different angles. To perform tomography on dynamic objects such as a liquid jet, one would require obtaining hundreds of radiographs from different angles, on a timescale hundreds of times smaller than the typical dynamic timescale

of the jet. This would mean spinning the jet at a high rate which would lead to non-negligible Coriolis effects, or having many X-ray beams targeted at the jet from multiple angles (similarly to what has been developed for lower speed two-phase flows, e.g. [85]). Therefore tomographic reconstruction is not yet accessible to high-speed hydrodynamics systems which leave us with the time-resolved 2D mapping of the liquid thickness. It is not the thickness of each droplet that is measured, but rather the equivalent path length (EPL) defined as the cumulative liquid path the beam went through.  $I$ ,  $I_0$ , and the EPL are connected through the Beer-Lambert law, defined in Eq. 2.1, in which  $\mu$  is the X-ray attenuation coefficient. Note that  $\mu$  is a function of both the material the beam passes through and the wavelength of the beam, and it is tabulated for monochromatic beams. In the case of a polychromatic X-ray beam, selective attenuation of lower energy photons is observed which is referred to as beam hardening. This effect is similar to that of a low-pass filter and the direct measurement of the EPL through the monitoring of ( $I$ ) and ( $I_0$ ) through Eq. 2.1 can become unreliable. If the beam is monochromatic,  $\mu$  is constant (in the case of a single homogeneous sample) and Eq. 2.1 can be simplified into Eq. 2.2, allowing for direct measurement of the EPL. In the case of water and air, the cumulative absorption of both phase add up to the overall absorption. The absorption coefficient of the gas phase being orders of magnitude smaller than the liquid's absorption coefficient, the contribution of the gas can be neglected.

$$I = \int I_0 e^{-\mu(\lambda) \text{EPL}} d\lambda \quad (2.1)$$

$$\text{EPL} = \frac{1}{\mu} \log \left( \frac{I_0}{I} \right) \quad (2.2)$$

Despite being less sensitive to deviation on interfaces than visible light, X-rays can undergo Fresnel diffraction, leading to interference patterns. As a result, the liquid-gas interfaces may be surrounded by such patterns and appear on a wider region, which is the case in our experiment illustrated in Fig. 2.16 and 2.17A) where a white, or a black and a white line surround the interfaces. When the intensity  $I$  of the beam coming out of the sample is recorded just after the beam exits the sample (with no propagation of the X-rays between the sample and the sensor) these weakly deviated beams do not lead to visible interference patterns. In this situation the EPL of the sample is retrieved using the Beer-Lambert law, and this technique is called absorption contrast imaging. If the beam's intensity  $I$  is monitored further away, which is the case in our experiment, the diffracted beams deviate from their original spot while they propagate, leading to the interference patterns previously described. This makes the computation of the EPL more complex since the interference patterns need to be taken into account during the processing. Phase contrast imaging is the name given to the techniques exploiting the phase variations of the X-ray beams coming out of a sample, to measure precise intensity variations of the beam and highlight interfaces.

Two main sources of X-rays are commonly used. The first one is a tube source X-ray, which consists of a vacuum tube in which a filament is heated by an electric current. Electrons are then emitted by the heated filament and accelerated, creating the X-ray beam. Tube source X-rays provide a white-beam X-ray in a conical shape. The term *white-beam* refers to the fact that the beam contains a wide range of photon energies (i.e. white, or broadband, energy spectra), meaning the determination of the EPL is done by inverting Eq. 2.1. This type of X-ray source only require a specific room (typically lined with lead) and some equipment, and is therefore the most practical to use. Unfortunately, they are relatively weak sources. The exposure time has to be set to several ms, which is too slow to capture the dynamics of the atomization process. These sources also are relatively divergent which leads to penumbra effects [86], blurring the images. Nevertheless, they have been used for instance to map the time-average EPL maps of the atomization process [84].

The second type of source of X-ray beams is synchrotrons. Synchrotrons accelerate electrons by spinning them inside a torus under vacuum using a guiding magnetic field. These sources are much brighter sources than the previously presented tube sources and are highly collimated. Their main downside is their unavailability: synchrotrons are massive facilities that are very solicited and it is therefore a challenging procedural and time-restrained experience to use them. Nonetheless, they provide a unique tool to probe dense systems. This kind of synchrotron-produced X-ray beam measurements has been conducted to probe atomization, at the Advanced Photon Source<sup>3</sup> (APS) at Argonne National Laboratory (in Lemont, Illinois). Two techniques were conducted and described in the literature. The first one is using focused-beam radiography of the liquid jet, for which the spectral bandwidth of the X-ray beam is reduced enough for it to be considered monochromatic when determining  $\mu$ . Reducing the bandwidth comes to the cost of brightness which is compensated by condensing the beam's energy by reducing its size. To put this into perspective, Li et al. [84] report a  $5 \times 6 \mu\text{m}$  size monochromatic synchrotron X-ray beam while doing this technique, while the original beam width is  $6 \times 8 \text{ mm}$ . This technique does not allow full cartography of the liquid jet's instantaneous EPL. Instead, they rather used a pin-diode to collect the focused X-ray beam and measure the EPL at a given location and collected multiple independent series done at different locations to characterize the liquid jet. Using a monochromatic beam, the determination of  $\mu$  is reliable and leads to a relatively precise measurement of the EPL but, being a pointwise measurement, does not allow for spatial correlation. Nonetheless, this technique was proven robust and validated some measurements conducted with back-lit imaging measurements of average spray images. A second approach consists of using the non-filtered synchrotron X-ray beam. This leads to a broader-band energy spectrum beam leading to a harder determination of  $\mu$ , however also to a high-energy beam which can be used to illuminate a wider window, typically allowing the imaging of a 3 mm wide liquid nozzle.

---

<sup>3</sup><https://www.aps.anl.gov/>

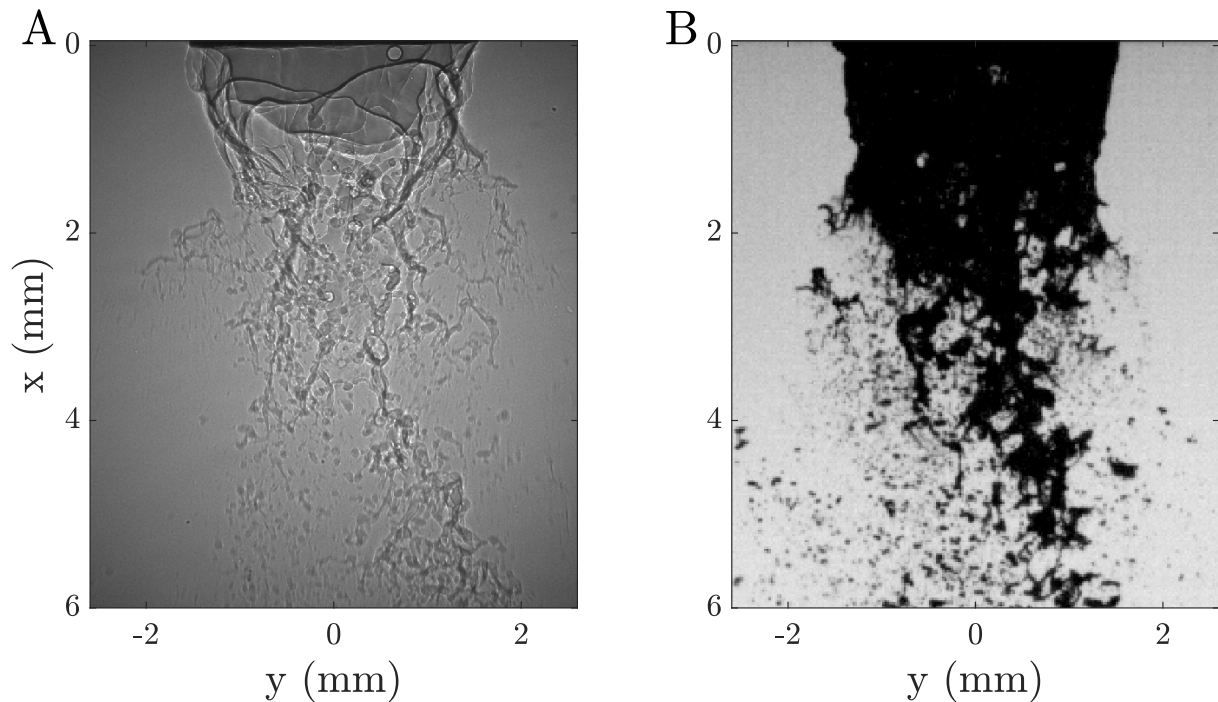


Figure 2.17: A) X-ray radiograph and B) back-lit image of the atomization process, captured with the same injection parameters  $U_l = 0.40$  m/s,  $U_g = 113$  m/s,  $Re_l = 750$  and  $We_g = 390$ .

Fig. 2.17 compares two images captured with A) X-ray radiography and B) back-lit imaging, for the same injection parameters. The complex geometry of the two-phase flow, visible on the X-ray radiograph, cannot be seen on the back-lit image. As discussed in the introduction, Machicoane et al. [3] identified regimes of the shape of the near-field breakup. Also, the liquid repartition is not as straightforward as what one might expect, qualitative observations of the breakup are discussed in sec. 4.2.

The experiment presented here uses the powerful beamline supplied by the ESRF facility to perform X-ray radiographs on a wide window (up to  $\approx 7\text{mm} \times 7\text{mm}$ ) with a relatively narrow spectrum beam. The experiment was conducted in the beam line ID19<sup>4</sup>, which is specialized in Microtomography and Phase contrast imaging. Propagation-based phase contrast imaging was performed, and the details of the image processing are described in Sec. 4.4.

<sup>4</sup><https://www.esrf.fr/home/UsersAndScience/Experiments/StructMaterials/ID19.html>

### 2.3.2.2 Experimental setup

Figure 2.18 shows the installation used for the X-ray imaging. The collimated X-ray beam passes through the spray and reaches a scintillator. The distance between the spray and the scintillator is 4 m. The scintillator consists of a YAG:Ce crystal, which fluoresces visible light and has an intensity proportional to the intensity of the incoming X-ray beam. If the scintillator is lit for too long it heats up and breaks, limiting the duration of each movie. With the final imaging setup, 2 s of X-ray exposition was too much and would break the scintillator. To control the duration of the illumination a fast shutter is installed in between the X-ray source and the scintillator and is set to open for 1.1 s (Fig. 2.18). The trigger of the camera is manually synchronized with the shutter opening to capture a movie. The visible light is then reflected by a mirror placed after the scintillator, reflecting the visible light onto a high-speed imaging camera (Photron FASTCAM SA-Z), preventing the camera from being on the path of the X-ray beam, which could damage it.

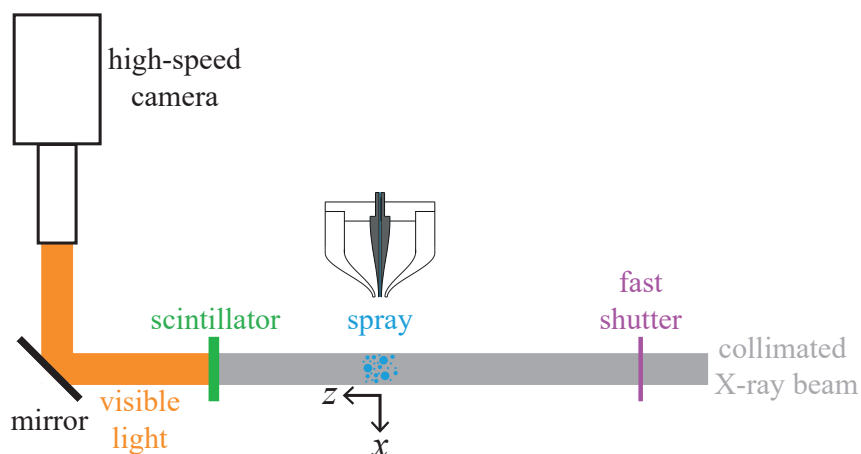


Figure 2.18: Sketch of the X-ray imaging line. The collimated X-ray beam provided by the ESRF facility is aimed at the spray and then impacts a scintillator. The scintillator converts X-ray light into visible light which is reflected on a high-speed camera. A shutter is placed in between the X-ray source and the spray to cut the X-ray source when needed.

The resolution of the imaging system (the size of a pixel), was set to  $6.7 \mu\text{m}$  (roughly 5 times smaller than with back-lit imaging). The size of the windows was maximized according to the required acquisition frequency. As explained in sec. 2.3.1.4, the acquisition frequency has to be increased when increasing the gas velocity. This was achieved by decreasing the number of pixels used, resulting in a smaller window size. Table 2.4 shows the different imaging parameters that were used. With a small window size but high acquisition frequency, the system is well-suited to analyze conditions with smaller spatial and temporal timescales than the conditions explored with shadowgraphy.

Window size height $\times$ width (mm)	Window size height $\times$ width (pixel)	Acquisition rate (Hz)
$6.86 \times 6.86$	$1024 \times 1024$	10000
$6.86 \times 6.86$	$1024 \times 1024$	20000
$6.86 \times 5.63$	$1024 \times 840$	25000
$6.86 \times 4.34$	$1024 \times 648$	32000
$6.86 \times 3.43$	$768 \times 512$	50000

Table 2.4: Imaging parameters used at the ESRF. The size of the windows was reduced to increase the acquisition rate. The pixel size and the exposure time are  $d_{\text{pixel size}} = 6.7 \mu\text{m}$  and  $\tau_{\text{exposure}} = 2.5 \mu\text{s}$  respectively and are kept constant for all the runs.

Note that the exposure time is 25 times higher than the smallest exposure time used in back-lit imaging and that the effective pixel size of the X-ray radiographs is around 3 times smaller than the one used for the highest acquisition frequency with back-lit imaging. Motion blur is avoided when the velocities of the objects within the field of view are below  $v_{\text{blur}} = d_{\text{pixel size}}/\tau_{\text{exposure}}$ , which is  $v_{\text{blur}} \simeq 2.68 \text{ m/s}$  in the case of our X-ray imaging and  $v_{\text{blur}} \simeq 230 \text{ m/s}$  in the case of the smallest field of view used for back-lit imaging. The X-ray imaging setup used in our case is therefore much more sensitive to motion blur than the previously presented back-lit imaging setup.



### 2.3.2.3 Beam characteristics

The creation and the conditioning of the X-ray beam is a technical, scientific, and engineering masterpiece and cannot be fully detailed in this manuscript. For an overview of the complexity of such systems, the reader may refer to [87]. The ESRF facility provides a stable, high-energy, coherent, and highly collimated X-ray source that is used to image the spray. The spectrum of the X-ray beam used is presented in Fig. 2.19. The spectrum contains three peaks. Although the beam is not purely monochromatic, the first peak corresponds to over 90% of the beam's photons flux and to over 85% of the total energy of the beam. The method used to measure the EPL, discussed in Sec. 4.4, is based on the assumption that the beam is monochromatic. This bias will be discussed and taken into account. It is possible to have a monochromatic X-ray beam, but this comes at the cost of brightness, and/or at the cost of a reduction of the size of the field of view.

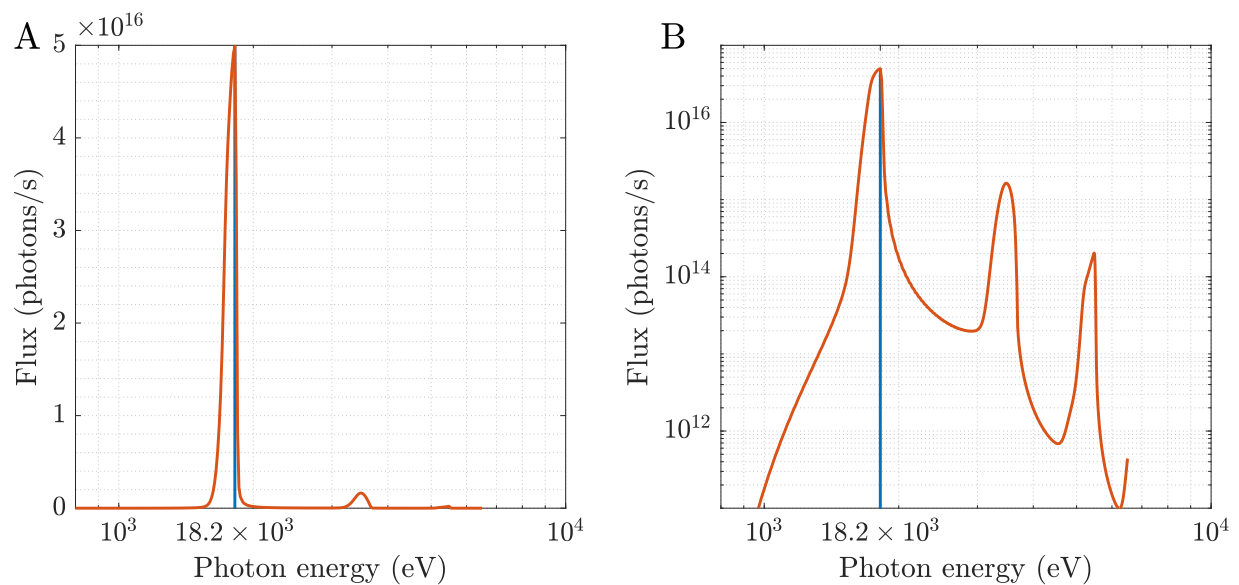


Figure 2.19: Photon flux per  $\text{mm}^2$  at the center of the X-ray beam in A) semi-logarithmic plot and B) logarithmic plot.

A study conducted on flat-field radiograph movies, corresponding to radiograph movies where no liquid is present in the field of view, is conducted in Sec. 4.3. It highlights that:

- The emission of photons is inhomogeneous in time. Although this does not disrupt the visualization of the images, it has a direct impact on quantitative measurements.
- The beam is non-uniform in space. However, using flat-field measurements, also referred to as background measurements, these spatial variations are well corrected.

## 2.3.2.4 Adapting the setup

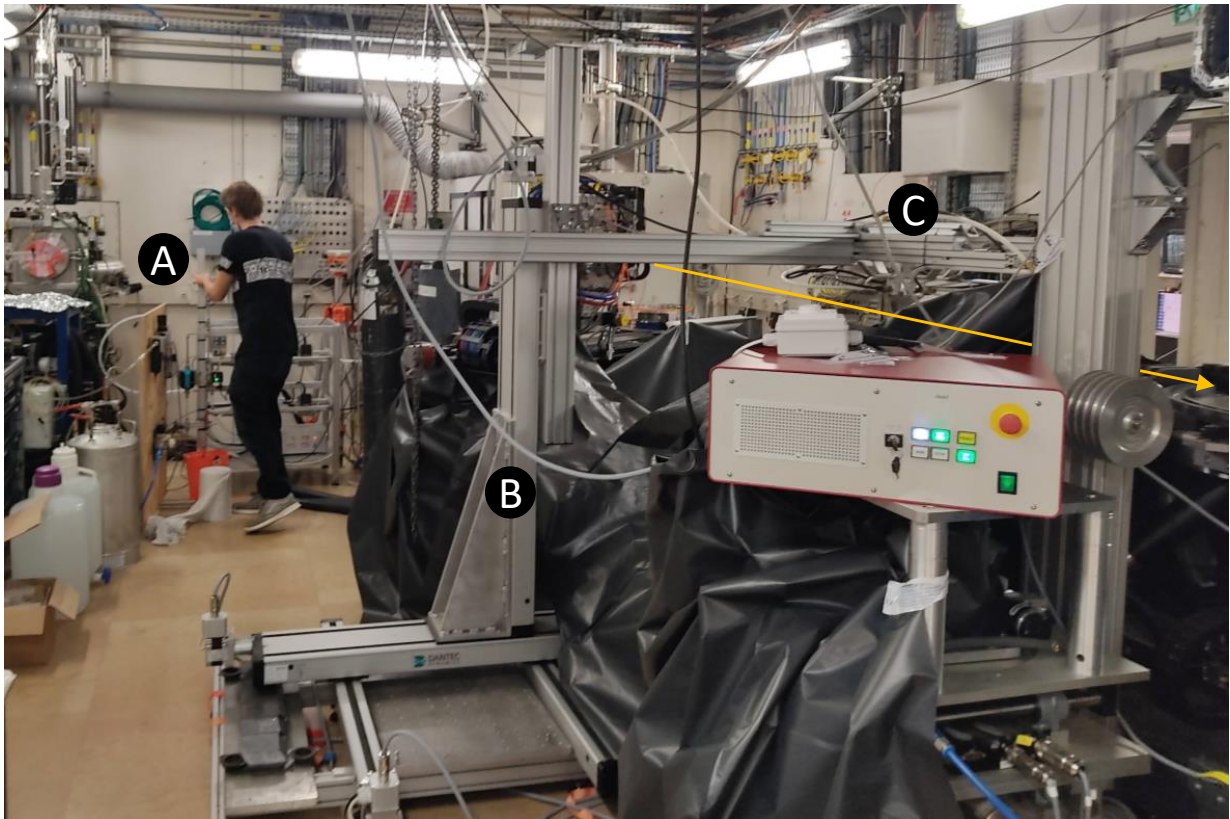


Figure 2.20: Image of the hutch at ESRF with the atomization setup. A) flow conditioning loop. B) translation stage. C) Atomizer. The yellow arrow illustrates the path of the X-ray beam, it comes into the hutch through a hole in the back wall, goes beneath the atomizer, and targets the imaging system which is further behind in the hutch.

The European Synchrotron Radiation Facility (ESRF) accepted to host us for 9 8-hour shifts to do X-Ray imaging with the coaxial atomizer previously presented. Running experiments at the ESRF facility required adaptation of the setup. The X-ray beam is lit inside a hutch (see Fig. 2.20) which cannot be accessed when the beam is operating for obvious safety reasons. The flow loop was installed inside the hutch (see Fig. 2.20A)) and its monitoring is done from a control station located in the next room. The X-ray experiment is well suited to the study of high gas Reynolds number conditions which yield a dense two-phase flow. To fully use this opportunity and to explore a new range of parameters the maximum value of gas Reynolds number accessible was extended by using high-pressure nitrogen cylinders. A gas conditioning system was added to the flow loop to use these cylinders. When back-lit imaging is performed at LEGI, the nozzle is fixed on a frame and the camera and lighting system are positioned to match the window position that the user wants to image. In the ESRF's hutch, the imaging system is at a fixed position (the X-ray beam always comes in at the same location) and it is therefore the injector that has to



be placed in agreement with the imaging system. The nozzle was attached to a 3D translation stage which was controlled to place the nozzle for each run (see Fig. 2.20B) and C)). All of the monitoring is done from a control station outside the hutch for safety reasons. Since time is sparse when conducting synchrotron measurements, the technical hardware and software aspects of this venture were tested and refined in depth at LEGI, prior to the scheduled beamtime.

The window sizes are much smaller than the ones available with back-lit imaging, as their are limited by the size of the X-ray beam. To capture the spray formation region, multiple imaging windows at different locations had to be done for injection conditions that yield long liquid cores, as illustrated in Fig. 2.21. This results in a total of 204 movies, corresponding to 102 unique injection conditions.

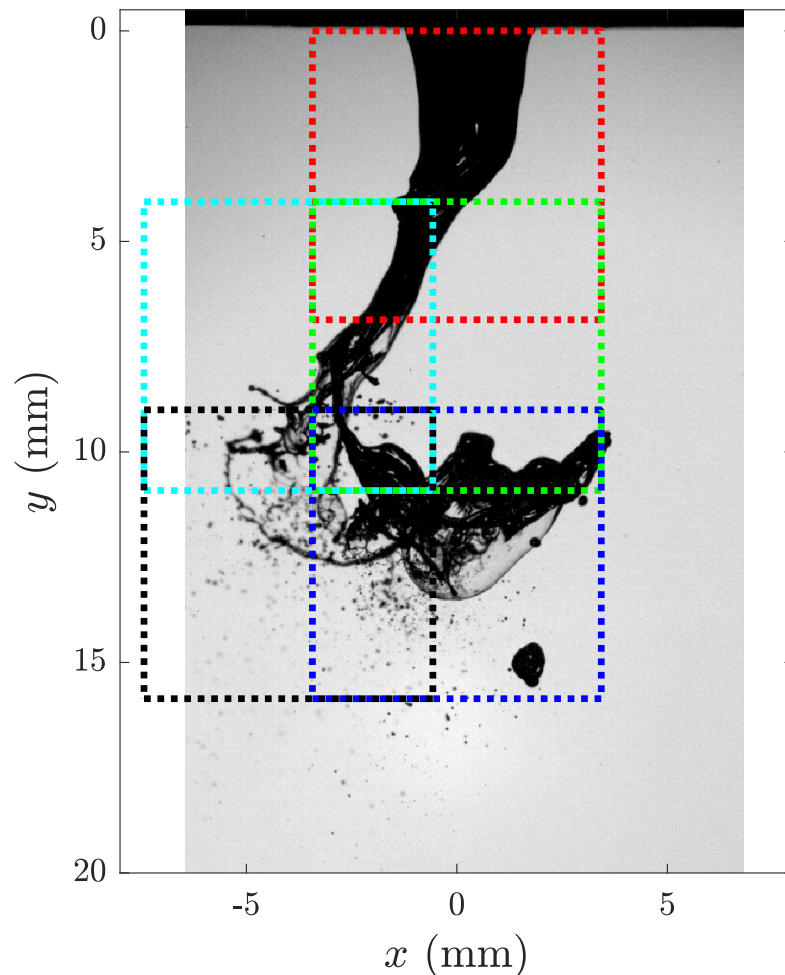


Figure 2.21: Back-lit image of the breakup of a liquid jet by a coaxial gas coflow, the injection parameters are  $U_l = 0,41$  m/s and  $U_g = 30$  m/s. The 5 colored squares highlight the positions of the 5 windows used for the independent X-ray movies for the same injection rates.

## 2.3.2.5 Parameter space explored

As explained in sec. 2.3.1.5, the parameter space is scanned through variations of the liquid and gas flow rates. Compared to the measurements conducted with shadowgraphy, the conditions explored with X-ray measurements had higher gas flow rates. An overlap between the conditions explored with shadowgraphy and the ones explored with X-ray was done to be able to compare both techniques. Table 2.5 summarizes the conditions explored during the X-ray measurement, which are also shown in the  $\{Re_l, We_g\}$  parameter space of Fig. 2.22.

$U_l$ (m/s)	$U_g$ (m/s)	$M$	$Re_l$	$Re_g$	$We_g$
0.42	30	<b>5.6</b>	<b>780</b>	<b>19000</b>	<b>27</b>
0.42	318	<b>631</b>	<b>780</b>	<b>200000</b>	<b>31000</b>
2.3	318	21.5	<b>4300</b>	<b>200000</b>	<b>31000</b>

Table 2.5: Sample from the operating conditions investigated with X-ray imaging, with their corresponding dimensionless parameters. The maximum and minimum values of the presented parameters are highlighted in bold.

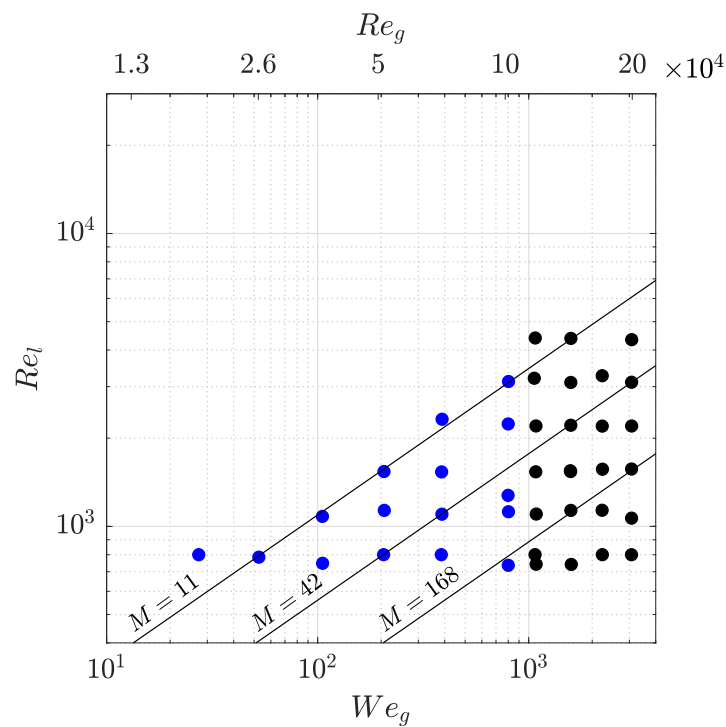


Figure 2.22: Explored conditions in the  $\{Re_l, We_g\}$  parameter space. The black lines correspond to iso-M curves. Black dots correspond to injection conditions that were studied using X-ray imaging only, and blue dots correspond to injection conditions that have been studied using both back-lit and X-ray imaging.



# Statistics and dynamics of a liquid jet under fragmentation by a gas jet

---

This chapter is published in *Physical Review Fluids* [1]. The work presented here was initiated thanks to the great work of Guillaume Deplus during an internship he did in LEGI, that was supervised by Nathanaël Machicoane and myself. I then collected additional data and expended the analysis after he finished his internship. More details on the image processing methods and biases as well as data convergence are given in the Appendix (Chap. [A](#), [B](#), and [C](#)).

PHYSICAL REVIEW FLUIDS 8, 044304 (2023)

---

## Statistics and dynamics of a liquid jet under fragmentation by a gas jet

Oliver Tolfts, Guillaume Deplus, and Nathanaël Machicoane

*Univ. Grenoble Alpes, CNRS, Grenoble INP, LEGI, 38000 Grenoble, France*

(Received 22 October 2022; accepted 11 April 2023; published 21 April 2023)

The breakup of a liquid jet by a surrounding gas jet is studied in a coaxial configuration using high-speed back-lit imaging. This work focuses on the time dynamics and the statistics of the length of the liquid jet. The inlet velocities are varied for both fluids to obtain a wide range of gas and liquid Reynolds numbers and equivalently a wide range of gas-to-liquid dynamic pressure ratio  $M$  and Weber number. The variety of scales exhibited throughout this range, exploring two breakup regimes, is covered by adapting the spatial and temporal resolutions as well as the field of view of the imaging system. An in-depth study of the distributions of the length of the liquid jet is presented, with the associated scalings for the evolution of the first three statistical moments with the relevant dimensionless parameters, fully describing the statistics through a unique function. The first two moments of the distributions are shown to be power laws of  $M$  and their ratio is observed to be constant. The temporal dynamics are studied using autocorrelation functions of

the length of the liquid jet. The correlation times are shown to be controlled by the gas jet, with a secondary influence of the liquid Reynolds number through a change of behavior that appears to be related to the onset of liquid turbulence. In addition, a transition between two regimes highlighted by a change of shape of both the probability density and autocorrelation functions of the liquid core length is introduced and its link to the turbulence characteristics of the gas jet and the underlying breakup mechanisms is discussed.

### 3.1 Introduction

The fragmentation of a liquid jet by a surrounding gas jet stands as a useful setting to study the fundamental mechanisms that take place in the transport, destabilization, and breakup of a liquid phase by a turbulent gas phase. This situation is at the base of gas-assisted, also called airblast, atomization, where atomization is defined as the breakup of a bulk of liquid into a cloud of droplets (spray). Atomization finds numerous applications in industry, e. g. combustion and manufacturing, but also in natural systems such as sea sprays [88–90]. In gas-assisted atomization, the interaction of a liquid jet with a surrounding high-speed gas jet leads to the fragmentation of the liquid phase into a spray through a cascade of destabilization and breakup mechanisms [7, 13–15, 22, 91]. A Kelvin-Helmholtz instability was identified as being responsible for the initial disturbance of the liquid-gas interface [13–17]. This creates a wave-shaped perturbation on the surface of the liquid jet, which is then destabilized by the gas jet. The subsequent mechanism can be described by taking an analogy to the breakup of a single drop with no initial velocity and suddenly accelerated by a gas flow, as studied by [18] (alternatively readers can refer to the review of Theofanous [92]). They report different drop breakup mechanisms and classify them according to the Weber number  $We$  at the drop scale, which compares aerodynamic stresses to the drop surface tension force read as  $We = \rho_g U^2 d / \sigma$ , where  $\rho_g$  is the gas density,  $U$  the relative velocity between the drop and the gas flow,  $d$  the drop diameter, and  $\sigma$  the surface tension coefficient. For low  $We$  values, they observed that the drop is first flattened into a disc-like shape, surrounded by a thick liquid rim. As the disc is further stretched and inflated by the gas flow, it thins into a membrane that will eventually break into small droplets, while the rim produces larger droplets. This breakup regime is referred to as bag-breakup or membrane-breakup. For high values of the Weber number, the drop initially flattens and the drop's interface, roughly transverse to the gas flow, is strongly accelerated, leading to a Rayleigh-Taylor instability. When the amplitude of this instability reaches the width of the flattened drop, it breaks into droplets. This breakup regime is referred to as catastrophic breakup. A similar classification of the qualitative visualization of the breakup of a liquid jet by a surrounding gas jet has been done [19, 20]. For low gas velocities, the wave-shaped perturbation is inflated, creating a thin membrane that will eventually break into droplets [25]. For higher gas velocities, the wave-shaped perturbation is stretched into a ligament that can detach from the liquid bulk, or undergo Rayleigh-Taylor instability, leading to the formation

of drops peeled off from the liquid jet. Both of these underlying breakup mechanisms define breakup regimes, respectively called membrane-breakup (alternatively bag-breakup) regime, and fiber-type atomization (alternatively stripping regime) [19]. In addition to the small-scale breakup mechanisms, a large-scale motion of the entire liquid jet can take a role in the cascade of breakup mechanisms. This large-scale instability is referred to as flapping [22–24, 93]. Each breakup mechanism participates in the fullness of the size and spatio-temporal distributions of the resulting droplets that form the spray.

The fragmentation of a liquid jet by a surrounding gas jet is a turbulent two-phase flow involving a wide range of temporal and spatial scales. The multiscale nature of spray formation prevents using a single approach to study the underlying mechanisms of the fragmentation cascade. Such complexity coupled with the broad scope of applications involving sprays led to the introduction of many dimensionless controlling parameters and reported metrics. The liquid core length  $L_B$ , defined as the longitudinal extent of the portion of liquid that is connected to the nozzle, stands as one of the first metrics that comes to mind and received attention early on in coaxial atomization [49]. Focusing on the average liquid core length, the gas-to-liquid dynamic pressure ratio  $M$  was identified as the driving parameter [2, 23, 30]. Using different fluids, geometries, and varying the velocity of the fluids at the injection, [2] proposed a power-law decay with  $M$ . [23, 30] reported a similar exponent along  $M$ , confirming the scaling and identifying that the prefactor of the power-law was influenced by the nozzle geometry. Modest interest has been given to the fluctuations of  $L_B$ . The ratio of the standard deviation to the average liquid core length was reported by [23, 94]. Recent studies have looked deeper into the statistics by describing the probability density function of  $L_B$  [24, 36], showing non-Gaussian behaviors. One could expect that the change in breakup regimes described above has a signature on the behavior of  $L_B$ . Nevertheless, to our best knowledge, no quantitative indicator of the change of breakup regime has yet been found when studying the liquid core length.

Considering temporal scales involved in spray formation processes, the flapping instability frequency was shown to be mostly governed by the gas jet velocity [22]. In addition, the inner vorticity layer of the annular gas jet was reported to directly influence the frequency of the Kelvin-Helmholtz and Rayleigh-Taylor instabilities [13, 14]. The timescale of the liquid core length was recently extracted using auto-correlation functions [36, 51]. Both studies conclude that the timescale diminishes with  $M$  but only the gas velocity was varied (constant laminar liquid injection). Since the gas jet is at the origin of the destabilization and breakup of the liquid jet, one can expect the timescales of the gas flow to drive the timescales of  $L_B$ . However, no study was pursued on the role of the liquid Reynolds number and of the onset of liquid turbulence on the temporal dynamics of the liquid core length.

The present work aims at addressing the questions raised on the effect of breakup regime

and liquid turbulence on the behavior of the liquid core length, through the introduction of a framework that adequately describes its statistics and temporal dynamics. Therefore, an experimental study is conducted on a wide range of liquid and gas Reynolds numbers, encompassing two breakup regimes and the transition from a laminar to a turbulent state of the liquid jet, resulting in over four orders of magnitude of variation of the gas-to-liquid dynamic pressure ratio  $M$ . While  $M$  appears to govern the evolution of the mean liquid core length along variations of injection parameters, the qualitative boundary between the membrane-breakup and fiber-type atomization regimes is almost vertical in the  $(Re_l, We_g)$  parameter space [19].  $Re_l$  stands here for the Reynolds number of the liquid jet (equivalently  $Re_g$  can be used for the gas jet), and  $We_g$  is the Weber number comparing the gas jet dynamic pressure to the surface tension force of the liquid jet. For a fixed couple of fluids, this means that the transition occurs at a given gas velocity. By increasing the gas velocity at several values of the liquid Reynolds number (liquid velocity), the explored parameter space crosses this transition many times at various values of  $M$ , giving the possibility to uncouple  $We_g$  (change of regimes) and  $M$  (scalings of  $L_B$ ). An alternate approach would be to vary the parameters of the fluids (in particular the fluids densities and the surface tension coefficient) [2, 95, 96], which is more challenging in the current setup. In the approach where only the liquid and gas velocities are varied, the effects of the gas velocity are equivalently described by  $We_g$  and  $Re_g$ . First, the previous introduction of a functional description of the full statistics of  $L_B$  [24] is validated in the extended range of non-dimensional parameters. This approach underlines a transition, that is confirmed by the temporal behavior and can be related to changes in breakup regime. In addition, the timescales of the liquid core length are reported to scale linearly with the inverse of the gas mean exit velocity but also show an increased prefactor when the injected liquid jet is turbulent. Throughout the manuscript, changes in atomization regimes and the onset of liquid turbulence are highlighted with the use of color bars and symbols (described accordingly in the captions of the figures), and the effect of both aspects on the statistics and temporal dynamics of the liquid core length are discussed in Sec. 3.5. Section 3.2 first describes the experimental setup and the analyses. The statistics and temporal dynamics are respectively presented in Sec. 3.3 and 3.4. The discussion (Sec. 3.5) is then followed by a conclusion (Sec. 3.6).

## 3.2 Materials and methods

### 3.2.1 Two-fluid coaxial atomizer

The experimental setup consists of a coaxial atomizer, shown in Fig. 3.1A (more details on the [open-source geometry](#) is given in [3]). The liquid nozzle is 100 mm long, with an inner diameter  $d_l = 1.98$  mm and an outer diameter  $D_l = 3.1$  mm. This geometry ensures a Poiseuille flow is fully established before the liquid exits the nozzle when operated in laminar conditions,



while a fully-developed plug flow is expected in turbulent conditions. The liquid nozzle is placed at the center of the gas nozzle. The outer wall of the liquid nozzle and the inner wall of the gas nozzle form a cavity that channels the gas into an annular exit plane with an inner diameter  $D_l$  and an outer diameter  $d_g = 9.985$  mm. Note that  $d_l$ ,  $D_l$ , and  $d_g$  are measured with the same accuracy of  $1 \mu\text{m}$ . Both of these walls present a cubic-spline shape ensuring the gas flow is longitudinal when it exits the nozzle. The working fluids are air and water at  $25^\circ\text{C}$ .

The volumetric flow rates of the gas and the liquid, respectively noted  $Q_g$  and  $Q_l$ , are monitored by flowmeters. A pressurized tank is used to produce the liquid flow. The tank's pressure is regulated to limit the fluctuations in the flow rate. The uncertainty of the liquid flow rate is given by the uncertainty of the associated flowmeter  $\Delta Q_l = 0.06$  L/min. Compressed air is used for the gas flow, with a pressure regulator set below the compressor's low-pressure point to ensure a steady gas flow. The uncertainty of the gas flow is dominated by the small variations caused by the feedback control loop that fixes the gas flow rate. This uncertainty, much larger than the flowmeter uncertainty, is calculated for each run and is typically of order  $\Delta Q_g = 2.5$  L/min.

We define the gas and liquid mean velocities at the exit plane respectively as  $U_g = \frac{Q_g}{A_g}$  and  $U_l = \frac{Q_l}{A_l}$ , with  $A_l = \pi \frac{d_l^2}{4}$  the liquid section and  $A_g = \frac{\pi}{4}(d_g^2 - D_l^2)$  the gas section. The liquid Reynolds number  $Re_l = \frac{U_l d_l}{\nu_l}$ , where  $\nu_l$  is the kinematic viscosity of water, is varied from 730 to 20000, encompassing the transition from a laminar to a turbulent exiting liquid jet. The gas Reynolds number  $Re_g = \frac{2Q_g}{\sqrt{\pi A_g} \nu_g}$ , with  $\nu_g$  the kinematic viscosity of air, ranges from  $10^4$  to  $10^5$ .

The Weber number based on the gas velocity and on the liquid inner diameter  $We_g = \frac{\rho_g U_g^2 d_l}{\sigma}$  ranges from 14 to 950. Note that with the  $\rho_g$  and  $\sigma$  being fixed, the gas Weber number and gas Reynolds number can be used equivalently to describe changes in gas velocity. Alternatively, when defined based on a slip velocity between each phase, the Weber number  $We_r = \frac{\rho_g (U_g - U_l)^2 d_l}{\sigma}$  range becomes  $11 \leq We_r \leq 940$ . An important dimensionless parameter for the liquid core length is the gas-to-liquid dynamic pressure ratio (also called gas-to-liquid momentum ratio)  $M = \frac{\rho_g U_g^2}{\rho_l U_l^2}$ , where  $\rho_l$  is the density of the liquid phase. The dynamic pressure ratio varies by over 4 orders of magnitude, from 0.02 to 230. The extrema of the investigated parameter space are summarized in Table 3.1. With these injection conditions, we observe two different breakup regimes referred to as fiber-type regime, see Fig. 3.2A and B, and membrane-breakup regime, see Fig. 3.2C. Note that conditions where both membrane formation and fiber-type atomization can occur will be referred to as a transitional regime, since both breakup mechanisms coexist. The determination of atomization regimes is discussed later on in Sec 3.5.



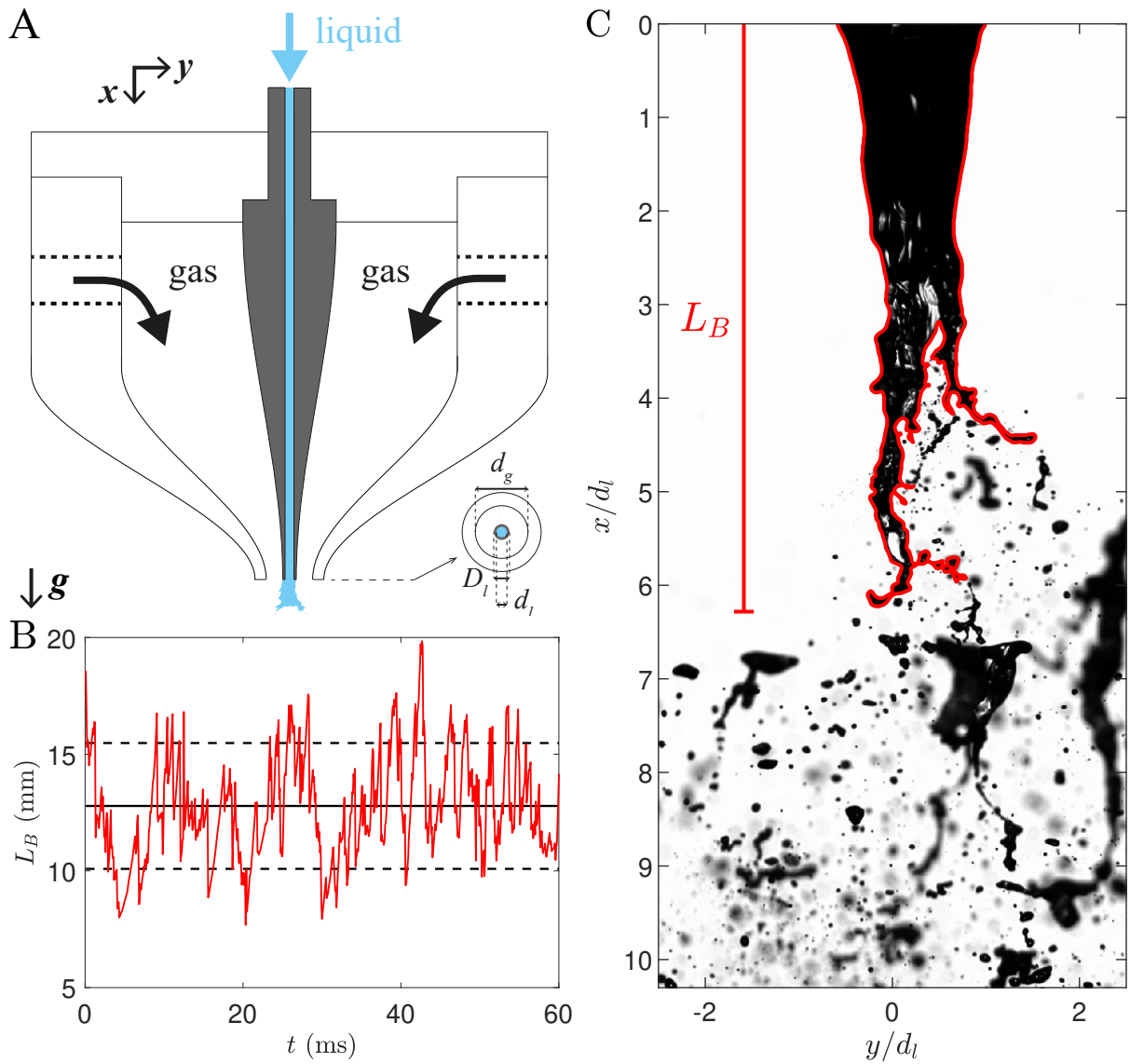


Figure 3.1: A: Schematic view of the atomizer, including a cross-section of the exit plane showing the relevant dimensions. B: Example sub-sample time series of liquid core length  $L_B$ . C: Detection of the liquid core length on an instantaneous image.

$U_l$ (m/s)	$U_g$ (m/s)	$M$	$Re_l$	$Re_g$	$m$	$We_g$
10	41.9	<b>0.019</b>	20 000	26 000	0.34	53
0.39	177	<b>230</b>	730	110 000	0.0031	950
0.39	113	94	<b>730</b>	71 000	0.0048	390
11	113	0.13	<b>20 000</b>	71 000	0.13	390
2.3	20.9	0.095	4 300	<b>13 000</b>	0.15	14
1.6	177	13.3	3 000	<b>111 000</b>	0.013	950

Table 3.1: Sample from the 93 investigated operating conditions, with their corresponding dimensionless parameters. The maximum and minimum values of the gas-to-liquid dynamic pressure ratio  $M = \frac{\rho_g U_g^2}{\rho_l U_l^2}$ , the liquid Reynolds number  $Re_l = \frac{U_l d_l}{\nu_l}$ , and the gas Reynolds number  $Re_g = \frac{4Q_g}{\sqrt{4\pi A_g} \nu_g}$  are highlighted in bold.  $m = \frac{\rho_l U_l A_l}{\rho_g U_g A_g}$  represents the liquid mass loading and  $We_g = \frac{\rho_g U_g^2 d_l}{\sigma}$  the Weber number based on the liquid diameter.

### 3.2.2 Data acquisition

We use back-lit imaging with a high-speed camera to measure the dynamics of the liquid jet breakup. The imaging parameters are adapted to the temporal and spatial scales of the spray formation mechanisms that vary on the considered parameter space. The frame rate used ranges from 12 000 Hz to 35 000 Hz and the imaging window varies from  $20 \times 10 \text{ mm}^2$  to  $80 \times 30 \text{ mm}^2$ . As the highest frame rates require reducing the number of pixels used, maintaining the targeted physical size of the imaging window is attained by lowering the magnification. The resulting spatial resolutions hence vary from 15 to 80  $\mu\text{m}/\text{pixels}$ . Each movie contains at least  $10^4$  frames, corresponding to 0.3 - 0.8 s depending on the frame rate, ensuring each acquisition is longer than a hundred times the timescale associated with the liquid jet length variations.

The image processing aims at measuring the liquid core length. Each frame goes through a normalization process, which consists in subtracting a reference background and then dividing by the reference background. Figures 3.2A, B, and C show normalized snapshots for different injection conditions. Movies of these three conditions are provided in the Supplementary Materials. The images are then binarized using thresholding to detect the liquid core. More details on the image processing can be found in [36]. The liquid core length  $L_B$  is then measured on each binarized image as the longitudinal extent of the detected object (see example in Fig. 3.1C).

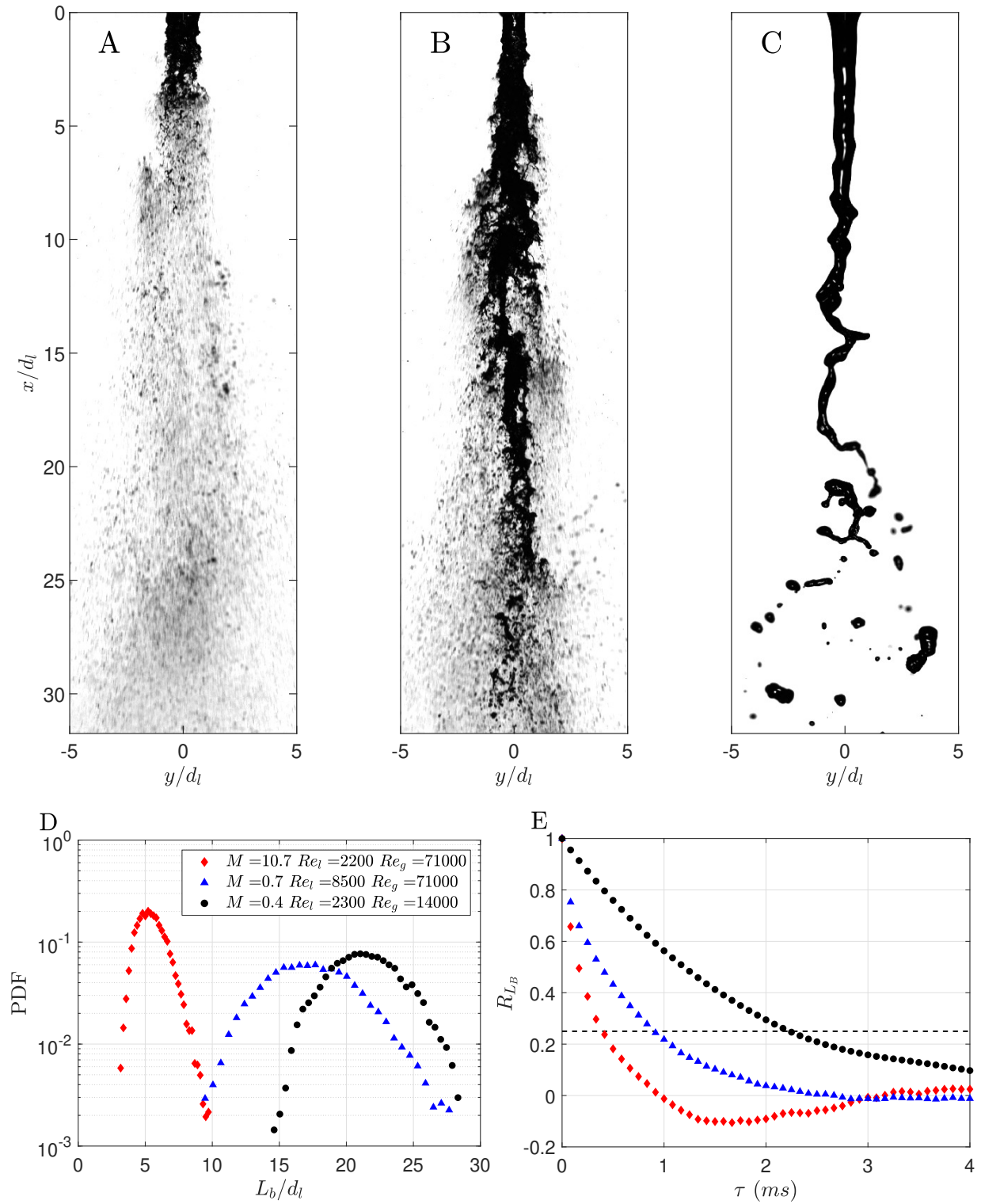


Figure 3.2: A, B and C: Normalized images of the jet for 3 different operating conditions. A:  $M = 10.7$ ,  $Re_l = 2200$ , and  $Re_g = 71000$ . B:  $M = 0.7$ ,  $Re_l = 8500$ , and  $Re_g = 71000$ . C:  $M = 0.4$ ,  $Re_l = 2300$ , and  $Re_g = 14000$ . Probability density functions (D) and auto-correlation functions (E) computed for the 3 injection conditions illustrated in A, B, and C.

### 3.2.3 Statistics and dynamics of the liquid core length

Probability density functions (PDF) are computed for each condition to describe the statistics of the liquid core length. Figure 3.2D shows the PDF for 3 different operating conditions. The shifts of the PDFs indicate that the average liquid core length  $\langle L_B \rangle$  decreases with  $M$ . This behavior is described in the literature [2, 23, 30]. In addition, the distribution is wider for  $M = 0.4$  (black circles) than for  $M = 10.7$  (red diamonds), indicating that the standard deviation seems to decrease with  $M$  as well. We discuss the evolution of the standard deviation with  $M$  in the following section. To further understand the liquid core length distributions we characterize the shape of the PDF. Figure 3.3 shows one probability density function with the addition of Gaussian, skew-Gaussian, and Gamma functions, whose parameters are directly obtained from the first three statistical moments of the data (no fitting parameter). The skew-Gaussian representation (see Eq. 3.1), with positive skewness, captures best the distribution. This is consistent with previous results [24]. This function as well as the scaling laws for the first 3 moments of the PDFs, namely the average  $\langle L_B \rangle$ , standard deviation  $L_{B,STD}$  and skewness  $\beta_{L_B}$  are discussed in Sec. 3.3.

The auto-correlation function  $R_{L_B}(\tau) = \langle L_B(t)L_B(t + \tau) \rangle / \langle L_B^2 \rangle$ ,  $\tau$  being the time-lag, is computed to study the temporal dynamics of the liquid core length. Figure 3.2E shows the auto-correlation functions computed for 3 different injection conditions. Following [36], we measure a correlation time  $\tau_c$  for each condition by integrating the auto-correlation function from 0 to  $\tau_{int}$ ,  $\tau_{int}$  being the time lag at which  $R_{L_B}$  crosses a threshold value of 0.25:  $\tau_c = \int_0^{\tau_{int}} R_{L_B}(\tau) d\tau$ , with  $R_{L_B}(\tau_{int}) = 0.25$ . The values of  $\tau_c$  measured for  $M = 10.7, 0.7$ , and  $0.4$  (red diamonds, blue triangles, and black circles) are respectively 0.20, 0.46, and 1.2 ms. Despite a factor of 10 on the values of  $M$  of the conditions represented by the red diamonds and of the blue triangles, the auto-correlation functions and the associated measured correlation times are fairly close, compared to the large differences observed for the conditions represented by the blue triangles and the black circles, which have similar values of  $M$ .  $\tau_c$  appears to have a non-monotonous evolution with  $M$ . The shape of the auto-correlation functions and the evolution of the associated correlation time are discussed in Sec. 3.4.

## 3.3 Statistical moments and distributions

### 3.3.1 Average and standard deviation of the liquid core length

Figures 3.4A and B respectively show the average and the standard deviation of the liquid core length normalized by the inner liquid diameter,  $\langle L_B \rangle / d_l$  and  $L_{B,STD} / d_l$ , both as a

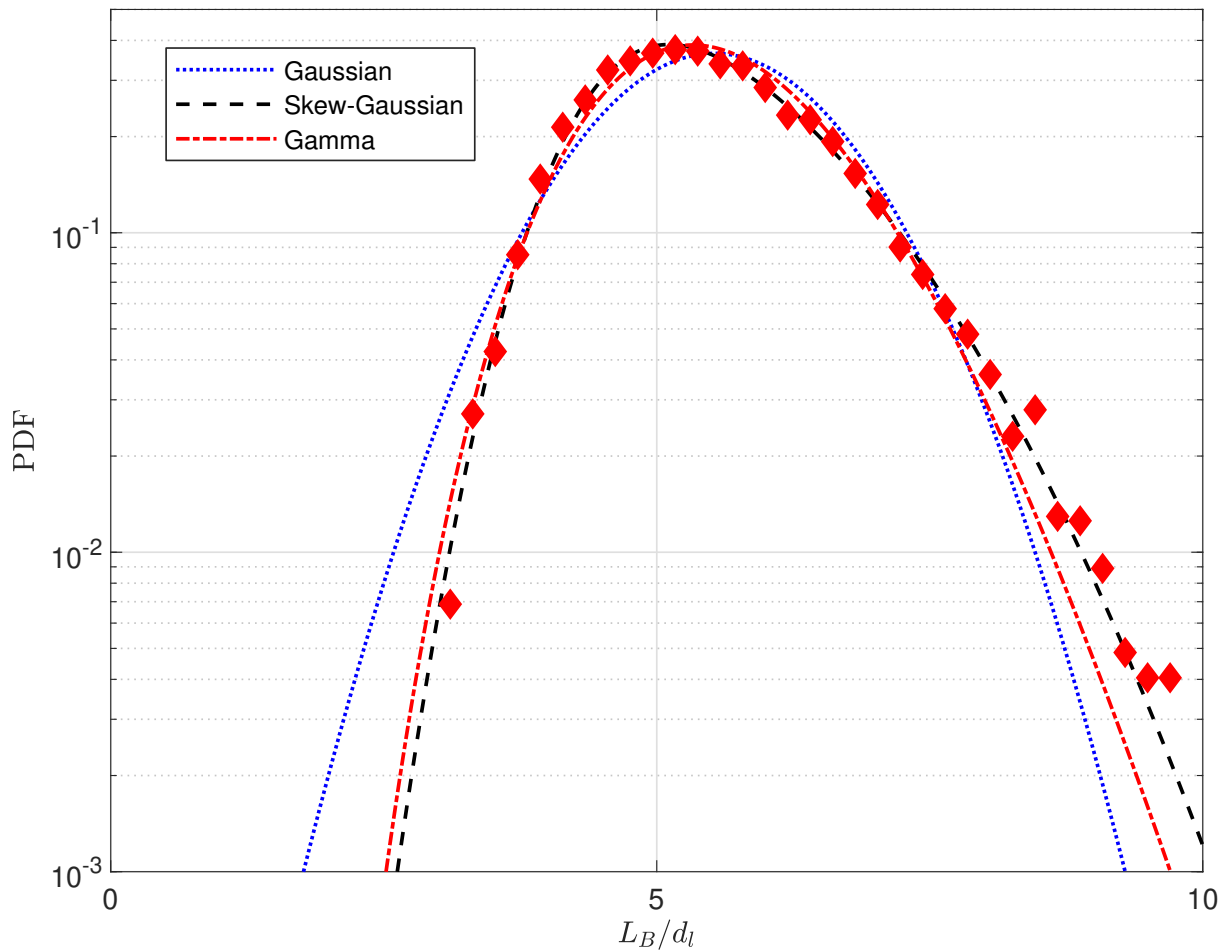


Figure 3.3: Probability density function of the liquid core length normalized by the inner liquid diameter (same condition as Fig. 3.2A). Gaussian, skew-Gaussian (see Eq. 3.1), and Gamma functions are represented respectively in blue dotted line, black dashed line, and red dash-dotted line (parameters directly obtained from the first three statistical moments of the data).

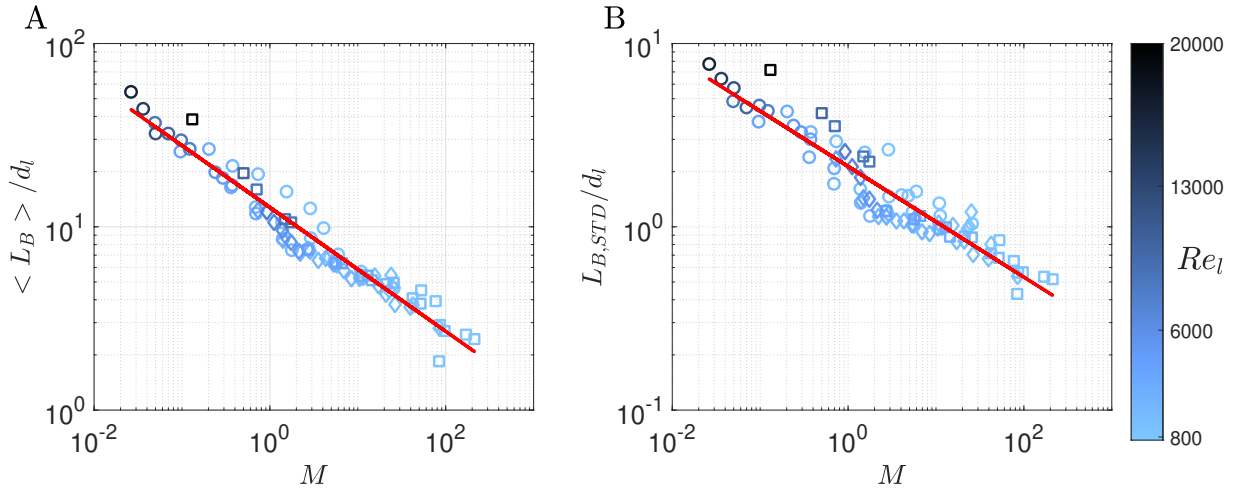


Figure 3.4: Average (A) and standard deviation (B) of the liquid core length normalized by the inner liquid diameter  $d_l$  as a function of the gas-to-liquid dynamic pressure ratio  $M$ . Membrane-breakup, fiber-type breakup, and transitional regimes are represented using circles, squares and diamonds respectively. Power law fits  $AM^n$  are shown in solid red line with A:  $A_{avg} = 12.8 \pm 0.8$  and  $n_{avg} = -0.34 \pm 0.04$ ; B:  $A_{STD} = 2.14 \pm 0.12$  and  $n_{STD} = -0.30 \pm 0.03$ .

function of the gas-to-liquid dynamic pressure ratio  $M$ . In both cases, the data collapse onto a master curve. We perform power-law fits, represented by the red curve in each plot, and find them to be in good agreement with the experimental data. The prefactor and exponent obtained when fitting the normalized average liquid core length by a power-law  $AM^n$  are respectively  $A_{avg} = 12.8 \pm 0.8$  and  $n_{avg} = -0.34 \pm 0.04$ . This is consistent with previous results from the literature. [2] showed that  $\langle L_B \rangle$  scales with  $M^{-0.3}$  on a different range of liquid Reynolds number  $45 < Re_l < 300$  and for a wide range of gas-to-liquid dynamic pressure ratio  $0.2 < M < 1000$ , obtained by changing the density of the liquid. They report a prefactor  $A_{Leroux} = 10$ . [23, 30] showed that  $\langle L_B \rangle$  also depends on the geometry of the nozzle, explaining the difference in terms of prefactor. The exponents they report are also in good agreement with the value found here.

The scaling of the standard deviation of the liquid core length with  $M$  was not reported before. The prefactor and exponent obtained when performing a power-law fit on  $L_{B,STD}/d_l$  are respectively  $A_{STD} = 2.14 \pm 0.12$  and  $n_{STD} = -0.30 \pm 0.03$ . The scalings of the average and standard deviation with  $M$  are almost identical, only the prefactor of the power-laws are different.

For both plots of Fig. 3.4, the membrane breakup and fiber-type atomization regimes are represented with circles and squares respectively. In addition, diamonds are used for conditions where both membrane formation and fiber-type atomization coexist. The determination of atom-

ization regimes is discussed later on in Sec 3.5. The liquid Reynolds number is also indicated with the color bar. No influence of atomization regimes or of  $Re_l$  is exhibited in the current dataset. The gas-to-liquid dynamic pressure ratio  $M$  is enough to capture variations of the liquid Reynolds number with a single power-law, both for the average and standard deviation of the liquid core length  $L_B$ .  $M$  hence appears to be the sole parameter controlling the first two moments of  $L_B$ .

### 3.3.2 Higher order moments of the liquid core length

To further investigate the general shape of the probability density function of the liquid core length we use the normalized and centered variable:  $\tilde{L}_B = \frac{L_B - \langle L_B \rangle}{L_{B,STD}}$ . Figure 3.5 displays the probability density functions of  $\tilde{L}_B$  for every experimental conditions, showing a remarkable collapse. The black curve is a normalized and centered skew-Gaussian function, whose general expression is given in eq. 3.1. It is solely defined by  $\alpha$ ,  $\omega$ , and  $\xi$ , the shape, scale, and location parameters respectively. In the case of Fig. 3.3, the 3 parameters are calculated using the first three moments of the distribution of  $L_B$ . However, the expression of the skew-Gaussian distribution is simplified in the case of a centered and normalized distribution (Fig. 3.5) where  $\mu = 0$  and  $\sigma = 1$ : the shape, scale, and location parameters depend only on one parameter, the skewness, directly measured from the data. In the case of the black curve in Fig. 3.5, this parameter is taken as the average of the skewness value of each condition.

$$f(x) = \frac{e^{-\frac{1}{2}\left(\frac{x-\xi}{\omega}\right)^2}}{\omega\sqrt{2\pi}} \left[ 1 + \operatorname{erf}\left(\frac{\alpha(x-\xi)}{\sqrt{2}\omega}\right) \right] \quad (3.1)$$

$$\alpha = \left( \frac{2}{\pi} \left[ 1 + \left( \frac{4-\pi}{2\beta} \right)^{2/3} \right] - 1 \right)^{-1/2} \quad (3.2)$$

$$\omega = \frac{\sigma}{\sqrt{1 - \frac{2\delta^2}{\pi}}} \quad (3.3)$$

$$\xi = \mu - \omega\delta\sqrt{\frac{2}{\pi}} \quad (3.4)$$

where erf is the error function,  $\delta = \frac{\alpha}{\sqrt{1+\alpha^2}}$ , and  $\mu$ ,  $\sigma$ , and  $\beta$  are respectively the average, standard deviation, and skewness.

The skew-Gaussian is in good agreement with the experimental data, confirming previous observations done in a narrower range of operating conditions [24]. Despite an apparent collapse of the curves around the average distribution (black line), close examination shows that the shape of the probability density function appears to vary slightly with the gas Reynolds number,



as highlighted by the color bar. The latter emphasizes (in green) conditions for  $Re_g > 33000$ , which appear to collapse onto a master curve, while conditions of lower gas Reynolds number values behave differently. Note that in the current study, since changes in non-dimensional groups only occur through changes in mean exit velocities ( $U_l$  and  $U_g$ ), this transition, occurring around  $U_g = 53$  m/s, is reported above in terms of gas Reynolds number for simplicity (since  $Re_g \sim U_g$ ) but it can also be expressed with the gas Weber number with  $We_g = 75$  and both threshold values will be used hereafter. To further understand these differences in shape we show in Fig. 3.6A and C the skewness of the liquid core length as a function of  $M$  and  $Re_g$ . While high dynamic pressure ratios seem to lead to a constant skewness, the behavior of  $\beta_{LB}$  with  $M$  is not very clear, and the color bar highlights that  $Re_g$  seems to be a better indicator (green symbols in Fig. 3.6A). The trend of the skewness of the liquid core length along the gas Reynolds number (Fig. 3.6C) is much clearer, as underlined by the box-and-whisker plot. The latter represents the averages and standard deviations of  $\beta_{LB}$  computed in 6 bins spaced along  $Re_g$ . The skewness tends to be lower when  $Re_g < 33000$  and shows an increasing trend although the spread is important. Focusing on the conditions with  $Re_g > 33000$ , we compute their average skewness,  $\langle \beta_{LB} \rangle = 0.46$ , and associated standard deviation,  $\beta_{LB,STD} = 0.07$ . The dashed line corresponds to  $\langle \beta_{LB} \rangle$  and the dashed-dotted lines to  $\langle \beta_{LB} \rangle \pm \beta_{LB,STD}$ . Despite a moderate spread still present above the transition, most of the data points are found to be less than a standard deviation (of the skewness) away from the average skewness. This indicates that the skewness increases with  $Re_g$  up to an asymptotic value at high gas Reynolds number, with no further dependency on other dimensionless parameters. Since the probability density functions collapse at high Reynolds numbers, higher-order statistical moments are not investigated.

We investigate the ratio of the first two statistical moments of the liquid core length to explore a potential signature of the transition observed on the skewness for  $Re_g > 33000$ , alternatively  $We_g > 75$ . Since both the standard deviation and the average of the liquid core length scale with  $M^{-0.3}$ , their ratio  $I_{LB} = \frac{L_{B,STD}}{\langle L_B \rangle}$  is expected to be constant. Figure 3.6B shows  $I_{LB}$  as a function of  $M$ . We compute the average and standard deviation of  $I_{LB}$ , respectively  $\langle I_{LB} \rangle = 18.1\%$  and  $I_{LB,STD} = 2.6\%$ . The ratio of the prefactors of the fits of  $\langle L_B \rangle$  and  $L_{B,STD}$ ,  $\frac{A_{STD}}{A_{avg}} = 0.17$ , is in good agreement with the value obtained for  $\langle I_{LB} \rangle$ . The dashed line corresponds to  $\langle I_{LB} \rangle$  and the dashed-dotted line to  $\langle I_{LB} \rangle \pm I_{LB,STD}$ . More than 60% of the conditions are within one standard deviation away from the average  $\langle I_{LB} \rangle$  and 96% the measurements are within two standard deviations of  $\langle I_{LB} \rangle$ , indicating that  $I_{LB}$  is indeed independent of  $M$ . The color bar does not indicate any further influence of the gas Reynolds number (alternatively gas Weber number) on  $I_{LB}$ , which is confirmed by an alternate representation along  $Re_g$  in Fig. 3.6D. In addition, circles, squares, and diamonds correspond to the membrane-breakup, fiber-type, and transitional regimes respectively. No effect of the atomization regime or of the liquid Reynolds number is observed on  $I_{LB}$ .

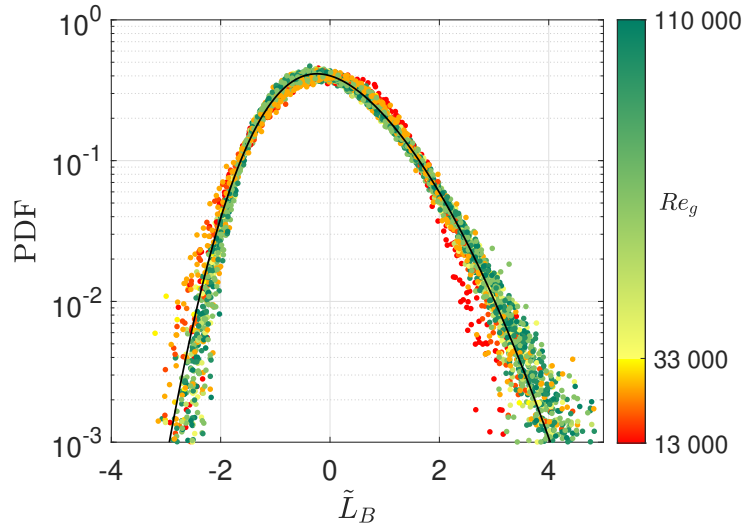


Figure 3.5: Probability density functions of the centered and normalized liquid core length  $\tilde{L}_B = \frac{L_B - \langle L_B \rangle}{L_{B,STD}}$  for every operating condition. The black curve corresponds to a skew-Gaussian function with zero average, unit standard deviation, and whose skewness is computed by averaging the skewness obtained for every experimental condition.

### 3.4 Time scales of the liquid core length

Figures 3.7A and B show, in linear and semi-logarithmic coordinates, the auto-correlation functions obtained for each condition as a function of the normalized time-lag  $\tau/\tau_c$ ,  $\tau_c$  being a correlation time obtained by a partial integration of the auto-correlation function (see Sec. 3.2.3). The color bar is the same as the one of Fig. 3.6A and B, and highlights in red and green the conditions with low and high gas velocities respectively. The solid black curve of Fig. 3.7B corresponds to the exponential function  $\exp\left(-\frac{\tau}{1.33\tau_c}\right)$  and captures the auto-correlation functions for conditions with low gas velocities ( $Re_g$  in the vicinity of 15000, alternatively  $We_g \sim 20$ ). The coefficient 1.33 comes from the computation of  $\tau_c$ : the time defined by the integral of a decreasing exponential function up to the crossing of 0.25 is equal to 1.33 times its exponential decay rate. Auto-correlation functions for conditions at higher gas velocities are found to initially decrease faster than an exponential function, and the initial decrease rate appears to be an increasing function of  $Re_g$  in the intermediate range of gas velocities (orange to yellow symbols). This is visible by the initial ordering of the curves (for  $\tau/\tau_c < 1$ ) where increases of  $Re_g$  (red to orange to green) yield a given decorrelation over shorter time periods. For  $Re_g > 33000$ , the rate seems to reach an asymptotic value and all functions (green symbols) collapse onto a master curve. The change of shape of the auto-correlation functions of the liquid core length also highlights the transition discussed in the previous section for the distributions of  $L_B$  (around a transition value of  $Re_g = 33000$  or  $We_g = 75$ ): conditions at low gas velocity are exponentially decreasing, and increases of  $U_g$  yield faster-decreasing functions, until reaching a constant decay

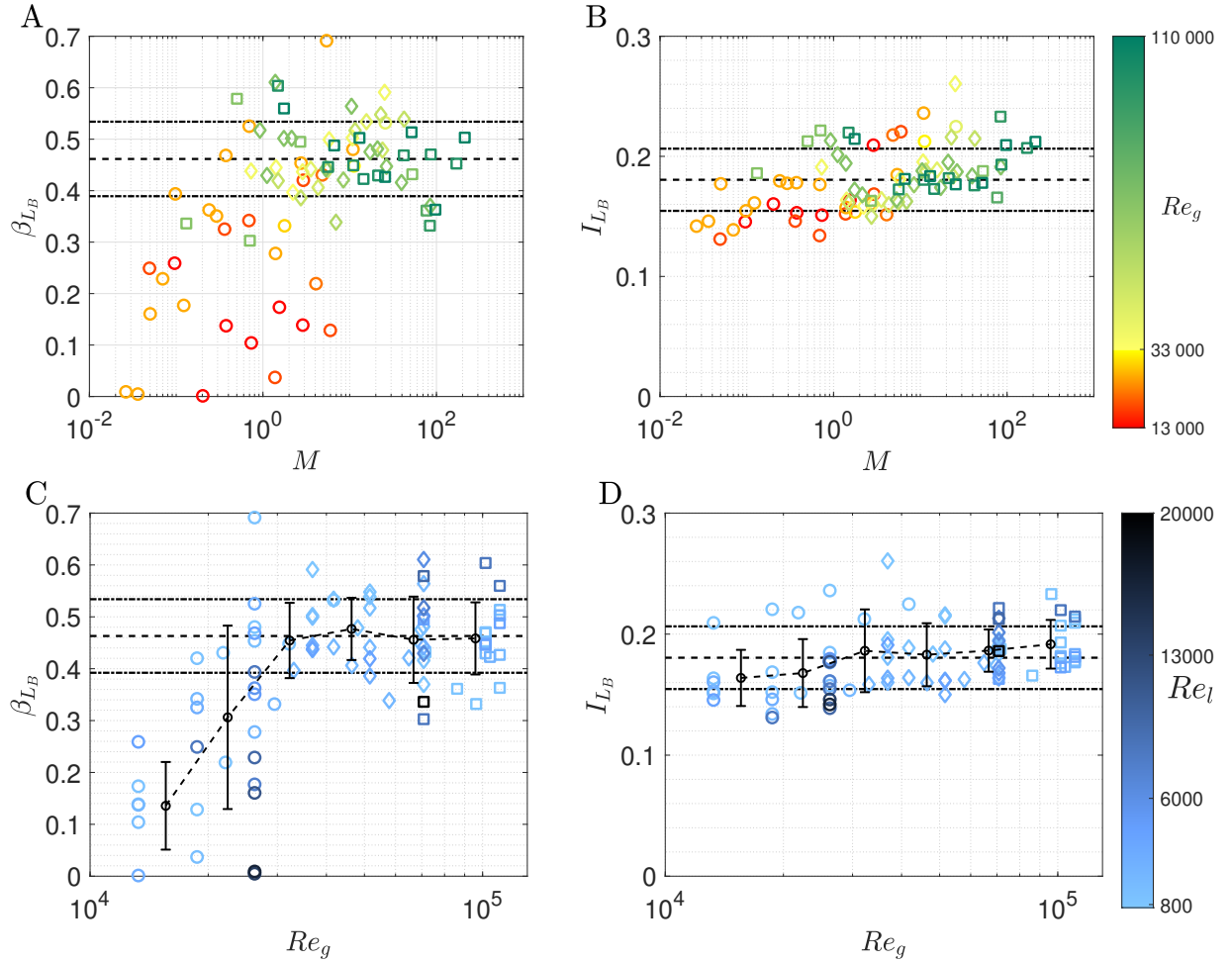


Figure 3.6: Skewness of the liquid core length as a function of the gas-to-liquid dynamic pressure ratio  $M$  (A) and gas Reynolds number  $Re_g$  (C). For conditions with  $Re_g > 33\,000$ , alternatively  $We_g = 75$ , we compute the average skewness  $\langle \beta_{LB} \rangle = 0.46$  and the standard deviation of the skewness,  $\beta_{LB,STD} = 0.07$ . The dashed line corresponds to  $\langle \beta_{LB} \rangle$  and the dashed-dotted line to  $\langle \beta_{LB} \rangle \pm \beta_{LB,STD}$ . Ratio of the standard deviation to the average value of the liquid core length  $I_{LB} = L_{B,STD}/\langle L_B \rangle$  as a function of  $M$  (B) and  $Re_g$  (D). We compute the average and standard deviation of  $I_{LB}$ , respectively  $\langle I_{LB} \rangle = 18.1\%$  and  $I_{LB,STD} = 2.6\%$ . The dashed line corresponds to  $\langle I_{LB} \rangle$  and the dashed-dotted line to  $\langle I_{LB} \rangle \pm I_{LB,STD}$ . The x-axes are divided into bins to compute averages and standard deviations of  $\beta_{LB}$  (C) and  $I_{LB}$  (D) to form box-and-whisker plots. Membrane-breakup, fiber-type breakup, and transitional regimes are represented using circles, squares and diamonds respectively.

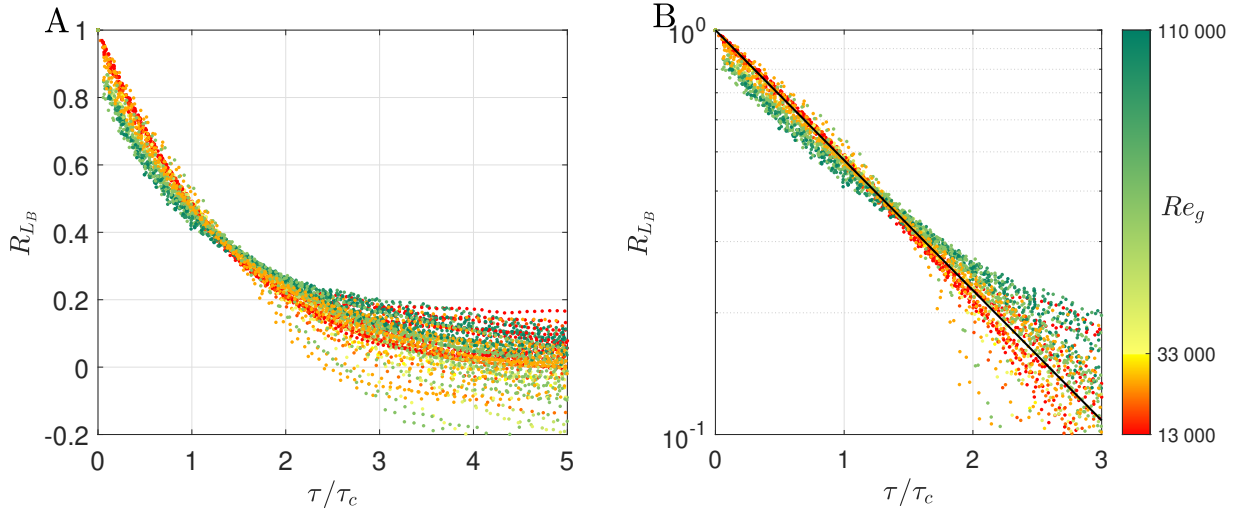


Figure 3.7: Auto-correlation functions of  $L_B$  as a function of the normalized time lag  $\frac{\tau}{\tau_c}$ . A: linear ordinate. B: logarithmic ordinate. The black curve corresponds to  $\exp\left(-\frac{\tau}{1.33\tau_c}\right)$ .

rate after the transition, when represented along the normalized time lag  $\tau/\tau_c$ .

To characterize the evolution of the correlation time  $\tau_c$ , we introduce a large-scale timescale of the gas jet  $T_g = \frac{d_g}{U_g} \propto Re_g^{-1}$ . Figure 3.8A shows the correlation time normalized by the gas jet timescale  $\frac{\tau_c}{T_g}$  as a function of the gas Reynolds number. We divide the range of gas Reynolds number into 7 bins and compute the average and standard deviation of  $\frac{\tau_c}{T_g}$  in each of these bins. The red dots correspond to the average and the errorbars to twice the standard deviation. Despite some spread, the average values do not appear to depend on the gas Reynolds number, when normalized by  $T_g$ . This shows that the correlation time  $\tau_c$  scales with  $Re_g^{-1}$ , with a proportionality coefficient of approximately 16.3 s.

Figure 3.8B shows the correlation time normalized by the timescale of the gas jet  $\frac{\tau_c}{T_g}$  as a function of the liquid Reynolds number. We divide the range of  $Re_l$  into 7 bins and compute the average and standard deviation of  $\frac{\tau_c}{T_g}$  in each of these bins. The black dots correspond to the average and the errorbars to twice the standard deviation. The normalized average values appear constant at lower liquid Reynolds number values, and finds higher values in the range of high  $Re_l$  (where a growing or constant trend remains indefinite with the current range explored). We compute the average and standard deviation for all conditions with  $Re_l < 4000$  and find  $\frac{\tau_c}{T_g} = 2.3 \pm 0.7$ , while  $Re_l > 8000$  yields  $\frac{\tau_c}{T_g} = 3.6 \pm .9$ . The change between both behaviors being gradual along  $Re_l$  and moderate in amplitude, we cannot establish a clear threshold value of liquid Reynolds number for this transition. The averaged trend highlighted by the black dashed line shows an increase starting between  $Re_l = 2000$  and  $4000$ , that may reach an asymptotic value for  $Re_l \geq 10000$ .

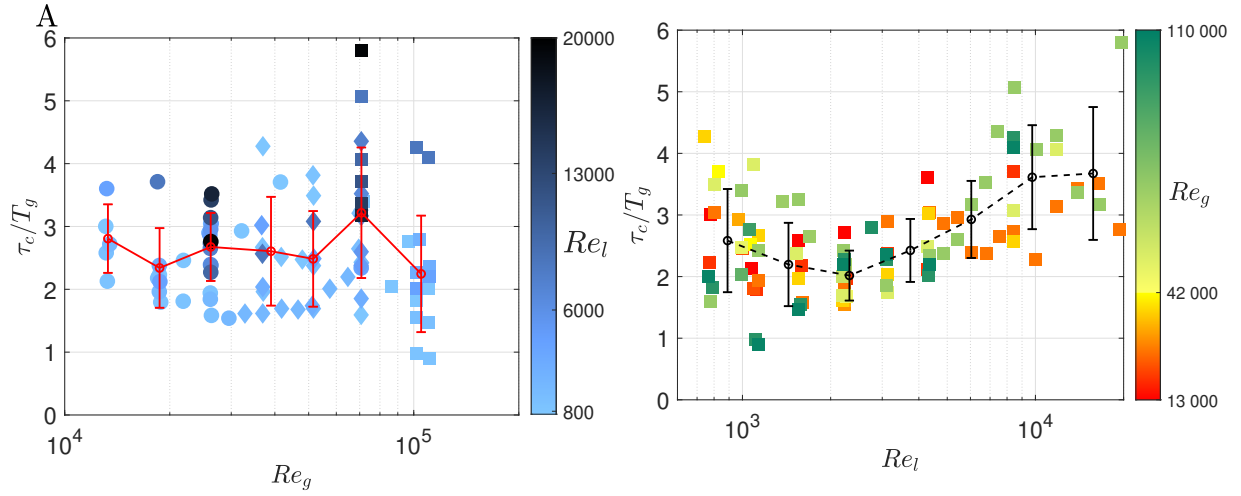


Figure 3.8: Correlation time  $\tau_c$  normalized by the timescale of the gas jet  $T_g$  as a function of A:  $Re_g$  and B:  $Re_l$ . The  $x$ -axes are divided into bins to compute averages and standard deviations of  $\frac{\tau_c}{T_g}$  to form box-and-whisker plots.

### 3.5 Discussion

Figure 3.4 shows that the gas-to-liquid dynamic pressure ratio  $M$  is the sole parameter controlling the first two moments of the probability density function of the liquid core length. The scaling laws for the average  $\langle L_B \rangle$  and the standard deviation  $L_{B,STD}$  of the liquid core length are power laws of  $M$  with approximately the same exponents and hence present a constant ratio. Thus, if gamma functions were used to describe the probability density functions, the rate parameter defined as  $b_\Gamma = \langle L_B \rangle / L_{B,STD}$  should be constant and the shape parameter defined as  $a_\Gamma = \langle L_B \rangle^2 / L_{B,STD}$  should depend on  $M$  only. With this representation, one obtains the skewness directly as  $2/\sqrt{a_\Gamma}$ , implying a scaling with  $M^{0.19}$  over the entire range of explored parameters. The observed variations of the skewness with  $Re_g$  (Fig. 3.6C) therefore cannot be reconciled when using gamma distributions to provide a reduced description of the liquid core length distributions. Thus we conclude that skew-Gaussian distributions provide the adequate framework to describe the liquid core length statistics, confirming previous observations [24] and extending them to a much wider range of liquid and gas Reynolds numbers (equivalently gas-to-liquid dynamic pressure ratio). This representation effectively reduces the full statistics to 3 parameters: the average, the standard deviation, and the skewness, which directly become only two parameters given that the ratio of the standard deviation to the average liquid core length  $L_{B,STD}/\langle L_B \rangle$  is constant.

The first parameter describing the full statistics is the average liquid core length, which is solely controlled by one dimensionless parameter: the gas-to-liquid dynamic pressure ratio  $M$ .

The second parameter corresponds to the skewness of the liquid core length, associated with the shape of the distributions. While the PDFs of  $\tilde{L}_B$  first appear to collapse onto a single curve, associated with a constant skewness, closer inspections reveal a richer behavior (Fig. 3.5). Two regimes are underlined, governed by the gas Reynolds number, with a transition in the vicinity of  $Re_g = 33\,000$ , alternatively  $We_g = 75$ . For higher values of  $Re_g$ , the skewness  $\beta_{L_B}$  appears constant with  $\beta_{L_B} = 0.46 \pm 0.07$ , see Fig. 3.6. Due to experimental constraints, fewer points were obtained for low gas Reynolds numbers and high liquid Reynolds numbers. While the imaging location can readily be chosen to be centered around the average value of  $L_B$ , high  $Re_l$  and low  $Re_g$  values would yield very low values of  $M$ , hence a very large standard deviation. Capturing the full range of the liquid core length variations would then require a very large field of view, which comes at a cost of spatial resolution and makes the detection of the liquid core challenging. Note also that conditions at both low  $Re_l$  and  $Re_g$  are outside of the studied breakup regimes. Despite the spread associated with the third order statistical moment, for  $Re_g < 33\,000$ , the skewness seems to increase with  $Re_g$  towards an asymptotic value reached at  $Re_g = 33\,000$ , alternatively  $We_g = 75$  (Fig. 3.6C). For low values of  $Re_g$ , small values of  $\beta_{L_B}$  are systematically found, while close to the transition, values can be found anywhere between 0 and approximately 0.5. On the contrary, for high gas Reynolds numbers, most of the value of the skewness are found within one  $\beta_{L_B,STD}$  of the asymptotic value  $\langle \beta_{L_B} \rangle$ . This explains why when displaying every distribution of the centered and normalized liquid core length  $\tilde{L}_B$  (Fig. 3.5), a master curve is highlighted only for high gas Reynolds (Weber) number values, while the PDF for lower values are found anywhere between a unit Normal distribution ( $\beta_{L_B} = 0$ ) and the master curve. Note that investigating this transition and the trend of  $\beta_{L_B}$  through the gas-to-liquid dynamic pressure ratio  $M$  is not found appropriate (Fig. 3.6A) since it seems to solely depends of the gas velocity  $U_g$ , i. e. independent of the liquid velocity  $U_l$  (Fig. 3.6C).

In opposition to the skewness, the auto-correlation functions of  $L_B$  (Fig. 3.7) are very well converged in the range of short time lags. The high-speed imaging measurements besides well resolve that range so that even slight change of function shape can be interpreted. Both auto-correlation functions and statistical distributions of  $L_B$  show very similar behaviors in the evolution of their shape. Starting from a decreasing exponential function at low gas Reynolds number (highlighted by the dashed line representing  $\exp\left(-\frac{\tau}{1.33\tau_c}\right)$ ), the decay rate increases slightly with  $Re_g$  (i. e. auto-correlation functions decreasing faster than an exponential) until reaching a master curve for conditions with  $Re_g > 33\,000$ . We conclude that the reported transition separates two regimes: i) for  $Re_g < 33\,000$ , the liquid core length presents correlations and statistics with a lower decay rate and skewness than at higher gas Reynolds number, and ii) for  $Re_g > 33\,000$ , the statistics of  $L_B$  are described by a constant skewness while presenting correlations that decrease faster than an exponential with a fixed decay rate. With the constant ratio of the standard deviation to the average liquid core length, the statistics of  $L_B$  are described by a single parameter in the second regime, and hence solely driven by  $M$ .



The transition between two regimes for the distributions and auto-correlation functions of  $L_B$  below and above the value of  $Re_g = 33000$  (alternatively  $We_g = 75$ ) is an unexpected finding, especially considering the reported behaviors of  $\langle L_B \rangle$ ,  $L_{B,STD}$  and  $\tau_c$ , each showing a single scaling with respect to a sole non-dimensional parameter (respectively  $M$  and  $Re_g$ ) over the whole range of parameters explored. A possible origin for this transition could be a change of behavior of the gas jet. [97] showed that a turbulent round jet exhibits a mixing transition when the gas Reynolds number is around  $Re_g \approx 10^4$ . Beyond this transition, the gas jet efficiently entrains the surrounding fluid around it (ambient air in our case) and the jet's turbulent properties become drastically different. The instabilities of the liquid jet's interface originate from interactions with the turbulent gas jet surrounding it. For instance, [31] showed that increasing the gas turbulence intensity leads to interfacial instabilities presenting higher frequencies, in a planar configuration. In the same configuration, high-fidelity simulations also show a faster growth and destabilization of the instabilities when the gas turbulence is increased [98]. These interactions are thus expected to differ below and above the mixing transition of the gas jet, which in turn can be expected to play a role on the liquid core length. The increased probability of having larger values of  $\tilde{L}_B$  (with respect to the average value and in proportion to the standard deviation) associated with larger skewness values, and the faster decorrelation at short times could then be explained by the difference in properties of the gas jet past its mixing transition. An in-depth characterization of the gas jet, like the work done by [97], would be required to confirm the value of the mixing transition in our situation and its link to the transition observed here at  $Re_g = 33000$ .

In an almost identical configuration, [82] reported a change of regime in the spatial gradient of the interfacial perturbation velocity around  $Re_g = 45000$ , alternatively  $We_g = 190$ . This supports the idea that a transition in the properties of the gas flow, thus in the interface instabilities, can participate to the change of regimes in the behavior of  $L_B$ . [82] suggested that this transition is linked to a change in breakup regimes from membrane-breakup to fiber-type atomization. We investigate this by looking at a qualitative phase diagram, obtained by visual inspections of the breakup phenomena over the range of explored parameters. Fig. 3.9 reports in the  $\{Re_l; We_g\}$  parameter space membrane break-up, fiber-type atomization, and the transitional regime where both processes coexist. In this representation, the reported transition at  $Re_g = 33000$  corresponds to a vertical line at  $We_g = 75$ . Thanks to the many Reynolds numbers sampled, the value of  $Re_g = 33000$  is tightly surrounded by experimental conditions. It is in good agreement with the change in atomization regimes found here, and with the transition boundary sketched by [19]. It appears that the change of behaviors presented here for  $We_g = 75$  occurs at the onset of fiber-type atomization, but with coexistence to the membrane formation process, while the one identified by [82] around  $We_g = 190$  marks the disappearance of membranes and the transition to fiber-type atomization only. Note that in both cases, the boundary appears to be (almost) vertical in this diagram in the  $\{Re_l; We_g\}$  parameter space. This means that the gas Weber number and not the relative Weber number stands as the good indicator for these transitions,



since they appear to be almost independent of the liquid velocity  $U_l$ . Drawing the phase diagram in the  $\{Re_l; We_r\}$  parameter space ( $\sim \{U_l; |U_g - U_l|\}$  parameter space) would only result in a less straightforward view with oblique transitions. While a relative Weber number defined on the phase slip velocity is commonplace in multiphase flow, it seems not to be suited here, as probably noted by [19] since they use both  $We_g$  and  $We_r$  but draw the phase diagram in the  $\{Re_l; We_g\}$  parameter space. The situation may be different and  $We_r$  may be more suited for the fragmentation of a liquid jet by a gas when the velocities of both phases are closer together, as may be interpreted by the curving of the boundary sketched in [19], as it nears the  $U_g = U_l$  line. This is the case for instance in the numerical investigations of [99, 100], where  $We_r$  is used for the regime maps describing the destabilization of a planar liquid sheet segment and a transient liquid jet within a low-speed gas jet respectively. In the case of a liquid jet surrounded by a high-speed gas jet however, the close inspection of the statistics and temporal dynamics of the liquid core length appears as a good candidate to provide a quantitative framework to describe the transition from membrane-breakup to fiber-type atomization.

One motivation of this study was to investigate the effect of the onset of turbulence in the liquid jet on the destabilization process. Considering the statistics of  $L_B$  we report no effect of the liquid Reynolds number  $Re_l$  beyond the influence of increased liquid velocity captured by  $M$ . The correlation time, when normalized by  $T_g$ , is besides found constant for low values of  $Re_l$  (Fig. 3.7B). However, at larger liquid Reynolds numbers the correlation time presents higher values than at low  $Re_l$  values and the increase of  $\tau_c/T_g$  seems to occur between  $Re_l = 4000$  and  $Re_l = 8000$ . The evolution of the normalized correlation time for high liquid Reynolds numbers is unclear and requires more conditions, exploring higher values, to be fully characterized. The unavailability of the range of high  $Re_l$  and low  $Re_g$  was described above. In addition, conditions with high  $Re_l$  and  $Re_g$  values require shorter spatial and temporal resolutions than the ones available, and would result in a very dense two-phase flow in the vicinity of the breakup, which can prevent proper identification of the liquid-gas interface [36]. One might think that the change in scaling of the correlation time above the transition is not due to the onset of liquid turbulence but simply to breakup occurring further downstream in the gas jet, where  $T_g$  does not adequately represent a characteristic timescale of the gas jet. For conditions above the transition, normalizing by a higher value of  $T_g$  (built from  $d_g$  and a value of velocity lower than  $U_g$ ) for the correlation time would indeed bring the data points to the lower values found for lower liquid Reynolds numbers. Nevertheless, we know from our study of the statistics of  $L_B$  that the region where the breakup occurs is only controlled by  $M$  and breakup is found to occur only up to  $5d_g$  downstream of the exit plane in the explored parameter space (even at very high  $Re_l$  values). Note that this range of breakup locations is similarly explored by conditions at lower  $Re_l$  values when  $Re_g$  is low (red points on Fig. 3.8B) which do not present higher correlation times. The gas velocity magnitude in this region is expected to still be well represented by  $U_g$  [16, 101], confirming that  $T_g$  is an appropriate timescale.

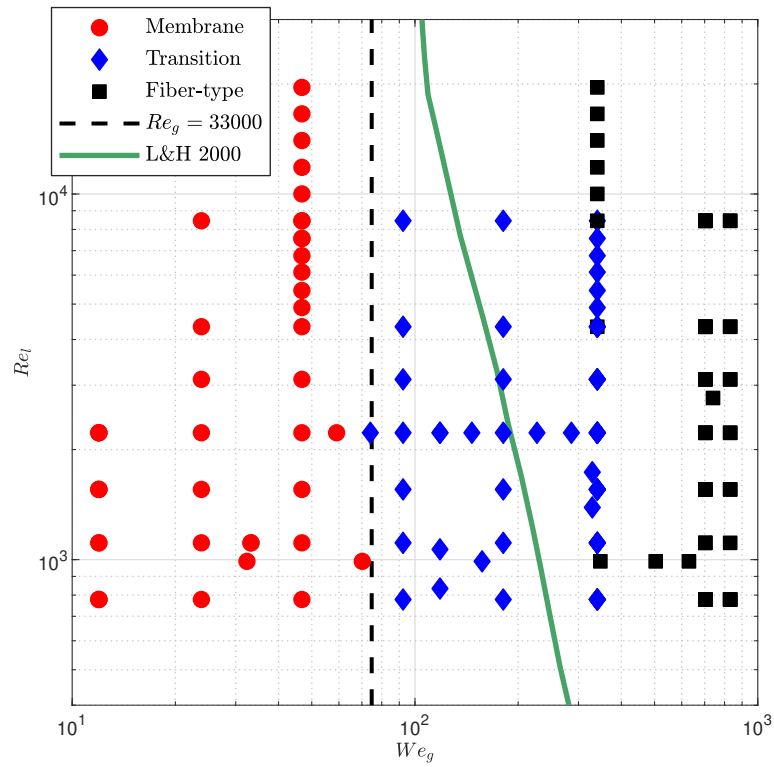


Figure 3.9: Qualitative phase diagram of breakup regimes in the  $\{Re_l; We_g\}$  parameter space. Red circles, black squares, and blue diamonds respectively correspond to membrane-breakup, fiber-type atomization, and to conditions where both of these breakup mechanisms coexist. The dashed line shows  $We_g = 75$  (equivalently  $Re_g = 33000$ ) and the green solid line corresponds to the transition reported by [19]. Note that the Weber number is defined as  $We_g = \rho_g U_g^2 d_l / \sigma$  in this figure.

We suspect that the change of behavior of the correlation time is related to the transition to a turbulent state of the liquid jet. Confirming this however would require velocity measurements within the liquid jet, which are challenging to implement in such setup. Lacking a clear quantitative indicator of the transition to turbulence of the liquid jet, we turn to the qualitative visualization of the liquid jet interface, as an indirect proxy to the measure of the agitation in the liquid jet. Figure 3.10 shows the liquid jet exiting the nozzle with no added gas flow, at  $Re_l = 2000$  (A),  $Re_l = 4000$  (B), and  $Re_l = 8000$  (C). In the vicinity of the nozzle exit (i. e. at longitudinal  $x$  far from the region where the break-up due to the Rayleigh-Plateau instability occurs) the interface of the liquid jet remains undisturbed for  $Re_l = 2000$ . We interpret this as a laminar liquid jet exiting the nozzle. The gas-liquid interface becomes slightly disturbed when  $Re_l = 4000$ , with localized corrugations of approximately the same size. These disturbances are a signature of a deviation from a fully laminar state of the liquid jet, translating for instance the presence of turbulence spots. The situation is much different at  $Re_l = 8000$ , as the jet is heavily disturbed by corrugations of a broad range of scales, right from the nozzle exit, a clear signature of a turbulent liquid jet. These visualizations strongly suggest that the departure from a laminar jet occurs for a value of the liquid Reynolds number found between these two bounds  $2000 < Re_l < 4000$ , and would be the cause of the change of behavior of the liquid core length timescale. In addition, when an established turbulent state is reached so that disturbances of various sizes are observed over the whole jet, i. e. in the vicinity of  $Re_l = 8000$ , the increase of  $\tau_c/T_g$  with  $Re_l$  is seen to either saturate or become less steep (Fig. 3.8B). Nevertheless, the color bars of Fig 3.4 and Fig 3.6C and D indicate in shades of blue the value of liquid Reynolds number and no trend is exhibited, confirming this change of regime with  $Re_l$  does not influence the moments of the probability density function. In the range currently explored, the effect of the onset of turbulence in the liquid jet seems to be limited to a secondary effect on the value of the liquid core length correlation time.

### 3.6 Conclusions

We performed high-speed back-lit imaging of the breakup of a liquid jet by a turbulent coaxial gas jet, over a wide range of liquid and gas Reynolds numbers, encompassing laminar and turbulent conditions of the liquid jet as well as two regimes of jet breakup. We focus on the liquid core length (longitudinal extent of the liquid jet, noted  $L_B$ ) and study its statistics and temporal dynamics. Using auto-correlation functions of the liquid core length, we showed that the correlation time  $\tau_c$  scales linearly with  $Re_g^{-1}$ . In opposition, the statistics are observed to be governed by the gas-to-liquid dynamic pressure ratio  $M$ . The average and standard deviation of the liquid core length both follow a power law with  $M$ . In addition, we find the ratio of these two statistical moments  $\langle L_B \rangle / L_{B,STD}$  to be constant, effectively reducing the number of parameters needed to describe the statistics of  $L_B$ . The skewness on the other hand does not present a clear scaling with  $M$  but appears to have a non-monotonous evolution with the

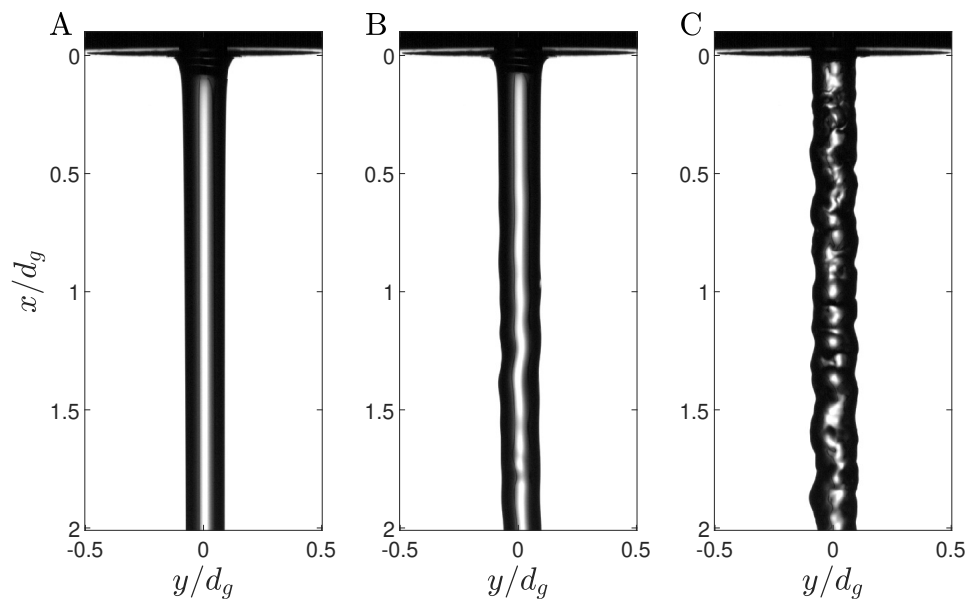


Figure 3.10: Snapshot of the liquid jet exiting the nozzle in a still gas environment. A:  $Re_l = 2000$ , the interface of the jet remains unperturbed in the vicinity of the nozzle and the liquid jet is laminar. B:  $Re_l = 4000$ , the interface of the jet only suffers from large-scale disturbances, which suggests that the liquid jet exiting the nozzle is laminar but presents some local flow perturbations. C:  $Re_l = 8000$ , the interface of the jet presents small-scale corrugations, suggesting that the liquid jet exiting the nozzle is turbulent.

gas Reynolds number  $Re_g$ . Nonetheless, thanks to a representation of the distributions of  $L_B$  with skew-Gaussian functions, we can fully describe its statistics using only two parameters: the average and skewness of  $L_B$ . The skewness is found to be constant for high  $Re_g$ , therefore further reducing the description to a single parameter in that case.

With the shape of the distributions of  $L_B$  fully characterized, we were able to identify a transition between two regimes. Conditions with  $Re_g > 33\,000$  collapse on a mastercurve (Fig. 3.5), while conditions with  $Re_g < 33\,000$  present smaller skewness values, that, despite some spread, increase with  $Re_g$  toward the asymptotic value found for high gas velocity conditions. This change of regime above and below the value of  $Re_g = 33\,000$  (alternatively  $We_g = 75$ ) is also evidenced with the auto-correlation functions: conditions at  $Re_g < 33\,000$  show exponentially decaying auto-correlation functions whereas for conditions with  $Re_g > 33\,000$  the decay is faster than an exponential. These unexpected changes of behavior of the temporal dynamics and the statistics of  $L_B$  can be explained in the light of the mixing transition of the turbulent gas jet, found to occur around  $Re_g \approx 10^4$  for round gas jets [97]. Asymptotic values of the skewness of the liquid core length as well as of the decay rate of its auto-correlation functions were exhibited and found to be reached at high gas velocity ( $Re_g > 33\,000$ , alternatively  $We_g > 75$ ), where no more dependence on operating parameter exists for these metrics. The base state found at low gas velocity remains however to be studied, along with the onset of the regime where these metrics depend on operating parameters. The transition in the behavior of the liquid core length seems also to be related to a change in breakup regime, from membrane-breakup to fiber-type atomization, which is qualitatively shown in the phase diagram presented in Fig. 3.9. The proposed framework, studying the distributions, auto-correlation functions, and their transition, appears as a candidate for a quantitative tool to describe the transition in breakup regimes.

Investigating the role of the onset of turbulence in the liquid jet on the liquid core length, we find no contribution on the statistics of  $L_B$ . However, the correlation time is shown to be proportional to a time based on the gas jet  $T_g = \frac{d_g}{U_g}$ , with a secondary weak dependence on the liquid Reynolds number. The values of  $\tau_c$  are found in the vicinity of  $2.3T_g$  at low liquid Reynolds numbers, while they neighbor  $3.6T_g$  at high  $Re_l$  values. The transition between the lower and upper range of correlation time gradually happens in the range  $4000 < Re_l < 8000$  through a monotonous increase. Before the increasing range, the liquid jet is laminar and is only destabilized by the Rayleigh-plateau instability that develops further downstream ( $Re_l \leq 2000$ ). Visualizations in the absence of a gas flow suggest that around  $Re_l = 4000$  the liquid jet is no longer laminar, as local disturbances are observed, a potential signature of turbulent spots. For higher liquid Reynolds number ( $Re_l \geq 8000$ ), the jet is heavily corrugated across a broad range of scales as it has now reached a turbulent state. We believe that the deviations from a laminar liquid jet followed by the establishment of a turbulent state are responsible for the increase in correlation time around  $Re_l \sim 4000$  and its potential saturation  $Re_l \sim 8000$  respectively.

As stated, the multiscale nature of spray formation prevents using a single approach to study every underlying mechanism of the fragmentation cascade. The liquid core length cannot be sufficient to fully describe gas-assisted atomization, in particular at high Weber numbers. Future work could hence encompass for instance the study of the signature of the change of atomization regimes and the onset of liquid turbulence highlighted here on other mechanisms, e. g. flapping instability, interfacial instabilities, break-up processes, and up to the droplet populations in the spray. In addition, confirming the changes of behaviors, that were observed here by varying the velocities of the fluids, but through modifications of the properties of the fluids as well would prove to be interesting future work.

## Acknowledgements

This work has been partially funded by the CNRS Energy unit (Cellule Energie) through the project MULTISPRAY.





# Synchrotron X-Ray high-speed radiography of the near-field of a coaxial two-fluid atomizer

---

The experiments presented in this chapter were conducted in collaboration with Dr. Alexander Rack, the senior beamline scientist at ID19 at ESRF. I wish to thank Dr. Bratislav Lukic and Herwig Requardt, working at ESRF, for their guidance and help in installing the experimental setup at ESRF. This work would not have been possible without the help of Pascal Meilleur, electrical engineer at LEGI who helped prepare and install the experimental setup at ESRF, Guillaume Deplus and Carlos Perez Fernandez, two scientists in training who did an internship in our team, and helped monitoring the experiments during data collection (split into day and night shifts over four days).

---

Previous work conducted with X-ray imaging in the field of atomization was presented in the introduction. A thorough description of the experimental setup used for the high-speed synchrotron X-ray imaging conducted during this Ph.D. was presented in Sec. 2.3.2, including a description of the challenges that such installation presents. In this chapter, I will present the results from the analysis of the time-resolved radiographs of the near-field of the atomization process captured throughout this Ph.D.

Figure 4.1 illustrates the different steps toward obtaining a map of the cumulative liquid path the beam went through, namely the equivalent path length (EPL) map of a radiograph. Each of these steps will be discussed in this chapter. First, a comparison of back-lit imaging and X-ray imaging is conducted in Sec. 4.1. Second, a qualitative analysis of the liquid jet's fragmentation supported by the observation of raw and normalized radiographs, along with a description of the morphology of the liquid jet under breakup of the liquid jet's breakup mechanism, in Sec. 4.2. Third, a discussion of the beam production and its influence on the quality of the radiographs, supported by a background analysis is presented in Sec. 4.3. A method to obtain quantitative measurements of the EPL thanks to X-ray measurements is presented in Sec. 4.4, with a description of the algorithm used to retrieve the phase map, followed by the calibration conducted to measure the EPL. Finally, the associated results of the EPL measurements are shown in Sec. 4.5.

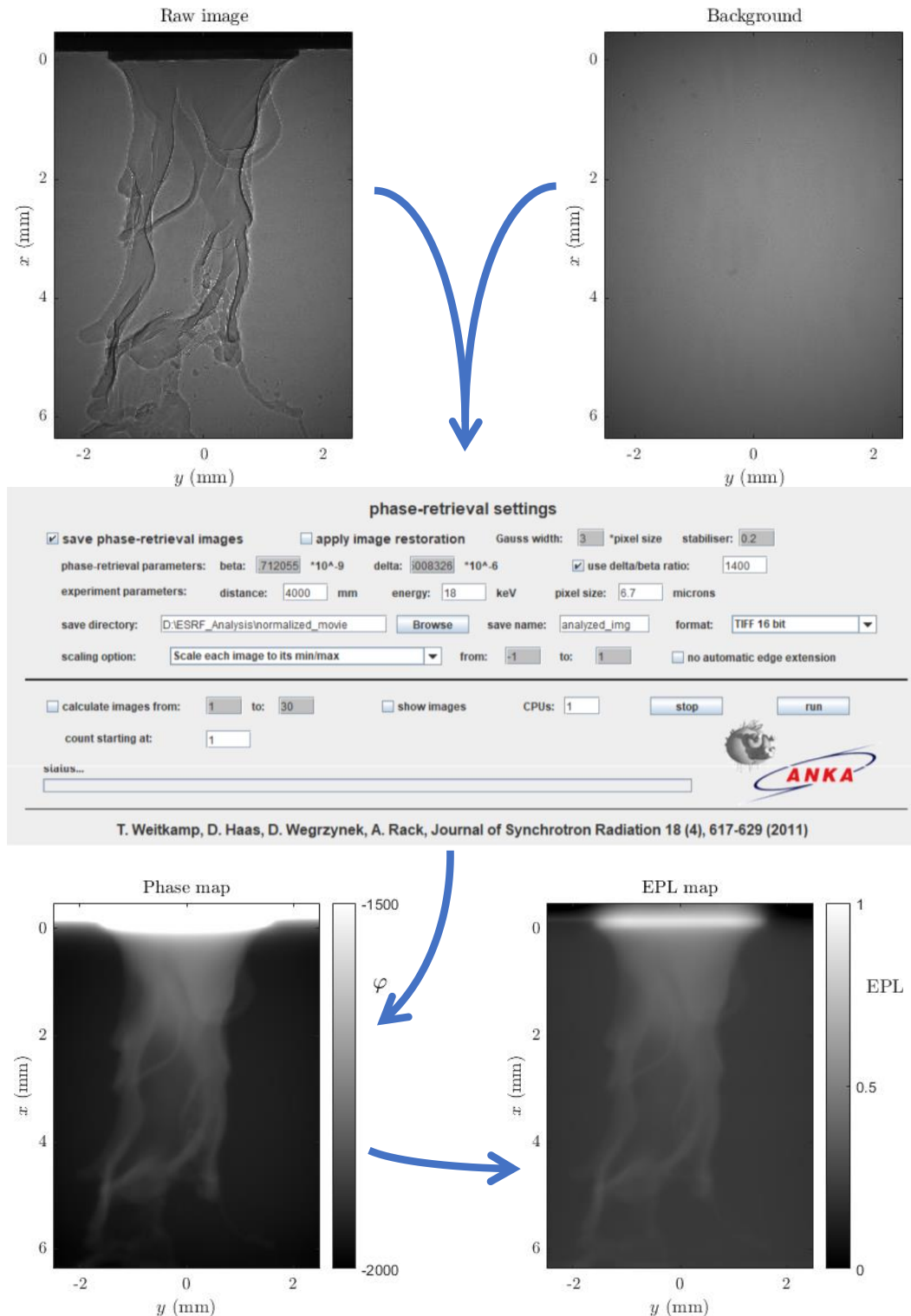


Figure 4.1: Illustration of the different steps towards quantitative analysis of X-ray radiographs. In Sec. 4.1, the raw radiographs are compared to raw back-lit images. Section 4.2 qualitatively discusses the liquid jets breakup mechanism using normalized radiographs. Section 4.3 highlights the issues encountered regarding the beam production and Section 4.4 shows an attempt to obtain quantitative measurements of the EPL.

## 4.1 Qualitative comparison of back-lit and X-ray imaging

X-ray radiographs contain an integrated 3D information, where the image intensity is related to the thickness of the material the X-ray beams went through, see Sec. 2.3.2.1 for more explanation on the physical principle. On the contrary, when using visible light, the beams deviate when going through a liquid-gas interface therefore the light does not reach the camera sensor. Back-lit imaging, therefore, leads to binary information: the beam either encountered or did not encounter water on its path. In addition, the lens selects a thin slice, perpendicular to the path of light, called the depth of field, while the full volume along the X-ray beam propagation is absorbed by the scintillator crystal (and then imaged by the camera).

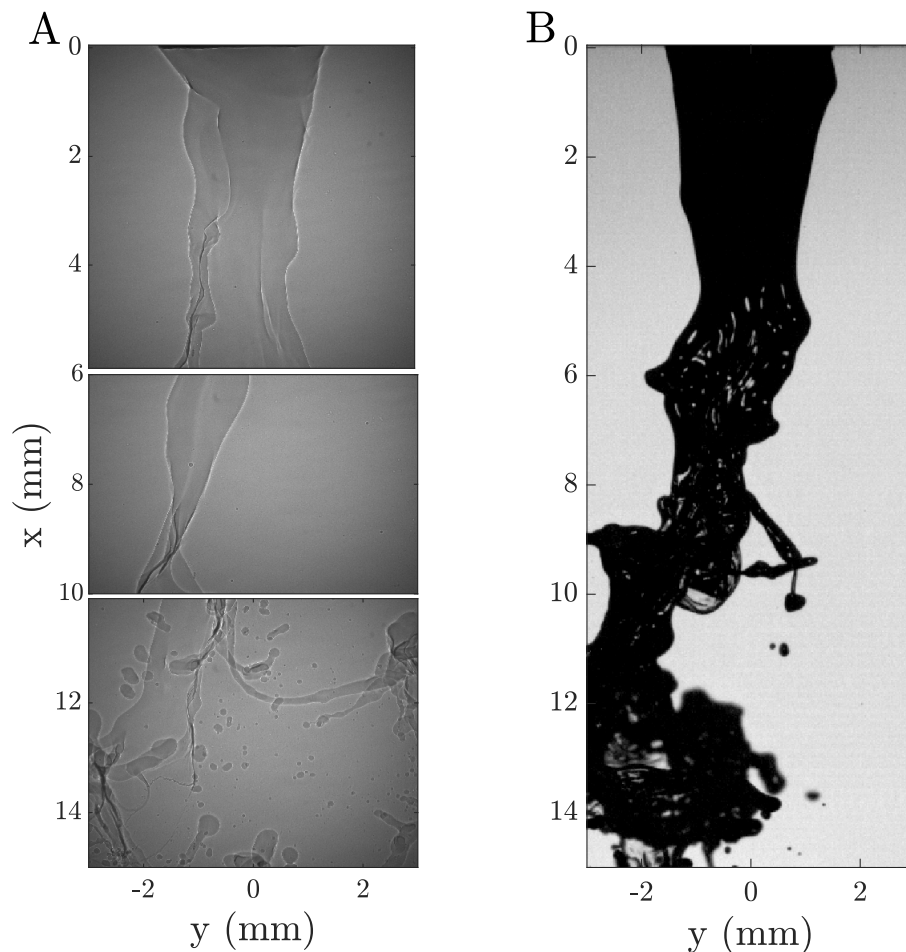


Figure 4.2: Atomization process at:  $U_l = 0.42$  m/s,  $U_g = 30$  m/s,  $Re_l = 780$ , and  $We_g = 24$ , captured using X-ray radiography A) and back-lit imaging B). For A), several windows captured at different times are put together to fill a region of similar dimension in the  $(x; y)$  plan than for B).

The next figures display an example radiograph and back-lit image of the atomization process for four different injection conditions, comparing both imaging techniques over the range of conditions explored using both methods. For injection conditions with low values of  $M$ , displaying long liquid jets, the beam size is too small to capture the entire liquid core on one imaging window (which at most is equal to 6.86 mm), see Fig. 4.2. To study these conditions, multiple movies were captured at different window locations, as illustrated in Fig. 2.21. Figure 4.2A) corresponds to 3 independent radiographs taken at different window locations and for different runs, but for the same injection parameters. Note that for these injection parameters, the atomization process is in the membrane breakup regime. Figure 4.3A) and B) show radiographs (normalized by a background) before, respectively after, the burst of a bag. Note that, unlike back-lit imaging, the normalization of a radiograph by a background consists of only the division of the radiograph by a flat field radiograph, namely a background, captured with the same imaging setup used to capture the radiograph, see Sec. 4.3. The thin membrane that makes up the bag barely absorbs the passing X-ray and is not visible in Fig. 4.3A), only the edges of the bag, where weak interference patterns occur, can be discerned. Since characteristic structures of the membrane breakup regime cannot be captured using X-ray radiography, in addition to the typically longer liquid core lengths associated with lower gas velocity, this technique is deemed inadequate for the study of this regime.

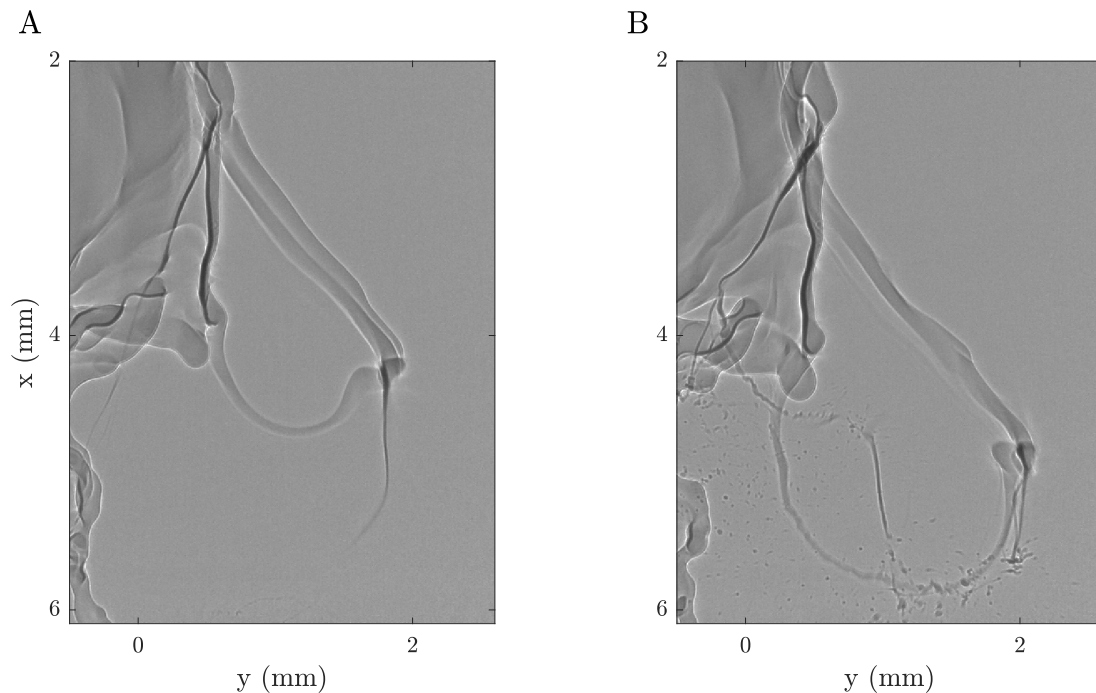


Figure 4.3: A) and B): Radiographs of a bag breakup before, respectively after, the bag bursts. The raw images are normalized by a background.

Increasing  $M$  by increasing the gas velocity, the imaging setup then becomes sufficient to capture the initial liquid breakup, as illustrated in Fig. 4.4. The presence of trapped bubbles within the liquid jet is visible in Fig. 4.4A), which cannot be seen on the back-lit images taken with the same injection parameters, see Fig. 4.4B). The bubbles are not observed to come from the injection process but are rather entrapped by the gas-liquid interface destabilization processes (as remarked by Machicoane et al. [3] as well). At first glance, both images are very similar but closer inspection already reveals overlapping interfaces in the center part of the jet. These structures correspond to destabilization processes occurring on the front and rear of the liquid jet.

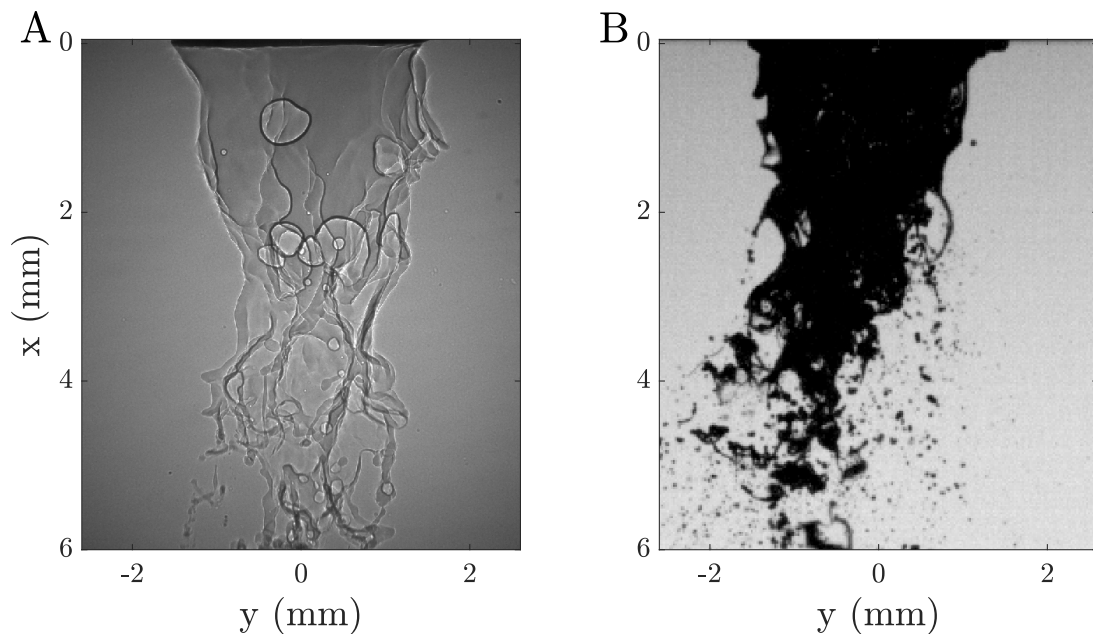


Figure 4.4: Atomization process at:  $U_l = 0.42$  m/s,  $U_g = 82$  m/s,  $Re_l = 780$  and  $We_g = 47$ , captured using X-ray radiography A) and back-lit imaging B).

Further increasing the gas velocity, the morphology of the liquid jet switches to a hollow liquid core, see Fig. 4.5A). This hollow morphology, found at high values of  $M$  ( $M > 55$ ) has already been observed and described in [3] and was referred to as a liquid crown since the center of the liquid core is hollow and ligaments are stripped by the gas jet from its periphery. Figure 4.6 shows a radiograph of the atomization process with a liquid jet in the crown configuration on two panels, the bottom panel corresponds to the free liquid jet, and the top panel to a visualization of the liquid inside the nozzle, through the aluminum walls. Both of these panels correspond to the same radiograph but the colorbar was adapted to enhance visibility on each panel. This image reveals that the hollow morphology of the liquid jet can reach inside the liquid nozzle, affecting the injection process of the liquid, effectively exiting through a reduced cross-section. These aspects of the atomization process cannot be captured using back-lit imaging. Note that this morphology cannot be perceived with back-lit imaging, see Fig. 4.5B).

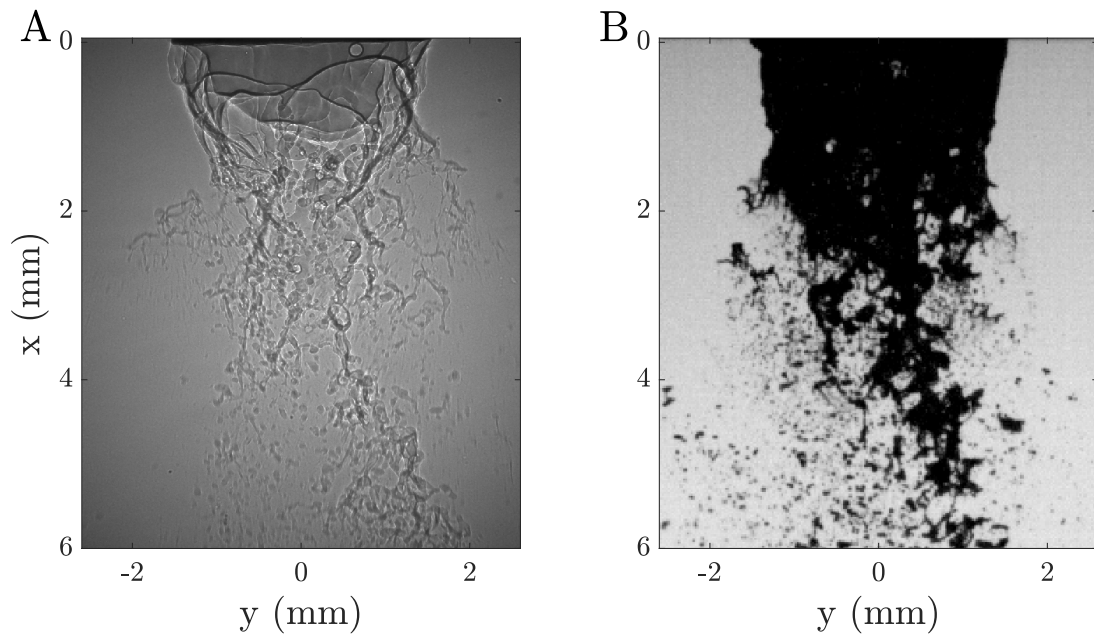


Figure 4.5: Atomization process at:  $U_l = 0.42$  m/s,  $U_g = 113$  m/s,  $Re_l = 780$  and  $We_g = 180$ , captured using X-ray radiography A) and back-lit imaging B).

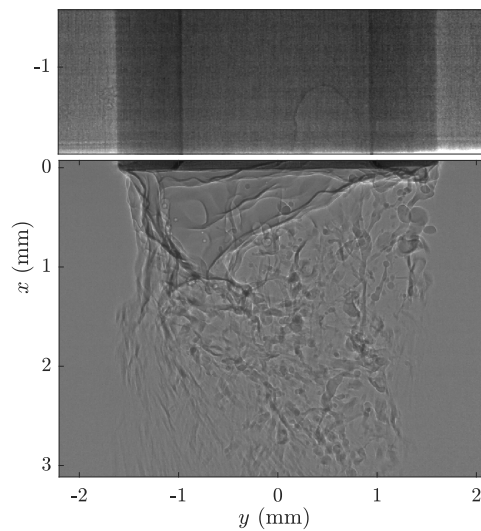


Figure 4.6: Radiograph of the interior of the nozzle during the atomization process. The top and the bottom panel have different colorbar ranges to enhance visibility. The injection parameters are:  $U_l = 0.42$  m/s,  $U_g = 190$  m/s,  $Re_l = 780$  and  $We_g = 950$ .



For high gas flow rates, the liquid crown becomes unstable and dewetting of the liquid jet along a portion of the liquid nozzle is observed, see Fig. 4.7. Note that despite being able to observe this partial dewetting in some conditions using back-lit imaging (see Fig. 4.7 B)), the complex dynamic around this unstable jet is much better seen with radiograph movies.

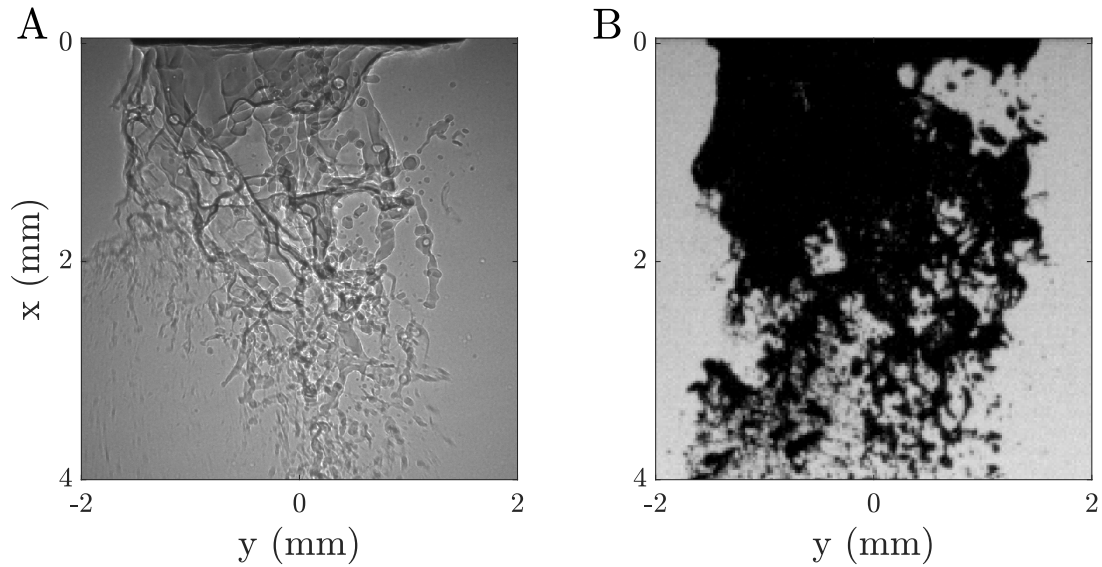


Figure 4.7: Atomization process at:  $U_l = 0.42$  m/s,  $U_g = 163$  m/s,  $Re_l = 780$  and  $We_g = 700$ , captured using X-ray radiography A) and back-lit imaging B).

The X-ray source provided by the ID-19 beamline of the ESRF facility is collimated, therefore the entire liquid quantity is projected along the beam's axis, namely the  $z$ -axis. All the inner structures are visible with this setup. Although these structures may be superimposed, their positions in the  $(x;y)$  plan are accurate and can be measured using a scale. This permits the observation of 3D phenomena using only one camera.

Being able to observe the inner structures of the liquid jet's breakup with X-ray imaging, the following section is dedicated to the characterization of the morphology of the liquid breakup.





## 4.2 Liquid jet breakup morphologies

As illustrated in the previous section, the inner details of the liquid jet's breakup process are visible on the X-ray radiographs. In this section, a description of the variety of breakup mechanisms is conducted, supported by time-series of radiographs of the atomization process for different injection parameters. This description is followed by a proposed explanation of the physical mechanism leading to the liquid jet morphologies observed.

### 4.2.1 Qualitative observations of the liquid jet breakup morphologies

Figure 4.8 shows the entire parameter space explored with X-ray radiography. Time-series of the highlighted points are shown in Fig. 4.9 to 4.13. These conditions were chosen to illustrate the effect of the gas velocity on the liquid jet morphology for a constant liquid velocity. The time series are ordered from the lowest to highest gas velocity.

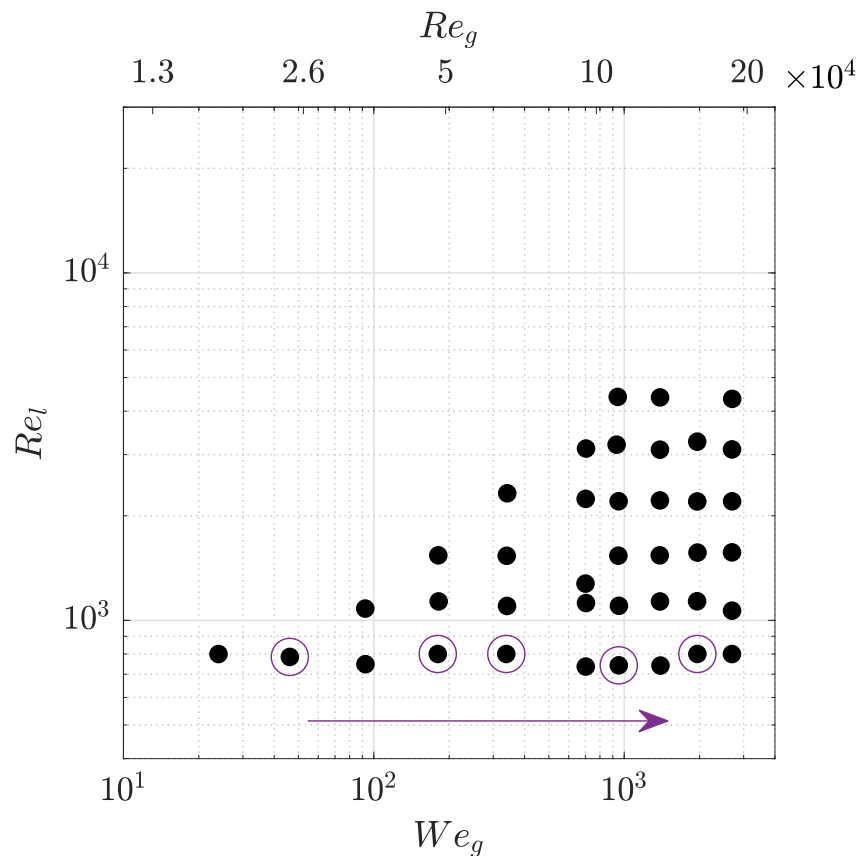


Figure 4.8: Parameter space of the X-ray radiograph movies acquired. Time-series of the highlighted points are shown in Fig. 4.9 to 4.13.

For low gas velocities, illustrated in Fig. 4.9, the liquid jet consists of an intact core surrounded by liquid sheets and ligaments that corrugate its outer surface. For these injection parameters, back-lit imaging studies revealed that one of the primary breakup mechanisms consists of bag breakups, which are barely visible on the X-ray images, as illustrated in Fig 4.3. The motion of the liquid structures traps air bubbles within the liquid jet's core, visible from  $t = 1.5 \mu\text{s}$  to  $t = 2.75 \mu\text{s}$  of Fig. 4.9. This phenomenon was previously observed and described in [3], in which the authors believe the bubbles then migrate further downstream, in the detached liquid structures, and could modify the secondary breakup events. Note that these bubbles are sometimes visible on back-lit images, although it is hard to decipher between entrapped air bubbles or an optical lens effect by the gas-liquid interfaces as described in Sec. 2.3.1.3.

When the gas injection velocity is increased up to the apparition of fibers, as shown in Fig. 4.10, more gas bubbles are entrapped within the liquid core therefore the surface area of encapsulated air bubbles, with respect to the liquid surface area, seems to increase as the gas velocity increases. Note that individual fibers are very well seen in Fig. 4.10. While they do not hold a significantly different amount of liquid than bags (a bag thickness is of the order of  $1 \mu\text{m}$  while a ligament can be a few to a dozen  $\mu\text{m}$  thick), the high curvature of the gas-liquid interface has a strong signature (with a grey pixel line) around ligaments, while only the reams of bags are highlighted by the interference patterns observable in this phase-contrast configuration. Upon further increasing the gas velocity up to the end of the transitional regime described in Chap. 3 (disappearance of bags), the liquid jet adopts a stable hollow shape, see Fig. 4.11, resembling an upside-down crown. This is described as the crown regime by [3]. Note that the two liquid-gas interfaces corresponding to the front and the back of the crown shape of the liquid jet are visible on almost all the radiographs for this regime.

When the gas velocity is further increased, the stability of the previously described crown is compromised, as shown in Fig. 4.12. At  $t = 0 \mu\text{s}$ , the liquid jet has a hollow crown shape. A gas recirculation then pushes the liquid jet away from the edge of the liquid nozzle, forcing dewetting of this portion of the nozzle. The recirculation then breakdowns at  $t = 2.5 \mu\text{s}$  and the liquid jet retrieves its crown shape. In some cases, the gas phase inside the crown can reach inside the nozzle, see Fig. 4.6. Figure 4.13 illustrates an unstable crown regime where the recirculation never breaks down. In this case, the gas recirculation moves within the liquid nozzle cross-section during long periods, which in turn displaces the liquid core. Since the liquid core position is no longer fixed, the regime is termed unstable crown. Note that the spatial and temporal resolutions are adapted to the changes in time and spatial scales of the two-phase flow as the gas velocity is increased, as illustrated by the scale bar length, growing to display the constant 1 mm scale.

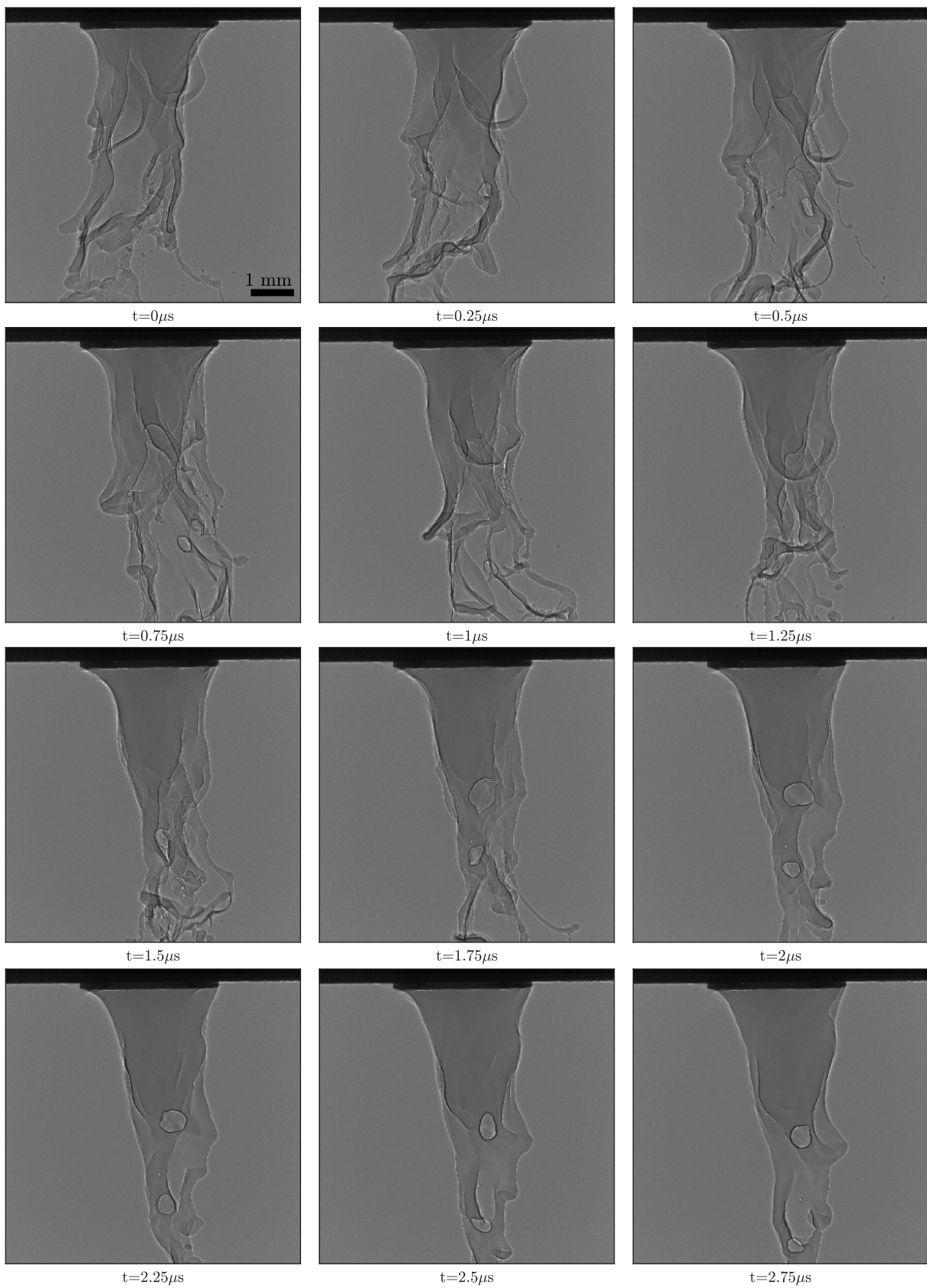


Figure 4.9: Time series of radiographs of the atomization process at the exit of the nozzle for  $U_l = 0.42$  m/s,  $U_g = 42$  m/s, i.e.  $Re_l = 780$  and  $We_g = 47$ .

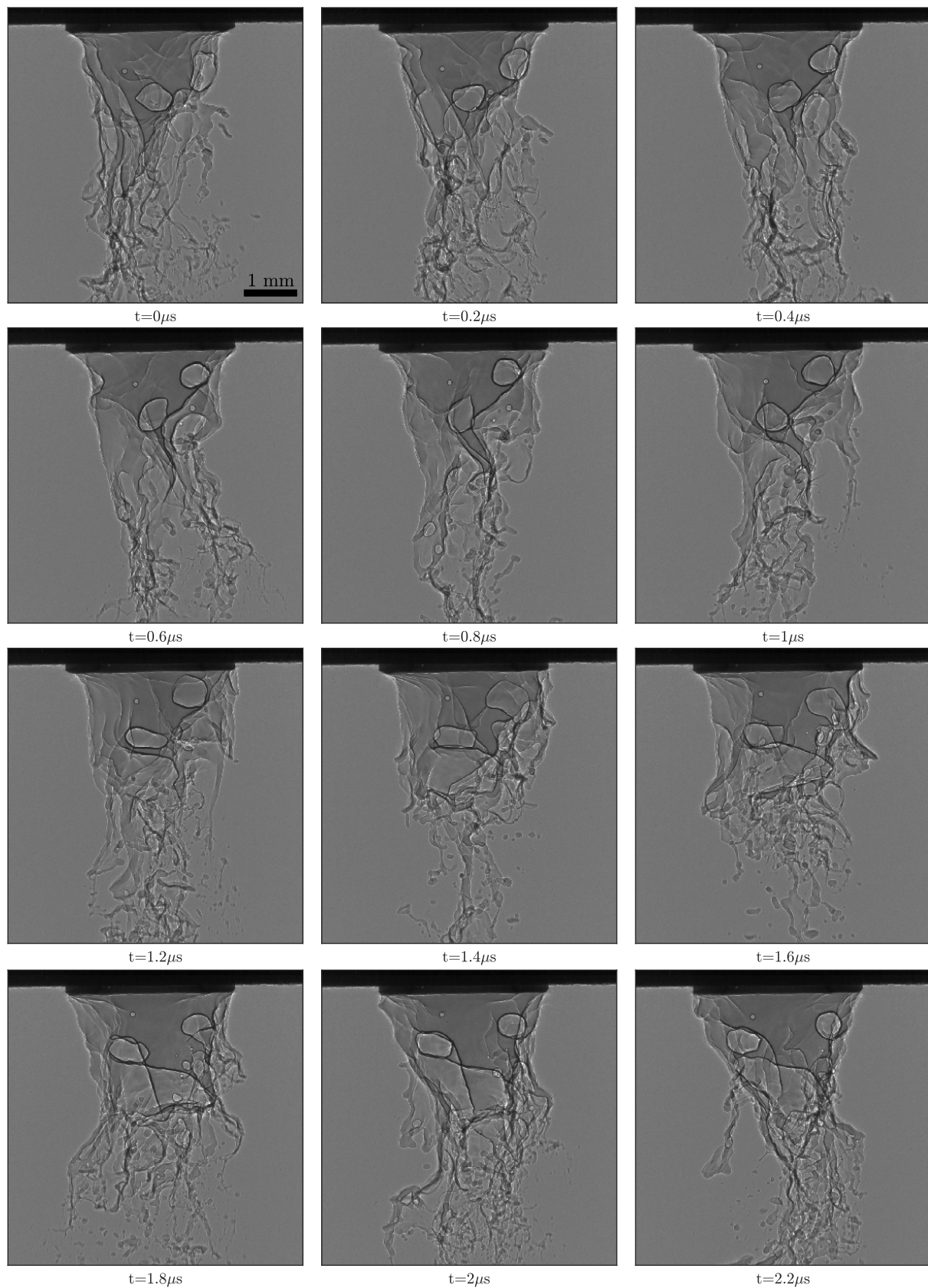


Figure 4.10: Time series of radiographs of the atomization process at the exit of the nozzle for  $U_l = 0.42$  m/s,  $U_g = 82$  m/s, i.e.  $Re_l = 780$  and  $We_g = 180$ .

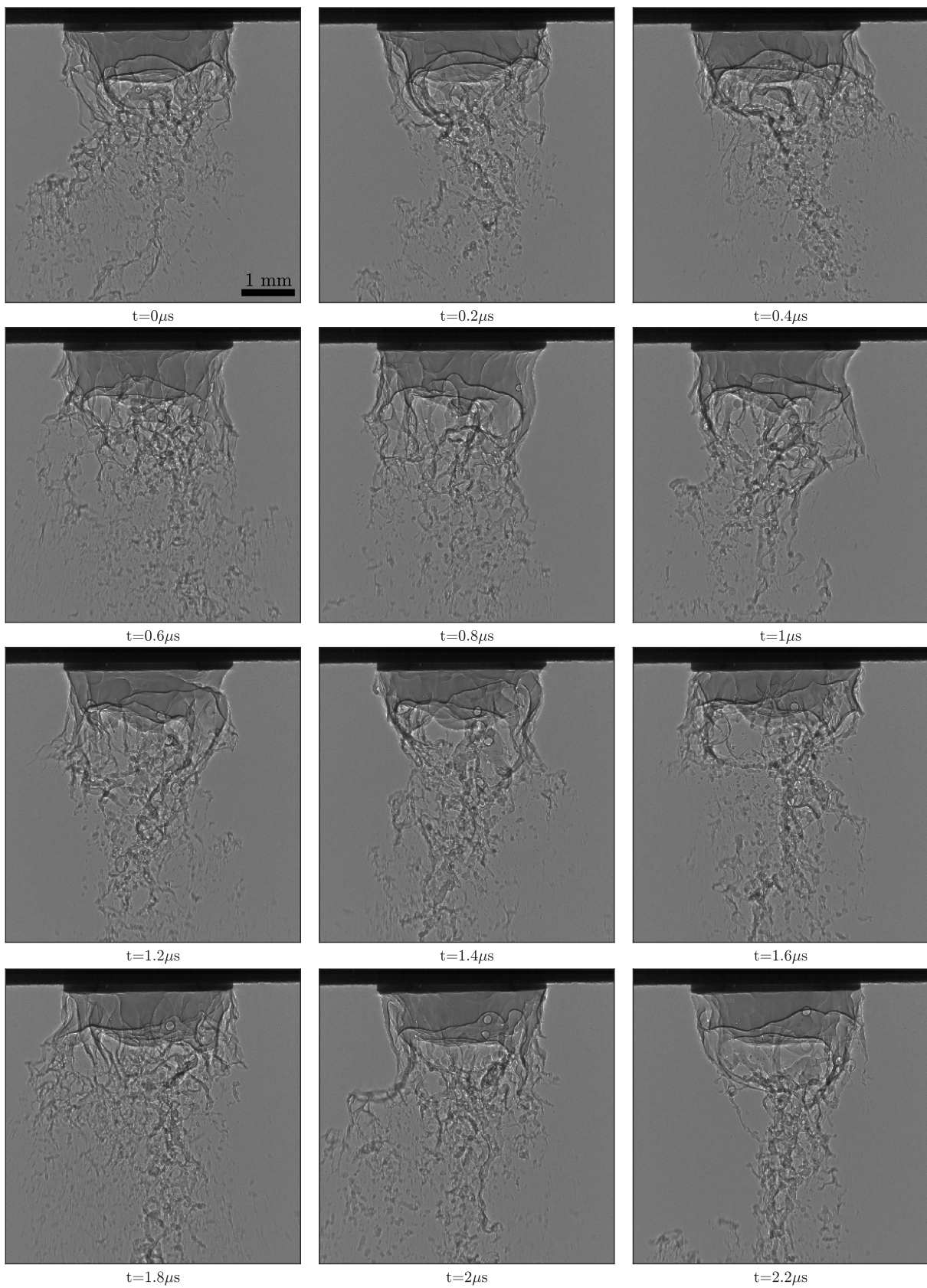


Figure 4.11: Time series of radiographs of the atomization process at the exit of the nozzle for  $U_l = 0.42$  m/s,  $U_g = 113$  m/s, i.e.  $Re_l = 780$  and  $We_g = 340$ .



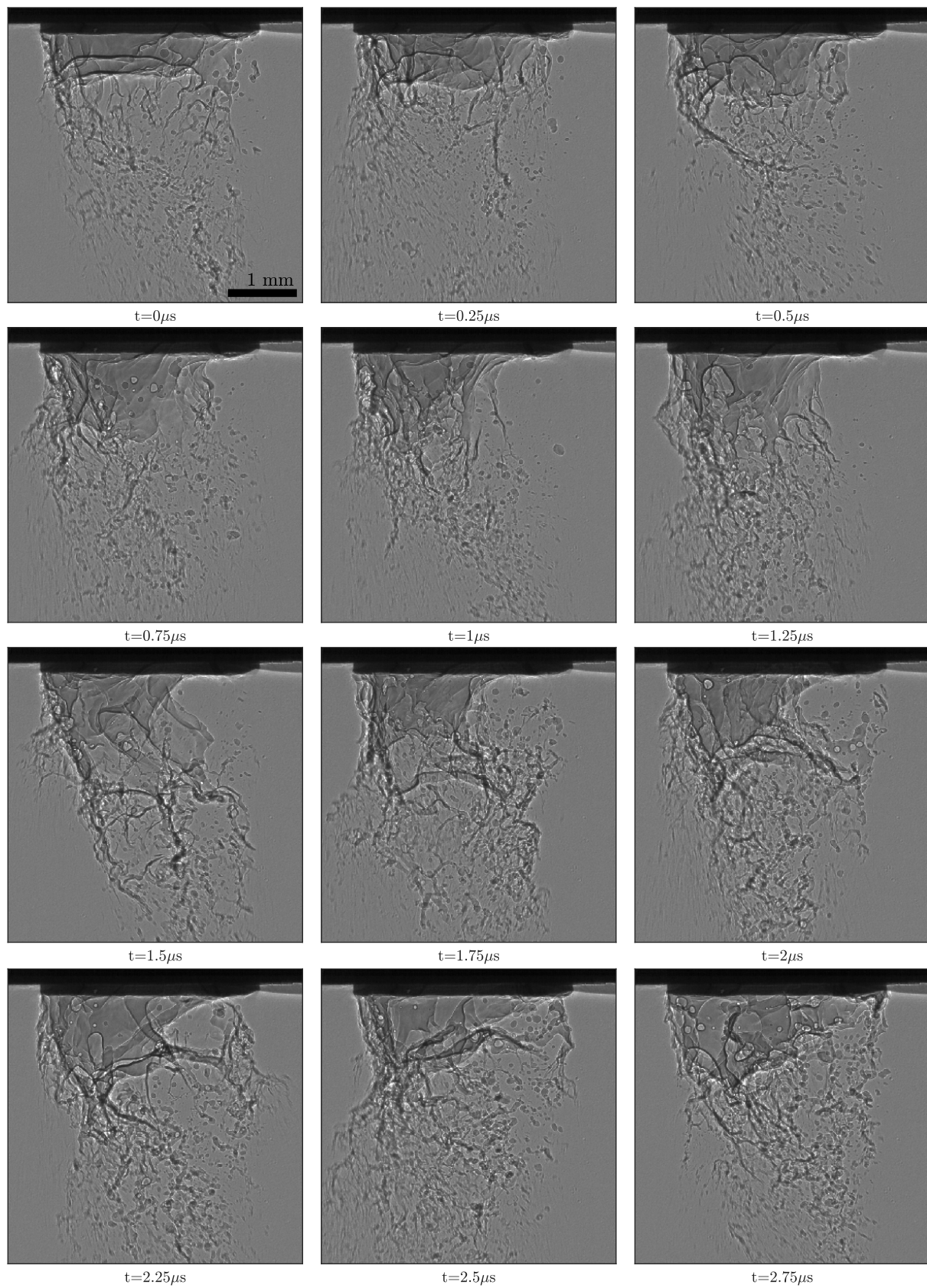


Figure 4.12: Time series of radiographs of the atomization process at the exit of the nozzle for  $U_l = 0.42$  m/s,  $U_g = 188$  m/s, i.e.  $Re_l = 780$  and  $We_g = 945$ .



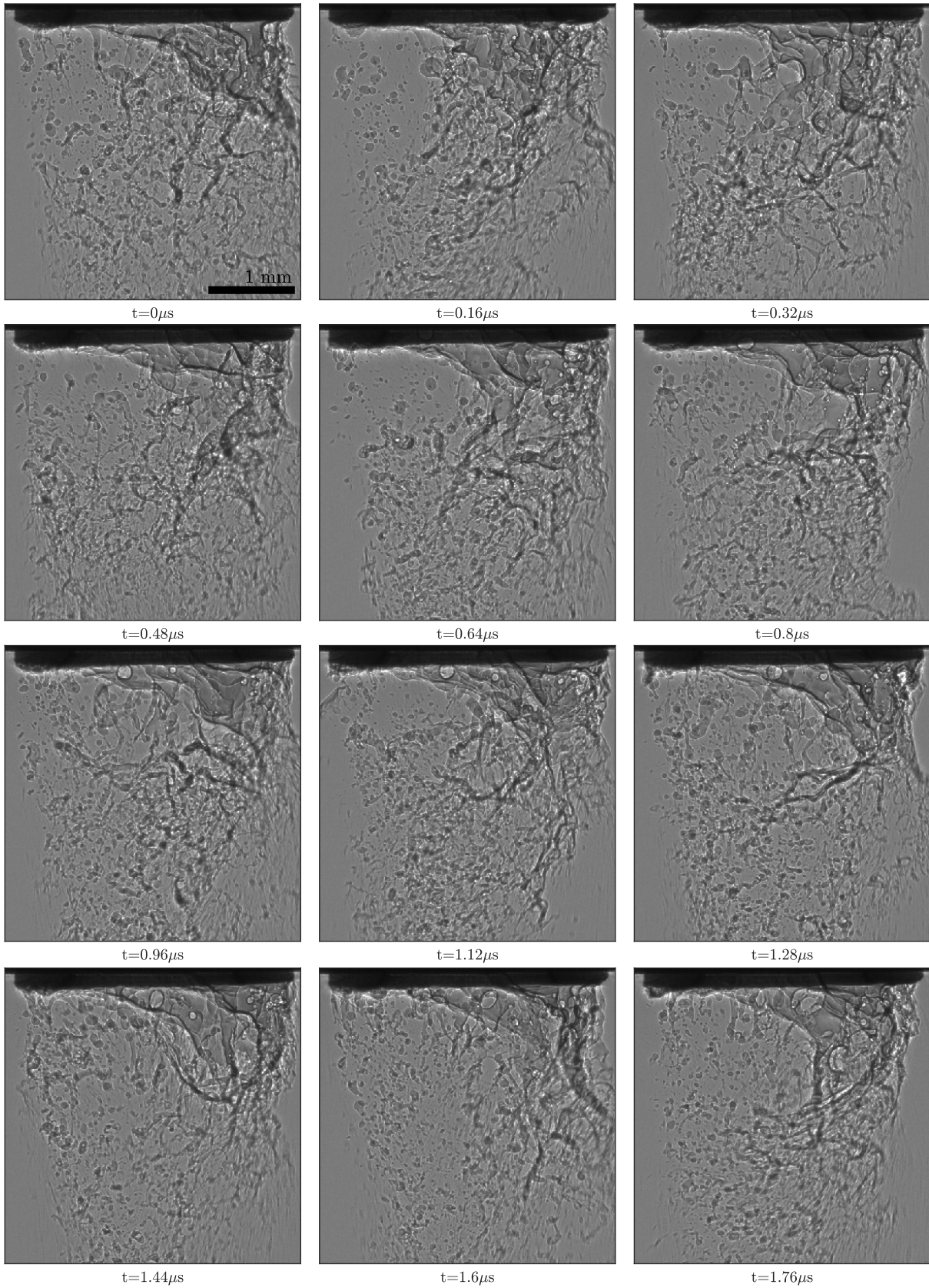


Figure 4.13: Time series of radiographs of the atomization process at the exit of the nozzle for  $U_l = 0.42$  m/s,  $U_g = 271$  m/s, i.e.  $Re_l = 780$  and  $We_g = 1950$ .

To further highlight the influence of the injection parameters, radiograph time-series of the liquid jet's morphology are shown along an increasing liquid velocity at a constant gas velocity. These time series correspond to the injection parameters highlighted on the phase diagram of Fig. 4.14. Starting with Fig. 4.12, the liquid velocity at injection is increased on the time series of Fig. 4.15 and 4.16.

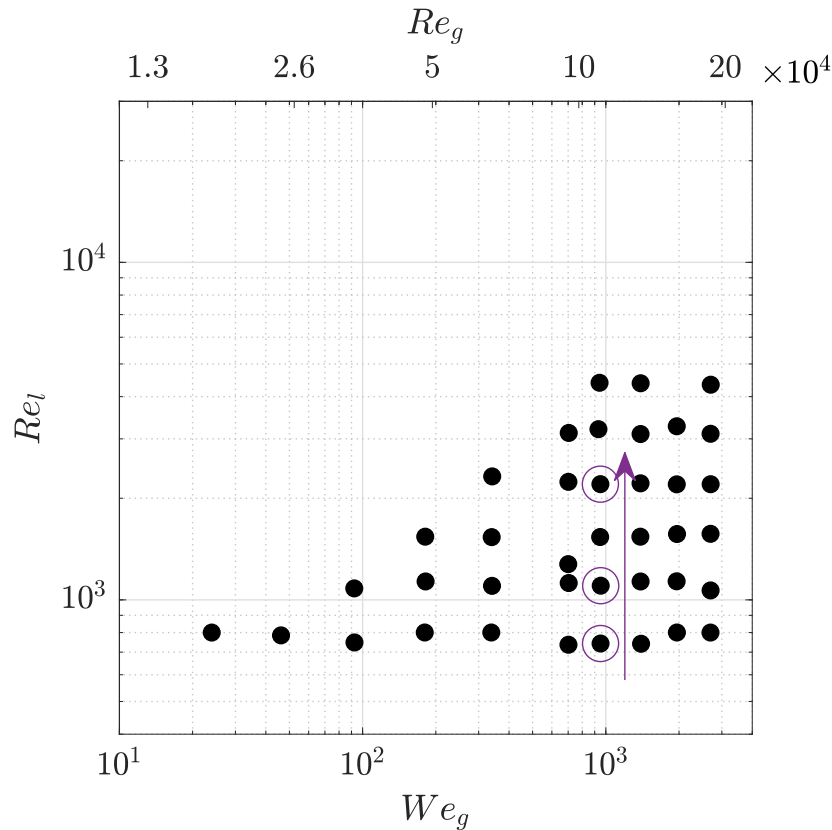


Figure 4.14: Parameter space of the X-ray radiograph movies acquired. Time-series of the highlighted points are shown in Fig. 4.12, 4.15, and 4.16.

Starting with the injection parameters of Fig. 4.12, corresponding to the unstable crown regime described above, increasing the liquid injection velocity stabilizes the liquid jet's hollow morphology, as shown on Fig. 4.15, displaying a stable liquid crown. Further increasing the liquid injection velocity up to the injection parameters of Fig. 4.16, the crown shape is not present anymore and the liquid jet then consists of a liquid core with multiple smaller-scale gas recirculations. This situation is unlike the liquid crown described above at lower liquid velocity, where two fairly stable gas-liquid interfaces were seen throughout recordings (the front and back part of the crown periphery projected onto the sensor plane). Many more interfaces are observable at a given instant, and their motion is orders of magnitude faster. These small-scale gas recirculations are also short-lived, many appear and then disappear in the small time-lapse presented in Fig. 4.16 already.

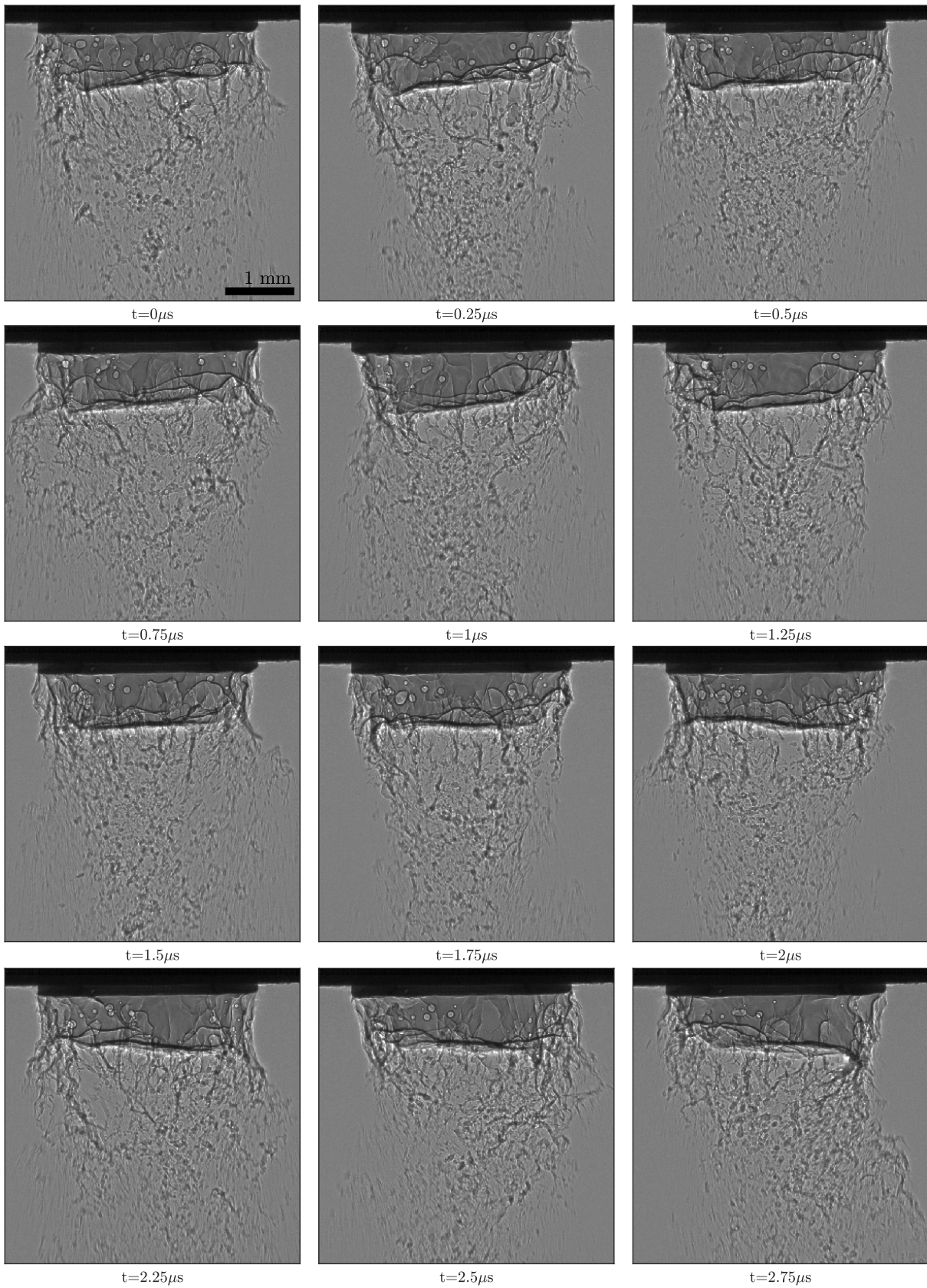


Figure 4.15: Time series of radiographs of the atomization process at the exit of the nozzle for  $U_l = 0.59$  m/s,  $U_g = 113$  m/s, i.e.  $Re_l = 1100$  and  $We_g = 340$ .

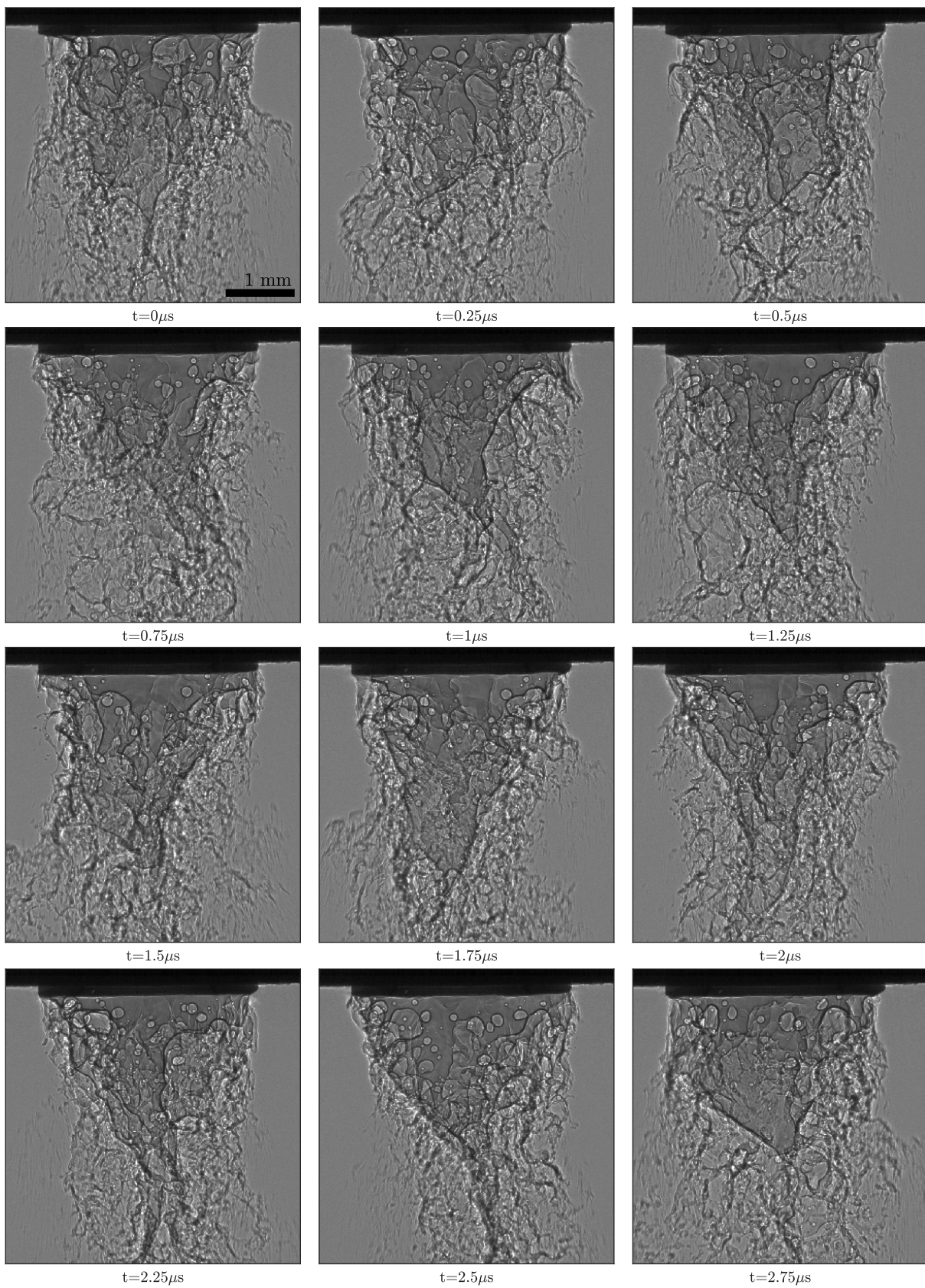


Figure 4.16: Time series of radiographs of the atomization process at the exit of the nozzle for  $U_l = 1.18$  m/s,  $U_g = 113$  m/s, i.e.  $Re_l = 2200$  and  $We_g = 340$ .



The previous qualitative observations revealed four different morphologies of the liquid core, which also seem to involve different break-up processes.

The first state is referred to as the intact core regime, shown in Fig. 4.9. This state is characterized by a liquid jet presenting an intact central bulk, destabilized on its outer surface by ligaments and sheets of liquid detaching from its outer periphery, while no penetration of the gas flow is seen within the liquid core. These liquid sheets entrap bubbles within the liquid core but no further inclusion of gas is observed.

The second state is named crown regime and is characterized by a hollow liquid core that takes the shape of a crown. The liquid jet is here destabilized both on an outer surface in contact with the gas jet and on an inner surface that contains the gas recirculations. This situation results mainly in ligaments being directly stripped by the lower edge of the liquid core (where both inner and outer surfaces meet), forming the crenelations in this picture of an upside-down crown. This state is illustrated in Fig. 4.11 and 4.15.

A transitional state between the first two states is illustrated in Fig. 4.10 and 4.16. In this transitional state, inclusions of gas are observed in the liquid core, in the form of many recirculations of small-to-intermediate scales. Note that in some instants of a movie of the atomization process in the transitional state the liquid jet adopts the crown shape previously described. When this is observed, shortly after, the liquid jet rapidly changes its morphology and regains that of an intact core with gas inclusions, confirming the transitional nature of this regime.

The last state observed corresponds to an unstable crown. Like the crown regime, this state is characterized by a hollow liquid core, but the liquid is blown off to a certain region of the liquid nozzle, leading to drastic dewetting of a large portion of the liquid nozzle periphery. This state is illustrated in Fig. 4.12 and 4.13. Note that for the case illustrated in Fig. 4.12, the drastic dewetting is not maintained at all times, but only shortly observed, supposedly caused by large fluctuations of the gas flow. In opposition, in the case illustrated in Fig. 4.13, the liquid dewets the nozzle at all times. This state has been reported in the literature [3], but the transition to this regime had been triggered by the addition of swirl in the gas jet. We report for the first time that this regime can be reached for high values of  $M$  ( $M > 180$ ) without adding swirl. (i.e. purely longitudinal gas jet). Note that uncovering this regime as well as the transitional regime is a direct consequence of the tight sampling of the parameter space and of the study of the effect of the liquid Reynolds number on spray formation (where here low  $M$  is attained thanks to the low  $Re_l$  value sampled).

Qualitative characterizations of the state of the liquid jet in these four regimes were conducted for all the injection parameters explored, shown in the phase diagram of Fig. 4.20.

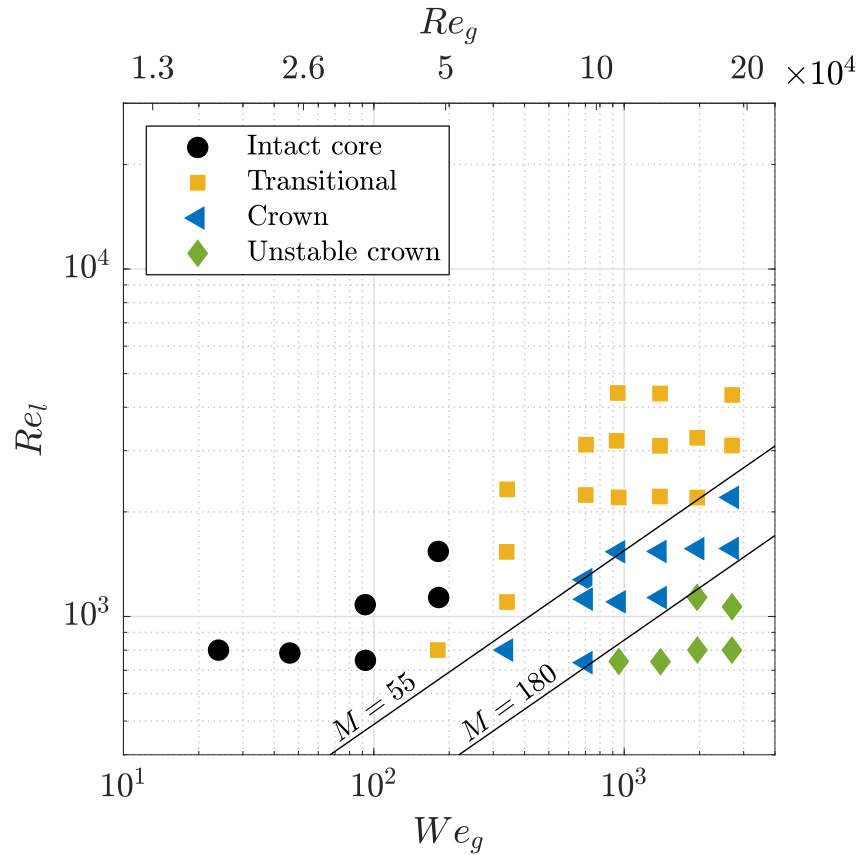


Figure 4.17: Qualitative phase diagram of breakup morphology regimes in the  $\{Re_l; We_g\}$  parameter space. Black circles, yellow squares, blue triangles, and green diamonds respectively correspond to the intact core, the transitional, the crown, and the unstable crown regimes. The black lines correspond to iso- $M$  lines of  $M = 55$  and  $M = 180$  respectively.

The transition from the transitional to the crown regime appears to be dominated by  $M$ , as shown in the phase diagram in Fig. 4.20 where the curve for  $M = 55$  separates both of these regimes. The transition from the crown to an unstable crown regime also appears to be triggered by an increase of  $M$ , with  $M = 180$  separating both regimes in the  $\{Re_l; We_g\}$  parameter space presented in Fig. 4.20.

## 4.2.2 Proposed mechanisms for the change of regimes in the liquid core morphology

The qualitative description of the liquid core's breakup highlights various morphologies. A possible explanation for the transition from an intact liquid core to a crown regime is illustrated in Fig. 4.18. Figure 4.18A) and B) respectively show radiographs of the liquid jet with no gas and of the gas jet with no liquid. The arrows on Fig. 4.18B) highlight the gas recirculation which originates from the gas flow exiting the nozzle into a still environment. Similarly to a backward-facing step flow<sup>1</sup>, this leads to recirculations towards the center of the injector. This was illustrated early on in the context of coaxial two-fluid atomization in Fig. 4 of [4], representing the streamlines exiting an annular gas nozzle. When the gas jet's kinetic energy is much greater than that of the liquid jet, the gas recirculations strongly affect the liquid core's dynamics, and a hollow liquid core is observed, as illustrated in Fig. 4.18C).

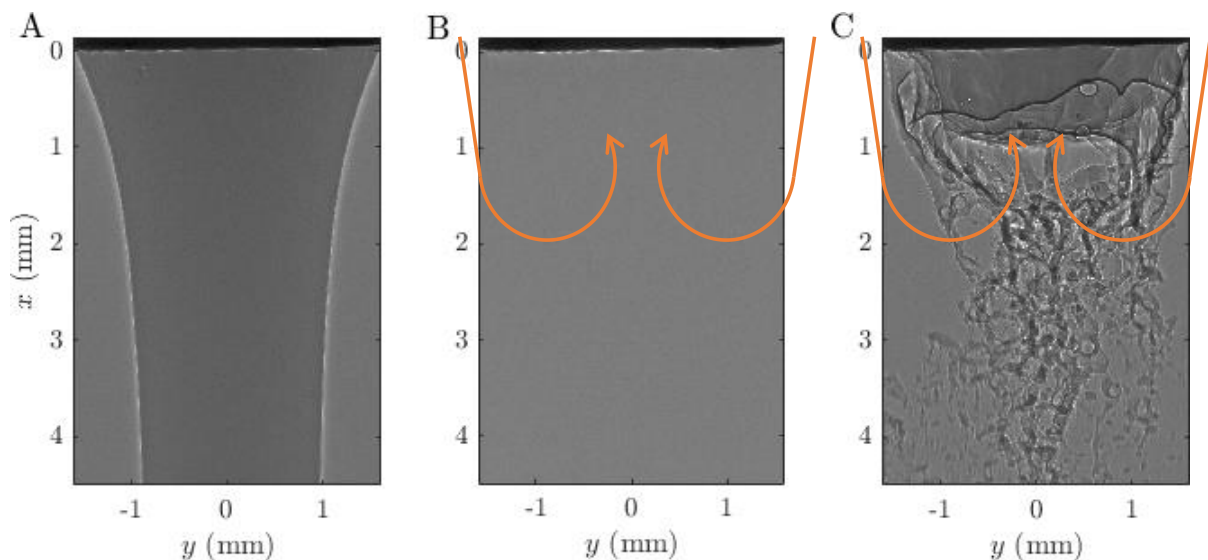


Figure 4.18: A) Radiograph of the liquid jet with no gas jet. B) Radiograph of the gas jet with no liquid jet, the orange arrows represent the gas recirculation. C) Radiograph of the liquid jet's breakup process in the crown regime.

This description also explains the other morphologies observed in the previous section. When the previously mentioned energy balance is just below the energy balance which leads to the crown shape of the liquid jet, inclusions of gas in the liquid jet are observed, as illustrated in Fig. 4.19A). When the gas kinetic energy completely overcomes that of the liquid jet, the recirculation completely pushes the liquid jet up to the point of dewetting the nozzle, as illustrated in Fig. 4.19B).

<sup>1</sup>Images of qualitatively similar flow configurations can be visualized on pages 13 to 15, and 43 of an Album of Fluid Motion by Van Dyke [102]



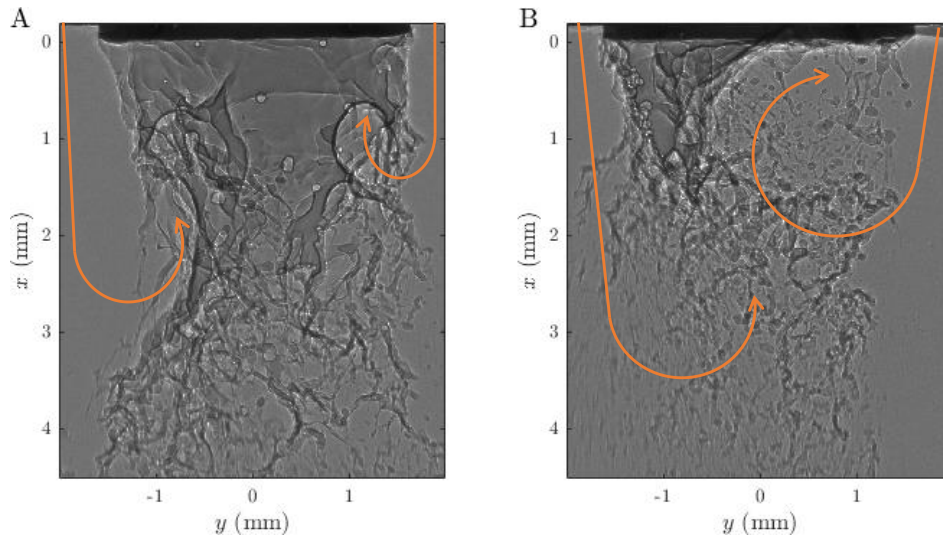


Figure 4.19: Time series of radiographs of the atomization process at the exit of the nozzle. The injection parameters are:  $U_l = 0.42$  m/s,  $U_g = 271$  m/s,  $Re_l = 780$  and  $We_g = 1950$ .

This description with kinetic energy would mean that the transition between the observed regimes is captured by  $M$ , being a proxy to the ratio of the kinetic energies of both phases, which is consistent with the previous discussion of the phase diagram presented in Fig. 4.20. Note that the gas-to-liquid dynamic pressure ratio is not a direct measure of the ratio of the kinetic energies of both phases. The gas-to-liquid momentum flux ratio  $MR = \rho_g A_g U_g^2 / \rho_l A_l U_l^2 = MA_g / A_l$  is a better evaluation of the kinetic energy balance between both phases. For  $M = 55$ , respectively  $M = 180$ , the momentum flux ratio is  $MR \simeq 1400$ , respectively  $MR \simeq 4500$ . These values indicate that the kinetic energy carried by the gas phase is much higher than the kinetic energy of the liquid phase in any case. Note that  $MR$  is related to the entire kinetic energy, but only an inner portion of the gas phase is involved in the primary breakup of the liquid jet. Considering the thickness of the inner boundary layer of the annular gas jet  $\delta_g$  as a measure of the gas thickness involved in this transition, we define a local gas-to-liquid momentum flux ratio  $MR_{\delta_g} = MA_{\delta_g} / A_l$  with  $A_{\delta_g} = 2\pi D_l \delta_g$  the area of the gas inner boundary layer. This dimensionless parameter compares the kinetic energy of the gas boundary layer with the kinetic energy of the entire liquid jet, since the regimes described above affect the entire liquid jet, and not just a portion of it. Using the empirical expression of the inner gas boundary layer thickness obtained by [14] for a coaxial injector,  $\delta_g = 5.6(d_g - D_l) / \sqrt{Re_g}$ , the expression of the gas to liquid momentum ratio defined on the gas inner boundary layer is:  $MR_{\delta_g} = 44.8M \frac{D_l(d_g - D_l)}{d_l^2} \frac{1}{\sqrt{Re_g}}$ .

Figure 4.20 represents the liquid core phase diagram in the  $\{Re_l; We_g\}$  parameter space, with two iso- $MR_{\delta_g}$  curves corresponding to  $MR_{\delta_g} = 50$  and  $MR_{\delta_g} = 150$  respectively. Note that iso- $MR_{\delta_g}$  curves in the  $\{Re_l; We_g\}$  parameter space follow  $We_g^{3/8}$ , and are steeper than iso- $M$  curves,

which follow  $We_g^{1/2}$ . The curve corresponding to  $MR_{\delta_g} = 50$  separates the injection conditions in the transitional state from the injection conditions in the crown regime. The transition to the crown regime seems to occur when the energy of the gas boundary layer overcomes that of the liquid jet. The gas can then overcome the liquid jet and a stable gas vortex settles within the liquid jet. Note that the curve representing  $MR_{\delta_g} = 150$  captures the transition from the crown to the unstable crown regime.

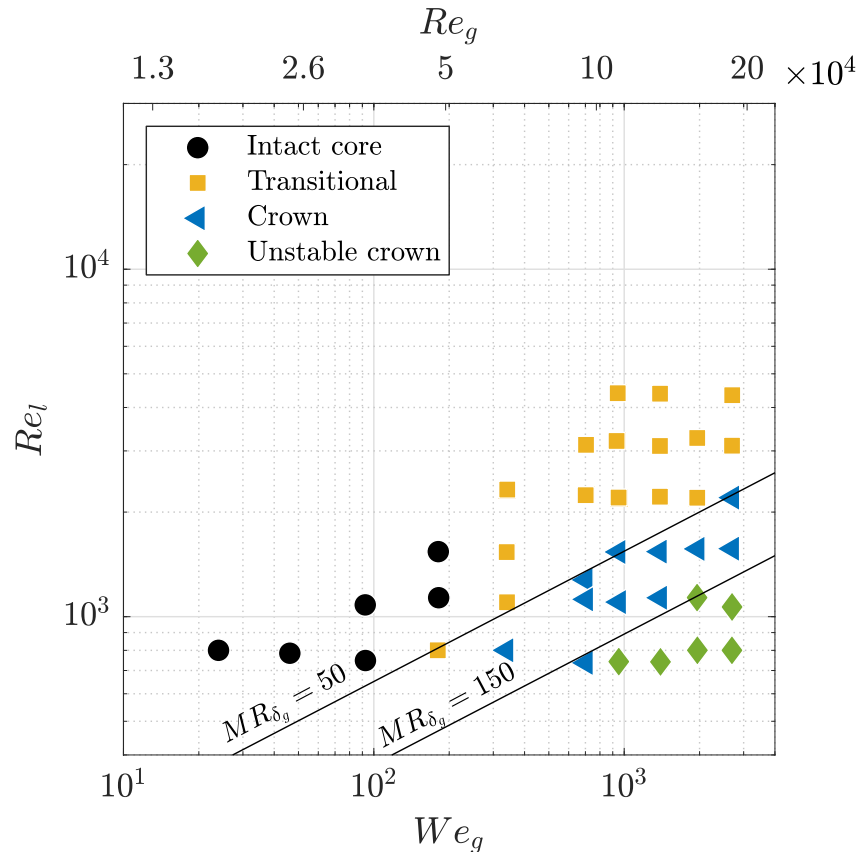


Figure 4.20: Qualitative phase diagram of breakup morphology regimes in the  $Re_l; We_g$  parameter space. Black circles, yellow squares, blue triangles, and green diamonds respectively correspond to the intact core, the transitional, the crown, and the unstable crown regimes. The black lines correspond to iso- $MR_{\delta_g}$  lines of  $MR_{\delta_g} = 50$  and  $MR_{\delta_g} = 150$  respectively.

## 4.3 Beam characteristics and backgrounds

### 4.3.1 Beam production

The X-ray beam is produced by the interaction of accelerated electrons, located in a ring under vacuum, with an undulator, located before each beamline. The interaction between the electrons and the undulator deducts energy from the electrons in the ring. The ring's internal energy is maintained by adding electrons to the ring every hour, therefore a decrease in the intensity of the X-ray produced is observed between two refills of the ring. Figure 4.21A) represents the energy stored in the ring as a function of time via a measure of the ring current, during the first 12 hours of experimental measurements. A 5% decrease in the ring's internal energy is observed between two refills.

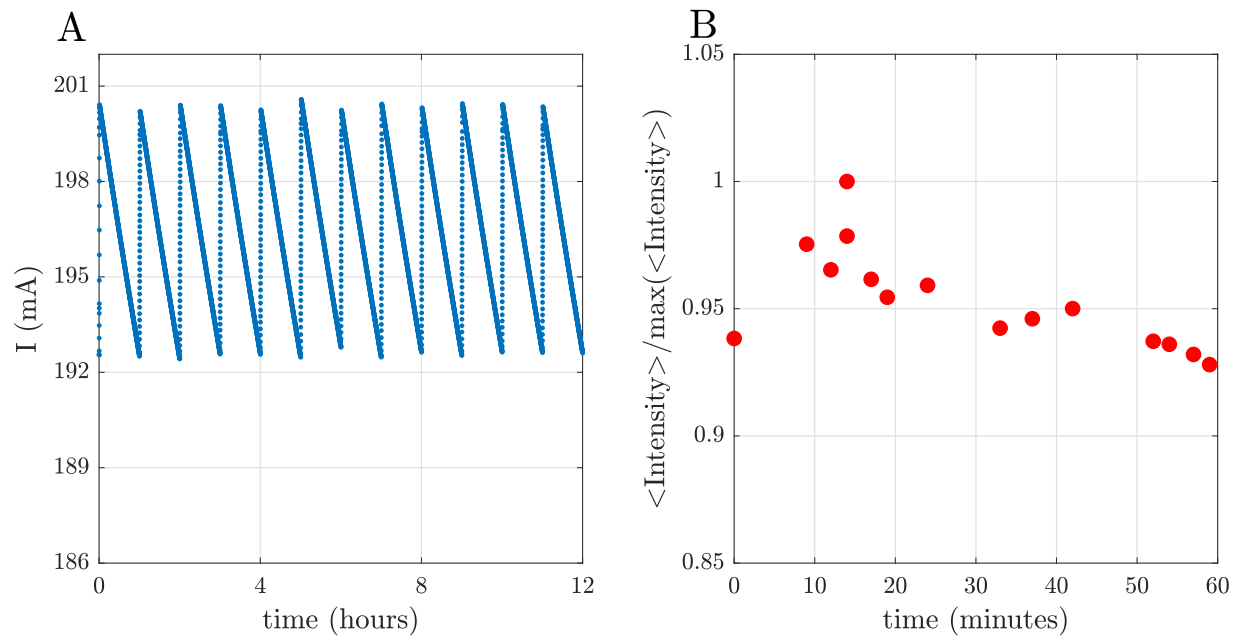


Figure 4.21: A) Current in the ring containing the rotating electrons as a function of time, during the first 12 hours of experimental measurements (the ring tension is kept constant). B) Average intensity of the backgrounds captured during the first 12 hours of data acquisition normalized by the maximum average intensity found during this period, as a function of the time passed after the beginning of the hour (approximate time after the filling of the ring) the data was acquired.

On top of that, the ring is only partially filled with electrons. Only  $7/8$  of the ring contains electrons, the last  $1/8$  being a vacuum. This means the X-ray production has a cutoff during a period  $\tau_{\text{cutoff}} = 1/8\tau_{\text{ring}}$ , where  $\tau_{\text{ring}}$  is the revolution period of the electrons in the ring, at a frequency  $f_{\text{cutoff}} = 1/\tau_{\text{ring}}$ . With an exposure time of  $\tau_{\text{exp}} = 2.5 \mu\text{s}$  for the camera, and  $\tau_{\text{ring}} = 2.81 \mu\text{s}$ , if the acquisition frequency is not synchronized with the passing of the electrons in the ring,

the integrated intensity of the X-ray beam captured by the imaging system fluctuates from one frame to another. This is the case with the presented measurements, and an attempt to account for the intensity fluctuations is presented in Sec. 4.4.3. One could choose  $\tau_{exp}$  as an integer multiple of  $\tau_{ring}$ , meaning the integrated energy captured by the imaging system would be the same for each frame. However, the exposure time was chosen to maximize contrast while tolerating a modest motion blur, only concerning the fastest small-scale liquid structures. Increasing  $\tau_{exp}$  to  $\tau_{ring}$  would result in additional motion blur on the images, preventing measurements of some of the fragmentation process. An alternative solution is to design a method to synchronize the acquisition frequency with the rotation of the electrons in the ring (which was not available).

### 4.3.2 Backgrounds

A background, also referred to as a flat field, is a radiograph captured with the imaging system when no object stands in front of the beam. Such measurement yields the spatial distribution of the incoming X-ray beam energy, noted  $I_0$ . Measurements of the EPL are conducted by considering the intensity ratio  $I_{img}/I_0$ , where  $I_{img}$  is the intensity distribution captured with the X-ray imaging setup with the atomization process occurring within the field of view. Each background is obtained by averaging the radiographs of a movie captured with the same imaging setup as that of the radiograph movies it is associated with. The background movies are shorter ( $\simeq 1000$  total frames) compared to the movies of the atomization process, which is sufficient to capture the spatial distribution of the X-ray beam and also reduces the saving time along with the storage needed. These images highlight the spatial inhomogeneity of the lighting system and can be used to correct this inhomogeneity on the radiographs of the atomization process. Figure 4.22A) shows an example background normalized by the highest intensity value of the background. There is up to 85% difference between the intensity in the corners and the intensity in the center of the radiograph.

Backgrounds were captured sporadically throughout the experimental session, with at least 2 backgrounds saved every hour. Figure 4.21B) shows the average intensity of the backgrounds captured during the first 12 hours of data acquisition, normalized by the maximum average intensity found during this period for a background, as a function of the time passed after the beginning of the hour the data was acquired (corresponding to the approximate time passed after a refill of the ring). This highlights that the intensity measured decreases between two refills, following the energy decrease inside the ring. Although the decrease of the intensity throughout one hour is clear, there is some spread around this decreasing trend. Figure 4.22B) shows the evolution of the average intensity of a background in time. A clear increase in background intensity is observed. This most likely originates from the heating up of the scintillator during the acquisition of the movie, changing the response of the scintillator. Note that the high-frequency variations of Fig. 4.22B) on top of the slow increase of the average intensity can be explained by the absence of synchronization of the beam production and of the movie acquisition explained in

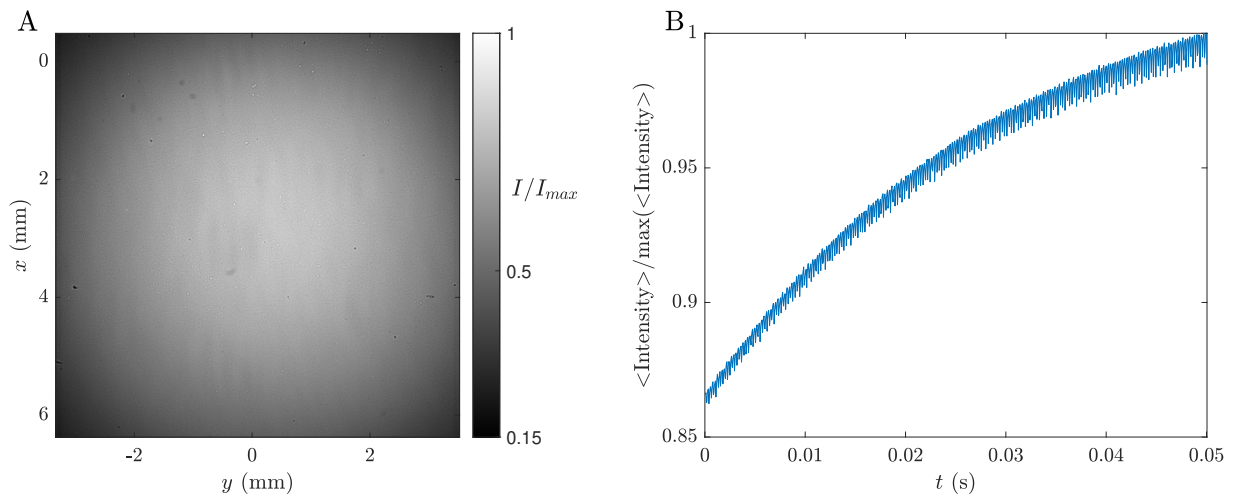


Figure 4.22: A) Example background radiograph, obtained by averaging 1000 radiographs with no objects in front of the beam. B) Average intensity of a background normalized by the maximum average intensity of the background as a function of time.

the previous section. Only 1000 frames are captured for each background but the X-ray shutter is always opened during 1.1 s for each acquisition, during which the scintillator heats up. The camera's buffer is set to record during 2 s, encompassing the time during which the shutter is opened. The operator then selects 1 s of the movie that will be saved, chosen to correspond to a period during which the shutter is opened. Small variations of the time passed between the opening of the shutter and the beginning of the saving are expected from one background to another (but also from one movie to another), and could explain the fluctuations observed in Fig. 4.21B). Note that the first point of Fig. 4.21B), captured close to  $t = 0$  min, is low and was certainly captured before the end of the refill of the ring. Backgrounds captured too close from the refill of the ring are therefore discarded.

In the latter, the closest background in time (in between two refills of the ring) is used. To best take into account the slow drift of energy in the ring, a background should be taken for each movie. Also, to have the same heating of the scintillator from one movie to another, the recording of the movie should ideally be electronically synchronized with the beam shutter.

## 4.4 Measuring the equivalent path length

As illustrated in Sec. 4.1, the characteristic feature of X-ray imaging is the integrated 3D information that it contains. In this section, I will show the method I developed to perform quantitative measurements of the equivalent path length (EPL) using radiographs.

The initial processing of the radiographs will be presented in Sec. 4.4.1, then calibration of the measurement is conducted in Sec. 4.4.2, followed by quantification of the error associated with this measurement method. Preliminary results based on this approach are shown in Sec. 4.5.

### 4.4.1 ANKPhase

ANKPhase is a computer program designed to process phase contrast images of X-ray radiographs to reconstruct the thickness of the imaged objects. It is an algorithm that was originally designed for the tomographic reconstruction of a sample. When a monochromatic X-ray wave  $\Psi(z)$  goes through a medium of thickness  $t$  with a complex refractive index  $n = 1 - \delta + i\alpha$ , it is described by  $\Psi(z) = E_0 e^{inkz}$ , where  $k$  is the wavenumber of the X-ray and  $E_0$  its initial amplitude. The propagation of the X-ray wave leads to an exponential decay of the amplitude by a factor  $\int_0^t e^{-k\alpha(z)} dz$ , related to the complex part of the refractive index of the medium, and a phase shift  $\Delta\phi = k \int_0^t \alpha(z) dz$ . If the medium has a homogeneous composition and density, the phase shift is simplified to  $\Delta\phi = kt\alpha$ . Note that the refractive index is wavelength dependent, making the computation of the phase shift more difficult for a polychromatic beam. Using the raw radiograph image and the associated background, ANKPhase computes the phase-shift maps at each position of the radiograph and outputs an image of  $\Delta\phi(x, y)$  referred to as a phase map. In the following, the phase shift will be noted  $\phi$  and referred to as the phase for simplicity. The code is written in Java and an ImageJ opensource plugin has been implemented to facilitate its use. A complete description of the algorithm and of the theory it relies on can be found in [103]. Contrary to tomographic reconstruction, the sample studied here is dynamic and therefore one cannot capture hundreds of images at different angles for each state of the atomization process. The approach developed in this section is based on the use of the features of this algorithm to obtain a reconstructed phase map and measure the projected thickness of the liquid on a 2D map for each of the frames of the radiograph movie.

The hypothesis done for the calculation of the phase image by ANKPhase is

- The object consists of a single homogeneous material;
- The X-ray beam used is monochromatic;

- The distance  $L$  in between the object and the detector fulfills the near-field condition of Eq. 4.1, where  $d$  is the size of the smallest imaged object and  $\lambda$  is the wavelength of the X-ray beam.

$$L \ll d^2/\lambda \quad (4.1)$$

In the case of the present study, purified water was used and the first hypothesis is fulfilled. As discussed in Sec. 2.3.2.3, the incoming X-ray beam is not purely monochromatic. Figure 2.19 shows the spectrum of the beam in the center line of the imaging window. More than 90% of the photons of the beam have their energy in the first peak, which corresponds to over 85% of the total energy of the X-ray beam. The second hypothesis is not respected which leads to biases when using the program. Nonetheless, most of the incoming beam energy is comprised in the first peak, therefore as a first approach, I will not account for the full complexity of the physics of the interaction of the X-ray beam with matter. In the following, the energy of the photons is assumed to be  $e_{\text{photon}} = 18.2$  keV, corresponding to a wavelength  $\lambda_{\text{photon}} = 6.8 \times 10^{-5}$  nm. The last hypothesis constitutes a limitation to the resolution of the imaging technique. Equation 4.1 can be rewritten as Eq. 4.2, which leads in our case to  $d \gg 5.22 \times 10^{-1} \mu\text{m}$ . This is ten times smaller than the effective pixel size of the imaging system, which is  $d_{\text{pixel size}} = 6.7 \mu\text{m}$ . The third hypothesis is therefore respected. In addition, [103] noted that respecting two out of three hypotheses is sufficient to yield accurate results.

$$\sqrt{L\lambda} \ll d \quad (4.2)$$

To process the images, ANKAphase requires the input of the distance between the object and the detector  $L$ , the energy of the photons  $e_{\text{photon}}$ , the size of each pixel  $d_{\text{pixel size}} = 6.7 \mu\text{m}$  and the real and imaginary parts of the estimated complex-valued X-ray index of refraction. The values for the index of refraction of water were taken from an online database<sup>2</sup>. Figure 4.23 shows the user interface of the ANKAphase program. Figure 4.24 shows the 2-step process conducted by ANKAphase. An initial division of the radiograph by its associated background is conducted, referred to as a flat-field correction or background normalization. Figure 4.24A) shows the raw radiograph and 4.24B) shows the flat-field corrected image. Then the phase map is computed, shown on 4.24C). The colorbars of Fig. 4.24A), B), and C) were adapted to enhance visibility.

It is important to point out that the aluminum nozzle is visible in the images. This means the first hypothesis, stating the object consists of a single homogeneous material, is not fulfilled. Adding aluminum in the field of view would lead to local variations of the phase map calculation, leading to an increase of the phase close to the injector, see Fig. 4.24, which is expected to limit the field on which measurements can be conducted. This will receive attention during the calibration process conducted in the following section.

<sup>2</sup>[https://henke.lbl.gov/optical\\_constants/getdb2.html](https://henke.lbl.gov/optical_constants/getdb2.html)



**general settings**

projection images directory:

dark-field images directory:

flat-field 1 images directory:

flat-field 2 images directory:

---

**flat-field settings**

save flat corrected images

save directory:   save name:  format:

scaling option:  from:  to:   interpolate flat-field samples

---

**phase-retrieval settings**

save phase-retrieval images  apply image restoration Gauss width:  \*pixel size stabiliser:

phase-retrieval parameters: beta:  \*10<sup>-9</sup> delta:  \*10<sup>-6</sup>  use delta/beta ratio:

experiment parameters: distance:  mm energy:  keV pixel size:  microns

save directory:   save name:  format:


scaling option:  from:  to:   no automatic edge extension

---

calculate images from:  to:   show images CPUs:

count starting at:

status...



T. Weitkamp, D. Haas, D. Wegrzynek, A. Rack, Journal of Synchrotron Radiation 18 (4), 617-629 (2011)

Figure 4.23: Image of the user interface of ANKPhase.

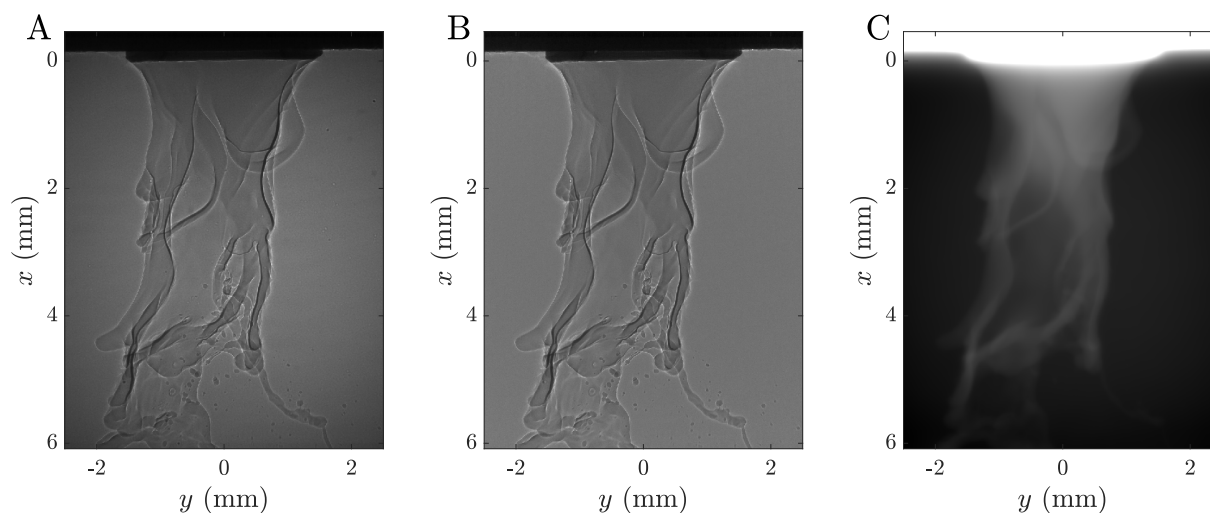


Figure 4.24: Three different stages of the process of radiographs of the atomization process with ANKPhase. A) raw image, B) raw image normalized by a background, and C) Phase map obtained with ANKPhase. The colorbars were adapted to enhance visibility.

### 4.4.2 Calibration

To convert the phase maps retrieved using ANKAphase into EPL maps, images of a laminar round liquid jet are used as a calibration. The liquid jet is assumed to be cylindrical, see Fig. 4.25, with a cross-section that slowly decreases with  $x$  as the liquid jet is accelerated by gravity. The thickness of liquid that the X-ray passes through  $h$ , follows equation 4.3.

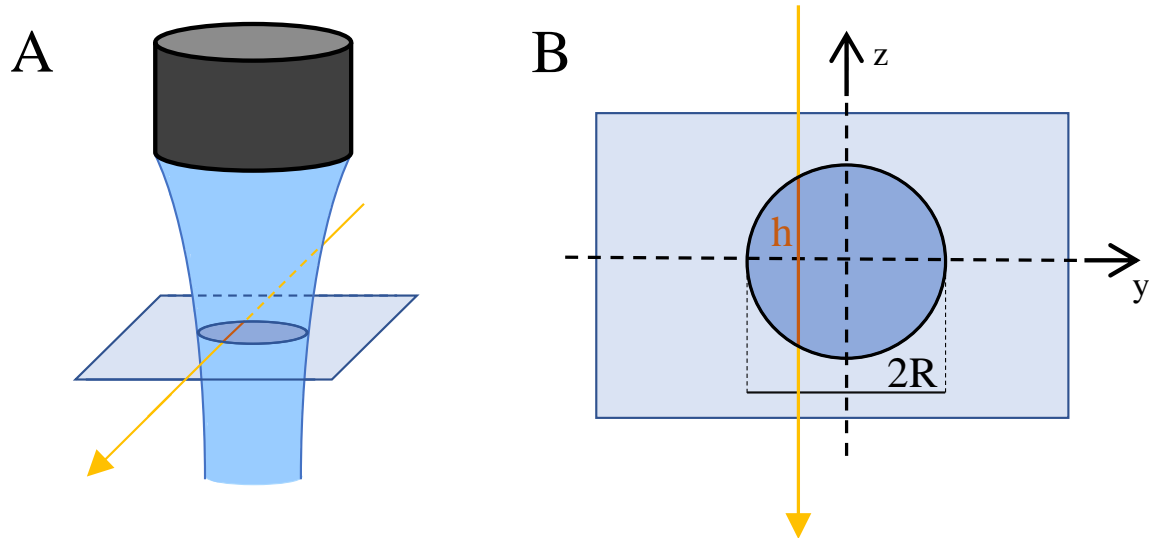


Figure 4.25: A) Sketch of an X-ray beam going through a laminar liquid jet. B)  $(y; z)$  plane, containing the X-ray beam shown in A). The liquid thickness, or EPL, the X-ray beam that goes through  $h$  is highlighted in red.

$$h(y) = 2R\sqrt{1 - \left(\frac{y}{R}\right)^2} \quad (4.3)$$

For a monochromatic beam, the phase map obtained via ANKAphase is proportional to the liquid thickness and should therefore follow Eq. 4.4, where  $\beta$  and  $\alpha$  are the offset and proportionality coefficient respectively.

$$\phi(y) = \alpha h(y) + \beta = 2R\alpha\sqrt{1 - \left(\frac{y}{R}\right)^2} + \beta \quad (4.4)$$

In order to determine  $\alpha$  and  $\beta$ , the phase is fitted according to Eq. 4.4. The offset  $\beta$ , the proportionality coefficient  $\alpha$ , and the radius of the liquid jet  $R$  are used as fitting parameters. Figure 4.26 describes the fitting process. Figure 4.26A) shows an example normalized image for a laminar liquid jet, Fig. 4.26B) shows the associated phase retrieved image of the liquid jet

obtained with ANKPhase and Fig. 4.26C) shows  $\phi(y)$  for one specific height, indicated in red on Fig. 4.26B), with the associated fit.

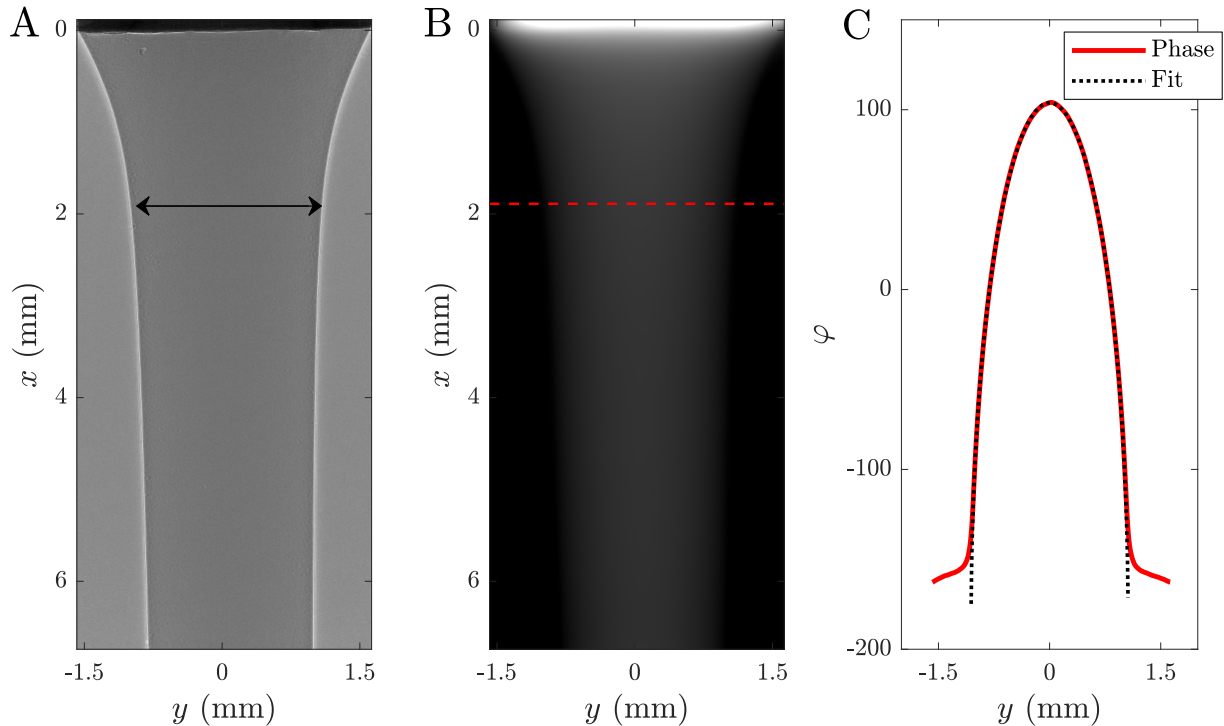


Figure 4.26: A) Radiograph of the liquid jet, normalized by a background. B) Corresponding phase retrieved image of the liquid jet, obtained with ANKPhase. C) The red curve corresponds to the line of the phase retrieved image shown in dashed-line in B), and the black dotted line corresponds to the associated fit, with  $r^2 = 0.9999$ . The radius of the liquid jet measured on the normalized image (shown with black arrows in A)) is  $R_{mes} = 1.045$  mm and the radius obtained with the fit of the phase retrieved image at the corresponding height is  $R_{fit} = 1.06$  mm

To quantify the quality of the fit for the example illustrated in Fig. 4.26, the radius of the liquid jet  $R_{mes}$  is measured on the normalized image of the liquid jet (indicated with the black arrow on Fig. 4.26A)) and is compared to the fitted radius  $R_{fit}$ . For this example  $R_{mes} = 1.045$  mm and  $R_{fit} = 1.06$  mm, corresponding to a relative error of 1.5%. The coefficient of determination of the fit is  $r^2 = 0.9999$ . This shows that the fit is in very good agreement with the data.

Fits of this type are performed for each line of pixel of the phase retrieved image of the laminar liquid jet. The radius measured on the normalized image  $R_{mes}$  and the fitted radius  $R_{fit}$  obtained when fitting at each height are shown in Fig. 4.27A). Figure 4.27B) shows the associated  $r^2$  obtained for each height. Note that  $r^2$  is always higher than 0.998. Both of these figures illustrate that each individual fit is in good agreement with the data. Note that for low values of  $x$ , corresponding to heights close to the aluminum nozzle,  $R_{fit}$  deviates from  $R_{mes}$  and  $r^2$  shrinks. This deviation close to the liquid nozzle most likely comes from the glare of the

aluminum nozzle previously mentioned.

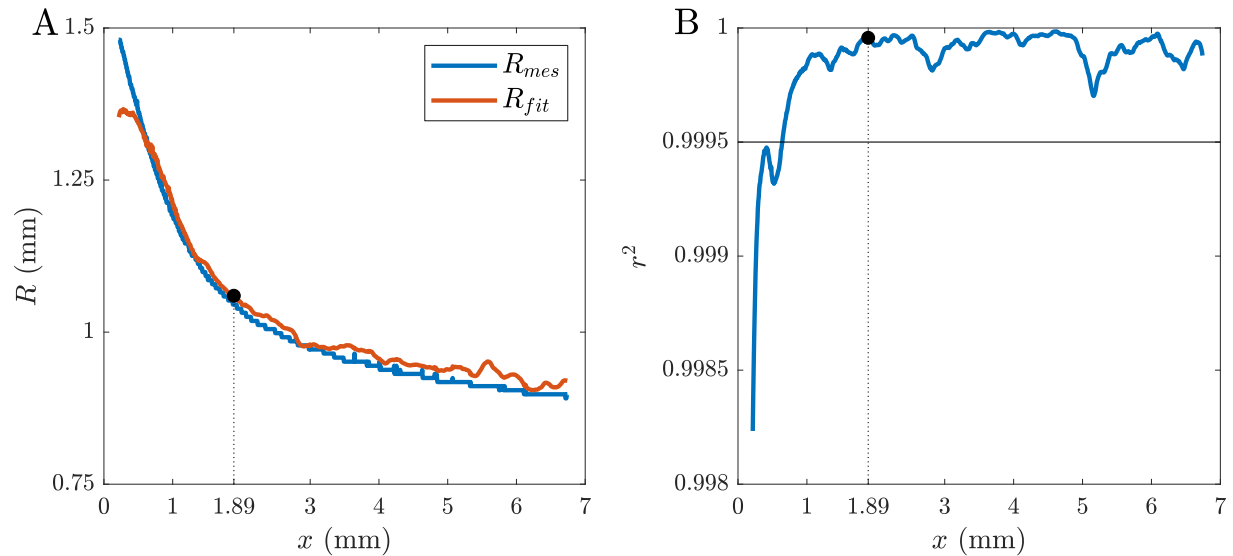


Figure 4.27: A) Radius measured using the normalized image  $R_{mes}$  (see Fig. 4.26A)) and fitted radius  $R_{fit}$  as a function of  $x$ . B)  $r^2$  of the fit done for each pixel line. The black dot highlights the pixel line illustrated in Fig. 4.26.

The method to measure  $\alpha$  and  $\beta$  appears to work correctly for each value of  $x$  on the previously presented example phase map, although this corresponds to a single image. As explained in Sec. 4.3, variations in time are expected. Therefore the time stability of this method is tested in the following section.

### 4.4.3 Time stability

In the previous section, the method to obtain  $\alpha$  and  $\beta$  was validated on one image. Using this method, the correction coefficients  $\alpha$  and  $\beta$  can be determined for multiple locations and at multiple time stamps. Fitting the phase retrieved images of a slice of liquid at a constant height for an entire movie of a laminar liquid jet, as illustrated in Fig. 4.28A), the associated values of  $\alpha$  and  $\beta$  are obtained. The time evolution of  $\alpha$  and  $\beta$  are shown in Fig. 4.28B) and C).

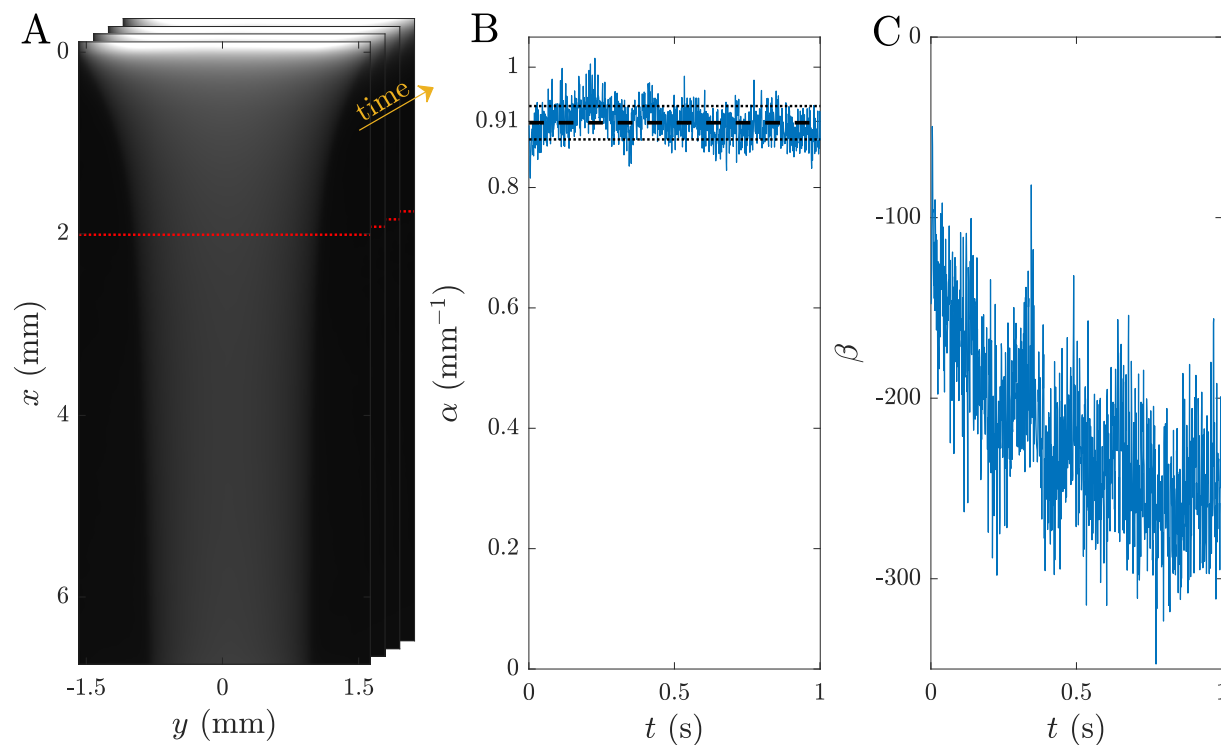


Figure 4.28: A) Representation of a movie, highlighting the pixel line at which  $\alpha$  and  $\beta$  are determined in this example. B) Fitted value of  $\alpha$  as a function of time, obtained for the pixel line highlighted in A). The dashed-line corresponds to  $\langle \alpha \rangle$  and the dotted-lines to  $\langle \alpha \rangle \pm \text{std}(\alpha)$ , with  $\langle \alpha \rangle = 0.91$  and  $\text{std}(\alpha) = 0.028$  being the average and the standard deviation of  $\alpha$  for the presented time series. C) Fitted value of  $\beta$  as a function of time, obtained for the pixel line highlighted in A).

The time-series of  $\alpha$  presented in Fig. 4.28B) shows that for a given height,  $\alpha$  is fairly constant in time. The average value  $\langle \alpha \rangle$  calculated for this time series is  $\langle \alpha \rangle = 0.91$  and the associated standard deviation is  $\text{std}(\alpha) = 0.028$ . The standard deviation is around 3% of the average value. With these modest variations of  $\alpha$  in time,  $\langle \alpha \rangle$  appears to be a reasonable evaluation of the proportionality coefficient between the phase and the thickness, at least for this line of pixels. On the other hand, the time series of  $\beta$  shown in Fig. 4.28C) reveals that  $\beta$  varies from  $-50$  to  $-350$ . Two types of variations of  $\beta$  are observed: a slow decrease on top of which

high-frequency fluctuations are present. These high-frequency fluctuations, from one frame to the next, can be explained by the fluctuations in the X-ray beam production described in Sec. 4.3. The slow decrease of  $\beta$  could be explained by the heating of the scintillator throughout the movie.  $\beta$  acting as an offset for the phase, a natural metric to look at when trying to explain the variations observed in the time series of  $\beta$  is the value of  $\varphi$  on the edges of the phase-retrieved image, where no liquid is found, acting as the background phase, see Fig. 4.26. To avoid fluctuations in the phase's background, the minimum value of the phase is used as an evaluation of the base level of the phase's background.

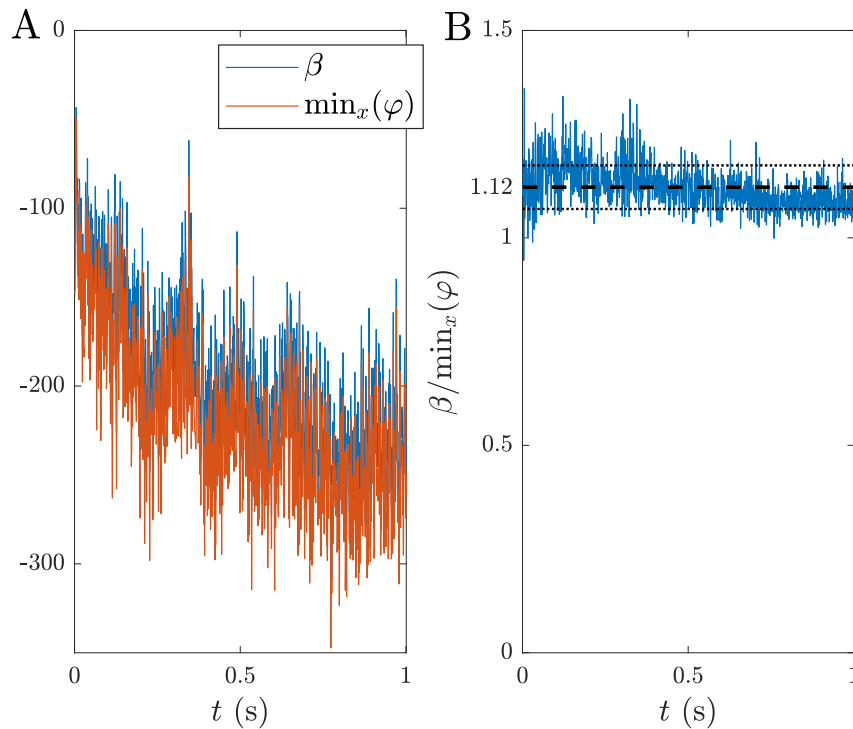


Figure 4.29: A) The blue curve represents the time series of  $\beta$  obtained by fitting the phase retrieved image at a fixed height  $x$ , as shown in Fig. 4.28A), and the red curve corresponds to the minimum of the phase of the pixel line ( $\min_x(\varphi)$ ) used to obtain  $\beta$  (red dotted line of Fig. 4.28A)) as a function of time (for each time step,  $\min_x(\varphi)$  stands as the minimum value of  $\varphi$  on the pixel line found at a given  $x$  location, meaning that  $\min_x(\varphi)$  is only a function of  $x$  and  $t$ ). B)  $\beta/\min_x(\varphi)$  as a function of time.

Figure 4.29A) shows a time series of  $\beta$  at one given downstream distance with the associated minimum value of the phase  $\min_x(\varphi)$ , used as a proxy for the phase background. Figure 4.29B) represents  $\beta$  normalized by  $\min_x(\varphi)$  as a function of time, the fluctuations of  $\beta$  in time seem to follow the fluctuations of the phase background. The average of  $\beta/\min_x(\varphi)$  along with the average  $\pm$  the standard variation of the ratio is shown in dashed lines and dotted lines respectively. The ratio  $\beta/\min_x(\varphi)$  has only small fluctuations around its mean value, the variations of  $\beta$  high-

lighted in Fig. 4.28C) can therefore be accounted for using the background phase, and  $\beta$  can be evaluated using the base level of the phase. Note that the background phase value, approximated by the minimum of the phase, is evaluated at the height at which the fit is performed. This way any spatial variations of the phase, due to spatial inhomogeneities of the X-ray beam or of the scintillator response, are also accounted for seamlessly.

#### 4.4.4 Spatial variations

In the previous section, the stability of the normalizing factors through time has been discussed for an individual location and one movie only. Using times series of  $\alpha$  and  $\beta$  every 50 pixel lines,  $\langle \alpha \rangle$ ,  $\text{std}(\alpha)$ ,  $\langle \beta / \min_x(\varphi) \rangle$  and  $\text{std}(\beta / \min_x(\varphi))$  are determined at 49 positions, for 4 different calibration movies (i.e. 4 independent movies of a laminar liquid jet at a different liquid flow rate  $Q_l$ , all in laminar conditions, with  $700 < Re_l < 2300$ ), see Fig. 4.30.  $\langle \rangle$  here describes a time average on the length of the entire movie.

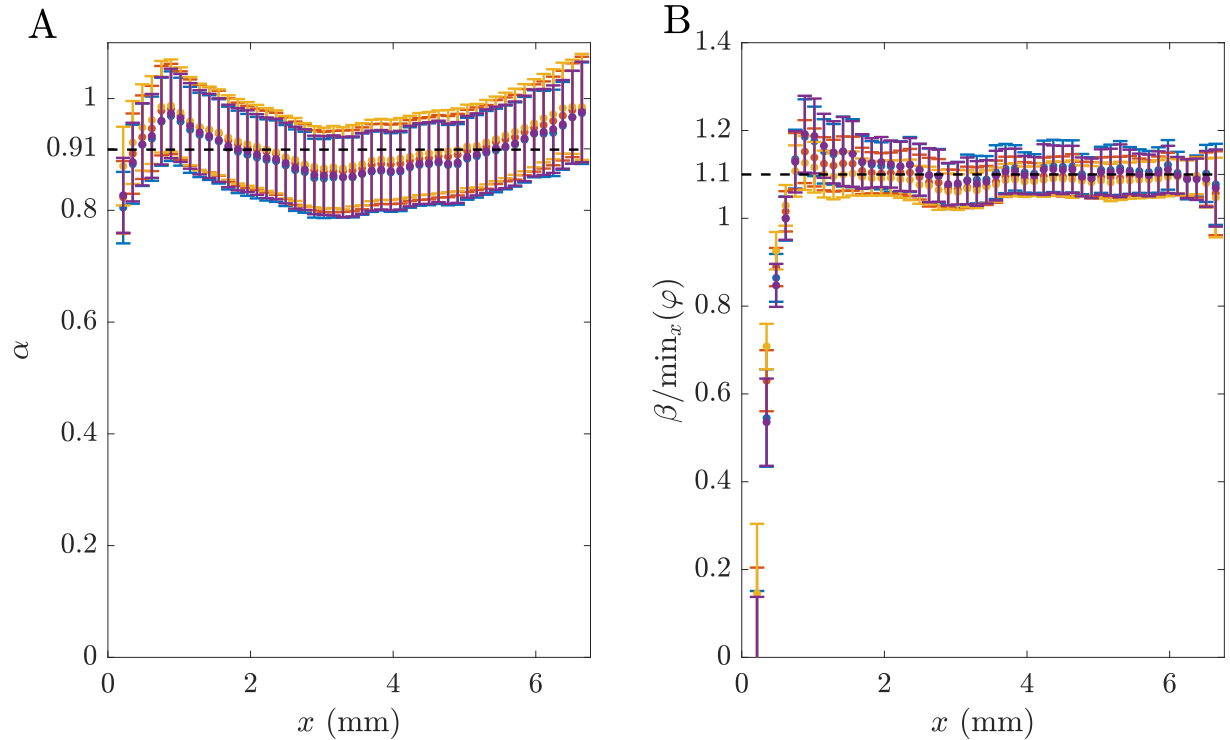


Figure 4.30: Time average of  $\alpha$  A) and  $\beta / \min_x(\varphi)$  B) as a function of the longitudinal distance  $x$ , for 4 independent movies of a laminar liquid jet. Each color corresponds to a different movie, with different liquid injection rates. The error bars correspond to the standard deviation of the time series of  $\alpha$ , respectively  $\beta / \min_x(\varphi)$  used to compute the average (see Fig. 4.28B and 4.29B).



The values of  $\langle \alpha \rangle$ , along with the associated standard deviation, obtained for the 4 movies (shown in 4 different colors in Fig. 4.30A)) are consistent at each location.  $\langle \alpha \rangle$  has a 20% fluctuation level (approximately equal to the fluctuations in time at a given  $x$  location) around the spatial average value of  $\langle \alpha \rangle$ , shown in dashed-line in Fig. 4.30A). These fluctuations may be caused by spatial variations of the response of the scintillator, along with inhomogeneities in the X-ray beam. Nonetheless, the spatial average value of  $\langle \alpha \rangle$  appears to be a reasonable evaluation of  $\alpha$  at each location and for each movie. In the following,  $\alpha = 0.91$  will be used to convert the phase maps into EPL maps.

For low values of  $x$ ,  $\langle \beta / \min_x(\varphi) \rangle$  varies from one calibration movie to another. This bias most likely comes from the proximity to the aluminum nozzle, which generates a glare on the phase images. For higher values of  $x$ ,  $\beta$  is constant in space and across conditions, when normalized instantaneously and locally by  $\min_x(\varphi)$ . Just like  $\alpha$ , the phase offset that will be used for the conversion of the phase maps into EPL maps is  $\beta = 1.1 \min_x(\varphi)$ .

An estimation of the error associated with this method for the determination of the EPL, along with an evaluation of how close to the nozzle this calibration stays applicable, is discussed in the following section.

#### 4.4.5 Error evaluation

To evaluate the error associated with the measurement technique, we compare the diameter  $D_{mes}$  of the liquid jet retrieved on the normalized radiographs (illustrated in Fig. 4.26A) to the EPL value measured at the center of the liquid jet, following Eq. 4.5.

$$\text{EPL} = (\varphi - 1.1\beta) / \alpha \quad (4.5)$$

Assuming each slice of liquid is a circle in the  $(y; z)$  plan, the EPL measured at the center of the laminar liquid jet and  $D_{mes}$  are expected to be the same length. Figure 4.31 shows the relative error  $Err = (D_{mes} - \text{EPL}) / D_{mes}$  obtained when measuring  $D_{mes}$  and the EPL at each  $x$  and for each frame of the four calibration movies. The relative error is below 20% for most of the locations, with a rise of the error close to the nozzle. The error close to the nozzle presumably comes from the interference of the aluminum nozzle during the phase map calculation done by ANKPhase. The black curve of Fig. 4.31 corresponds to the average relative error obtained at each height. It is below 20% for  $x > x_{lim} = 0.36$  mm. This will be considered as the minimum working distance from the nozzle to measure the EPL.

Considering each slice of liquid is a circle in the  $(y; z)$  plan, the liquid thickness varies from 0 to  $2R$  continuously in between the side of the liquid jet and its center. A second approach to evaluate the error of the EPL consists of comparing the theoretical thickness of the liquid jet, given

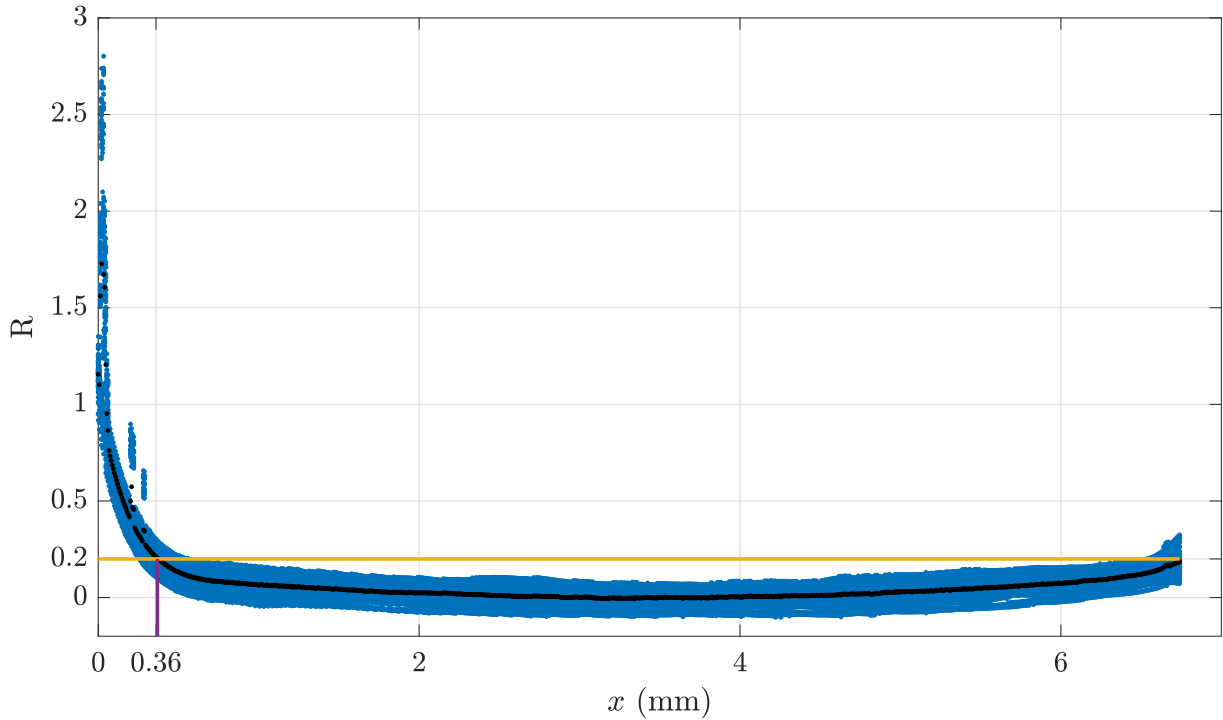


Figure 4.31: Relative error  $Err$  between the measurement of the diameter of the liquid jet via determination of the EPL and the expected diameter  $D_{mes}$ , as a function of  $x$ .

by Eq. 4.3, to the EPL retrieved from the phase of the associated slice of liquid. This method has the advantage to test a wider range of liquid thicknesses and is therefore complementary to the previous one presented. For 8 values of  $x$ , from  $x = 0.36$  mm to  $x = 7$  mm, the liquid EPL is measured on all the images of the 4 calibration movies, and compared to the theoretical thickness of the liquid jet, obtained from the measurement  $D_{mes}$  of the diameter of the liquid jet on the normalized image. Figure 4.32A) displays the 2D probability density function of the EPL as a function of the theoretical thickness, where each column is populated by the measurements of a given thickness, i.e. a given point in space (technically a given point in the parameter space defined by Eq. 4.3 sampled at various downstream locations  $x$ ), across time. The red curve of Fig. 4.32B) corresponds to the maximum probability for each theoretical thickness (i.e. for each column). The measured EPL is close to the expected value of the liquid thickness on a wide range of liquid thicknesses (with a relative error lower than 20% for  $x > 0.73$  mm, and lower than 10% for  $x > 0.96$  mm) and starts to undervalue measurements for lower liquid thickness. Note that this assessment of the quality of the EPL measurement may be biased (toward larger errors) due to the lack of representation of small thickness in the comparison data set. Due to interferences caused by X-ray diffraction near curved interfaces (white edges around the liquid jet on the raw radiographs), some regions of the flow are not as well resolved. In spray formation measurements, these locations strongly fluctuate across time and space, and may not necessarily prevent measurements of smaller liquid thicknesses. However, in the current test, these regions

only concern the edge of the liquid columns, which stand as the only locations that present small thicknesses. Since this study has a strong focus on the liquid core, it does not present a strong issue, but it is a caveat worth resolving if one wants to study the small-scale structures of spray formation or the primary breakup populations.

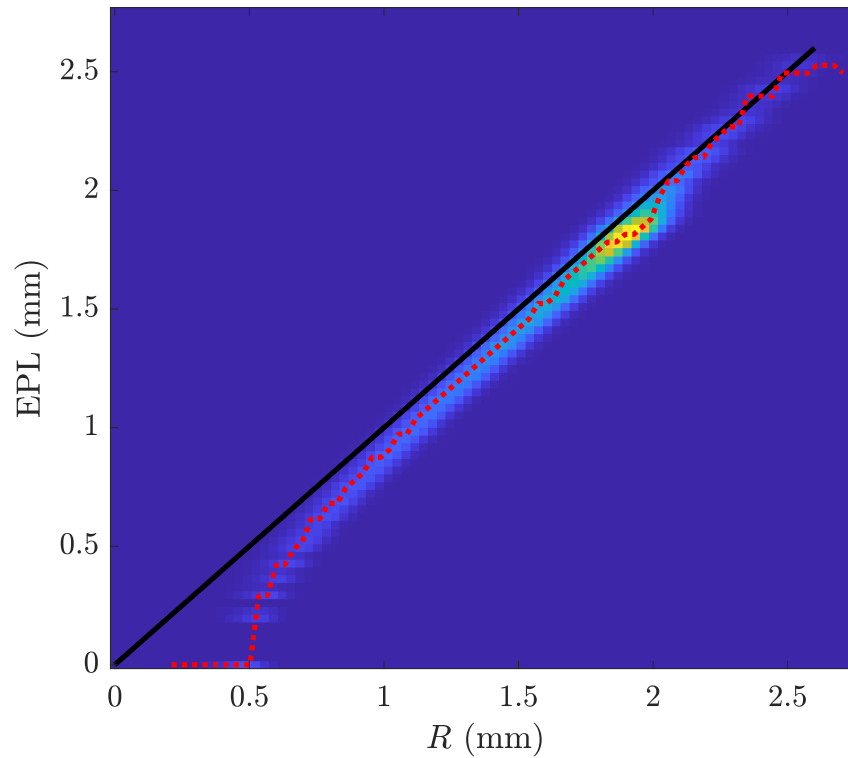


Figure 4.32: Probability density function of the EPL as a function of the local thicknesses (estimated from direct measurements and geometrical considerations). The maximum probability for each column is displayed in red.

## 4.5 Quantitative measurements of the equivalent path length

In the previous section, we introduced a method to measure the spatial distribution of the liquid in the near field of the atomizer. In this section, the EPL measurement technique previously introduced is implemented on a subset of conditions to extract quantitative results of the large-scale motions of the liquid core.

### 4.5.1 Quantitative indicator for dewetting of the nozzle

For the five injection conditions indicated in Fig. 4.8, showing the four different morphological states of the liquid core introduced in Sec. 4.2, we evaluate the center of mass of the liquid jet by measuring the equivalent path length (EPL) at  $x = d_l/2$  throughout the movie. Note that, having access to the projection of the liquid distribution (the EPL), we measure the coordinate of the center of mass projected on the  $y$ -axis, noted  $Y_M$ . In this method, we consider all the liquid measured at  $x = d_l/2$ , regardless of whether it is part of the liquid core or part of a detached liquid structure. Being close to the injector, we make the hypothesis that the vast majority of the liquid measured at  $x = d_l/2$  is part of the liquid core and that the center of mass of the entire liquid is close to that of the center of mass of the liquid core itself. This hypothesis means that  $Y_M(t)$  corresponds to the time series of the motion of the liquid core along the  $y$  axis.

The probability density functions (PDF) of the center of mass of the liquid core normalized by the liquid diameter  $d_l$ , are shown on Fig. 4.33A) to F). Fig. 4.33A to E show the PDF of the normalized center of mass for a constant liquid injection velocity with increasing injection gas velocity. In the case of situations A, B, and C, respectively corresponding to the intact core, the transitional, and the crown regime, the probability density function of the normalized center of mass of the liquid jet consists of one centered peak. However, in situations D and E, both corresponding to the unstable crown regime, the probability density function of the normalized center of mass of the liquid jet is lowered in the center and has two peaks, one on each side.

In the intact core, the transitional and the crown regimes, observations of the liquid jet (see Figs. 4.9, 4.10 and 4.11) revealed that the liquid jet is centered. For these regimes, the center of mass is expected to be centered around  $Y_M = 0$ , which is observed in Fig. 4.33A, B, and C. Moderate fluctuations around  $Y_M = 0$  are expected due to the passing of interfacial perturbations of the liquid jet or to the flapping motion of the liquid jet, which are at the origin of the width of the peak of the PDF of  $Y_M/d_l$ . The widest width is observed here for case B ( $Reg = 52000$ ) which is thought to be the case of strongest flapping motions close to the nozzle exit (with a liquid core short enough to observe meandering for  $x < d_l$  and long enough to allow for the flapping motion to pick up enough amplitude).

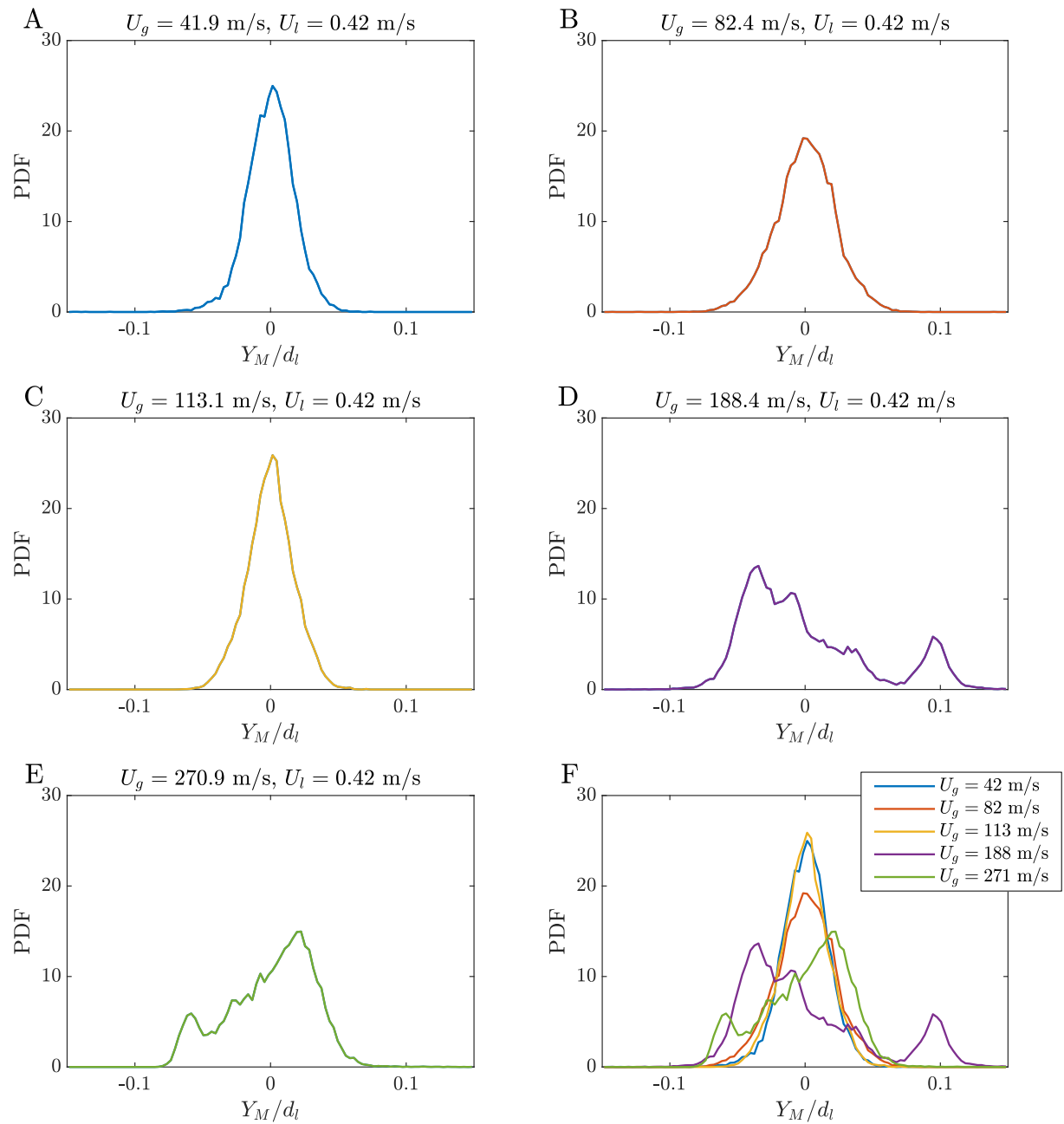


Figure 4.33: A) to E): Probability density function of the normalized center of mass  $Y_M/d_l$  calculated from the equivalent path length measurements of the liquid jet at  $x = d_l/2$ , for increasing values of the injection gas velocity (corresponding to  $We_g = 47, 180, 340, 945, 1950$ ), at constant liquid injection velocity ( $Re_l = 780$ ). F): Superposition of the probability density functions presented in A) to E).

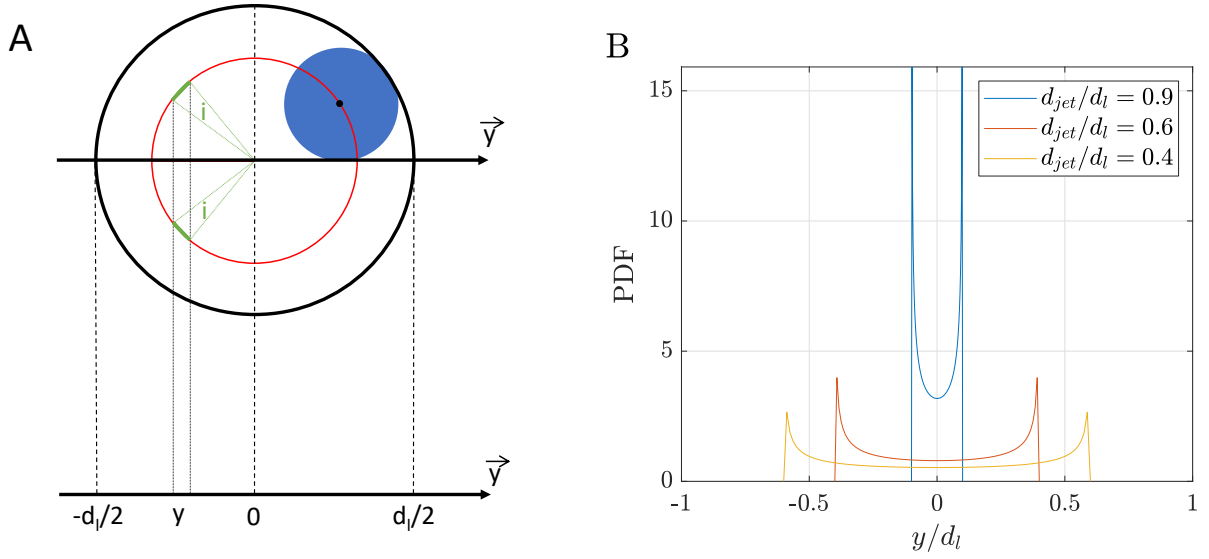


Figure 4.34: A) Schematic representation of the liquid jet morphology in the unstable crown regime used to explain the shape of the PDF observed in Fig. 4.33D) and E). B) Probability density function of the center of mass projected on the  $y$ -axis obtained with the model sketched in A), corresponding to Eq. 4.7

In the unstable crown regime, the two peaks observed can be explained by considering a simple model for the liquid jet's position. In this regime, only a portion of the liquid jet is wetting the liquid nozzle. We approximate the morphology of the liquid core with the simple situation sketched in Fig. 4.34, where the liquid jet (blue disc) is a round liquid jet of diameter  $d_{jet} < d_l$ . The liquid jet's center freely moves along the red circle (of radius  $r_C = (d_l - d_{jet})/2$ ), such that the round liquid jet is always touching (wetting) one side of the liquid nozzle, sketched in black. In this situation, where the liquid jet's center homogeneously explores the red circle, the probability  $P(y')dy'$  for the center of mass to be between  $y'$  and  $y' + dy'$  (with  $y' = y/r_C$ ) corresponds to the ratio of the length of the circular arc corresponding to  $y \in [y', y' + dy']$ ,  $2ir_C$  (shown in green in Fig. 4.34), to the perimeter of the red circle  $2\pi r_C$ , as expressed in Eq. 4.6.

$$P(y')dy' = \frac{2i}{2\pi} = \frac{\arccos(y') - \arccos(y' + dy')}{\pi} = \frac{d(\arccos(y'))dy'}{\pi} = \frac{dy'}{\pi\sqrt{1-y'^2}} \quad (4.6)$$

The probability for the center of mass to be between  $y$  and  $y + dy$  can then be found using a simple change of variable  $y' = y/r_C$ , as expressed in Eq. 4.7 (for  $|y| < r_C$ ).

$$P(y)dy = \frac{dy}{\pi\sqrt{1-(y/r_c)^2}} \quad (4.7)$$

The shape of the probability density function obtained with this simplistic model is shown in Fig. 4.34 B) for different values of the ratio  $d_{jet}/d_l$ . The distribution is lower in the center with two peaks on the sides. This shape is qualitatively similar to the shape of the PDF found for the center of mass of the liquid jet in the unstable crown regime shown in Fig. 4.33D) and E). Although the model previously presented could be refined by considering a crescent shape for the liquid jet to best match the observations of Sec. 4.2, this naive approach is enough to explain the two peaks observed on the PDF of  $Y_M$ , which seem to originate from the dewetting of a portion of the nozzle. This stands as an indicator of the change of regime between the unstable crown and the other regimes.



### 4.5.2 Temporal dynamics and influence of swirl

As previously highlighted, the center of mass contains a signature of the dewetting of the liquid nozzle by the liquid jet in the unstable crown regime. In this section, we will focus on the injection condition of Fig. 4.33D ( $U_l = 0.41$  m/s,  $U_g = 188$  m/s,  $Re_l = 780$  and  $We_g = 945$ ) corresponding to the unstable crown regime (note that a time-series radiograph of this movie is shown in Fig. 4.12). Using the center of mass to characterize when the liquid jet is dewetting the nozzle, one can evaluate the residence time at a given location of the gas recirculation, pushing the liquid jet away from the injector (see Sec. 4.2.2). Machicoane et al. [3] were able to observe the unstable crown regime by adding swirl in the gas jet. Although we showed that swirl was not required to trigger the transition to the unstable crown, we try to characterize its effect on the dynamics of the liquid core in the unstable crown regime. Figure 4.35A) and B) show the time series of the normalized center of mass of the liquid core without A) and with B) swirl, in the case of the breakup of the liquid jet being in the unstable crown regime. Note that only the swirl ratio varies between both of these cases (from  $SR = 0$  to  $SR = 0.8$ ), the liquid and gas total flow rates are the same in both conditions.

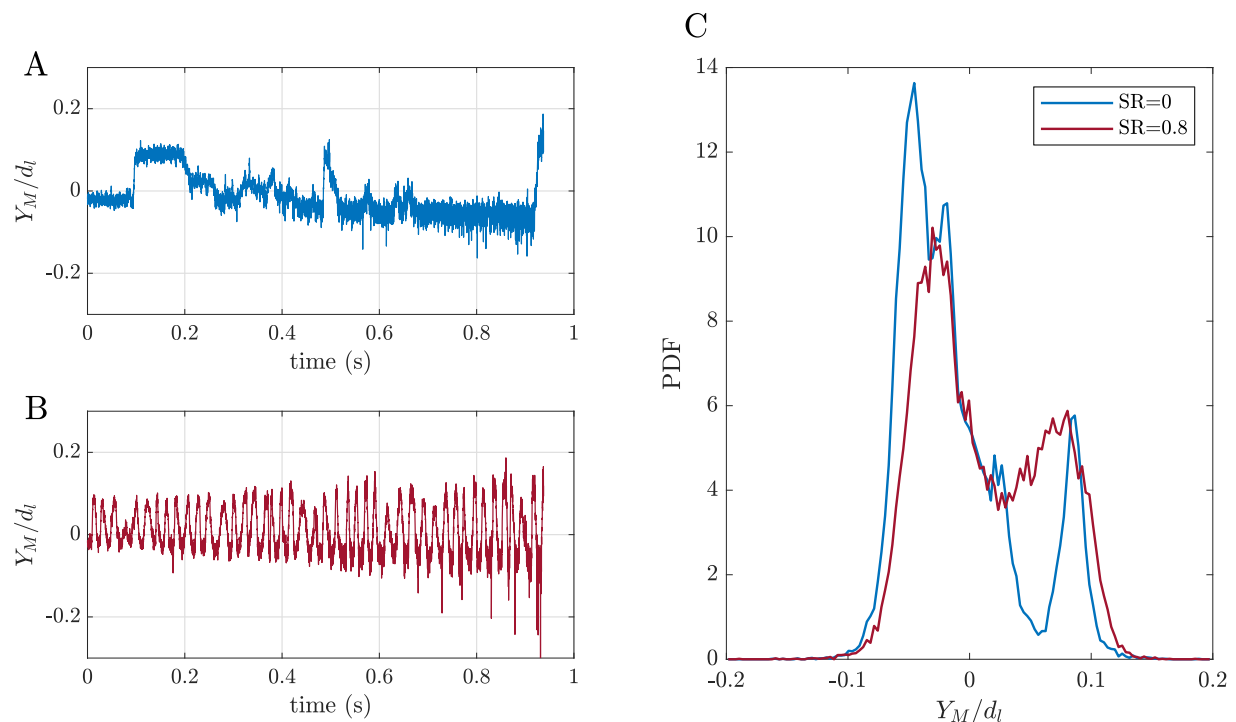


Figure 4.35: Time-series of the center of mass of the liquid jet in the unstable crown regime without A) and with B) swirl in the gas co-flow, for  $U_l = 0.41$  m/s,  $U_g = 188$  m/s,  $Re_l = 780$  and  $We_g = 945$  (corresponding to the unstable crown regime). C) Probability density function of the center of mass of the liquid core of A) and B).

When no swirl is added (case of Fig. 4.35A)), the change of position of the center of mass from one side to another occurs on a wide range of timescales, and the liquid core can remain in a given position during a long period of time. Adding swirl in the gas co-flow (case of Fig. 4.35B)), changes in the position of the center of mass of the liquid jet occur much more often and seem periodic. Note that despite having different time dynamics, the PDF of the center of mass appears very similar in both of these cases, as illustrated in Fig. 4.35C). To further characterize the time dynamics associated with the change in position of the center of mass of the liquid core, we compute the spectrum and the autocorrelation function of the center of mass in both situations (with and without swirl), see Fig. 4.36.

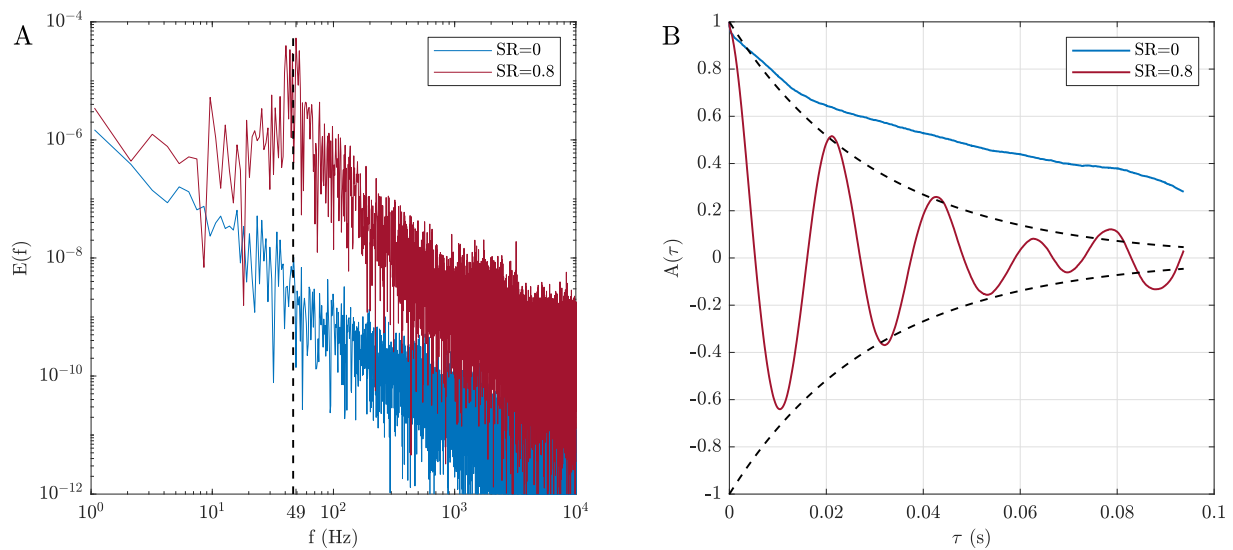


Figure 4.36: Spectra A) and autocorrelation functions B) of the time-series of the center of mass of the liquid core, with (red) and without (blue) swirl in the gas co-flow, for  $Re_l = 780$  and  $We_g = 945$  (corresponding to the unstable crown regime). The spectra were artificially separated by dividing the spectrum corresponding to  $SR = 0$  (blue curve) by 100.

The blue curves of Fig. 4.36A) and B) correspond to the spectrum, respectively to the autocorrelation function, of the time-series of the center of mass of the liquid jet in the unstable crown regime when no swirl is added. While no characteristic timescale leaves a signature on the spectrum, two slopes are highlighted by the autocorrelation function. The initial slope, steeper than the following one, corresponds to the short correlation time of the high-frequency fluctuations of the center of mass. The second slope is expected to be related to the longer correlations related to the slow changes in the position of the liquid jet. Both longer acquisitions and more statistics would be required to investigate the long-time dynamics exhibited here.

The red curves of Fig. 4.36A) and B) correspond to the spectrum, respectively to the autocorrelation function, of  $Y_M/d_l$  in the unstable crown regime when swirl is added. At low frequencies, a plateau is observed on the spectrum followed by a peak around  $f = 50$  Hz. This is already very

different from the power law found at low frequency, and the absence of peak, signature of a long-time dynamics without any characteristic frequency observed without swirl. The associated autocorrelation function initially resembles a cosinus function with an exponential decay. Fitting the autocorrelation function by  $f(t) = \cos(t/2\pi f_{fit})e^{-t/\tau_{fit}}$  up to  $t = 50$  ms, we find  $f_{fit} = 47$  Hz and  $\tau_{fit} = 30$  ms. The dashed lines of Fig. 4.36B) represents  $\pm e^{-t/\tau_{fit}}$ , showing that  $\tau_{fit}$  is a correct evaluation of the exponential decay observed on the autocorrelation function. Note that the frequency  $f_{fit}$  is compatible with the position of the peak on the associated spectrum. This shows that the liquid core has a quasi-periodic motion when swirl is added. Both the initial fast decorrelation (linked to the oscillations and crossing zero around 5 ms) and the slow decay of the exponential envelope happen faster than the decorrelation in the absence of swirl.

Note that a qualitatively similar spectra could be obtained using the model presented in Sec. 4.5.1 by introducing a temporal evolution of the circle motion within the liquid nozzle. The simplest approach would be to consider a Langevin equation for the increment of the angular position  $\theta$  of this circle, driven by a linear growth rate and some white or correlated noise to account for the fluctuations. This would typically yield a quasi-periodic signal with some fluctuation for the projection of  $\theta$  along the  $y$ -axis, corresponding to  $Y_M$ . Future work could then tackle how this dynamic evolves with the swirl ratio and try and capture it phonologically in the model.

Even though the study of the liquid core length was not conducted for such high gas velocity (see previous chapter), note that the predicted correlation time for the liquid core length  $L_B$  at this gas injection velocity (See Sec. 3.4) is  $\tau_c \simeq 0.14$  ms. The dewetting of the liquid nozzle and the breakup of the liquid jet seem to operate on timescales separated by two orders of magnitude.

A different approach to characterize the stability of the liquid core in a given position is to look at the residence time of the liquid jet at each position. In the case with no swirl (Fig. 4.35) we report three long plateaus (which have a duration of respectively 0.26 s, 0.10 s, and 0.065 s), 5 plateaus of duration spanning from 0.03 s to 0.05 s, and 13 of shorter durations ( $< 0.02$  s). To be able to conclude on the distribution of the lifetime of each position we would need many more changes in position (in other words longer movies), but it already seems that these changes in position occur on a wide range of timescales.

To measure the residence time of the liquid core in a given state when swirl is induced in the gas co-flow, we transform the time series of the center of mass in a ternary signal for which the lower value corresponds to a liquid jet being on the left ( $Y_M < -Y_C$ ), the highest value corresponds to a liquid jet positioned to the right ( $Y_M > Y_C$ ) and a value of 0 is assigned if the liquid jet is centered ( $|Y_M| < Y_C$ ), where  $Y_C$  is a threshold value separating the three possible stages for the center of mass. With the model introduced in Sec. 4.5.1 in mind, this separates the projection of the azimuthal motion of the liquid core into three categories: liquid core measured to the apparent left and right (left and right part of the circle when looking at the situation along the  $y$  axis, as sketched in Fig. 4.34), and liquid core in the center (which corresponds to a liquid core

being in front or behind in that representation, which as stated is less probable).

Note that the differences in terms of temporal dynamics found between the no-swirl or swirl cases are reminiscent to the differences found in the case of the wake behind a bluff body or sphere [104, 105] and further exploring this analogy poses itself as interesting future work.

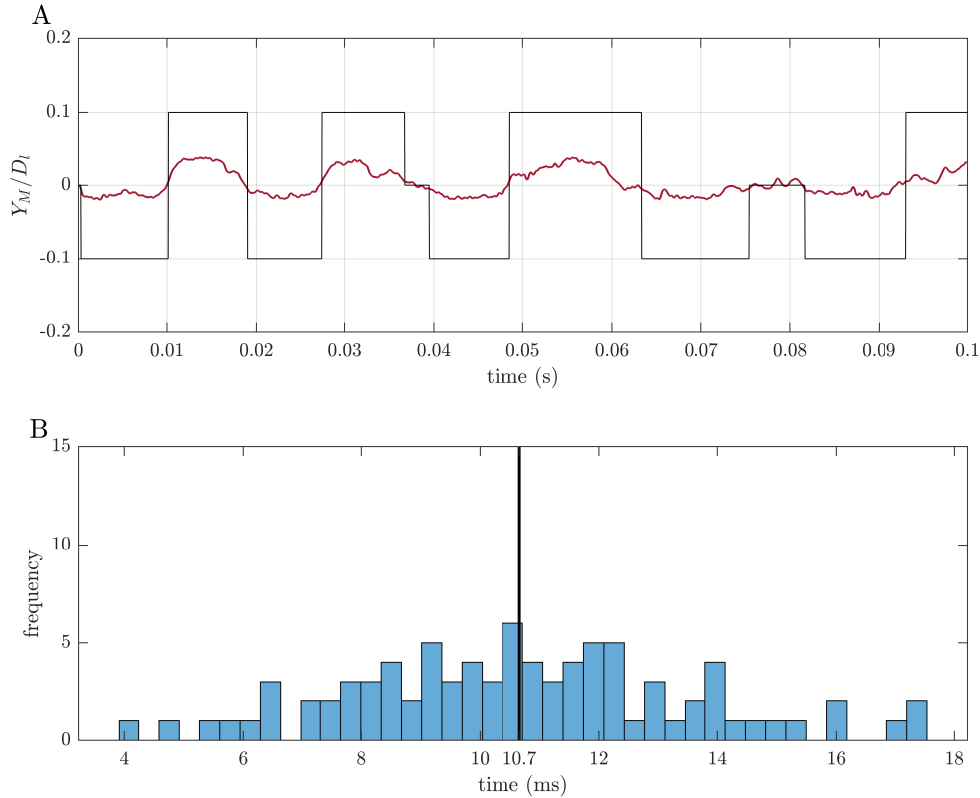


Figure 4.37: A) The red curve corresponds to the time series of the center of mass of the liquid jet in the unstable crown regime when swirl is added, the black curve is the associated ternary signal. B) Histogram of the residence time of the liquid jet on the side of the nozzle.

Figure 4.37A) shows the time series of  $Y_M/d_l$  obtained by measurements of the EPL when swirl was added in red, and the associated ternary signal in black. Figure 4.37B) shows a histogram of the residence time of the liquid jet in each position (corresponding to the duration of each plateau of the black ternary signal of Fig. 4.37A)). The black solid line corresponds to the average residence time. The residence times ranges from 4 to 18 ms. Evaluating the residence time with the frequency  $f_{fit}$  measured from the autocorrelation function of the signal  $\tau_{res} = 1/2f_{fit}$  (the factor 2 standing for the fact that the liquid jet hovers from the left to the right during  $1/f_{fit}$ ), we find  $\tau_{res} = 10.6$  ms. This evaluation of the residence time using the frequency of the quasi-periodic signal compares well with the maximum probability displayed by the distribution of residence times shown in Fig. 4.37.

## 4.6 Discussion and future work

Using X-ray imaging, we were able to study the dense two-phase flow of the near-field of coaxial gas-assisted atomization, at high gas velocities (up to Mach numbers of 0.94), on a wide range of injection parameters. Following the work of Machicoane et al. [3], we validate that the intact core and the crown regimes can be triggered by changes of  $We_g$ . Thanks to a tight sampling of the parameter space, we established for the first time a phase diagram of the state of the liquid core in the  $\{Re_l; We_g\}$  parameter space and showed for the first time that the unstable crown regime was reached for high values of  $M$ , without adding swirl in the gas coflow. A simple model of the mechanisms involved in the change of morphology of the liquid core was introduced, leading to the identification of a dimensionless parameter characterizing the boundaries between each regime in the  $\{Re_l; We_g\}$  phase diagram. A new method for the analysis of radiographs was implemented, along with a thorough study of its limitations. Using this method to measure the center of mass of the liquid core, we were able to find a quantitative indicator of the transition from the crown regime to the unstable crown regime. We were also able to study the dewetting of the liquid nozzle in the unstable crown regime by characterizing the associated time dynamics and showed that it operates on timescales much longer than that of the breakup of the liquid jet occurring further downstream. We showed that swirl has a drastic impact on the time dynamics of the dewetting of the nozzle.

One of the goals of this experimental project was to try to extract quantitative measurements of the radiograph movies. The technique introduced in this manuscript showed some promising results, despite its limitations. To improve this analysis technique, I have identified a few key points that could be improved in future work. As explained in Sec. 4.3, the X-ray beam production had a periodic cutoff during the experiments. With the exposure time of the camera set to a different (but close) value than the time between two cutoffs, we observe fluctuations in the background intensity from one frame to another. Even though they were partially taken into account, these fluctuations could have been avoided if the acquisition frequency of the camera was synchronized with the beam production. A different way of taking these fluctuations into account could be to have a calibration object on all the images. The calibration object could then be used to correct spatial and temporal changes in intensity. Before retrieving the EPL maps, ANKAphase conducts a flat-field correction of each image which consists of dividing each frame by an averaged background movie (a movie with nothing on the path of the X-ray beam). ANKAphase proposes to use two background movies (one before and one after the movie being analyzed), which should be used to best take into account the slow drift of the intensity of the X-ray beam throughout time. In addition, taking background on the same duration as the movies would be much better, to account for the variation of the intensity along the heating of the scintillator. Similarly, the entirety of the 1.1 s acquisition window should be systematically saved for this purpose, so that the  $t = 0$  of all movies rigorously and reproducibly corresponds to the start of the heat load on the crystal. Finally, the computation of the EPL map conducted by

ANKAphase appears to be corrupted by the presence of aluminum within the radiographs. This could be fixed by artificially removing the nozzle during the post-processing.

# Conclusion and perspectives

We built a coaxial gas-assisted atomization setup capable of inducing angular momentum in the gas jet (swirl) and with the unique ability to modulate the turbulent rate of the gas jet. A study of the liquid core length  $L_B$ , defined as the longitudinal extent of the portion of liquid hydraulically connected to the injected was conducted using high-speed back-lit imaging. We completed previous studies of the statistics of  $L_B$ , which had primarily focused on the average, by showing that the probability density function of the liquid core length can be described using a skew-Gaussian function. The scaling law found for the average liquid core length with the dynamic pressure ratio  $M$  is compatible with prior studies (e.g. [2]) and we reported for the first time a scaling law for the standard deviation of  $L_B$ , also scaling with  $M$ . We found the ratio of the average to the standard deviation of  $L_B$  to be constant, reducing the number of parameters needed to describe the statistics of  $L_B$ . On the other hand, the third-order statistical moment, the skewness, presents a non-monotonous evolution with the gas Reynolds number  $Re_g$ . Representing the probability density function of the liquid core length with a skew-Gaussian function, it can be fully described using only two parameters: the average and the skewness of the liquid core length. We found the skewness to be constant for conditions at  $Re_g > 33000$ , reducing the number of parameters needed to describe the probability density function of  $L_B$  to one in those cases.

The statistics of the liquid core length being fully described, we further characterized  $L_B$  by studying its temporal dynamics and showed that it is governed by the gas jet. Two regimes were identified: for conditions at  $Re_g < 33000$ , equivalently  $We_g < 75$ , the autocorrelation functions of  $L_B$  follow an exponential decay, whereas conditions at  $Re_g > 33000$  initially decay faster than an exponential. However, in both cases, the correlation time is found proportional to a time based on the gas jet  $T_g = \frac{d_g}{U_g} \propto Re_g^{-1}$ , with a weak dependency of the turbulent state of the liquid jet.

The wide range of operating conditions (93 different operating conditions), encompasses the transition from the bag-breakup regime to fiber-type atomization. We presented a phase diagram for the breakup mechanisms based on qualitative observations of the breakup process, and the boundary between the region corresponding to membrane breakup and the region corresponding to fiber-type atomization is compatible with previous work [19]. Thanks to a tight sampling of the parameter space, we found that the onset of fiber-type atomization occurs around  $Re_g = 33000$  (equivalently  $We_g = 75$ ), corresponding to the change of shape of the autocorrelation functions. Furthermore, a change of the shape of the distributions of  $L_B$  also occurs around  $Re_g = 33000$ . Conditions with  $Re_g > 33000$  collapse on a mastercurve while conditions with  $Re_g < 33000$  present smaller skewness values. Both the shape of the probability density function and the shape of the autocorrelation function contain a signature of the rise of fiber-type atomization, which constitutes two quantitative indicators of the change of atomization regime.



These results are based on measurements conducted on a wide range of operating conditions, and the standardized process developed for the acquisition and the post-processing of back-lit imaging ensures the reproducibility of the results. This constitutes a solid foundation for the study of the influence of the turbulent properties of the gas flow and of the influence of swirl which can be conducted on the experimental setup.

Despite the wide range of operating parameters for which the breakup process can be studied using visible light, conditions with high gas velocities yield a dense two-phase flow which prevents proper identification of the liquid-gas interface. To study these conditions, we conducted propagation-based phase contrast imaging with penetrative light (X-rays). With this technique, the numerous small liquid structures overlapping the liquid core are filtered, leading to proper visualization of the liquid cores breakup.

We reported 4 morphologies for the breakup of the liquid core. 1) The intact core regime, characterized by an intact central bulk whose surface is destabilized by ligaments and sheets of liquid; 2) the crown regime, where the liquid core is hollow and ligaments are directly stripped on the edge of the liquid core; 3) a transitional state between the intact core and the crown regime, where small inclusions of gas are observed in the liquid core; and 4) the unstable crown regime in which the liquid cores morphology is close to that of the crown regime, with the addition of drastic dewetting of the liquid injector. While the intact core and the crown were reported previously over several values of the Weber number, Machicoane et al. only observed unstable crowns for conditions with gas swirl [3]. In addition the influence of liquid injection on the breakup morphology regime had not been studied, and its exploration led to uncover the existence of high- $M$  unstable crown without gas swirl, and of the transitional liquid core. Thanks to a wide parameter space explored (102 operating conditions distributed on a parameter space with  $19000 < Re_g < 200000$  and  $780 < Re_l < 4300$ ), we established for the first time the breakup morphology phase diagram in the  $\{Re_l; We_g\}$  parameter space. Considering a simple kinetic energy balance argument, we expect the gas-to-liquid momentum ratio defined on the gas inner boundary layer  $MR_{\delta_g}$  to capture the transitions from the transitional regime to the crown regime, and from the crown regime to the unstable crown regime. This was verified on the phase diagram, with the frontier between these regimes following iso- $MR_{\delta_g}$  lines.

A framework to perform quantitative measurements of the liquid's spatial distribution from the X-ray radiographs was developed, adapted from pre-existing post-processing method. We showed the limitations of the method and were able to measure the coordinate of the center of mass of the liquid core on individual frames. Studying the time series of the center of mass of the liquid core, we found a quantitative indicator of the transition from the crown to the unstable crown regime. We were also able to study the dynamics of the dewetting of the liquid nozzle in the unstable crown regime and showed that the associated timescales are orders of magnitude longer than that of the breakup of the liquid jet. We also highlighted that swirl has a strong influence on the dynamics of the liquid core in the unstable crown regime.

Up to now, the dynamics of mechanisms involved in the breakup of a liquid jet in coaxial gas-assisted atomization have been shown to depend on the properties of the gas jet only, here for instance with the liquid core correlation time, but also for other mechanisms of gas-assisted atomization [13, 15, 22, 31]. We showed that the transition to the unstable crown regime can be triggered by variations of  $MR_{\delta_g}$  (hence the velocity of the liquid at injection), suggesting that the liquid velocity at injection has a strong influence on the stability of the liquid core, and therefore influences the associated dynamics.

The solid basis of measurements conducted on a wide parameter range, along with the development of the post-processing method constitutes a solid basis for the experimental study of the breakup in the near-field of coaxial gas-assisted atomization at high gas flow rates.

# List of Figures

1.1	Sketch of an aircraft turbojet engine. Source: Jeff Dahl, CC BY-SA 4.0 . . . . .	2
1.2	Stability curve of a cylindrical liquid jet. The average liquid breakup length is plotted as a function of the liquid Reynolds number $Re_l$ . The measurements were conducted on the experimental setup built during this Ph.D. . . . .	4
1.3	Sketch of the experimental setup used by Matas et al. [31] to modulate the turbulent intensity in the gas flow of a planar atomization setup. . . . .	10
1.4	Back-lit image of the near field of the atomization process in a coaxial two-fluid configuration. The red contour highlights the outline of the liquid core and its longitudinal extent $L_B$ is shown on the left. . . . .	12
2.1	Image of the coaxial two-fluid atomizer at LEGI. The nozzle is attached to a frame on the top of the image and the flowloop regulating the flows is shown in the back. . . . .	17
2.2	a) Schematic side-view of the atomizer showing the different inlets of the atomizer. $D_l$ , $d_l$ , and $d_g$ are shown on the sectional view of the bottom of the atomizer pointed to by an arrow. b) Horizontal cross-section of the atomizer, highlighting the relative position of the swirl inlets to the main inlets. c) Cross-section of the atomizer, showing the position of the turbulent tuning inlets. . . . .	19
2.3	A) Structures holding the flow loop. 1) Structure holding the flow conditioning system. 2) Pressure vessel. 3) Structure holding the gas and liquid lines. B) Sketch of the different components of the flow loop. The orange circles regroup the components found on the 3 structures described in A). The elements regrouped in the orange dashed-line circle labeled 4) are not shown in A) and will be discussed in Sec. 2.1.3. . . . .	20
2.4	Front panel of the Labview program designed for the experiment. . . . .	21

- 2.5 Output of the Labview program for a typical run. The red and blue solid curves respectively show the measured main gas flow rate and swirl flow rate. The black solid curve shows the measured liquid flow rate. The red, blue, and black dotted lines represent the target flow rates set by the user for the main gas flow rate, swirl gas flow rate, and liquid flow rate respectively. The dashed line highlights the trigger sent to the camera, and the orange area corresponds to the duration of the associated movie. . . . . 22
- 2.6 Measured liquid flow rate as a function of the set liquid flow rate. The inset figure shows the corresponding relative error  $R = (Q_{l,set} - Q_{l,mes}) / Q_{l,set}$  as a function of the set liquid flow rate. . . . . 24
- 2.7 Recovering pool for the spray. 4 layers of metallic grids, as well as 6 exhaust fans, are installed in the pool to prevent gas recirculations that would affect the spray and carry small droplets. . . . . 25
- 2.8 A) Image of the jet with high-velocity gas and liquid injection without the anti-recirculation device. A signature of the gas recirculations is seen by the presence of liquid droplets next to the spray. B) Image of the jet with the same injection parameters as A), shown with the anti-recirculation device. No droplets are seen next to the spray. . . . . 25
- 2.9 Buffer tank used at the inlet of the turbulent tuning gas line . . . . . 28
- 2.10 Conditions explored throughout this Ph.D in the  $\{We_g; Re_l\}$  parameter space. The error bars are calculated with the uncertainty of the flow rates. The circled points correspond to the conditions highlighted in Table 3.1. . . . . 30
- 2.11 Snapshot of the atomization process captured using back-lit imaging,  $U_l = 0.41$  m/s,  $U_g = 30$  m/s,  $Re_l = 770$  and  $We_g = 27$ . . . . . 31
- 2.12 Sketch of the back-lit imaging. The spray is lit from one side and imaged from the opposite side. The liquid phase shadows the light targeted at the camera. . . . 32
- 2.13 Four stages of the binarization of an image of the breakup of a liquid jet. This example represents cases with a light source that presents the most inhomogeneities among the different sources used. A) Raw image on a 12-bit scale. B) Image normalized by a background, the image is displayed using the full range of the colormap [0 1]. C) Binarized image using a threshold. D) Filled binarized image. 33
- 2.14 A) Liquid jet lighted by a LED panel. B) Liquid jet lighted by a LED spotlight with a Fresnel lens. The rings observed correspond to the sections of the Fresnel lens. C) Sinuous liquid jet lighted by a LED panel (same lighting as A)). The arrow points to a region where the jet boundary becomes very narrow. . . . . 34

- 2.15 Conditions explored with back-lit imaging in the  $\{Re_l, We_g\}$  parameter space. The black lines correspond to iso-M curves. Since the mean liquid core length scales with M, cutting the parameter space into iso-M indicates the different fields of view that are required. . . . . 37
- 2.16 X-ray high-speed radiograph of the atomization process, captured at the European Synchrotron Radiation Facility,  $U_l = 0.59$  m/s,  $U_g = 160$  m/s,  $Re_l = 1100$  and  $We_g = 703$ . . . . . 38
- 2.17 A) X-ray radiograph and B) back-lit image of the atomization process, captured with the same injection parameters  $U_l = 0.40$  m/s,  $U_g = 113$  m/s,  $Re_l = 750$  and  $We_g = 390$ . . . . . 41
- 2.18 Sketch of the X-ray imaging line. The collimated X-ray beam provided by the ESRF facility is aimed at the spray and then impacts a scintillator. The scintillator converts X-ray light into visible light which is reflected on a high-speed camera. A shutter is placed in between the X-ray source and the spray to cut the X-ray source when needed. . . . . 42
- 2.19 Photon flux per  $\text{mm}^2$  at the center of the X-ray beam in A) semi-logarithmic plot and B) logarithmic plot. . . . . 44
- 2.20 Image of the hutch at ESRF with the atomization setup. A) flow conditioning loop. B) translation stage. C) Atomizer. The yellow arrow illustrates the path of the X-ray beam, it comes into the hutch through a hole in the back wall, goes beneath the atomizer, and targets the imaging system which is further behind in the hutch. . . . . 45
- 2.21 Back-lit image of the breakup of a liquid jet by a coaxial gas coflow, the injection parameters are  $U_l = 0,41$  m/s and  $U_g = 30$  m/s. The 5 colored squares highlight the positions of the 5 windows used for the independent X-ray movies for the same injection rates. . . . . 46
- 2.22 Explored conditions in the  $\{Re_l, We_g\}$  parameter space. The black lines correspond to iso-M curves. Black dots correspond to injection conditions that were studied using X-ray imaging only, and blue dots correspond to injection conditions that have been studied using both back-lit and X-ray imaging. . . . . 47
- 3.1 A: Schematic view of the atomizer, including a cross-section of the exit plane showing the relevant dimensions. B: Example sub-sample time series of liquid core length  $L_B$ . C: Detection of the liquid core length on an instantaneous image. 54

- 3.2 A, B and C: Normalized images of the jet for 3 different operating conditions. A:  $M = 10.7$ ,  $Re_l = 2200$ , and  $Re_g = 71000$ . B:  $M = 0.7$ ,  $Re_l = 8500$ , and  $Re_g = 71000$ . C:  $M = 0.4$ ,  $Re_l = 2300$ , and  $Re_g = 14000$ . Probability density functions (D) and auto-correlation functions (E) computed for the 3 injection conditions illustrated in A, B, and C. . . . . 56
- 3.3 Probability density function of the liquid core length normalized by the inner liquid diameter (same condition as Fig. 3.2A). Gaussian, skew-Gaussian (see Eq. 3.1), and Gamma functions are represented respectively in blue dotted line, black dashed line, and red dash-dotted line (parameters directly obtained from the first three statistical moments of the data). . . . . 58
- 3.4 Average (A) and standard deviation (B) of the liquid core length normalized by the inner liquid diameter  $d_l$  as a function of the gas-to-liquid dynamic pressure ratio  $M$ . Membrane-breakup, fiber-type breakup, and transitional regimes are represented using circles, squares and diamonds respectively. Power law fits  $AM^n$  are shown in solid red line with A:  $A_{avg} = 12.8 \pm 0.8$  and  $n_{avg} = -0.34 \pm 0.04$ ; B:  $A_{STD} = 2.14 \pm 0.12$  and  $n_{STD} = -0.30 \pm 0.03$ . . . . . 59
- 3.5 Probability density functions of the centered and normalized liquid core length  $\tilde{L}_B = \frac{L_B - \langle L_B \rangle}{L_{B,STD}}$  for every operating condition. The black curve corresponds to a skew-Gaussian function with zero average, unit standard deviation, and whose skewness is computed by averaging the skewness obtained for every experimental condition. . . . . 62
- 3.6 Skewness of the liquid core length as a function of the gas-to-liquid dynamic pressure ratio  $M$  (A) and gas Reynolds number  $Re_g$  (C). For conditions with  $Re_g > 33000$ , alternatively  $We_g = 75$ , we compute the average skewness  $\langle \beta_{L_B} \rangle = 0.46$  and the standard deviation of the skewness,  $\beta_{L_B,STD} = 0.07$ . The dashed line corresponds to  $\langle \beta_{L_B} \rangle$  and the dashed-dotted line to  $\langle \beta_{L_B} \rangle \pm \beta_{L_B,STD}$ . Ratio of the standard deviation to the average value of the liquid core length  $I_{L_B} = L_{B,STD} / \langle L_B \rangle$  as a function of  $M$  (B) and  $Re_g$  (D). We compute the average and standard deviation of  $I_{L_B}$ , respectively  $\langle I_{L_B} \rangle = 18.1\%$  and  $I_{L_B,STD} = 2.6\%$ . The dashed line corresponds to  $\langle I_{L_B} \rangle$  and the dashed-dotted line to  $\langle I_{L_B} \rangle \pm I_{L_B,STD}$ . The x-axes are divided into bins to compute averages and standard deviations of  $\beta_{L_B}$  (C) and  $I_{L_B}$  (D) to form box-and-whisker plots. Membrane-breakup, fiber-type breakup, and transitional regimes are represented using circles, squares and diamonds respectively. . . . . 63
- 3.7 Auto-correlation functions of  $L_B$  as a function of the normalized time lag  $\frac{\tau}{\tau_c}$ . A: linear ordinate. B: logarithmic ordinate. The black curve corresponds to  $\exp\left(-\frac{\tau}{1.33\tau_c}\right)$ . . . . . 64

- 3.8 Correlation time  $\tau_c$  normalized by the timescale of the gas jet  $T_g$  as a function of A:  $Re_g$  and B:  $Re_l$ . The x-axes are divided into bins to compute averages and standard deviations of  $\frac{\tau_c}{T_g}$  to form box-and-whisker plots. . . . . 65
- 3.9 Qualitative phase diagram of breakup regimes in the  $\{Re_l; We_g\}$  parameter space. Red circles, black squares, and blue diamonds respectively correspond to membrane-breakup, fiber-type atomization, and to conditions where both of these breakup mechanisms coexist. The dashed line shows  $We_g = 75$  (equivalently  $Re_g = 33000$ ) and the green solid line corresponds to the transition reported by [19]. Note that the Weber number is defined as  $We_g = \rho_g U_g^2 d_l / \sigma$  in this figure. . . . . 69
- 3.10 Snapshot of the liquid jet exiting the nozzle in a still gas environment. A:  $Re_l = 2000$ , the interface of the jet remains unperturbed in the vicinity of the nozzle and the liquid jet is laminar. B:  $Re_l = 4000$ , the interface of the jet only suffers from large-scale disturbances, which suggests that the liquid jet exiting the nozzle is laminar but presents some local flow perturbations. C:  $Re_l = 8000$ , the interface of the jet presents small-scale corrugations, suggesting that the liquid jet exiting the nozzle is turbulent. . . . . 71
- 4.1 Illustration of the different steps towards quantitative analysis of X-ray radiographs. In Sec. 4.1, the raw radiographs are compared to raw back-lit images. Section 4.2 qualitatively discusses the liquid jets breakup mechanism using normalized radiographs. Section 4.3 highlights the issues encountered regarding the beam production and Section 4.4 shows an attempt to obtain quantitative measurements of the EPL. . . . . 76
- 4.2 Atomization process at:  $U_l = 0.42$  m/s,  $U_g = 30$  m/s,  $Re_l = 780$ , and  $We_g = 24$ , captured using X-ray radiography A) and back-lit imaging B). For A), several windows captured at different times are put together to fill a region of similar dimension in the  $(x; y)$  plan than for B). . . . . 77
- 4.3 A) and B): Radiographs of a bag breakup before, respectively after, the bag bursts. The raw images are normalized by a background. . . . . 78
- 4.4 Atomization process at:  $U_l = 0.42$  m/s,  $U_g = 82$  m/s,  $Re_l = 780$  and  $We_g = 47$ , captured using X-ray radiography A) and back-lit imaging B). . . . . 79
- 4.5 Atomization process at:  $U_l = 0.42$  m/s,  $U_g = 113$  m/s,  $Re_l = 780$  and  $We_g = 180$ , captured using X-ray radiography A) and back-lit imaging B). . . . . 80



- 4.6 Radiograph of the interior of the nozzle during the atomization process. The top and the bottom panel have different colorbar ranges to enhance visibility. The injection parameters are:  $U_l = 0.42$  m/s,  $U_g = 190$  m/s,  $Re_l = 780$  and  $We_g = 950$ . 80
- 4.7 Atomization process at:  $U_l = 0.42$  m/s,  $U_g = 163$  m/s,  $Re_l = 780$  and  $We_g = 700$ , captured using X-ray radiography A) and back-lit imaging B). . . . . 81
- 4.8 Parameter space of the X-ray radiograph movies acquired. Time-series of the highlighted points are shown in Fig. 4.9 to 4.13. . . . . 82
- 4.9 Time series of radiographs of the atomization process at the exit of the nozzle for  $U_l = 0.42$  m/s,  $U_g = 42$  m/s, i.e.  $Re_l = 780$  and  $We_g = 47$ . . . . . 84
- 4.10 Time series of radiographs of the atomization process at the exit of the nozzle for  $U_l = 0.42$  m/s,  $U_g = 82$  m/s, i.e.  $Re_l = 780$  and  $We_g = 180$ . . . . . 85
- 4.11 Time series of radiographs of the atomization process at the exit of the nozzle for  $U_l = 0.42$  m/s,  $U_g = 113$  m/s, i.e.  $Re_l = 780$  and  $We_g = 340$ . . . . . 86
- 4.12 Time series of radiographs of the atomization process at the exit of the nozzle for  $U_l = 0.42$  m/s,  $U_g = 188$  m/s, i.e.  $Re_l = 780$  and  $We_g = 945$ . . . . . 87
- 4.13 Time series of radiographs of the atomization process at the exit of the nozzle for  $U_l = 0.42$  m/s,  $U_g = 271$  m/s, i.e.  $Re_l = 780$  and  $We_g = 1950$ . . . . . 88
- 4.14 Parameter space of the X-ray radiograph movies acquired. Time-series of the highlighted points are shown in Fig. 4.12, 4.15, and 4.16. . . . . 89
- 4.15 Time series of radiographs of the atomization process at the exit of the nozzle for  $U_l = 0.59$  m/s,  $U_g = 113$  m/s, i.e.  $Re_l = 1100$  and  $We_g = 340$ . . . . . 90
- 4.16 Time series of radiographs of the atomization process at the exit of the nozzle for  $U_l = 1.18$  m/s,  $U_g = 113$  m/s, i.e.  $Re_l = 2200$  and  $We_g = 340$ . . . . . 91
- 4.17 Qualitative phase diagram of breakup morphology regimes in the  $\{Re_l; We_g\}$  parameter space. Black circles, yellow squares, blue triangles, and green diamonds respectively correspond to the intact core, the transitional, the crown, and the unstable crown regimes. The black lines correspond to iso- $M$  lines of  $M = 55$  and  $M = 180$  respectively. . . . . 93
- 4.18 A) Radiograph of the liquid jet with no gas jet. B) Radiograph of the gas jet with no liquid jet, the orange arrows represent the gas recirculation. C) Radiograph of the liquid jet's breakup process in the crown regime. . . . . 94

- 4.19 Time series of radiographs of the atomization process at the exit of the nozzle. The injection parameters are:  $U_l = 0.42$  m/s,  $U_g = 271$  m/s,  $Re_l = 780$  and  $We_g = 1950$ . . . . . 95
- 4.20 Qualitative phase diagram of breakup morphology regimes in the  $Re_l; We_g$  parameter space. Black circles, yellow squares, blue triangles, and green diamonds respectively correspond to the intact core, the transitional, the crown, and the unstable crown regimes. The black lines correspond to iso- $MR_{\delta_g}$  lines of  $MR_{\delta_g} = 50$  and  $MR_{\delta_g} = 150$  respectively. . . . . 96
- 4.21 A) Current in the ring containing the rotating electrons as a function of time, during the first 12 hours of experimental measurements (the ring tension is kept constant). B) Average intensity of the backgrounds captured during the first 12 hours of data acquisition normalized by the maximum average intensity found during this period, as a function of the time passed after the beginning of the hour (approximate time after the filling of the ring) the data was acquired. . . . . 97
- 4.22 A) Example background radiograph, obtained by averaging 1000 radiographs with no objects in front of the beam. B) Average intensity of a background normalized by the maximum average intensity of the background as a function of time. . . . . 99
- 4.23 Image of the user interface of ANKAphase. . . . . 102
- 4.24 Three different stages of the process of radiographs of the atomization process with ANKAphase. A) raw image, B) raw image normalized by a background, and C) Phase map obtained with ANKAphase. The colorbars were adapted to enhance visibility. . . . . 102
- 4.25 A) Sketch of an X-ray beam going through a laminar liquid jet. B)  $(y; z)$  plane, containing the X-ray beam shown in A). The liquid thickness, or EPL, the X-ray beam that goes through  $h$  is highlighted in red. . . . . 103
- 4.26 A) Radiograph of the liquid jet, normalized by a background. B) Corresponding phase retrieved image of the liquid jet, obtained with ANKAphase. C) The red curve corresponds to the line of the phase retrieved image shown in dashed-line in B), and the black dotted line corresponds to the associated fit, with  $r^2 = 0.9999$ . The radius of the liquid jet measured on the normalized image (shown with black arrows in A)) is  $R_{mes} = 1.045$  mm and the radius obtained with the fit of the phase retrieved image at the corresponding height is  $R_{fit} = 1.06$  mm . . . . 104

- 4.27 A) Radius measured using the normalized image  $R_{mes}$  (see Fig. 4.26A)) and fitted radius  $R_{fit}$  as a function of  $x$ . B)  $r^2$  of the fit done for each pixel line. The black dot highlights the pixel line illustrated in Fig. 4.26. . . . . 105
- 4.28 A) Representation of a movie, highlighting the pixel line at which  $\alpha$  and  $\beta$  are determined in this example. B) Fitted value of  $\alpha$  as a function of time, obtained for the pixel line highlighted in A). The dashed-line corresponds to  $\langle \alpha \rangle$  and the dotted-lines to  $\langle \alpha \rangle \pm \text{std}(\alpha)$ , with  $\langle \alpha \rangle = 0.91$  and  $\text{std}(\alpha) = 0.028$  being the average and the standard deviation of  $\alpha$  for the presented time series. C) Fitted value of  $\beta$  as a function of time, obtained for the pixel line highlighted in A). . . 106
- 4.29 A) The blue curve represents the time series of  $\beta$  obtained by fitting the phase retrieved image at a fixed height  $x$ , as shown in Fig. 4.28A), and the red curve corresponds to the minimum of the phase of the pixel line ( $\min_x(\varphi)$ ) used to obtain  $\beta$  (red dotted line of Fig. 4.28A)) as a function of time (for each time step,  $\min_x(\varphi)$  stands as the minimum value of  $\varphi$  on the pixel line found at a given  $x$  location, meaning that  $\min_x(\varphi)$  is only a function of  $x$  and  $t$ ). B)  $\beta/\min_x(\varphi)$  as a function of time. . . . . 107
- 4.30 Time average of  $\alpha$  A) and  $\beta/\min_x(\varphi)$  B) as a function of the longitudinal distance  $x$ , for 4 independent movies of a laminar liquid jet. Each color corresponds to a different movie, with different liquid injection rates. The error bars correspond to the standard deviation of the time series of  $\alpha$ , respectively  $\beta/\min_x(\varphi)$  used to compute the average (see Fig. 4.28B and 4.29B). . . . . 108
- 4.31 Relative error  $Err$  between the measurement of the diameter of the liquid jet via determination of the EPL and the expected diameter  $D_{mes}$ , as a function of  $x$ . . . 110
- 4.32 Probability density function of the EPL as a function of the local thicknesses (estimated from direct measurements and geometrical considerations). The maximum probability for each column is displayed in red. . . . . 111
- 4.33 A) to E): Probability density function of the normalized center of mass  $Y_M/d_l$  calculated from the equivalent path length measurements of the liquid jet at  $x = d_l/2$ , for increasing values of the injection gas velocity (corresponding to  $We_g = 47, 180, 340, 945, 1950$ ), at constant liquid injection velocity ( $Re_l = 780$ ). F): Superposition of the probability density functions presented in A) to E). . . . . 113
- 4.34 A) Schematic representation of the liquid jet morphology in the unstable crown regime used to explain the shape of the PDF observed in Fig. 4.33D) and E). B) Probability density function of the center of mass projected on the  $y$ -axis obtained with the model sketched in A), corresponding to Eq. 4.7 . . . . . 114

- 4.35 Time-series of the center of mass of the liquid jet in the unstable crown regime without A) and with B) swirl in the gas co-flow, for  $U_l = 0.41$  m/s,  $U_g = 188$  m/s,  $Re_l = 780$  and  $We_g = 945$  (corresponding to the unstable crown regime). C) Probability density function of the center of mass of the liquid core of A) and B). 116
- 4.36 Spectra A) and autocorrelation functions B) of the time-series of the center of mass of the liquid core, with (red) and without (blue) swirl in the gas co-flow, for  $Re_l = 780$  and  $We_g = 945$  (corresponding to the unstable crown regime). The spectra were artificially separated by dividing the spectrum corresponding to  $SR = 0$  (blue curve) by 100. . . . . 117
- 4.37 A) The red curve corresponds to the time series of the center of mass of the liquid jet in the unstable crown regime when swirl is added, the black curve is the associated ternary signal. B) Histogram of the residence time of the liquid jet on the side of the nozzle. . . . . 119
- A.1 A) B) Average, respectively standard deviation, of  $L_B/d_l$  as a function of the threshold used to compute the time series of  $L_B$ . The vertical lines correspond to the threshold values chosen by the user for both of the conditions. . . . . 145
- A.2 A) B) Skewness, respectively correlation time, of  $L_B$  as a function of the threshold used to compute the time series of  $L_B$ . The vertical lines correspond to the threshold values chosen by the user for both of the conditions. . . . . 146
- B.1 Sketch of the 2-camera back-lit imaging setup. For each of the orthogonal cameras, the spray is lit from one side and imaged from the opposite side. . . . . 147
- B.2 Joint probability functions  $P(L_{B1}; L_{B2})$  for A) the membrane breakup regime and B) the fiber-type regime. . . . . 148
- B.3 A) Average and B) standard deviation of the time series of the liquid core length  $L_B$  computed using only one camera as a function of the average, respectively the standard deviation, computed using the corrected time-series  $L_{B0}$ . The inset of each figure represents the relative error of the statistical moment computed with the corrected time-series  $L_{B0}$  and with the time series measured using only one camera, as a function of  $Re_g$ . The errorbars correspond to the average  $\pm$  the standard deviation of the relative error obtained for conditions with the same  $Re_g$ . 149

- B.4 A) Skewness of the time series of the liquid core length  $L_B$  computed using one camera, as a function of the skewness computed using the corrected time-series  $L_{B0}$ . The inset represents the error of the skewness computed with the corrected time-series  $L_{B0}$  and with the time-series measured using only one camera, as a function of  $Re_g$ . B) Correlation time obtained with the time series of the liquid core length  $L_B$  computed using one camera, as a function of the correlation time computed using the corrected time-series  $L_{B0}$ . The inset represents the relative error of the correlation time computed with the corrected time-series  $L_{B0}$  and with the time-series measured using only one camera, as a function of  $Re_g$ . . . . 150
- C.1 Convergence study showing the relative error on the three first statistical moments as a function of the number of independent frames, assessed against 2600 total independent frames (140000 captured frames). The dashed and dot-dashed surrounding the zero-error solid lines respectively represent 2 and 5% errors. . . 153
- C.2 A) PDF of the centered and normalized liquid core length used for this example. Full statistics in black with the associated skew-Gaussian fit in solid line; Clipped data to a maximum liquid core length of respectively one and two standard deviations beyond the mean value in green and blue, with the respective fit in dot-dashed and dashed lines. B) Relative error on the three first statistical moments and correlation time of the liquid core length, as the vector is artificially clipped to  $\max(L_B)$  from two standard deviations below the mean to four standard deviations above the mean (corresponding to the full statistics here). . . 154

# List of Tables

2.1	Sample from the investigated operating conditions, with their corresponding dimensionless parameters. The maximum and minimum values of the presented parameters are highlighted in bold. The last column indicates the points highlighted in Fig. 2.10. . . . .	30
2.2	Table of a subset of imaging parameters used to acquire the liquid jet with back-lit imaging. . . . .	36
2.3	Sample from the investigated operating conditions for back-lit imaging, with their corresponding dimensionless parameters. The maximum and minimum values of the gas-to-liquid dynamic pressure ratio $M = \frac{\rho_g U_g^2}{\rho_l U_l^2}$ , the liquid Reynolds number $Re_l = \frac{U_l d_l}{\nu_l}$ , and the gas Reynolds number $Re_g = \frac{4Q_g}{\sqrt{4\pi A_g} \nu_g}$ are highlighted in bold. $We_g = \frac{\rho_g U_g^2 d_l}{\sigma}$ is the Weber number based on the liquid diameter. . . . .	37
2.4	Imaging parameters used at the ESRF. The size of the windows was reduced to increase the acquisition rate. The pixel size and the exposure time are $d_{\text{pixel size}} = 6.7 \mu\text{m}$ and $\tau_{\text{exposure}} = 2.5 \mu\text{s}$ respectively and are kept constant for all the runs. . . . .	43
2.5	Sample from the operating conditions investigated with X-ray imaging, with their corresponding dimensionless parameters. The maximum and minimum values of the presented parameters are highlighted in bold. . . . .	47
3.1	Sample from the 93 investigated operating conditions, with their corresponding dimensionless parameters. The maximum and minimum values of the gas-to-liquid dynamic pressure ratio $M = \frac{\rho_g U_g^2}{\rho_l U_l^2}$ , the liquid Reynolds number $Re_l = \frac{U_l d_l}{\nu_l}$ , and the gas Reynolds number $Re_g = \frac{4Q_g}{\sqrt{4\pi A_g} \nu_g}$ are highlighted in bold. $m = \frac{\rho_l U_l A_l}{\rho_g U_g A_g}$ represents the liquid mass loading and $We_g = \frac{\rho_g U_g^2 d_l}{\sigma}$ the Weber number based on the liquid diameter. . . . .	55

# Bibliography

1. Tolfts, O., Deplus, G. & Machicoane, N. Statistics and dynamics of a liquid jet under fragmentation by a gas jet. *Physical Review Fluids* **8**, 044304 (2023) (cit. on pp. [iii](#), [49](#)).
2. Leroux, B., Delabroy, O. & Lacas, F. Experimental study of coaxial atomizers scaling. Part I: dense core zone. *Atomization and Sprays* **17** (2007) (cit. on pp. [iii](#), [11](#), [12](#), [51](#), [52](#), [57](#), [59](#), [122](#)).
3. Machicoane, N. *et al.* Synchrotron radiography characterization of the liquid core dynamics in a canonical two-fluid coaxial atomizer. *International Journal of Multiphase Flow* **115**, 1–8 (2019) (cit. on pp. [iv](#), [10](#), [16](#), [18](#), [29](#), [38](#), [41](#), [52](#), [79](#), [83](#), [92](#), [116](#), [120](#), [123](#)).
4. Chigier, N. & Beér, J. Velocity and static-pressure distributions in swirling air jets issuing from annular and divergent nozzles (1964) (cit. on pp. [v](#), [94](#)).
5. Wilm, M. Principles of electrospray ionization. *Molecular & cellular proteomics* **10** (2011) (cit. on p. [3](#)).
6. Rayleigh, L. On the instability of jets. *Proceedings of the London mathematical society* **1**, 4–13 (1878) (cit. on pp. [4](#), [5](#)).
7. Dumouchel, C. On the experimental investigation on primary atomization of liquid streams. *Experiments in fluids* **45**, 371–422 (2008) (cit. on pp. [4](#), [6](#), [29](#), [50](#)).
8. McCarthy, M. & Molloy, N. Review of stability of liquid jets and the influence of nozzle design. *The Chemical Engineering Journal* **7**, 1–20 (1974) (cit. on p. [4](#)).
9. Lin, S. P. & Reitz, R. D. Drop and spray formation from a liquid jet. *Annual review of fluid mechanics* **30**, 85–105 (1998) (cit. on pp. [4](#), [5](#)).
10. Constantin, W. Zum Zerfall eines Flüssigkeitsstrahles. *ZAMM-Zeitschrift für Angewandte Mathematik und Mechanik* **11**, 136–154 (1931) (cit. on p. [5](#)).
11. Faeth, G., Hsiang, L.-P. & Wu, P.-K. Structure and breakup properties of sprays. *International Journal of Multiphase Flow* **21**, 99–127 (1995) (cit. on p. [5](#)).
12. Chigier, N. Regimes of jet breakup and breakup mechanisms (physical aspects). *Progress in astronautics and aeronautics* **166**, 109–134 (1996) (cit. on pp. [5](#), [6](#), [16](#)).
13. Raynal, L. *Instabilité et entraînement à l'interface d'une couche de mélange liquide-gaz* PhD thesis (Grenoble 1, 1997) (cit. on pp. [6](#), [7](#), [50](#), [51](#), [124](#)).
14. Marmottant, P. & Villermaux, E. On spray formation. *Journal of fluid mechanics* **498**, 73–111 (2004) (cit. on pp. [6](#), [50](#), [51](#), [95](#)).
15. Matas, J.-P., Delon, A. & Cartellier, A. Shear instability of an axisymmetric air–water coaxial jet. *Journal of Fluid Mechanics* **843**, 575–600 (2018) (cit. on pp. [6](#), [50](#), [124](#)).



16. Varga, C. M., Lasheras, J. C. & Hopfinger, E. J. Initial breakup of a small-diameter liquid jet by a high-speed gas stream. *Journal of Fluid Mechanics* **497**, 405–434 (2003) (cit. on pp. [6](#), [7](#), [50](#), [68](#)).
17. Fuster, D. *et al.* Instability regimes in the primary breakup region of planar coflowing sheets. *Journal of Fluid Mechanics* **736**, 150–176 (2013) (cit. on pp. [6](#), [11](#), [50](#)).
18. Pilch, M & Erdman, C. Use of breakup time data and velocity history data to predict the maximum size of stable fragments for acceleration-induced breakup of a liquid drop. *International journal of multiphase flow* **13**, 741–757 (1987) (cit. on pp. [6](#), [50](#)).
19. Lasheras, J. C. & Hopfinger, E. Liquid jet instability and atomization in a coaxial gas stream. *Annual review of fluid mechanics* **32**, 275–308 (2000) (cit. on pp. [6](#), [9](#), [50–52](#), [67–69](#), [122](#)).
20. Chigier, N. & Farago, Z. Morphological classification of disintegration of round liquid jets in a coaxial air stream. *Atomization and sprays* **2** (1992) (cit. on pp. [6](#), [11](#), [50](#)).
21. Machicoane, N., Osuna-Orozco, R. & Aliseda, A. Regimes of the length of a laminar liquid jet fragmented by a gas co-flow. *International Journal of Multiphase Flow*, 104475 (2023) (cit. on p. [6](#)).
22. Delon, A., Cartellier, A. & Matas, J.-P. Flapping instability of a liquid jet. *Physical Review Fluids* **3**, 043901 (2018) (cit. on pp. [6](#), [50](#), [51](#), [124](#)).
23. Kumar, A. & Sahu, S. Influence of nozzle geometry on primary and large-scale instabilities in coaxial injectors. *Chemical Engineering Science* **221**, 115694 (2020) (cit. on pp. [6](#), [11](#), [51](#), [57](#), [59](#)).
24. Kaczmarek, M., Osuna-Orozco, R., Huck, P. D., Aliseda, A. & Machicoane, N. Spatial characterization of the flapping instability of a laminar liquid jet fragmented by a swirled gas co-flow. *International Journal of Multiphase Flow* **152**, 104056 (2022) (cit. on pp. [6](#), [12](#), [23](#), [29](#), [51](#), [52](#), [57](#), [60](#), [65](#)).
25. Zhao, H., Liu, H.-F., Li, W.-F. & Xu, J.-L. Morphological classification of low viscosity drop bag breakup in a continuous air jet stream. *Physics of Fluids* **22**, 114103 (2010) (cit. on pp. [6](#), [50](#)).
26. Ben Rayana, F. *Contribution à l'étude des instabilités interfaciales liquide-gaz en atomisation assistée et taille de gouttes* PhD thesis (Grenoble INPG, 2007) (cit. on p. [7](#)).
27. Marmottant, P. *Atomisation d'un jet liquide par un courant gazeux* PhD thesis (Grenoble INPG, 2001) (cit. on p. [7](#)).
28. Aliseda, A. *et al.* Atomization of viscous and non-Newtonian liquids by a coaxial, high-speed gas jet. Experiments and droplet size modeling. *International Journal of Multiphase Flow* **34**, 161–175 (2008) (cit. on p. [7](#)).

29. Singh, G, Kourmatzis, A, Gutteridge, A & Masri, A. Instability growth and fragment formation in air assisted atomization. *Journal of Fluid Mechanics* **892**, A29 (2020) (cit. on p. 7).
30. Zhao, H. *et al.* Influence of atomizer exit area ratio on the breakup morphology of coaxial air and round water jets. *AIChE Journal* **60**, 2335–2345 (2014) (cit. on pp. 9, 11, 12, 51, 57, 59).
31. Matas, J.-P., Marty, S., Dem, M. S. & Cartellier, A. Influence of gas turbulence on the instability of an air-water mixing layer. *Physical review letters* **115**, 074501 (2015) (cit. on pp. 9, 10, 19, 26, 67, 124).
32. Hopfinger, E. & Lasheras, J. Explosive breakup of a liquid jet by a swirling coaxial gas jet. *Physics of Fluids* **8**, 1696–1698 (1996) (cit. on p. 10).
33. Hardalupas, Y & Whitelaw, J. Coaxial airblast atomizers with swirling air stream. *Recent advances in spray combustion: Spray combustion measurements and model simulation*. **2**, 201–232 (1996) (cit. on p. 10).
34. Syred, N & Beér, J. Combustion in swirling flows: a review. *Combustion and flame* **23**, 143–201 (1974) (cit. on p. 10).
35. Dunand, A., Carreau, J.-L. & Roger, F. Liquid jet breakup and atomization by annular swirling gas jet. *Atomization and sprays* **15** (2005) (cit. on p. 10).
36. Machicoane, N., Ricard, G., Osuna-Orozco, R., Huck, P. D. & Aliseda, A. Influence of steady and oscillating swirl on the near-field spray characteristics in a two-fluid coaxial atomizer. *International Journal of Multiphase Flow* **129**, 103318 (2020) (cit. on pp. 10, 12, 23, 29, 33, 36, 51, 55, 57, 68).
37. Kumar, A. & Sahu, S. Optical visualization and measurement of liquid jet core in a coaxial atomizer with annular swirling air. *Journal of Flow Visualization and Image Processing* **25** (2018) (cit. on p. 10).
38. Kumar, A. & Sahu, S. Large scale instabilities in coaxial air-water jets with annular air swirl. *Physics of Fluids* **31**, 124103 (2019) (cit. on pp. 10, 12).
39. Desjardins, O., Moureau, V. & Pitsch, H. An accurate conservative level set/ghost fluid method for simulating turbulent atomization. *Journal of computational physics* **227**, 8395–8416 (2008) (cit. on p. 10).
40. Desjardins, O. & Pitsch, H. Detailed numerical investigation of turbulent atomization of liquid jets. *Atomization and Sprays* **20** (2010) (cit. on p. 10).
41. Desjardins, O., McCaslin, J., Owkes, M. & Brady, P. Direct numerical and large-eddy simulation of primary atomization in complex geometries. *Atomization and Sprays* **23** (2013) (cit. on p. 10).
42. Bianchi, G. M. *et al.* *Improving the knowledge of high-speed liquid jets atomization by using quasi-direct 3D simulation* tech. rep. (SAE Technical Paper, 2005) (cit. on p. 10).

43. Fuster, D. *et al.* Simulation of primary atomization with an octree adaptive mesh refinement and VOF method. *International Journal of Multiphase Flow* **35**, 550–565 (2009) (cit. on p. 10).
44. Gorokhovski, M. & Herrmann, M. Modeling primary atomization. *Annu. Rev. Fluid Mech.* **40**, 343–366 (2008) (cit. on p. 10).
45. Vu, L. X. *Multi-Scale Modeling and Control of Liquid-Gas Flows with a Focus on Spray Atomization* PhD thesis (Cornell University, 2022) (cit. on p. 11).
46. Lefebvre, A. H. & McDonell, V. G. *Atomization and sprays* (CRC press, 2017) (cit. on p. 11).
47. Farago, Z. & Chigier, N. *Parametric experiments on coaxial airblast jet atomization in Turbo Expo: Power for Land, Sea, and Air* **79061** (1990), V003T06A016 (cit. on p. 11).
48. Krülle, G, Mayer, W & Schley, C.-A. *Recent advances in H<sub>2</sub>/O<sub>2</sub> high pressure coaxial injector performance analysis in 26th Joint Propulsion Conference* (1990), 1959 (cit. on p. 11).
49. Eroglu, H., Chigier, N. & Farago, Z. Coaxial atomizer liquid intact lengths. *Physics of Fluids A: Fluid Dynamics* **3**, 303–308 (1991) (cit. on pp. 11, 13, 51).
50. Delon, A. *Instabilité de flapping: origine et effets sur la structure et le spray d'un jet atomisé* PhD thesis (Université Grenoble Alpes (ComUE), 2016) (cit. on p. 11).
51. Charalampous, G., Hadjiyiannis, C. & Hardalupas, Y. Proper orthogonal decomposition of primary breakup and spray in co-axial airblast atomizers. *Physics of Fluids* **31**, 043304 (2019) (cit. on pp. 12, 51).
52. Hiroyasu, H. *The breakup of high speed jet in a high pressure gaseous atmosphere in Proceedings of 2<sup>nd</sup> International Conference on Liquid Atomization and Spray Systems* (1982), 69–74 (cit. on p. 13).
53. Chehroudi, B., Chen, S.-H., Bracco, F. V. & Onuma, Y. On the intact core of full-cone sprays. *SAE transactions*, 764–773 (1985) (cit. on p. 13).
54. Yule, A. J. & Salters, D. A conductivity probe technique for investigating the breakup of diesel sprays. *Atomization and sprays* **4** (1994) (cit. on p. 13).
55. Charalampous, G, Hardalupas, Y & Taylor, A. Novel technique for measurements of continuous liquid jet core in an atomizer. *AIAA journal* **47**, 2605–2615 (2009) (cit. on p. 13).
56. Charalampous, G., Hardalupas, Y. & Taylor, A. Structure of the continuous liquid jet core during coaxial air-blast atomisation. *International journal of spray and combustion dynamics* **1**, 389–415 (2009) (cit. on p. 13).
57. Charalampous, G., Hadjiyiannis, C. & Hardalupas, Y. Comparative measurement of the breakup length of liquid jets in airblast atomisers using optical connectivity, electrical connectivity and shadowgraphy. *Measurement* **89**, 288–299 (2016) (cit. on p. 13).

58. Aliseda, A. & Heindel, T. J. X-ray flow visualization in multiphase flows. *Annual Review of Fluid Mechanics* **53**, 543–567 (2021) (cit. on p. 13).
59. Toye, D., Marchot, P., Crine, M. & L'Homme, G. Modelling of multiphase flow in packed beds by computer-assisted x-ray tomography. *Measurement Science and Technology* **7**, 436 (1996) (cit. on pp. 13, 15).
60. Heindel, T. J. X-ray imaging techniques to quantify spray characteristics in the near field. *Atomization and Sprays* **28** (2018) (cit. on p. 15).
61. Bennett, B., Hewitt, G., Kearsley, H., Keeys, R. & Lacey, P. *Paper 5: Flow visualization studies of boiling at high pressure in Proceedings of the Institution of Mechanical Engineers, Conference Proceedings* **180** (1965), 260–283 (cit. on p. 15).
62. Hewitt, G. F. & Roberts, D. *Studies of two-phase flow patterns by simultaneous x-ray and fast photography* tech. rep. (Atomic Energy Research Establishment, Harwell, England (United Kingdom), 1969) (cit. on p. 15).
63. Heindel, T. J. A review of X-ray flow visualization with applications to multiphase flows. *Journal of Fluids Engineering* **133** (2011) (cit. on p. 15).
64. Kantzas, A. Computation of holdups in fluidized and trickle beds by computer-assisted tomography. *AIChE journal* **40**, 1254–1261 (1994) (cit. on p. 15).
65. Kai, T. *et al.* Application of fast X-ray CT scanner to visualization of bubbles in fluidized bed. *Journal of chemical engineering of Japan* **33**, 906–909 (2000) (cit. on p. 15).
66. Bieberle, M. *et al.* Ultrafast cross-sectional imaging of gas-particle flow in a fluidized bed. *AIChE journal* **56**, 2221–2225 (2010) (cit. on p. 15).
67. Neumann, M., Bieberle, M., Wagner, M., Bieberle, A. & Hampel, U. Improved axial plane distance and velocity determination for ultrafast electron beam x-ray computed tomography. *Measurement Science and Technology* **30**, 084001 (2019) (cit. on p. 15).
68. Aeschlimann, V., Barre, S. & Legoupil, S. X-ray attenuation measurements in a cavitating mixing layer for instantaneous two-dimensional void ratio determination. *Physics of Fluids* **23**, 055101 (2011) (cit. on p. 15).
69. Ganesh, H., Mäkiharju, S. A. & Ceccio, S. L. Bubbly shock propagation as a mechanism for sheet-to-cloud transition of partial cavities. *Journal of Fluid Mechanics* **802**, 37–78 (2016) (cit. on p. 15).
70. Zhang, G., Khelifa, I. & Coutier-Delgosha, O. A comparative study of quasi-stable sheet cavities at different stages based on fast synchrotron x-ray imaging. *Physics of Fluids* **32**, 123316 (2020) (cit. on p. 15).
71. Zhang, G., Khelifa, I., Fezzaa, K., Ge, M. & Coutier-Delgosha, O. Experimental investigation of internal two-phase flow structures and dynamics of quasi-stable sheet cavitation by fast synchrotron x-ray imaging. *Physics of Fluids* **32**, 113310 (2020) (cit. on p. 15).

72. Khlifa, I. *et al.* Fast X-ray imaging of cavitating flows. *Experiments in fluids* **58**, 1–22 (2017) (cit. on p. 15).
73. Powell, C. F., Yue, Y., Poola, R. & Wang, J. Time-resolved measurements of supersonic fuel sprays using synchrotron X-rays. *Journal of synchrotron radiation* **7**, 356–360 (2000) (cit. on p. 16).
74. Kastengren, A. L., Powell, C. F., Arms, D., Dufresne, E. M. & Wang, J. *Spray diagnostics at the advanced photon source 7-bm beamline in ILASS Americas, 22nd annual conference on liquid atomization and spray systems, Cincinnati, OH* (2010) (cit. on p. 16).
75. Cai, W. *et al.* Quantitative analysis of highly transient fuel sprays by time-resolved x-radiography. *Applied Physics Letters* **83**, 1671–1673 (2003) (cit. on p. 16).
76. Duke, D. J., Swantek, A. B., Kastengren, A. L. & Powell, C. F. *X-ray diagnostics for cavitating nozzle flow* in *Journal of Physics: Conference Series* **656** (2015), 012110 (cit. on p. 16).
77. Wang, Y. *et al.* Ultrafast X-ray study of dense-liquid-jet flow dynamics using structure-tracking velocimetry. *Nature Physics* **4**, 305–309 (2008) (cit. on pp. 16, 38).
78. Bothell, J. K. *et al.* Comparison of X-ray and optical measurements in the near-field of an optically dense coaxial air-assisted atomizer. *International Journal of Multiphase Flow* **125**, 103219 (2020) (cit. on pp. 16, 38).
79. Huck, P., Machicoane, N., Osuna-Orozco, R & Aliseda, A. *Experimental characterization of a canonical two-fluid coaxial atomizer* in *ICLASS 2018, 14th Triennial International Conference on Liquid Atomization and Spray Systems* (2018) (cit. on pp. 18, 29).
80. Bergman, T. L., Bergman, T. L., Incropera, F. P., Dewitt, D. P. & Lavine, A. S. *Fundamentals of heat and mass transfer* (John Wiley & Sons, 2011) (cit. on pp. 18, 29).
81. Poorte, R. & Biesheuvel, A. Experiments on the motion of gas bubbles in turbulence generated by an active grid. *Journal of Fluid Mechanics* **461**, 127–154 (2002) (cit. on p. 26).
82. Ricard, G., Machicoane, N., Osuna-Orozco, R., Huck, P. D. & Aliseda, A. Role of convective acceleration in the interfacial instability of liquid-gas coaxial jets. *Physical Review Fluids* **6**, 084302 (2021) (cit. on pp. 29, 67).
83. Morgan, T *et al.* *Feasibility of Monochromatic X-ray Imaging of the Near-Field Region of an Airblast Atomizer* in *ICLASS 2018, 14th Triennial International Conference on Liquid Atomization and Spray Systems* (2018) (cit. on p. 38).
84. Li, D. *et al.* Time-averaged spray analysis in the near-field region using broadband and narrowband X-ray measurements. *Atomization and Sprays* **29** (2019) (cit. on pp. 38, 40).
85. Bieberle, M., Barthel, F., Menz, H.-J., Mayer, H.-G. & Hampel, U. Ultrafast three-dimensional x-ray computed tomography. *Applied Physics Letters* **98**, 034101 (2011) (cit. on p. 39).

86. Dawson, D., Harper, J. & Akinradewo, A. Analysis of physical parameters associated with the measurement of high-energy x-ray penumbra. *Medical physics* **11**, 491–497 (1984) (cit. on p. 40).
87. Weitkamp, T. *et al.* Status and evolution of the ESRF beamline ID19 in *AIP Conference Proceedings* **1221** (2010), 33–38 (cit. on p. 44).
88. Reveillon, J. & Vervisch, L. Analysis of weakly turbulent dilute-spray flames and spray combustion regimes. *Journal of Fluid Mechanics* **537**, 317–347 (2005) (cit. on p. 50).
89. Villermaux, E. Fragmentation. *Annu. Rev. Fluid Mech.* **39**, 419–446 (2007) (cit. on p. 50).
90. Wen, J. *et al.* A flamelet LES of turbulent dense spray flame using a detailed high-resolution VOF simulation of liquid fuel atomization. *Combustion and Flame* **237**, 111742 (2022) (cit. on p. 50).
91. Ling, Y, Fuster, D., Tryggvason, G & Zaleski, S. A two-phase mixing layer between parallel gas and liquid streams: multiphase turbulence statistics and influence of interfacial instability. *Journal of Fluid Mechanics* **859**, 268–307 (2019) (cit. on p. 50).
92. Theofanous, T. Aerobreakup of Newtonian and viscoelastic liquids. *Annual Review of Fluid Mechanics* **43**, 661–690 (2011) (cit. on p. 50).
93. Huck, P., Osuna-Orozco, R, Machicoane, N. & Aliseda, A. Spray dispersion regimes following atomization in a turbulent co-axial gas jet. *Journal of Fluid Mechanics* **932**, A36 (2022) (cit. on p. 51).
94. Kumar, A. & Sahu, S. Liquid jet breakup unsteadiness in a coaxial air-blast atomizer. *International journal of spray and combustion dynamics* **10**, 211–230 (2018) (cit. on p. 51).
95. Singh, G, Jayanandan, K, Kourmatzis, A & Masri, A. Spray atomization and links to flame stability over a range of Weber numbers and pressure ratios. *Energy & Fuels* **35**, 16115–16127 (2021) (cit. on p. 52).
96. Fong, K. O., Xue, X., Osuna-Orozco, R & Aliseda, A. Two-fluid coaxial atomization in a high-pressure environment. *Journal of Fluid Mechanics* **946**, A4 (2022) (cit. on p. 52).
97. Dimotakis, P. E. The mixing transition in turbulent flows. *Journal of Fluid Mechanics* **409**, 69–98 (2000) (cit. on pp. 67, 72).
98. Jiang, D., Ling, Y., Tryggvason, G. & Zaleski, S. *Impact of inlet gas turbulent intensity on the characteristics of droplets generated in airblast atomization* in *AIAA Aviation 2019 Forum* (2019), 3721 (cit. on p. 67).
99. Zandian, A., Sirignano, W. A. & Hussain, F. Understanding liquid-jet atomization cascades via vortex dynamics. *Journal of Fluid Mechanics* **843**, 293–354 (2018) (cit. on p. 68).
100. Zandian, A, Sirignano, W. & Hussain, F. Vorticity dynamics in a spatially developing liquid jet inside a co-flowing gas. *Journal of Fluid Mechanics* **877**, 429–470 (2019) (cit. on p. 68).



101. Pope, S. B. *Turbulent flows* (Cambridge university press, 2000) (cit. on p. 68).
102. Van Dyke, M. *An album of fluid motion* (Parabolic Press Stanford, 1982) (cit. on p. 94).
103. Weitkamp, T., Haas, D., Wegrzynek, D. & Rack, A. ANKPhase: software for single-distance phase retrieval from inline X-ray phase-contrast radiographs. *Journal of Synchrotron Radiation* **18**, 617–629 (2011) (cit. on pp. 100, 101).
104. Grandemange, M., Cadot, O. & Gohlke, M. Reflectional symmetry breaking of the separated flow over three-dimensional bluff bodies. *Physical review E* **86**, 035302 (2012) (cit. on p. 119).
105. Grandemange, M, Gohlke, M & Cadot, O. Statistical axisymmetry of the turbulent sphere wake. *Experiments in fluids* **55**, 1–11 (2014) (cit. on p. 119).



## Influence of the user-defined threshold

---

As discussed in Sec. 2.3.1, the raw images obtained with back-lit imaging are converted into binary images, where dark pixels stand where liquid is encountered and bright pixels stand where no liquid is encountered. After image normalization, this binarization process requires the use of a gray-level threshold, user-defined, corresponding to the minimum gray level of a pixel to be considered as dark (in other words this pixel corresponds to liquid, where normalized images are used with the convention that background values are close to 0 while liquid structures display values up to 1). To evaluate the influence of the choice of the threshold on the measurement of the time series of the liquid core length  $L_B$  using the method described in Sec. 2.3.1.2, a time-series of  $L_B$  is computed for each threshold value from 0.01 to 0.99 with steps of 0.01. Note that once the raw images are normalized, their values stand between 0 and 1, therefore the threshold sampling chosen here explores all the possible threshold values.

Figure A.1A) and B) show the average, respectively the standard deviation, of the liquid core length normalized by the inner liquid diameter  $d_l$ , as a function of the threshold value used for measuring  $L_B$ , in the case of fiber-type atomization and the case of membrane atomization. The value of the user-defined threshold used for both of these movies (the determination of the threshold is explained in Sec. 2.3.1.2) are shown as vertical lines in Fig. A.1.

In the case of membrane breakup atomization, the threshold values chosen by the user can vary between 0.4 and 0.8, depending on the imaging setup. The user-defined threshold for the presented movie is 0.5. Less than 3% variations of the average liquid core length are observed between a threshold value of 0.4 and of 0.5, and less than 4% variations of the standard deviation of the liquid core length are observed in the 0.4 to 0.8 range. In this regime, moderate variations of the average liquid core length with the threshold around the user-defined value of the threshold are observed.

For fiber-type atomization, the threshold values used are higher but chosen in a narrower range (typically between 0.9 and 0.95). In the case of the movie presented here, the user-defined threshold value is 0.9. We report less than 8% variations for both the average and the standard deviation of the liquid core length between a threshold value of 0.9 and a threshold value of 0.95. This higher sensitivity originates from the fact that contrary to the membrane breakup regime, in the fiber-type regime a dense two-fluid flow is observed in the near field of the atomization process. The choice of the threshold becomes more critical and has to receive more attention

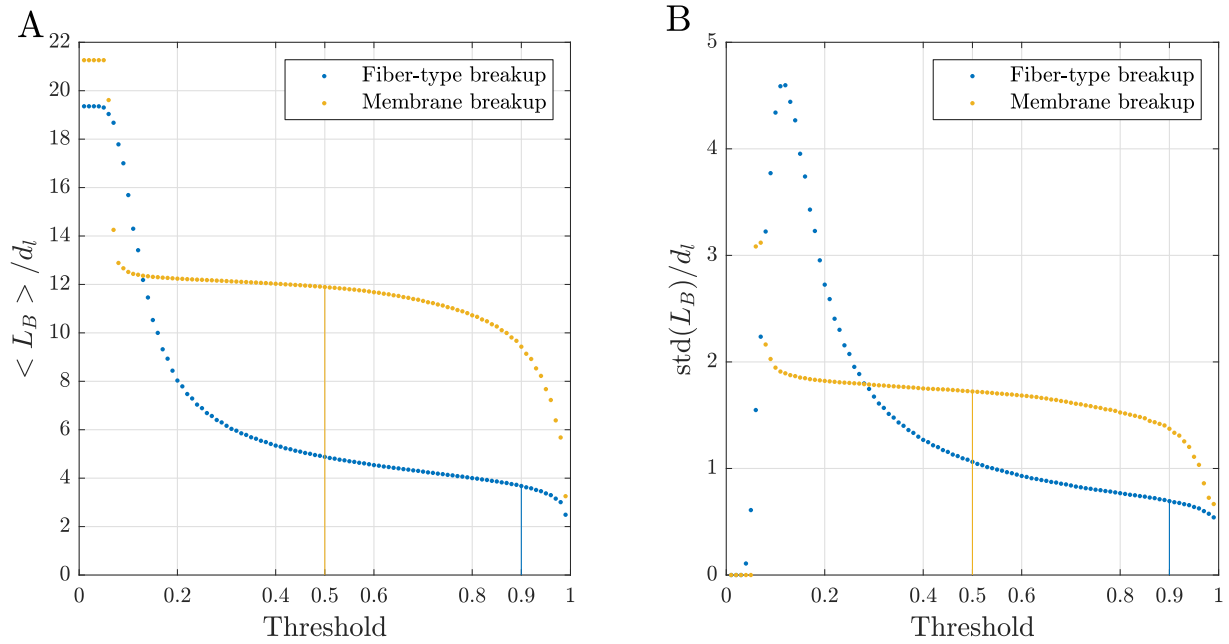


Figure A.1: A) B) Average, respectively standard deviation, of  $L_B/d_l$  as a function of the threshold used to compute the time series of  $L_B$ . The vertical lines correspond to the threshold values chosen by the user for both of the conditions.

from the user. Note that a critical value for the gas velocity was identified on the experimental system presented in this manuscript,  $U_{g,c} = 177$  m/s (equivalently  $Re_g = 110000$ ), over which proper identification of the liquid core length was considered to be too prone to thresholding biases to be able to use back-lit images.

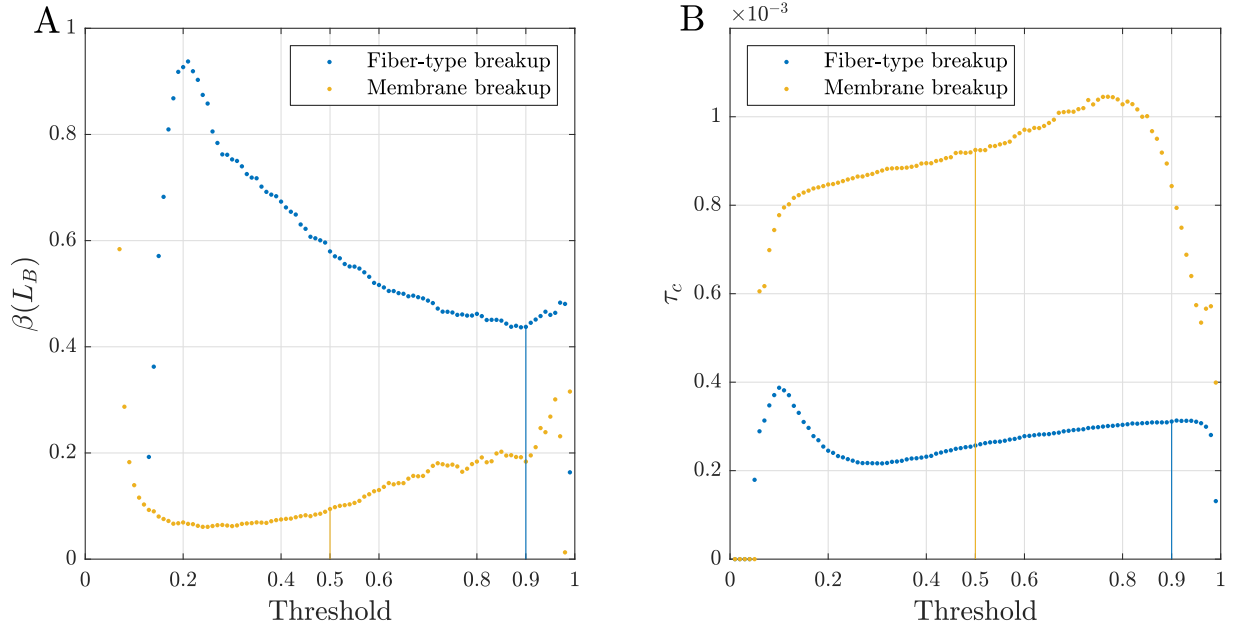


Figure A.2: A) B) Skewness, respectively correlation time, of  $L_B$  as a function of the threshold used to compute the time series of  $L_B$ . The vertical lines correspond to the threshold values chosen by the user for both of the conditions.

Figure A.2A) and B) show the skewness, respectively the correlation time, of the liquid core length normalized by the inner liquid diameter  $d_l$ , as a function of the threshold value used for measuring  $L_B$ , in the case of fiber-type atomization and the case of membrane atomization. In the case of membrane breakup, where low values of the skewness are expected, the skewness varies from 0.07 to 0.18, in the 0.4 to 0.8 range of threshold. In the case of fiber-type atomization, the skewness varies from 0.44 to 0.46 on the narrow range of threshold that is used in this regime. The uncertainty associated on the determination of the skewness associated to the choice of the threshold therefore appears smaller than the variations that are observed around the transition of the value of the skewness identified in Chap. 3, from the neighborhood of zero skewness to the asymptotic value 0.46 reached for  $Re_g > 33000$ .

We report a 10% variation of the determination of the correlation time  $\tau_c$  on the 0.4 to 0.8 range of threshold, in the case of membrane-breakup atomization, and less than 5% variation for fiber-type atomization. These fluctuations are much smaller than the spread that is observed in Fig. 3.8. The uncertainty associated to this measurement is therefore expected to be dominated by other sources of fluctuations than the user-defined thresholding process.

# Influence of the 2D projection on the determination of the statistical moments of $L_B$

---

When using back-lit imaging to capture the breakup of a liquid jet, the images correspond to a 2D projection of the liquid core. Breakup events of the liquid jet could be hidden behind overlapping liquid structures, leading to a false measure of the liquid core length. An experimental setup using two synchronized orthogonal cameras was developed to evaluate the influence of the 2D projection on the measurements of  $L_B$ , see Fig. B.1. The time series of the liquid core length is computed twice (once for each camera), and both time series are then compared. We note  $L_{B1}$ , respectively  $L_{B2}$ , the time-series of  $L_B$  computed using the movie of the first, respectively the second, camera.

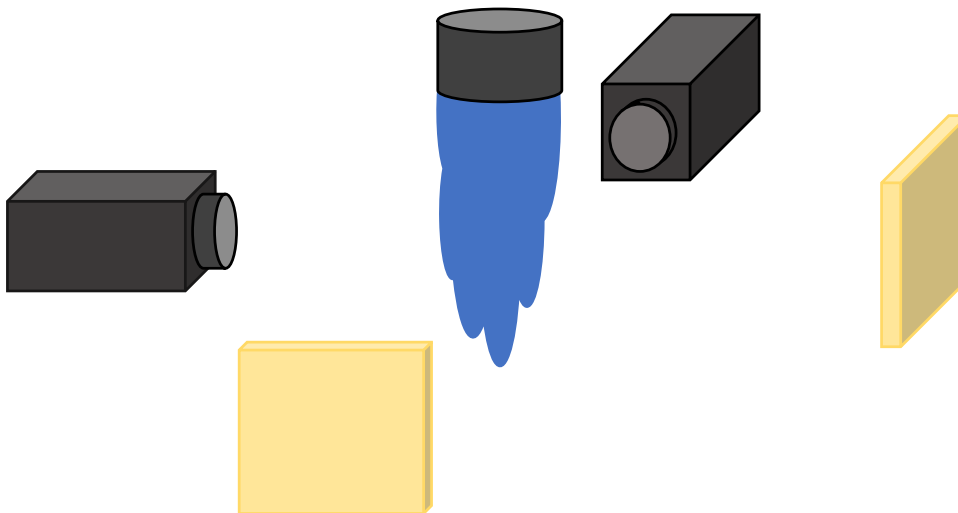


Figure B.1: Sketch of the 2-camera back-lit imaging setup. For each of the orthogonal cameras, the spray is lit from one side and imaged from the opposite side.

Figure B.2 shows two joint probability functions  $P(L_{B1}; L_{B2})$  for A) the membrane breakup regime and B) fiber-type atomization. In the membrane regime, the 2D density graph is centered around  $y = x$ . The measurements of  $L_B$  using each camera are very close, and the moderate spread shows that some breakup events are detected by one camera and not the other. Similarly, in the fiber-type regime, the 2D density plot is centered around  $y = x$  but there is more spread than in the membrane-breakup regime. Detection errors seem more prone to occur in this regime than in the previous one.

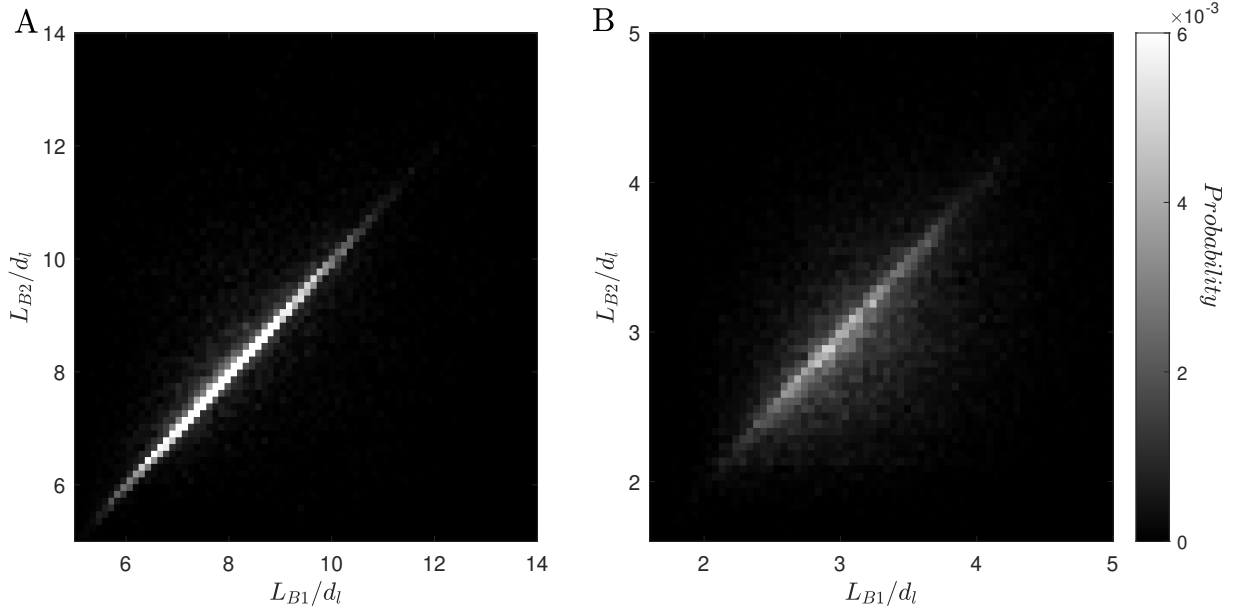


Figure B.2: Joint probability functions  $P(L_{B1}; L_{B2})$  for A) the membrane breakup regime and B) the fiber-type regime.

Assuming at least one of the two orthogonal cameras correctly detects each breakup event, we compute a corrected time-series  $L_{B0}$  by taking the minimum value of  $L_{B1}$  and  $L_{B2}$  at each time stamps, following:  $L_{B0} = \min(L_{B1}; L_{B2})$ . To characterize the influence of detection errors on the computation of the statistical moments of the distribution of  $L_B$ , we compare the statistical moments computed using the corrected liquid core length time series  $L_{B0}$  (considered here as an accurate measure of the liquid core length) with those computed using the liquid core length time-series measured using one camera. This analysis is conducted on 97 independent runs, each of which represents a different injection condition, extensively exploring the parameter space that was studied during the Ph.D.

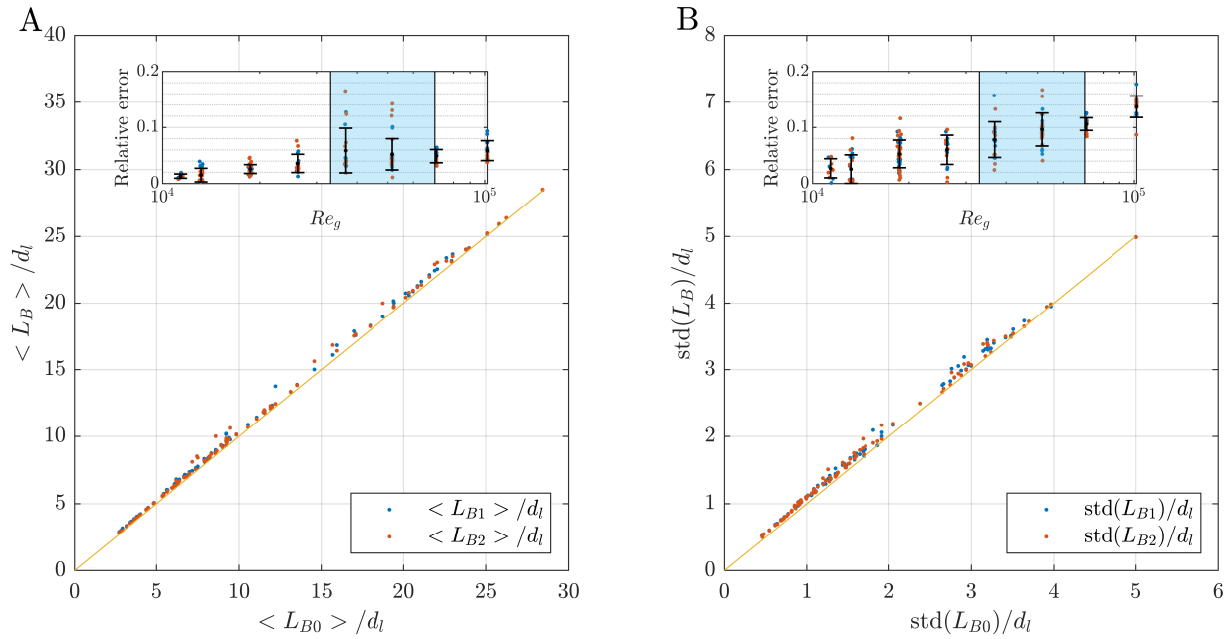


Figure B.3: A) Average and B) standard deviation of the time series of the liquid core length  $L_B$  computed using only one camera as a function of the average, respectively the standard deviation, computed using the corrected time-series  $L_{B0}$ . The inset of each figure represents the relative error of the statistical moment computed with the corrected time-series  $L_{B0}$  and with the time series measured using only one camera, as a function of  $Re_g$ . The errorbars correspond to the average  $\pm$  the standard deviation of the relative error obtained for conditions with the same  $Re_g$ .

Figure B.3A) and B) show the average, respectively the standard deviation, of the liquid core length computed using the time series of the liquid core length measured using one camera, as a function of the average, respectively the standard deviation, of the liquid core length computed using the corrected time-series of the liquid core length  $L_{B0}$ , for each of the 97 independent injection conditions that were tested. Both of these statistical moments are normalized by the inner liquid diameter, and the curve  $y = x$  is represented in orange on each plot. The average and standard deviation measured using one camera is larger than those measured using the corrected time-series  $L_{B0}$ . This is expected in the case of the average, since  $L_{B0} \leq L_{B1}$  and  $L_{B0} \leq L_{B2}$ . The inset of Fig. B.3A) and B) show the relative error between the measure of each statistical moment using the corrected time series and the measure conducted using only one camera, as a function of the gas Reynolds number  $Re_g$ . The error on each of these moments can reach up to 20% relative error, therefore detection errors most likely represent the largest source of uncertainty when measuring one of the two first-order statistical moments of the liquid core length. The blue area corresponds to the transitional state where the breakup process is a combination of fiber-type atomization and membrane breakup (corresponding to the blue points in Fig. 3.9). In the case of the computation of the average of  $L_B$ , the largest measurement errors are found to occur in this transitional state, highlighted by the errorbars. This corresponds to a regime where the choice of

the threshold is a trade-off between an accurate detection of membrane breakup events and an accurate detection of fiber-type breakup events (see Appendix A). In the case of the computation of  $\langle L_B \rangle$ , the detection errors are limited to 10% relative error for conditions that are not in the transitional state and 20% relative error for conditions in the transitional state. Although the increase of the relative error of the measure of the standard deviation in the transitional state is not as apparent as the increase observed with the average, an increase of the relative error between the computation of  $std(L_B)$  in the transitional state remains visible.

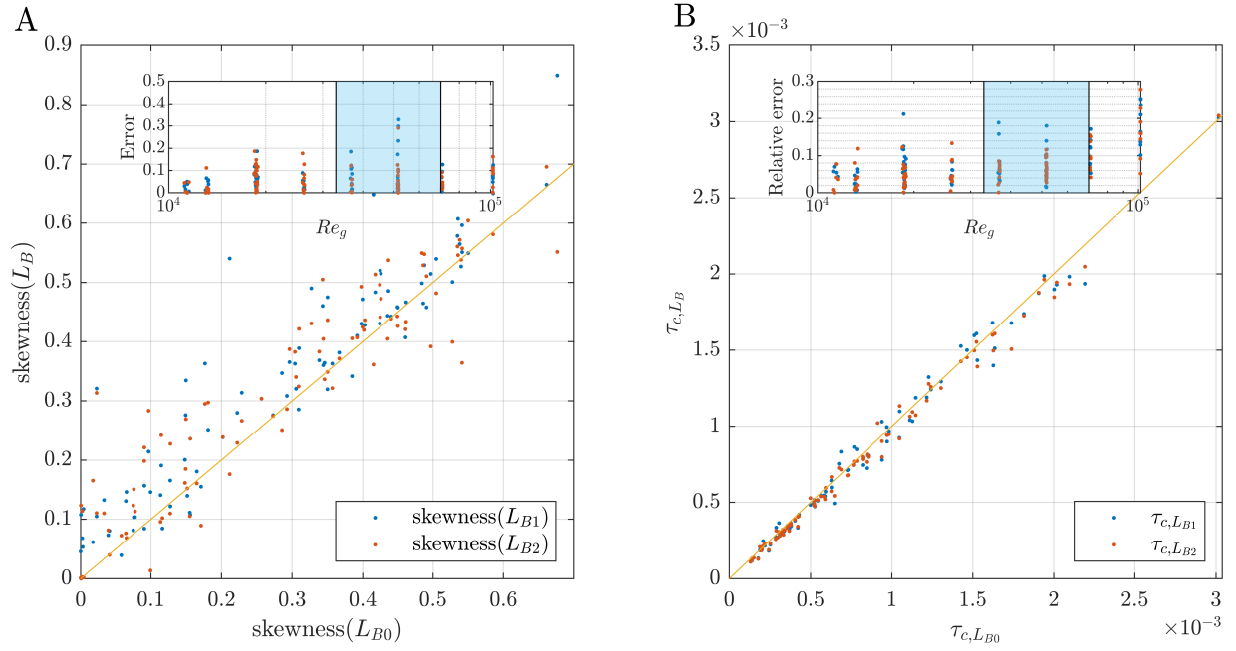


Figure B.4: A) Skewness of the time series of the liquid core length  $L_B$  computed using one camera, as a function of the skewness computed using the corrected time-series  $L_{B0}$ . The inset represents the error of the skewness computed with the corrected time-series  $L_{B0}$  and with the time-series measured using only one camera, as a function of  $Re_g$ . B) Correlation time obtained with the time series of the liquid core length  $L_B$  computed using one camera, as a function of the correlation time computed using the corrected time-series  $L_{B0}$ . The inset represents the relative error of the correlation time computed with the corrected time-series  $L_{B0}$  and with the time-series measured using only one camera, as a function of  $Re_g$ .

The same analysis is conducted with the third-order statistical moment of  $L_B$ , the skewness, and is presented in Fig. B.4A. The error between the skewness measured using only one camera and the skewness measured with the corrected time-series  $L_{B0}$  is always smaller than 0.2, except in the transitional regime where it can reach up to 0.4. This error is smaller than the increased of the skewness with the gas Reynolds number described in Chap. 3. Note that the absolute error was used here, in opposition to the relative error that was used for the other graphs of this appendix. As explained in Chap. 3, the uncertainty associated with the measure



of the skewness is higher than for the average and the standard deviation, which could be explained by a high sensitivity to errors in the detection of breakup events (as highlighted in Fig. B.4), along with the higher amount of points required to accurately measure the skewness compared to the number of points required to measure the average or the standard deviation.

Figure B.4B compares the correlation time  $\tau_c$ , obtained using one camera to the correlation time obtained using the two-orthogonal camera setup previously described. Except for one point in the membrane-breakup regime, all the other runs in this regime show less than 15% relative error between both measuring techniques. We also report a maximum of 20% relative error for conditions in the transitional regime and 30% relative error for conditions in the fiber-type breakup regime. Despite a bit of spread, the computation of the correlation time using only one camera appears robust when compared to the measure of the correlation time using two-cameras.

# Determination of the statistical moments and convergence

---

## C.1 Convergence study

To conclude the study of error analysis on the statistics and temporal dynamics of the liquid core length, we show an example convergence study. When capturing additional frames (here 4 s of data compared to the typical 1 s), one can measure the relative error on statistical quantities obtained with less data with respect to the theoretically converged value assessed from the full statistics. This study is not conducted on the correlation time, since the short times of auto-correlation functions are highly converged. However, the correlation time, or rather the number of frames it takes to reach a correlation of 0, is used to express the convergence analysis in terms of number of independent frames in Fig. C.1. As expected, higher order moments converge slower than the mean values, which become very well converge rapidly. Approximately 1000 independent snapshots would converge all moments within 2%. With the typical 500 independent frames recording throughout the experimental study of  $L_B$ , we estimate the convergence error as 3 and 12% for the standard deviation and skewness. Once some initial experiments were conducted to obtain the behavior of the moments and correlation time of the liquid core length, the remaining conditions (which constitute the majority of the parameter space sampling) were then planned out to record at framerates such that i) at least 15 points would be present on auto-correlation functions before decorrelation, ii) the number of independent frames (estimated from the knowledge of the correlation time, frame rates and total number of frames) was at least 500, and iii) the liquid core length variation were “mostly” within the field of view. This last point is detailed below.

## C.2 Overcoming clipping biases

Since the average and standard deviation of the liquid core length are both governed by the gas-to-liquid dynamic pressure ratio  $M$ , the parameter space can be divided into sections that are separated by iso- $M$  lines that indicate similar regions of variations of  $L_B$ , which can be probed by

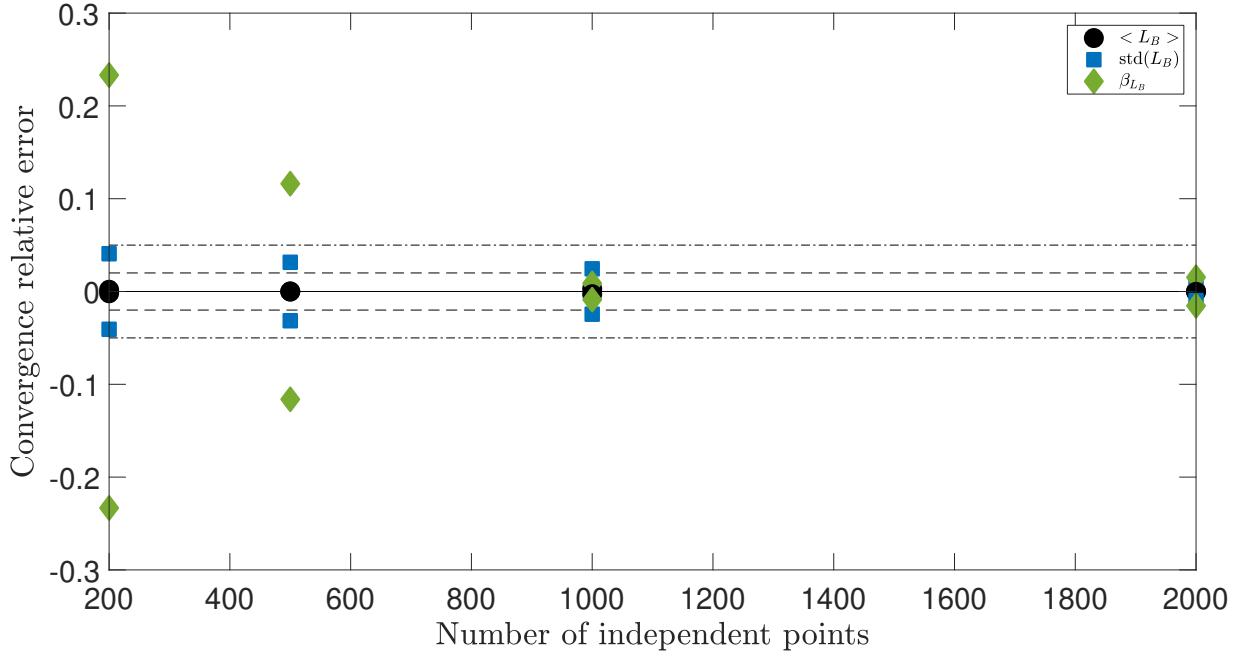


Figure C.1: Convergence study showing the relative error on the three first statistical moments as a function of the number of independent frames, assessed against 2600 total independent frames (140 000 captured frames). The dashed and dot-dashed surrounding the zero-error solid lines respectively represent 2 and 5% errors.

a similar camera's position and lens arrangement. This ensures the optimization of the imaging resolution and the detection of  $L_B$ . However, there are some conditions, typically at low  $M$  where the range of variation of the liquid core length is larger than the imaging window (that can be limited by the illumination system size but also by the compromise that needs to be met in terms of spatial resolution, given the fixed size of the camera's sensor). Note that only the standard deviation of  $L_B$  comes as a limiting factor, as the increase in average length can be tackled by changing the camera position along the spray's axis. On the one hand, it is of utmost importance to measure the minimum liquid core length, as break-up events happening before the imaging window could lead to wrong detections of  $L_B$  (with a detached liquid ligament partially on the image and touching the top boundary for instance). On the other hand, detecting an unbroken jet on the imaging window simply indicates that the liquid core length is longer than the measurement range, and one ends up with no detection (labeled *not a number* for instance, which do not limit the ability to estimate probability density or auto-correlation functions) instead of a wrong one. This results in resolving the lower liquid core length (left part of the PDF) but not all the higher values (right part) and hence a clipped signal, where the maximum measured length is smaller than the one in reality.

To measure the potential biases of clipping on the estimation of the statistics and temporal dynamics, Figure C.2 displays the full statistics obtained in a case where  $\max(L_B)$  is smaller

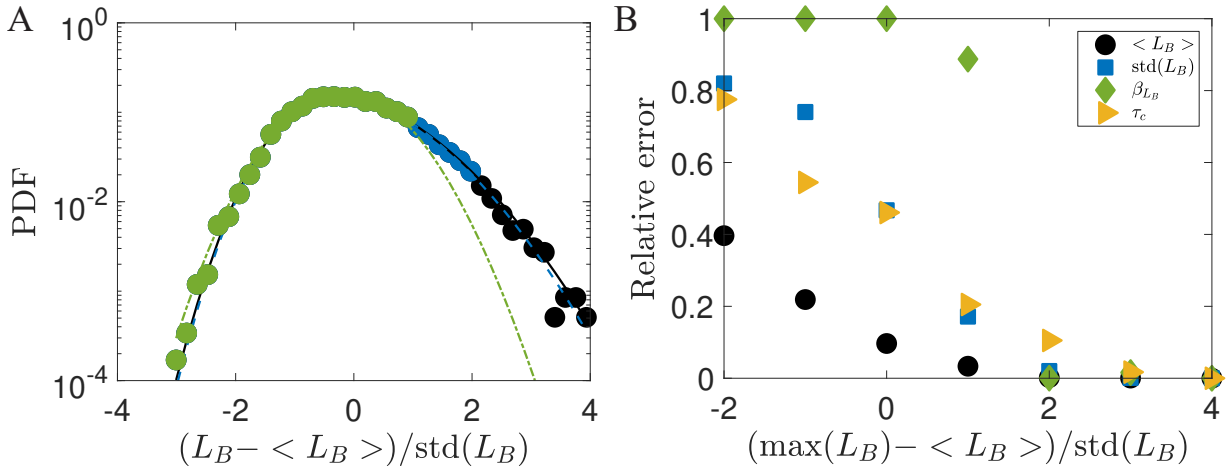


Figure C.2: A) PDF of the centered and normalized liquid core length used for this example. Full statistics in black with the associated skew-Gaussian fit in solid line; Clipped data to a maximum liquid core length of respectively one and two standard deviations beyond the mean value in green and blue, with the respective fit in dot-dashed and dashed lines. B) Relative error on the three first statistical moments and correlation time of the liquid core length, as the vector is artificially clipped to  $\max(L_B)$  from two standard deviations below the mean to four standard deviations above the mean (corresponding to the full statistics here).

than the imaging window length, along with the statistics obtained with the same vector but artificially clipped to various values of  $\max(L_B)$ . These values are expressed in terms of the standard deviation of the liquid core length obtained with the full statistics, both for better clarity and to allow for the ability to use these results when planning future experiments (since  $\text{std}(L_B)$  follows a known power law with  $M$ ). Estimating the statistics from the arithmetic definitions of the statistical moments would of course give very biased results. However, since the PDF's general shape is known to be a skew-Gaussian distribution, one can retrieve their values by fitting the clipped statistics. With that method, as long as the imaging window probes at least two standard deviations above the average value, the error from clipping is less than 2% for the average, standard deviation, and skewness of the liquid core length. That strategy cannot be employed for the auto-correlation function, which displays a clipping bias of approximately 10% in that case. Thus, the rest of the experiments were planned out to capture from the minimum value to at least two standard deviations above the average liquid core length (and 3 in most cases where the error on  $\tau_c$  is less than 2%).



**Résumé :** Nous nous intéressons à la rupture d'un jet liquide dans le cas de l'atomisation assistée en géométrie coaxiale, une situation commune à de nombreux procédés industriels. Un écoulement diphasique complexe avec une large gamme d'échelles temporelles et spatiales est observé dans le champ proche, impliquant différents mécanismes de rupture définissant différents régimes d'atomisation.

À l'aide d'imagerie haute fréquence rétro-éclairée nous nous intéressons au cœur liquide, défini comme la portion de liquide hydrauliquement connectée à l'injecteur, en étudiant les séries temporelles de son extension longitudinale  $L_B$  sur une grande gamme de paramètres. Nous démontrons que la fonction de densité de probabilité de  $L_B$  peut être représentée par une fonction gaussienne asymétrique et que le paramètre d'asymétrie contient une signature des changements de régimes d'atomisation. La dynamique temporelle de  $L_B$  est régie par l'écoulement gazeux, avec des temps caractéristiques suivant une loi d'échelle en  $Re_g^{-1}$  et une faible influence de la transition à la turbulence du jet liquide.

Pour les vitesses de gaz élevées, l'écoulement diphasique sortant de l'injecteur est optiquement dense et ne peut être observé par imagerie visible. Pour augmenter la gamme des vitesses de gaz que nous pouvons étudier, nous utilisons la radiographie haute fréquence à rayons X produits par un synchrotron. Cette technique d'imagerie pénétrante nous permet d'observer différents états de la morphologie du cœur liquide durant sa rupture et d'établir le diagramme de phase associé sur une large gamme de paramètres d'injection. Nous avons observé deux nouvelles morphologies et expliquons les transitions à l'aide d'arguments simples sur l'équilibre des énergies cinétiques de chaque phase. Une méthode de détermination de la quantité de liquide à partir des radiographies est présentée et permet de caractériser quantitativement les morphologies du jet liquide.

**Mots clés :** atomisation, écoulement diphasique turbulent, fragmentation liquide, spray, imagerie rapide, radiographie par rayon X, jets

---

**Abstract:** We are interested in the breakup of the liquid jet in the case of coaxial two-fluid atomization, a canonical breakup situation found in many natural and engineering phenomena. The breakup process is a complex two-phase flow displaying a broad range of time and spatial scales, involving different physical mechanisms that define various atomization regimes.

Using high-speed backlit imaging, we study the liquid core, defined as the liquid portion hydraulically connected to the injector, focusing on the time series of its longitudinal extent  $L_B$  on a broad parameter space. We demonstrate that the associated statistical distributions can be represented by a skew-Gaussian function and that the skewness contains a signature of changes in atomization regimes. We show that the temporal dynamics of the liquid core length are governed by the gas jet, with time scales scaling with  $Re_g^{-1}$ , and presenting a weak influence of the turbulent state in the liquid jet.

For high gas velocities, the two-phase flow exiting the injector is optically dense to visible light. To increase the range of gas velocity we can study, we perform time-resolved phase contrast radiography using synchrotron-produced X-rays. With this penetrative imaging technique, we can observe different states of the morphology of the liquid core during its breakup and establish the associated phase diagram. Two new morphologies are highlighted thanks to the broad sampling of the parameter space, and transitions are explained by simple kinetic energy balance arguments. A method is presented to extract liquid quantity from radiographs and quantitatively define the liquid core morphologies.

**Keywords:** atomization, two-phase turbulent flows, liquid fragmentation, spray, high-speed imaging, X-ray radiography, jets